THE UNIVERSITY
of EDINBURGH

This thesis has been submitted in fulfilment of the requirements for a postgraduate degree (e.g. PhD, MPhil, DClinPsychol) at the University of Edinburgh. Please note the following terms and conditions of use:

On Finite-Difference Time-Domain Sub-Gridding Algorithms for Efficient Modelling of Ground-Penetrating Radar

John Hartley

Doctor of Philosophy

University of Edinburgh

2020

Abstract

Introducing finely detailed models of GPR antennas into finite-difference time-domain forward models often results in large computation overheads. In many cases the solution becomes intractable.

The overhead increases due to the larger size of the model. This is as a result of the increase in spatial and temporal sampling required by the antenna geometry and the conditionally stable nature of the FDTD method respectively. This problem is compounded for predictive applications where the model-parameter space is non-linear and solutions derived from heuristic optimisation schemes require multiple simulation runs.

To overcome this issue this work presents a novel sub-gridded FDTD approach to model for the first time realistic descriptions of GPR antennas in half-space type problems.

The sub-gridding is performed using Huygens Sub-Gridding (HSG). This method does not limit the sub-gridding ratio and therefore a wide range of applications are possible. Also, a new method is developed called the Switched Huygens Sub-Gridding (SHSG). This method significantly improves upon the stability of the HSG, and has a superior computational performance. In addition, it is simpler to implement and optimise its performance owing to the simple nature of its stabilisation mechanism. In resonant problems, stability is shown to increase by a factor of 5.6. And computational speed is increased by a factor of 28 and 17 for a realistically modelled antenna over a buried water-filled plastic pipe using the SHSG and HSG respectively.

Furthermore, a novel effective permittivity scheme is developed for Debye media that can be applied to dielectric-dispersive and dispersive-dispersive interfaces. This technique resolves the issue of reduction in accuracy at material interfaces outside sub-gridded regions. And it can be used to increase the accuracy of the FDTD method for dispersive materials generally. The relative error is reduced from 5% to 0.6% for

the field transmitted and received by a Hertzian dipole over a dispersive half-space containing a water pipe. In addition, analytical results confirm a significant increase in accuracy for a range of soil types.

Moreover, these advances are implemented in open-source package gprMax and will be made available in a forthcoming release. The implementations take advantage of parallel architectures and are therefore very efficient. In addition, these advances are general and can be applied to several problems in GPR and to many problems in computational electrodynamics.

Acknowledgements

I would like to thank my supervisor, Dr Antonios Giannopoulos, for his guidance, expertise, humour over the past few years. Without his enthusiasm, I would have not enjoyed the experience nearly as much, nor would this thesis be nearly as interesting.

Thank you for the support from Dr Nigel Davidson and helpful technical discussions with the group at DSTL.

I would also like to say a big thank you to Dr Craig Warren for his help with the gprMax codebase, discussions over coffee and the opportunity to participate in Google Summer of Code.

Kostis Chatziioannou and Rania Patsia thank you for the daily chats, hilarity, and to my generation of John Muirians thank you for the drinks, dinners and lunches. A big thank you also to Isabel O'Hagan and Elspeth Parsons for their friendship and warm acceptance into Edinburgh life and the spectacular Wellington Place for the high ceilings.

To Katy Joy Lamb, thank you for your unwavering belief i'd get there and your perennial fresh outlook on all things.

Finally, and most of all thank you to my parents Diane and Phil. With your support, love and encouragement you have motivated me all the way along. And thank you to my brother Daniel for the hilarious impersonations of the doctor!

Contents

Appendices   **254**

A FDTD Update Equations   **255**

List of Figures

xviii

List of Tables

1

Chapter 1

Introduction

Ground-penetrating radar (GPR) was initially developed as a geophysical technique for mapping the structure of the earth's sub-surface. Now, it is also routinely used to map materials with internal structures that can't be observed directly. The fundamental idea is that electromagnetic energy radiated from an antenna penetrates a structure, and the subsequent observation and interpretation of the character of reflected energy gives rise to a description of the structure's interior. This generality results in a great range of applications. For example, from locating glacial floors to detecting the depths or re-bar in concrete.

Interpreting GPR data is often extremely difficult. This is because the reflections from finely detailed structures in the sub-surface and the radiation patterns of GPR antennas are highly complex. This in combination with the the coupling of the antenna to the ground and the excitation of resonances result in highly cluttered signals, and non-uniform field distributions. For instance, it can be difficult to determine the position of a landmine buried in a complex environment due to scattering from the surface topology and sub-surface soil structure.

For decades forward modelling of GPR problems using finite-difference time-domain (FDTD) has provided a greater insight into the behaviour of GPR. Forward modelling enables the modeller to approximate the behaviour of a real GPR system. In addition, inverse modelling can be used to estimate unknown model parameter by inversion of the real data. For instance, making a prediction of the the depth of re-bar depth in concrete from the signal recorded by the GPR device. Crucially, accurate results can only be obtained when the forward model is a good representation of the GPR system and the surrounding environment.

A great deal of work has gone into developing accurate models of antennas, soils and domain truncation boundary conditions. However, simple models of Hertzian dipoles have been used to approximate GPR antennas in many inversion models. This is problematic because although a good approximation to a GPR antenna can be found in the far field of the dipole, the field distribution of real GPR antennas in the near field is not well represented. This is especially true when the antenna is in close proximity to the surface of a half-space or close to the side of a borehole. Consequently, over the past decade much GPR research has emphasised the inclusion of realistic GPR antennas in forward models.

The main drawback of including realistic GPR antennas in forward FDTD models is that the resulting model is very computationally intensive to solve. This is because a fine discretisation must be used to model the components of the antenna. In addition, the entire computational domain must also be finely discretised when the antenna is above a half-space. Consequently, a large number of cells need to be solved in comparison to a simple antenna case. This issue is compounded in inverse problems and optimisation problems where iterative approaches require the forward model to run many times.

Although there are a number of sub-cell approaches which model objects containing details smaller than the resolution of the grid, these methods require complex pre-processing and therefore do not generalise well. A more generic solution is to use sub-gridding. Sub-gridding divides the computational domain into fine and coarsely resolved regions. Complex structures can be embedded in the fine regions, whilst broader structures can be embedded in the coarse regions. This scheme reduces the overall computational cost since there are fewer finely resolved cells and time steps to solve for.

The main aim of this research was to develop a useful and versatile FDTD sub-gridding algorithm to model realistic GPR antennas. This enables even existing models to be computed at a much faster rate. And most importantly, facilitates the computation of very large models which were previously intractable.

1.1 Overview of the thesis

Each chapter starts with a brief discussion on the chapter's contents. This is followed at the end by a summary consisting of the main findings in the chapter and some remarks. A breakdown of the chapters is as follows:

Chapter 2 - An introduction to ground-penetrating radar is given. This includes a short history of the origins of GPR, its development and common uses. This is proceeded by a discussion of operational methodologies and design principles.

Chapter 3 - Reviews forward modelling for GPR problems. First Maxwell's equations are discussed as a means to model GPR problems, and then limitations of modelling antennas over half-space using analytical techniques are explored. Subsequently, the FDTD method is discussed as a versatile numerical method for modelling GPR problems. This leads to a discussion of the benefits of sub-gridding for modelling realistic and practical antenna designs.

Chapter 4 - A novel method for smoothing Debye materials properties at dielectric dispersive interfaces is given. The method is tested against analytical results and then applied to the half-space problem. The method has been developed to enhance the accuracy of modelling complex dielectric objects and their boundaries.

Chapter 5 - Reviews FDTD sub-gridding methods. The review covers the applications of sub-gridding methods to GPR problems and their limitations.

Chapter 6 - The Huygen's sub-gridding theory is discussed. The method is known to be accurate but suffers from instabilities. Therefore an argument is made for its successful application to modelling half-space problems using data from previous numerical experiments.

Chapter 7 - A discussion is given on the implementation of the Huygen's sub-gridding as part of the open source software gprMax. Then the optimisation of the algorithm using the Cython programming language and parallelism using openMP are presented.

Chapter 8 - Numerical examples for Hertzian dipole problems are given. Novel models of sub-gridded commercial GPR antenna above and in contact with dispersive interfaces are presented. The improvements due to the new effective permittivity smoothing are shown.

Chapter 9 - The HSG is known to be unstable. A new novel sub-gridding method called the Switched Huygen's sub-gridding is presented. The method improves the stability using an artificial loss mechanism. Numerical experiments are given which show the accuracy and stability of this new method in comparison with the HSG. In addition, the effects of a range of loss factors are investigated.

Chapter 10 - The SHSG is used to sub-grid a realistic GPR antenna model over

a dispersive half-space. A comparison of the stability, accuracy and computational performance of the two methods is given.

Chapter 11 - A summary of the main findings is given. Conclusions are drawn from the findings and ideas for future work are given.

Chapter 2

Principles of Ground Penetrating Radar

2.1 Introduction

Mapping the structure and contents of earth's subsurface is of great importance to civil and environmental engineering, archaeology and the mining industry. Geophysical investigations are carried out by several techniques: seismics, electrical resistivity tomography, induced polarisation, magnetic surveying and ground-penetrating radar (Daniels, 2007a). Ground-penetrating radar responds to variations in both the dielectric and conductive properties of the sub-surface. Therefore it is particularly successful in applications where a range of different materials exist. For instance, in a survey containing plastics and metals, the two materials can be separated since they produce different responses.

GPR's efficiency and sensitivity have been improved by several technical innovations. This has led to an increase in the usage of GPR in many fields. The following historical overview is intended to provide some insight into the depth of GPR research. However, a more detailed review is given by Annan (2002); Daniels (2007a).

Electromagnetic radiation was first used to detect remote objects in an experiment performed by Hüelsmeyer (1904). In this experiment radiation from dipole antennas was reflected by a remote metal object and then captured by a receiving antenna.

During the Second World War, the need to remotely detect enemy targets such as ships and planes grew larger. This led to an increase in remote sensing with antennas.

The technique came to be known as Radio Detection and Ranging (RADAR) or radar.

The first applications of sub-surface object detection which could be called GPR were made in the 1950s and 60s. In these experiments, the depths of ice sheets and glaciers in the Yukon, Greenland and the Antarctic were measured using low-frequency radio-wave soundings (Steenson, 1951; Waite and Schmidt, 1962; Bailey et al., 1964). Also during this period, H. El-said (1956) located water tables in deserts by analysing measurements of reflections of subsurface radio-waves.

In the 1970s there was an increase in understanding of the response of materials to electromagnetic radiation (Annan, 1973). Subsequently, the use of GPR became more widespread. This can be seen in the expansion of the commercial sector. For instance, in the availability of commercial GPR systems such as the Geophysical Survey Systems International (GSSI) impulse response radar (Morey, 1974). Applications at the time included surveying for coal (Cook, 1975a) and salt deposits in the mining industry (Unterberger, 1978), archaeological surveys, and lunar exploration in the Apollo 17 mission (Porcello et al., 1974).

The 1980s and 1990s marked a new application of GPR to high-frequency mapping of the subsurface. This was in part due to interest in the remediation of contaminated land in the US and UK (Benson, 1995), and in research focused on the recovery of the unexploded ordinance from the shallow sub-surface (Chaudhuri et al., 1990). From the 2000s onward increases computational power enhanced the capability to realistically model GPR antennas in complex environments (Warren and Giannopoulos, 2011; Giannakis et al., 2015). Concurrently, this generated a greater interest in numerical inversion techniques designed to map subsurface material properties using real data as input (Klotzsche et al., 2010).

2.2   Operation of GPR

The key operating principle of GPR is that subsurface features of interest are sensed by their interaction with broadband electromagnetic pulses. The transmission and reception of pulses are achieved using antennas. Antennas are electromagnetic radiators. They transform currents in cables into electromagnetic fields in space and vice versa (Balanis, 2005).

The basic operation of a GPR system is as follows. A short current pulse is fed to a transmitting antenna and a broadband electromagnetic pulse is radiated into the surrounding area/ground collectively termed the half-space. The propagation of the

pulse in the ground is dependent on the material properties of the medium. Therefore, when the pulse encounters a change in the material properties its propagation is directly affected. Part of the pulse is reflected towards the GPR receiver. When the reflected pulse reaches the surface it is sensed by the receiving antenna. The pulse generated in the antenna is detected by a measurement of the potential across the antenna terminals. The depth of the target is calculated from the delay between transmission and reception of the pulse provided the electrical properties of the background medium that the GPR pulse propagates through are known.

2.2.1 Signal Paths

The field radiated by the transmitter travels along a number of paths. For illustrative purposes the paths are considered as rays. Theses are drawn as arrows which are perpendicular to the wavefront of the travelling wave. The paths most significant in GPR are shown in figure 2.1.
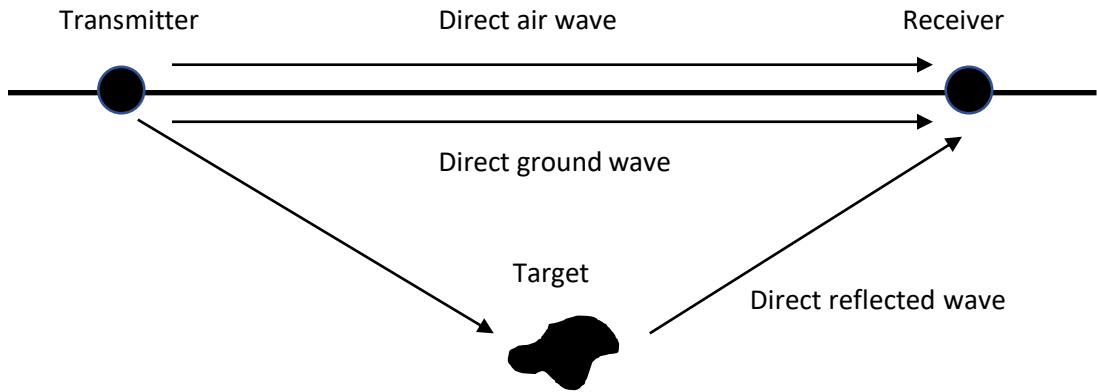
Figure 2.1: Ray-paths of significant wavelets in simple GPR half-space survey.

The direct air wave proceeds directly from the transmitting antenna to the receiving antenna. Similarly, the direct ground wave passes from the transmitting antenna into the ground and to the receiver. The direct reflected wave travels into the ground and up towards the receiver from the target. There are also the critically refracted paths. These are reflections from the target which meet the surface at the critical angle and then propagate along the surface in and out of the ground.

In reality, the transmitting antenna radiates in a 3d pattern. And consequently illuminates the entire surrounding region. Therefore, there are infinitely many paths

along which the radiation travels both above and below the ground. And therefore, in realistic scenarios where the ground is inhomogeneous, the antenna response is more complex and the exact pulse is not easily and simply obtainable.

2.2.2 Signal Propagation

The success of GPR partially depends on a clear transmission of the GPR pulse. Pulse distortion produces at best a time-dependent envelope and at worse causes the pulse to break down entirely leading to total dissipation. This is problematic as the target depths cannot be determined using the propagation characteristics of the pulse (Annan, 2005). In addition, smearing or ringing in the pulse can mask target responses, and reduce the system's ability to separate targets.

Pulse distortion is observed in the wave's physical properties, velocity v, attenuation α, and impedance Z. Since the pulse is a super-position of waves with a broad range of frequencies, any frequency dependence in the wave properties introduces dispersion in the pulse. To counter these effects the wave properties of the pulse must have at best a small frequency dependence.

The character of the wave properties at low frequencies is strongly frequency-dependent in real materials. Consequently, the character of the electric field is diffusive in this frequency regime. At higher frequencies, the wave properties are less frequency-dependent and the radiation of the electric field is wave-like. This is only the case when the underlying physical properties of the propagating material have a small frequency dependence. And therefore only materials which have a low-frequency dependence outside the low-frequency diffusive regime are suitable for GPR.

The wave properties are also dependent on the electromagnetic properties of the soil. The material parameters typically found in GPR surveys are the relative complex dielectric permittivity $\tilde{\epsilon}_r = \epsilon_r' + j\epsilon_r''$ and the electric conductivity σ [$\mathrm{S\,m^{-1}}$]. Their precise effects on wave propagation are demonstrated in the next chapter. For now, a heuristic description is useful to describe their influence in GPR problems.

σ and ϵ_r'' both have a strong effect on the attenuation of the pulse. Excessively high values reduce the amplitude of the pulse below the sensitivity of the GPR system and the signal cannot be detected. In the low-frequency range conductive losses dominate. In the higher frequency range displacement currents dominate. At frequencies above around $100\,\mathrm{MHz}$ the dielectric losses dominate due to the water content of the soil.

Dielectric losses in water occur due to the dipole relaxation effect. Water is made up

Material	Attenuation at 100 MHz [dB m^{-1}]	Attenuation at 1 GHz [dB m^{-1}]
Clay (moist)	5-300	50-3000
Loamy soil (moist)	1-60	10-600
Sand (dry)	0.01-2	0.1-20
Ice	0.1-5	1-50
Fresh water	0.1	1
Sea water	100	1000
Concrete (dry)	0.5-2.5	5-25
Brick	0.3-2	3-20

Table 2.1: Attenuation factors of materials common to GPR at 100 MHz and 1 GHz (Daniels, 2007a)

of molecules which tend to distribute charge unevenly. These molecules have a dipole moment. Under an applied electric field the dipole moments align with the field. However the work done by the field on the dipole moment against random thermodynamic forces in the water is dissipated as heat. This effect is observed as an attenuation of the electric field.

It has been established that the volumetric water content of soils is a key determining factor in the ability of a soil to attenuate radiation (Topp et al., 1980). The porosity of the soil determines the concentration of water in the soil (Annan, 2005). Other studies indicate that grain size is an important factor in determining the conductivity of the soil. An overview of the loss due to the combined effects of conductivity and dielectric loss are given in Table 2.1. The table shows that the losses at frequencies above 1 GHz are high. This indicates that only shallow GPR measurements can be made with high-frequency signals (Annan, 2005). Furthermore, clay type soils and seawater are less suited to GPR measurements than sandy soils as they have higher levels of attenuation.

2.2.3 Data Collection and Representation

GPR systems measure the variation in potential across the receiver antenna terminals. A measure of the electric field at the receiver is obtained by assuming the field between the terminals is constant and then dividing through by the separation distance of the terminals. Typically the variation in the field with time at a single survey point is represented in a plot called an A-scan.

An example of an A-scan for an antenna above a cylindrical target in an inhomogeneous half-space is shown in Figure 2.2. The first wavelet which arrives at the receiver is a combination of the direct airwave and the direct ground wave. The second wavelet is a combination of the wavelets directly reflected from the top surface of the cylinder. The arrival time for the wavelet is dependent on the dielectric properties of the half-space and the positions of the antenna, receiver and target.
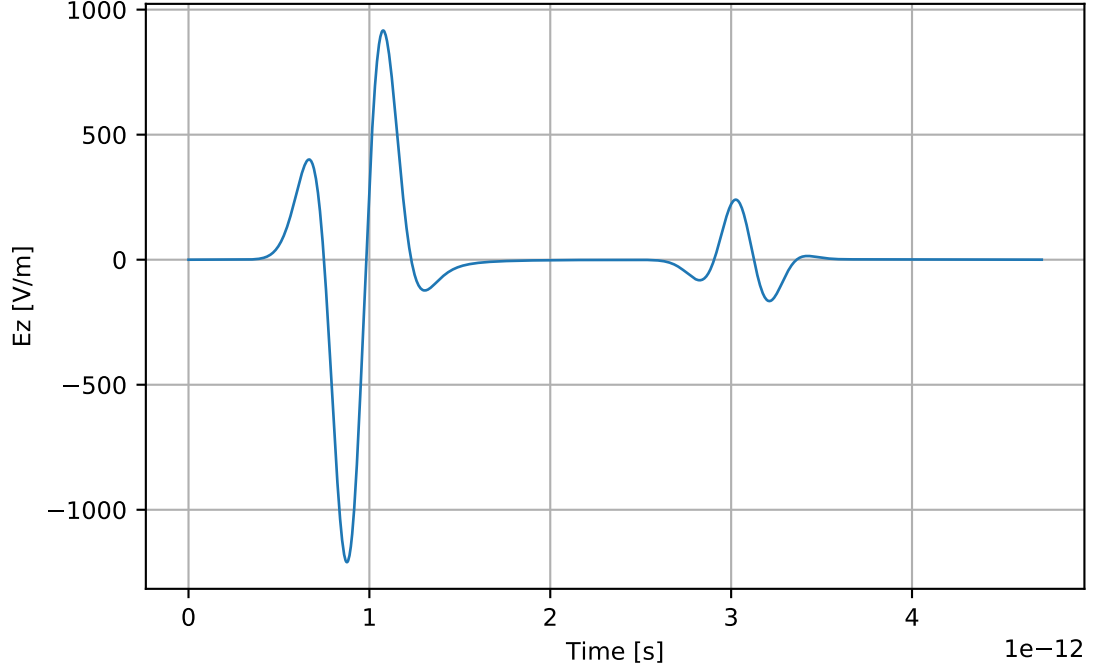
Figure 2.2: Simulated A-scan for simple antenna above a half-space containing a cylindrical PEC pipe.

An A-scan shows the response at a single point above the surface. A cross-sectional area of interest below the ground is investigated by moving the transmitter and receiver along the surface and collecting traces at several sample points. A number of arrangements of the antennas are possible. Typically the antennas are kept at a constant separation known as the common offset and moved in synchronisation over the survey line.

A 2d image of the sub-surface is called a B-scan. It is created by colour mapping each trace in the survey and positioning it on a distance scale representative of the survey line.

Figure 2.3 shows a B-scan generated from a survey over a buried metal cylinder. The survey was simulated using gprMax (Warren et al., 2016b). The coloured bands between 0.5×10^{-9} s and 1.5×10^{-9} s show the direct wave response at positions along the survey line. The image appears to resemble a slice of the sub-surface. However,

11

the underlying data is only a measure of the potential across the receiver's terminal. Therefore, events visible in the B-scan can also correspond to reflections from objects above the surface and reflections from objects not directly below the GPR system.

For example, a hyperbola spanning the survey window is observed after the direct wave. The hyperbola corresponds to the system response of the metal cylinder which is placed at the location of trace number 30. The hyperbola appears because the GPR system radiates in all directions normal to the surface and up to the critical angle. For example, a pulse received at trace 1 has travelled a greater distance to the cylinder than at trace 30 in which the ray has travelled only along the paths vertical component. The arrival time of the pulse at each position can be fit by the equation of a hyperbola.
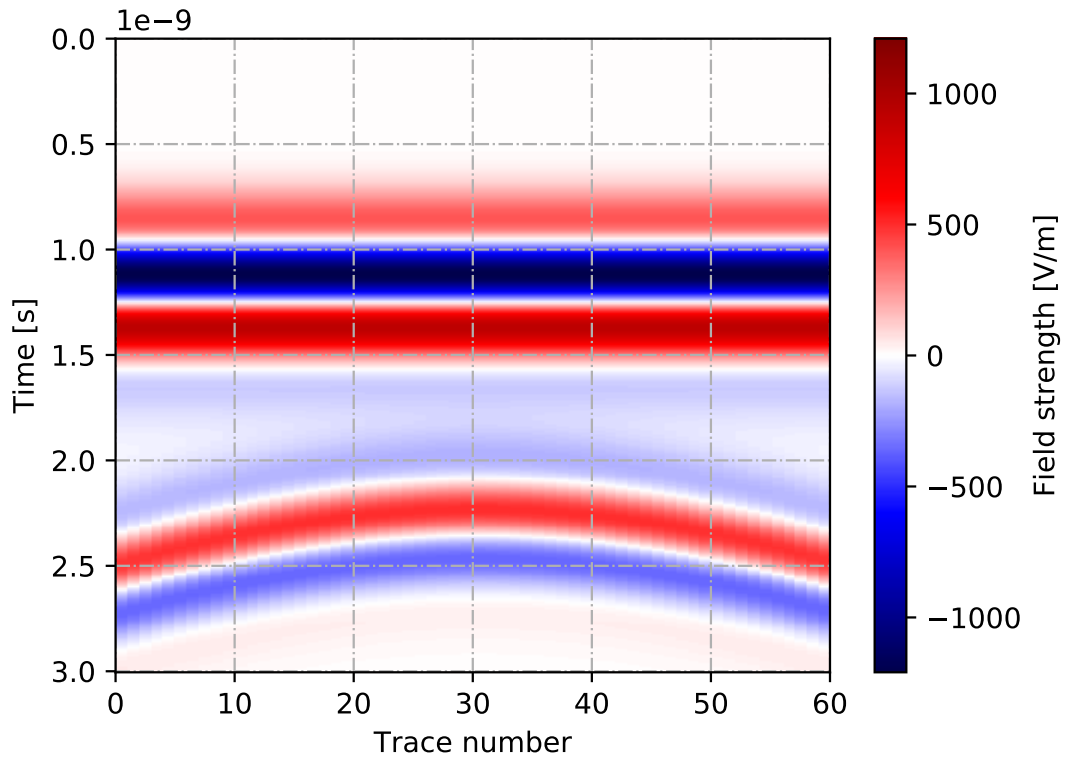
Figure 2.3: Simulated B-scan for a survey of a simple antenna above a cylindrical PEC pipe.

2.3   GPR Systems

A typical GPR system comprises of a control unit, a display, and a set of antennas mounted on a movable trolley or separable units. The control unit manages the timing of the send and receive signals and/or logs the receive antenna response. The display

unit selects survey parameters, and can also provide visual feedback in the form of A-scans and B-scans.

2.3.1 Resolution

One way of interpreting the resolution of a GPR system is its ability to distinguish between separate reflection events. It's generally accepted that events are separable when the reception times of the pulses are at least half the pulse-width apart. Also, minimum horizontal and vertical separation of objects can be considered by decomposing the resolution into these components.

An expression for the depth resolution is given by equation 2.1 where W is the temporal pulse width and v is the group velocity within the medium (Annan, 2005). The equation shows that narrowing the pulse increases the depth resolution. As does an increase in the permittivity of the medium. However dielectric losses at higher frequencies act to counter this effect due to pulse broadening (Daniels, 2007a).

$$\Delta r \geq \frac{Wv}{4} \tag{2.1}$$

The lateral resolution can be described by equation 2.2 where d is vertical the distance to the target. In this case the lateral resolution decreases as the target is moved away from the antenna (Annan, 2005).

$$\Delta r \geq \sqrt{\frac{vdW}{2}} \tag{2.2}$$

Operational frequencies of a GPR system are governed by balancing the required resolution and penetration depth (Davis and Annan, 1989). Penetration depths worsen with frequency as the attenuation due to heat and scattering losses increases. Conversely, the resolution improves with frequency as pulses are better resolved in space and time. GPR operates across a wide frequency spectrum in order to meet both requirements. However, a GPR system cannot be infinitely broadband due to the finite nature and bandwidth of the antennas. Consequently, a concession to resolution is usually made so that reasonable penetration is possible.

Practically, GPR systems are designed in groups which operate over some useful frequency band. These bands are usually specified by the centre frequency of the pulse. For example, Table 2.2 shows each GPR system in the Sensors and Software

pulseEKKO range by centre frequency their intended application. A limitation of this nomenclature is GPR systems operate in the time-domain. A more useful nomenclature would have been to use the pulse length in seconds of the radiated pulse. However, using the antenna centre frequency is very well established in commercial GPR systems and it will be difficult to change.

Centre Frequency [MHz]	Deep Geology, Glaciology	Geology	Utilities	Archaeology	Forensics / Snow and Ice	Mining Quarrying	Concrete, Roads, Bridges
12.5	✓						
25	✓						
50	✓	✓					
100		✓	✓				
200		✓					
250			✓	✓	✓		
500				✓	✓		
1000						✓	✓

Table 2.2: Sensors and software pulseEKKO range. Applications for each GPR system grouped by centre frequency (Sensors and Software, 2016)

2.3.2 Antennas

Impulse response radar is the most common type of GPR systems. Their design requires that the radiated pulse is not dispersed. This is achieved by using antennas with a linear phase response such as dipoles and bow-ties (Daniels, 2007a). In air-coupled GPR surveys, Vivaldi or horn antennas are also used.

The levels of dispersion, efficiency and ground coupling vary between antenna designs. Dipole antennas are inherently resonant and thus have limited bandwidth. Consequently, these antennas are usually loaded with resistors in order to increase their bandwidth. The main drawback of this approach is that antenna efficiency is also reduced due to heat loss across the resistance. Shortening the antenna elements can

also increase bandwidth since the antenna more closely resembles a frequency independent infinitesimal dipole. For instance, Ultra-wideband (UWB) responses have been obtained for very short dipoles however the magnitude of the transfer function of these antennas is very low, $-50\,\mathrm{dB}$ (Randa et al., 1991). The bow-tie antenna design is more broadband. However, its increased surface area results in behaviour which is more dependent on the surrounding environment. In contrast, the smaller size of the dipole offers greater invariance to the operational environment but at the cost of reduced efficiency.

2.3.3 Ground Coupling

The behaviours of a variety of dipole antennas are well understood in free-space (Balanis, 2005). However, they are more complex in GPR surveys where the antenna is contact with or close to the ground. Geometric optics methods have provided solutions under the assumption that the radiation tends to plane waves far and near to the antenna (Smith, 1984a). The main limitation of this approach is that the reactive field near to the GPR antenna/ground interface is not considered. In fact, it is known that the interaction of the reactive field in the half space significantly alters the behaviour of the antenna. For instance, Junkin and Anderson (1988) showed that the reactive field in lossy dielectrics can induce currents which radiate travelling waves. In addition, when the antenna is in contact with a dielectric the current distribution on the antenna surface is altered. This has the effect of increasing the coupling between the antenna and the ground (Daniels, 2007a). Both Smith (1984a); Junkin and Anderson (1988) report that a good coupling is achieved for antenna heights above the ground of $\leq 0.1\lambda$ where λ is the centre wavelength of the pulse distribution in free-space. In addition, Diamanti and Annan (2013) reported that the edge of the near-field is closer to the antenna than is suggested in the standard literature on dipoles in free-space.

2.4 Summary

In this chapter, the main principles of ground-penetrating radar were examined. A short overview was given of the history and applications of GPR. Subsequently, the operation of a GPR system was described in terms of the signal path of the radiation from a GPR antenna. The propagation of the radiation was shown to be dependent on the range of frequencies in the radiated pulse and the material properties of the half-space. Subsequently, a short description was given of a typical impulse radar operating in common offset mode over a half-space. This was discussed with reference to antenna

design and the impacts of ground coupling. Finally, a brief discussion was given on basic ground-coupled surveys and the typical data outputs.

The next chapter discusses Maxwell's equations - the underlying equations which govern the behaviour of GPR systems. Additionally, the FDTD method is described as a means of modelling the complex behaviour of GPR systems in instances where analytical methods are not applicable.

Chapter 3

The Forward GPR Problem

In the previous chapter, the GPR problem was described in qualitative terms. The effects of the soil and the antenna on the propagation of the pulse were described with reference to the operating frequency of the antenna and general material characteristics. Although this description is useful to understand the essential operation of GPR, a forward model provides greater insight into the GPR problem.

Forward models specify completely the evolution of a system in space and time. In the GPR context, this means predicting the behaviour of a GPR system during its operation. This is particularly useful as an accurate forward model can be used to numerically design more efficient and invariant GPR systems, and help to solve inverse GPR problems. i.e. the problem of finding initial model parameters given the system state at a later time.

The most natural choice for a GPR forward model is Maxwell's equations. Since in solving the GPR forward problem we are concerned with the evolution of electromagnetic fields at macroscopic scales. Often however the solutions to Maxwell's equations cannot be obtained analytically. In these cases, approximate methods must be used. In GPR modelling a popular numerical method for solving Maxwell's equations approximately is the Finite-Difference-Time-Domain (FDTD) method.

The first half of this chapter deals with Maxwell's equations in the context of the GPR problem. In the second half, the approximation of Maxwell's equation using the FDTD method is discussed.

3.1 Maxwell's equations

3.1.1 Field Theory

In nature, there are four fundamental forces: strong interaction, weak interaction, electromagnetic and gravitational. In ground-penetrating radar, we are interested in the electromagnetic force since it is the interaction of electromagnetic radiation with charged matter which gives rise to the reflections between materials in the earth and thus the ability to detect targets (Griffiths, 2019).

In electromagnetism, all of matter is made up of electrically charged particles. And all charged particles exert a force on other charged particles. The law which describes the force between two charges is Coulomb's Law.

$$\vec{F} = \hat{r}_{12} \frac{1}{4\pi\epsilon_0} \frac{q_1 q_2}{r_{12}^2} \tag{3.1}$$

where, $\hat{r_{12}}$ is the unit vector from the q_1 to q_2, ϵ_0 is a constant of proportionality called the permittivity of free space and has the value $8.85 \times 10^{-12}\,\mathrm{C^2/Nm^2}$, q_1 and q_2 are the charges of the point charges in coulombs (C), r_{12} is the distance from q_1 to q_2 in metres (m).

The force between the charges falls off as the inverse square of their separation. The law is of the same form as Newton's universal law of gravitation with the exception that the charges can be positive or negative such that the force between charges can be attractive or repulsive.

Coulomb's law predicts the force between two stationary charges correctly. However, it also predicts that if one of the charges is moved the force experienced by the other is reflected instantaneously. This is incorrect as it is known from the theory of special relativity that the speed of light is finite. Coulomb's law must be modified to incorporate these changes. However the law for moving charges is far more complex - it is easier instead to formulate electromagnetics as a field theory in which the field itself carries energy and momentum (Kibble and Berkshire, 2004).

In the field theory, a charge q_1 produces an electric field about itself regardless of q_2. The force on q_2 at any time is the field at its position multiplied by its charge.

$$\vec{F} = q_2 \vec{E} \tag{3.2}$$

where $\vec{E}$ is the electric field in volts per meter, $\mathrm{V\,m^{-1}}$

In addition to electric fields generated by static charges, magnetic fields are generated by moving charges or currents. The magnetic field generated by a steady current of moving charge and produces a force perpendicular to the field and the motion. The Lorentz law describes the combined effect on a charge moving with speed v in an electric and magnetic field. It is given by

$$\vec{F} = q_2(\vec{E} + (\vec{v} \times \vec{B})) \tag{3.3}$$

where, $\vec{v}$ is the velocity of the particle in metres per second, $\mathrm{m\,s^{-1}}$ and $\vec{B}$ is the magnetic field in webers per meters squared, $\mathrm{Wb\,m^{-2}}$.

Since in the GPR problem we are concerned with finding the variation in voltage at the receiver it is sufficient to calculate only the electric and magnetic fields.

3.1.2 Maxwell's Equations in Free-Space

Maxwell's equations describe completely the behaviour of time-depend electromagnetic fields generated by electric charges. In differential form, they are given by

$$\nabla \cdot \vec{E} = \frac{1}{\epsilon_0}\rho \tag{3.4}$$

$$\nabla \cdot \vec{B} = 0 \tag{3.5}$$

$$\nabla \times \vec{E} + \frac{\partial \vec{B}}{\partial t} = 0 \tag{3.6}$$

$$\nabla \times \vec{B} - \mu_0\epsilon_0\frac{\partial \vec{E}}{\partial t} = \mu_0\vec{J} \tag{3.7}$$

where ϵ_0 is the permittivity of free space in $8.85 \times 10^{-12}\,\mathrm{C^2\,N\,m^2}$, ρ is the volumetric charge density, $\mathrm{C\,m^{-3}}$ and $\vec{J}$ is the current density, $\mathrm{A\,m^{-2}}$

The equations constitute four differential equations and can be solved to find $\vec{E}$ and $\vec{B}$ at any point in time and space provided that there are no discontinuities in material or charge in the region of interest.

The Helmholtz theorem states that a vector field is completely described by its curl and divergence. Therefore an insight into the shape of the electric and magnetic fields can be gained by a physical interpretation of the curl and divergence operators. The divergence of a vector field represents the degree to which the field spreads out from a point. A positive divergence indicates the field spreads out from a point and a negative divergence indicates that the field converges to the point. The curl of a vector field indicates the rotational motion of the field.

Applying these insights to Maxwell's equations some observations can be made. Gauss's law for electric fields, equation 3.4, states that the electric field diverges from a point in proportion to the electric charge at that point. Faraday's law, equation 3.6, shows that an electric field is generated by a time-varying magnetic field. Additionally, the rotation of the electric field is in proportion to the rate of change of the magnetic field.

Gauss law for magnetic fields, equation 3.5, states that the magnetic field does not diverge. This is due to the absence of a physical realisable magnetic charge (Balanis, 2012). The Ampere-Maxwell law, equation 3.7, shows that the rotation of the magnetic field is in proportion to the rate of change of the electric field and a current density.

It can be shown that free space is a non-dispersive medium by solving Maxwell's equations in free space where there are no free charges or currents. Taking the curl of equation 3.6 and equation 3.7 and substituting these equations into the result, $\vec{E}$ and $\vec{B}$ are given by

$$\nabla^2 \vec{E} = \mu_0 \epsilon_0 \frac{\partial^2 \vec{E}}{\partial t^2} \tag{3.8}$$

$$\nabla^2 \vec{B} = \mu_0 \epsilon_0 \frac{\partial^2 \vec{B}}{\partial t^2} \tag{3.9}$$

Since the curl part of the equation is removed each component in space maps onto the same component in time. Therefore each component independently satisfies the 1d wave equation. For instance, taking equation 3.8 and substituting in the complex trial solution for a plane wave travelling in the x-direction, $\tilde{E}_z = \tilde{E}_0 e^{j(kx-\omega t)}$ the phase velocity is given by

$$v_p = \frac{\omega}{k} = \frac{1}{\sqrt{\mu_0 \epsilon_0}} = c \tag{3.10}$$

This result shows the electromagnetic radiation in free-space without sources travels as a plane wave at the speed of light for all frequencies. Notice that replacing ϵ_0 with $\epsilon = \epsilon_r \epsilon_0$ results in a simple scaling of the velocity by a factor $\frac{1}{\sqrt{\epsilon_r}}$. Therefore the pulse in a medium with a relative permittivity ϵ_r travels at a reduced velocity.

By substituting the trial solution into Faraday's law, equation 3.6, the relationship between the electric and magnetic field is found

$$\frac{k}{\omega}\tilde{E}_z = \tilde{B}_y \tag{3.11}$$

Equation 3.11 shows that the electric and magnetic fields in free-space are mutually perpendicular. This is also the case for simple dielectrics $\epsilon = \epsilon_r \epsilon_0$. The amplitudes of the real fields are in the ratio $\frac{1}{v_p}$ and thus the impedance of the wave is a constant.

3.1.3 Maxwell's Equations in Matter

Although matter can be approximated with a constant ϵ_r, in general, it is made up of charged particles which influence the applied field. For instance, the applied field deforms the distribution of charge in atoms and molecules which have some charge distribution. The macroscopic effect of which is to create bound charges and currents within and on the surface of the material. The propagating radiation is affected by the fields generated by the bound charges and currents. Therefore it is useful to write Maxwell's equations in terms of the free charge and currents that can be directly controlled (Griffiths, 2019).

$$\nabla \cdot \vec{D} = \rho_f \tag{3.12}$$

$$\nabla \cdot \vec{B} = 0 \tag{3.13}$$

$$\nabla \times \vec{E} = -\frac{\partial \vec{B}}{\partial t} \tag{3.14}$$

$$\nabla \times \vec{H} = \frac{\partial \vec{D}}{\partial t} + \vec{J}_c + \vec{J}_i \tag{3.15}$$

Where $\vec{D}$ is the displacement field in $\mathrm{C\,m^{-2}}$, $\vec{H}$ is the intensity of the magnetic field in $\mathrm{A^2\,m^{-1}}$, ρ_f is the free volumetric charge density, $\vec{J_c}$ is the current density due to conduction, $\vec{J_i}$ is the impressed or source current density.

$\vec{D}$ is generated by the free charge and $\vec{H}$ is field generated by impressed current density $\vec{J_i}$ and the displacement current $\frac{\partial \vec{D}}{\partial t}$. It is important to remember that $\vec{D}$ and $\vec{H}$ are not the physical fields. Commonly $\vec{H}$ is referred to as the magnetic field as it is more frequently measured experimentally than $\vec{B}$. Therefore the rest of the thesis will refer to the *magnetic field* $\vec{H}$ and the *magnetic flux density* as $\vec{B}$.

Maxwell's equations in matter must be supplemented by the constitutive relations which relate the quantities $\vec{E}$, $\vec{H}$ to $\vec{D}$, $\vec{B}$, $\vec{J_c}$ in terms of the underlying material properties. The effects of the constitutive parameters on wave propagation are shown in the next section.

$$\vec{J_c} = \bar{\sigma} * \vec{E} \tag{3.16}$$

$$\vec{D} = \bar{\epsilon} * \vec{E} \tag{3.17}$$

$$\vec{B} = \bar{\mu} * \vec{H} \tag{3.18}$$

where $\bar{\epsilon}$ is the electric permittivity tensor , $\bar{\mu}$ is the magnetic permeability tensor and $\bar{\sigma}$ is the electric conductivity tensor and $*$ is the convolution operation. These three quantities, known as the constitutive parameters, describe the macroscopic material properties of polarisation, magnetisation and conduction respectively.

Macroscopic properties of materials vary in terms of linearity, homogeneity, isotropy and dispersivity. Linearity refers to how the property varies with applied field strength. It is specified as a function of the vector field strength. Homogeneity how a property varies with position. Isotropy, how the material responds to the direction of the field is specified as a tensor formulation of the parameter. Many materials in GPR surveys are linear and non-isotropic in this case the parameters are scalar quantities. Dispersivity refers to the variation in the material property with frequency. Where materials do not vary with frequency the constitutive parameters are constants.

The propagation of light through matter is complicated by the macroscopic effects of polarisation, magnetisation and conductivity. The constitutive parameters which

describe matter are time-dependent. This is due to the finite amount of time it takes the material to respond to a change in the applied field. The delay between the physical phenomenon and the applied field is accounted for by complex constitutive parameters. A constant constitutive parameter is an approximation of instantaneous behaviour (Balanis, 2012).

3.1.4 Conductivity

Conductivity refers to the ease at which electrons travel in material under an applied electric field. Materials with high conductivity are known as conductors. They have free electrons which respond near-instantaneously to an applied field. Materials with a conductivity $1 \times 10^{-3}\,\mathrm{S\,m^{-1}}$ are insulators. Currents do not flow in these materials because the electrons are bound. Materials which have a conductivity $1\,\mathrm{S\,m^{-1}}$ - $3\,\mathrm{S\,m^{-1}}$ are known as semiconductors. Above a certain temperature, they have free electrons and support conduction currents. In GPR dry and wet soils are typical semi-conductors (Balanis, 2012). However, they are usually treated as lossy-dielectrics in the GPR literature.

A derivation of the dispersive relation in conductors follows. The constitutive relation for conductivity reduces to multiplication when the conductivity is isotropic and frequency independent. In this case, Ampere's law and Faraday's law are given by

$$\nabla \times \vec{E} = -\mu \frac{\partial \vec{H}}{\partial t} \tag{3.19}$$

$$\nabla \times \vec{H} = \epsilon \frac{\partial \vec{E}}{\partial t} + \sigma \vec{E} \tag{3.20}$$

Taking the curl of equation 3.19 and substituting equation 3.20 into the result gives

$$\nabla(\nabla \cdot \vec{E}) - \nabla^2 \vec{E} = -\mu\epsilon \frac{\partial^2 \vec{E}}{\partial t^2} - \mu\sigma \frac{\partial \vec{E}}{\partial t} \tag{3.21}$$

Under the assumption that free charge has dissipated this reduces to

$$\nabla^2 \vec{E} = \mu\epsilon \frac{\partial^2 \vec{E}}{\partial t^2} + \mu\sigma \frac{\partial \vec{E}}{\partial t} \tag{3.22}$$

Substituting in the trial solution the dispersion relation is given by

23

$$\tilde{k}^2 = \omega^2 \mu\epsilon + j\omega\mu\sigma \tag{3.23}$$

From this expression it's clear that the conduction term results in a complex wavenumber, $\tilde{k}$.

$$\tilde{k} = k + j\kappa \tag{3.24}$$

The real and imaginary parts of $\tilde{k}$ are given by

$$k = \omega\sqrt{\frac{\epsilon\mu}{2}}\left[\sqrt{1 + \left(\frac{\sigma}{\epsilon\omega}\right)^2} + 1\right]^{\frac{1}{2}} (\mathrm{rad\,m^{-1}}) \tag{3.25}$$

and

$$\kappa = \omega\sqrt{\frac{\epsilon\mu}{2}}\left[\sqrt{1 + \left(\frac{\sigma}{\epsilon\omega}\right)^2} - 1\right]^{\frac{1}{2}} (\mathrm{Np\,m^{-1}}) \tag{3.26}$$

Substituting $\tilde{k}$ for k in the plane wave solution gives

$$\tilde{E}_z = \tilde{E}_0 e^{-j\kappa} e^{j(kx - \omega t)} \tag{3.27}$$

The real part k of $\tilde{k}$ shows that the phase velocity, $\frac{\omega}{k}$ within a conductive medium is frequency dependent. This variation in velocity is dependent on the effectiveness of the conductor.

The imaginary part of $\tilde{k}$ represents an attenuation factor of an exponential decay term in equation 3.27. This shows that a travelling wave in a conductor is attenuated exponentially. The level of the attenuation is dependent on the conductivity (Griffiths, 2019).

For example, for a poor conductor $\sigma << \omega\epsilon$. This is expressed by the first order Taylor expansion.

$$\sqrt{1 + \left(\frac{\sigma}{\epsilon\omega}\right)^2} = 1 + \frac{1}{2}\left(\frac{\sigma}{\epsilon\omega}\right)^2 + O((\tfrac{\sigma}{\epsilon\omega})^4) \tag{3.28}$$

Substituting the expansion into equation 3.26 gives

$$\kappa = \sqrt{\frac{\mu}{\epsilon}} \frac{\sigma}{2} \tag{3.29}$$

Equation 3.29 shows that the attenuation of the wave is independent of frequency in poor conductors. Therefore poor conductors lie in the region of the GPR plateau and are suitable for GPR. The attenuation is also dependent on the characteristic impedance of the material. A larger permittivity reduces the attenuation of the wave provided the $\epsilon(\omega)$ does not vary greatly

For a good conductor $\sigma >> \omega\epsilon$. In this case $\frac{\sigma}{\epsilon\omega}$ dominates the argument of the LHS of equation 3.28 and κ is given by

$$\kappa = \sqrt{\frac{\omega\mu\sigma}{2}} \tag{3.30}$$

In this case, the attenuation is frequency-dependent. The largest variation is for lower frequencies and most strongly for lower frequencies. Good conductors lie in the diffusive region and are not ideal materials for GPR particularly at low frequencies.

The variation in κ with frequency is shown in Figure 3.1. The constitutive parameters $\epsilon_r = 9$, $\sigma = 10\,\mathrm{mS\,m^{-1}}$ are chosen to be representative of a dry silt or shale (Annan, 2005). The figure shows a large variation in attenuation below $100\,\mathrm{MHz}$ and low variation above. The region above $100\,\mathrm{MHz}$ is the representative of the GPR plateau and thus defines the range of frequencies suitable for GPR in the material.

3.1.5 Frequency Dependent Permittivity

All real materials exhibit frequency dependent behaviour. However, when the dependence is small, permittivity can be approximated by ϵ_r . When the dependence is great the permittivity must be characterised using a model which describes the underlying microscopic behaviour of the material.

Pure dielectrics have no unbound electrons and therefore do not support conduction currents. However local variations in the charge distributions of molecules do exist called dipole moments. In ordinary conditions, the dipoles are randomly orientated. However, under the influence of an applied field, the dipoles are forced into alignment. The macroscopic effect of their polarisation is to form bound charge.

25
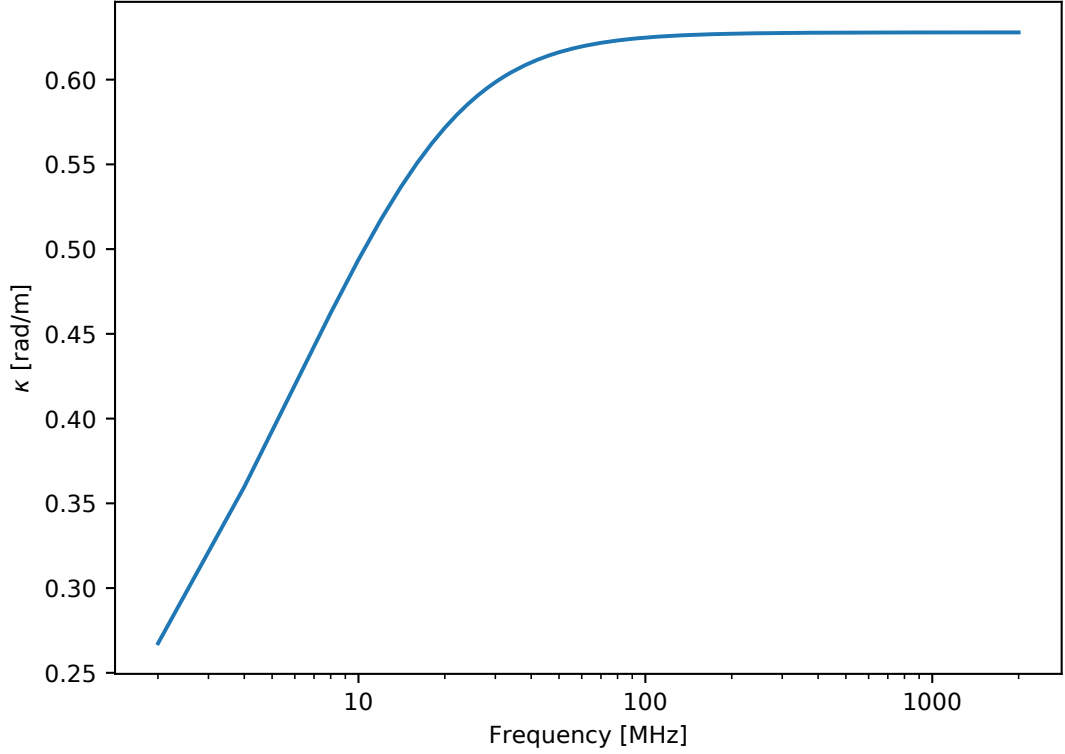
Figure 3.1: Variation in κ with frequency. Material $\epsilon_r = 9$ and $\sigma = 10 \text{ mS m}^{-1}$

The displacement field takes account of the bound charge and represents only the field which is generated by free charge. In the frequency domain, the displacement field can be expressed as a field in free-space $\epsilon_0 \vec{E}$ and the field due to the net polarisation of the dipole moments, $\vec{P}$.

$$\vec{D}(\omega) = \tilde{\epsilon}(\omega)\vec{E}(\omega) = \epsilon_0 \vec{E}(\omega) + \vec{P}(\omega) \tag{3.31}$$

where $\tilde{\epsilon}(\omega)$ is the complex permittivity. The net polarisation is specified according to a mechanical model which describes the variation in charge separation $p = qd$ where d is the separation. Typically a Debye, Lorentz or Drude model is used. However, for illustrative purposes, a general complex permittivity can be considered given by

$$\tilde{\epsilon}(\omega) = \epsilon'(\omega) + j\epsilon''(\omega) \tag{3.32}$$

Now the dispersion relation for dispersive dielectrics can be derived by considering the time-harmonic forms of equation 3.15 and equation 3.14.

26

$$\nabla \times \vec{E} = j\omega\mu\vec{H} \tag{3.33}$$

$$\nabla \times \vec{H} = -j\omega\vec{D} \tag{3.34}$$

Taking the curl of equation 3.33 and substituting in equation 3.34 gives

$$-\nabla^2\vec{E} = \omega^2\mu\vec{D} = \omega^2\mu\tilde{\epsilon}(\omega)\vec{E} \tag{3.35}$$

Considering a single component of the plane-wave solution $\vec{E}$ the dispersion relation is

$$\tilde{k} = \omega\sqrt{\mu\tilde{\epsilon}(\omega)} \tag{3.36}$$

where the κ

$$\kappa = \omega\sqrt{\frac{\mu\epsilon'}{2}\left[\sqrt{1 + \left(\frac{\epsilon''}{\epsilon}\right)^2} - 1\right]^{\frac{1}{2}}} \tag{3.37}$$

and k is

$$k = \omega\sqrt{\frac{\mu\epsilon'}{2}\left[\sqrt{1 + \left(\frac{\epsilon''}{\epsilon}\right)^2} + 1\right]^{\frac{1}{2}}} \tag{3.38}$$

Similarly to the dispersion relation for conductive loss, the dispersion relation has a real and imaginary part which define the velocity, wavelength and the attenuation respectively. Notice that the form of the dispersive relation and the conductive relation are the same. The conductive parameter therefore can be written

$$\frac{\epsilon''}{\epsilon'} = \frac{\sigma}{\epsilon'\omega} \tag{3.39}$$

thus

$$\sigma = \omega\epsilon'' \tag{3.40}$$

equation 3.40 shows that the conductive loss is equivalent to a dielectric loss. In a real GPR system, only the resulting attenuation in the wave is observed and therefore it is impossible to distinguish between them. Accordingly, a real effective conductivity is assigned

$$\bar{\sigma}_e = \sigma' + \omega\epsilon'' \tag{3.41}$$

Nevertheless in GPR modelling, materials are commonly specified with a frequency independent conductivity and a frequency dependent permittivity.

A common source of dielectric loss in GPR environments is loss due to dipole relaxation in water within the soil.

The water molecule is a natural dipole and thus experiences a torque within an applied field which serves to align it in the field direction. For time varying fields the relaxation to equilibrium can be described by the Debye model using a single pole. Its behaviour under an applied field can described by the Debye model with a single relaxation time King and Smith (1981).

$$\tilde{\epsilon} = \epsilon_\infty + \frac{\epsilon_s - \epsilon_\infty}{1 + j\omega\tau} \tag{3.42}$$

where ϵ_∞ and ϵ_s are the permitivitties associated with a static field and a field of infinite frequency and τ is the relaxation time.

Figure 3.2 shows the variation in complex permittivity of pure water over the range of operative GPR frequencies. The real part is relatively constant over this bandwidth however the attenuation rises into the upper microwave region. Within this range dipole losses associated with water content in soils should be considered.

Note that the constitutive equation for the magnetic field is not discussed. The reason for this is magnetic materials are not commonly found in GPR surveys. When this is case $\tilde{\mu} = \mu_0$ and the field propagates in a magnetic vacuum.
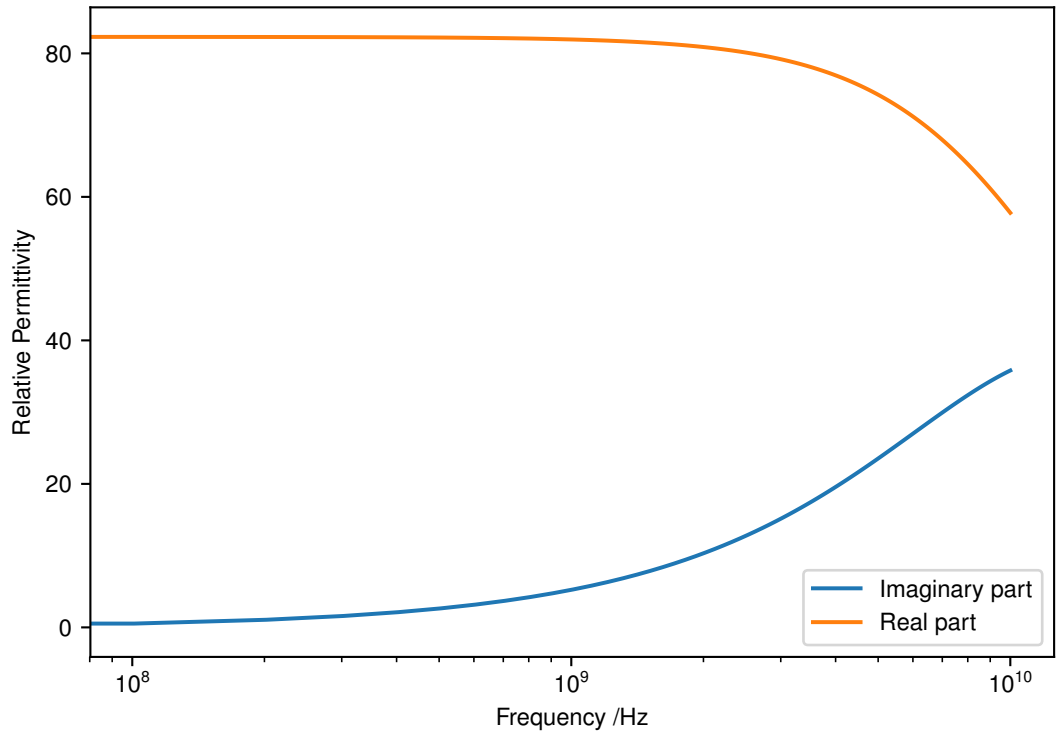
Figure 3.2: Variation in complex permittivity for water modelled using a single pole Debye function. $\epsilon_\infty = 5.5$, $\epsilon_s = 82.2$, $\tau = 10.9 \times 10^{-12}\,\text{s}$

3.2 The FDTD Method

3.2.1 Approximate Solutions

Maxwell's equations were described in the previous section. They were shown to provide a complete description of the electromagnetic fields in macroscopic media, and therefore they provide a solid foundation to describe the behaviour of GPR. However, an analytical solution to a GPR problem is not always possible and an approximate numerical solution must be found.

Real GPR systems contain a range of antenna designs such as bow-ties and resistively loaded bow-ties. For these antennas, the current distribution is not well known and therefore approximate methods must be used (Balanis, 2005).

Also, the parameters of an antenna are known to be highly affected by the ground. To achieve good coupling GPR antennas are required to be near the ground. Analytical methods can be used to understand this behaviour using the case of the infinitesimal dipole over homogeneous, lossy half spaces within the far-field (Smith, 1984a) (Engheta et al., 1982) (Annan et al., 1975). However most real interactions with the ground and the components that house the antenna occur within the antennas near field. Antenna parameters are affected directly by the interaction of the near field with the ground (Daniels, 2007b). This behaviour is further complicated by the dispersive, heterogeneous nature of the soil within the operating frequency of GPR (Hallikainen et al., 1985). The field response is further complicated by surface clutter resulting from the surface roughness of the ground. Overall this set of interactions with the ground cannot be easily parameterised using analytical methods and numerical method must be used (Diamanti and Annan, 2013) (Giannakis et al., 2016a).

Integral equation methods have been used to model electromagnetic scattering problems (Harrington, 1993; Umashankar, 1988). The advantage of these methods is they can accurate map the shape of complex antennas. However there are are two main drawbacks to the methods. The first is that the frequency domain nature of the methods is problematic for time-domain applications such as GPR. This is because a number of single frequency simulations must be run to construct a time-domain response. The second is these methods produce systems of linear equations. For large scale problems, it becomes impractical to solve these systems exactly using matrix methods.

The finite-difference time-domain technique (FDTD) is by far the most popular numerical method for solving Maxwell's equation in GPR problems. It's primary ad-

vantage is inherently a time-domain solution and therefore can be applied to GPR straightforwardly. In addition, FDTD does not require a matrix solution and therefore scales better with model size.

FDTD has been used to model a variety of GPR antennas; bow-tie (Bourgeois and Smith, 1996), resistive bow-tie (Nishioka, 1999), capacitively-loaded bow-ties (Lestari, 2007), resistively loaded Vee (Lee et al., 2004), TEM bow-tie (Yarovoy et al., 2002) and the Vivaldi antenna (Sato et al., 2004). Also, soil models have been implemented in FDTD using homogeneous dispersive material to describe a particle soil type where the real and imaginary parts are fitted to known material (Bergmann et al., 1998) (Uduwawala et al., 2005). This approach was extended to the 2.5d inhomogeneous case by Teixeira et al. (1998). More recently Giannakis et al. (2016a) gave the bulk properties of a mix of soils are given by the terms of a multi-pole Debye expansion and distributed stochastically using a fractal distribution where the complex permittivity is given by mixing models in (Dobson et al., 1985) and (Peplinski et al., 1995). This paper also includes the ability to model surface roughness using a fractal distribution method developed from an earlier 2d implementation (Giannopoulos and Diamanti, 2008).

3.2.2   Formulation

The FDTD method defines a set of explicit update equations which solve for both the electric and magnetic fields. The update equations result from central finite-difference approximations to the spatial and temporal derivatives in Maxwell's curl equations.

The update equations were first derived by Kane Yee (1966). Yee defined the lattice positions of the electric and magnetic fields such that the resulting update equations can be performed consistently in space and time. The positions of the electric and magnetic fields for a single Yee cell are shown in figure 3.3.

Figure 3.3 shows each magnetic component normal to the centre of each cell's face and the orthogonal electric components circling on the edge centres of the face. Equally each electric component can be viewed on the face of a cube circled by orthogonal magnetic components. This arrangement of field components can be extended arbitrarily to model a region of space. In addition to the spatial layout, the electric and magnetic fields are also offset by half a time-step.

Each update equation can be derived by evaluated each field component in the curl equations at each point in the Yee lattice. The derivation for the E_x update equation is given as an example.
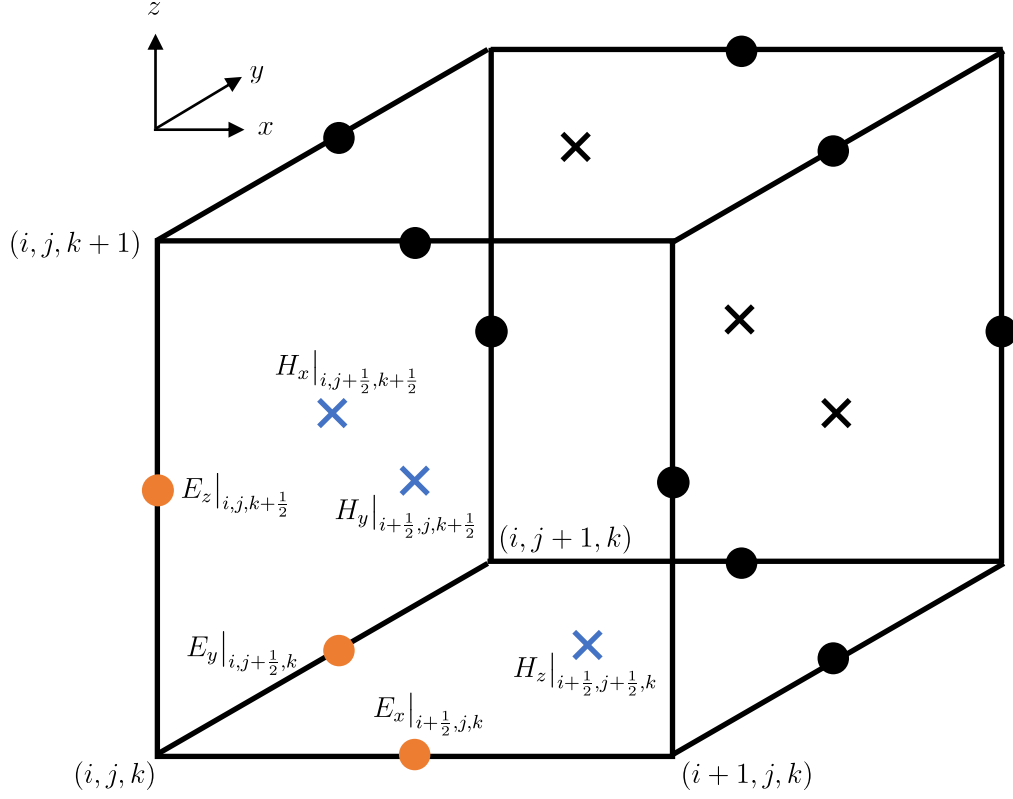
Figure 3.3: Locations of the E and H components in a Yee cell. The labelled orange and blue components are shown for a single Yee cell. The black components show the components in adjacent Yee cell's which combine to form the problem space.

Firstly, Maxwell's curl equation for the magnetic field can be decomposed into 3 components. The x directed component of the electric field and x component of the curl operation is given by

$$\frac{\partial E_x}{\partial t} = \frac{1}{\epsilon}\left(\frac{\partial H_z}{\partial y} - \frac{\partial H_y}{\partial z}\right) - J_i - \sigma E_x \tag{3.43}$$

Next, the continuous variables x, y, z, t in equation 3.43 are replaced with discretised variables $(i\Delta x, j\Delta y, k\Delta z, q\Delta t)$ such that the derivatives can be replaced with central differences. $\Delta x, \Delta y, \Delta z, \Delta q$ are the distances between the spatial sampling points and sampling points. The indexes i, j, k, q correspond to the specific Yee cell in the lattice and point in time.

The central difference equations are derived by considering the Taylor expansion of a 1d field about a point $i\Delta x$ given by

$$E_x(x) = E(i\Delta x) + E'(i\Delta x)(x - i\Delta x) + O(\Delta x^2) \tag{3.44}$$

Evaluating the series at $i\Delta x + \frac{\Delta x}{2}$ and $i\Delta x - \frac{\Delta x}{2}$ gives

$$E_x(i\Delta x + \tfrac{\Delta x}{2}) = E(i\Delta x) + E'(i\Delta x)(\tfrac{\Delta x}{2}) + O(\Delta x^2) \tag{3.45}$$

$$E_x(i\Delta x - \tfrac{\Delta x}{2}) = E(i\Delta x) - E'(i\Delta x)(\tfrac{\Delta x}{2}) + O(\Delta x^2) \tag{3.46}$$

Subtracting equation 3.46 from equation 3.45 and rearranging the result gives an expression for the derivative evaluated at $i\Delta x$.

$$E'_x(i\Delta x) = (E_x(i\Delta x + \tfrac{\Delta x}{2}) - E_x(i\Delta x - \tfrac{\Delta x}{2}))/\Delta x + O(\Delta x^2) \tag{3.47}$$

At this point the expansion is exact. Truncating the series results in an approximation which is second-order accurate. Included more terms reduces the error further. However material boundaries become less well defined as fields beyond the boundary are introduced into the stencil.

Now, applying the second-order central difference equations and evaluating the fields in equation 3.43 at the point $(i + 1/2, j, k, q)$ in the Yee lattice gives

$$\frac{E_x\Big|_{i+1/2,j,k}^{q+1/2} - E_x\Big|_{i+1/2,j,k}^{q-1/2}}{\Delta t} = \frac{1}{\epsilon_{i+1/2,j,k}} \tag{3.48}$$

$$\left(\frac{H_z\Big|_{i+1/2,j+1/2,k}^{q} - H_z\Big|_{i+1/2,j-1/2,k}^{q}}{\Delta y}\right.$$

$$-\frac{H_y\Big|_{i+1/2,j,k+1/2}^{q} - H_y\Big|_{i+1/2,j,k-1/2}^{q}}{\Delta z}$$

$$-J_{ix}\Big|_{i+1/2,j,k}^{q}$$

$$\left.-\sigma_{i+1/2,j,k}E_x\Big|_{i+1/2,j,k}^{q}\right)$$

Note that the position notation $(i\Delta x, j\Delta y, k\Delta z)$ has been replaced with the index notation (i, j, k).

The E_x term for the conduction current in equation 3.48 is evaluated at the time $q\Delta t$. However, this value does not exist in the difference scheme as the central difference equation samples the field at time $(q + 1/2)$ multiples of Δt only. The correct field value is obtained by averaging the field values at $(q + 1/2)\Delta t$ and $(q - 1/2)\Delta t$. This approximation is known as the semi-implicit approximation (Taflove and Hagness, 2005) and is given by

$$E_x\Big|_{i+1/2,j,k}^{q} = \frac{E_x\Big|_{i+1/2,j,k}^{q+1/2} - E_x\Big|_{i+1/2,j,k}^{q-1/2}}{2} \tag{3.49}$$

Substituting equation 3.49 into equation 3.48 gives the finite difference update equation for the E_x component. It is given by

$$E_x\Big|_{i+1/2,j,k}^{q+1/2} = \frac{1 - \frac{\sigma\Delta t}{2\epsilon}}{1 + \frac{\sigma\Delta t}{2\epsilon}} E_x\Big|_{i+1/2,j,k}^{q-1/2} + \frac{\frac{\Delta t}{\epsilon}}{1 + \frac{\sigma\Delta t}{2\epsilon}}\left(\frac{H_z\Big|_{i+1/2,j+1/2,k}^{q} - H_z\Big|_{i+1/2,j-1/2,k}^{q}}{\Delta y}\right.$$

$$-\frac{H_y\Big|_{i+1/2,j,k+1/2}^{q} - H_y\Big|_{i+1/2,j,k-1/2}^{q}}{\Delta z}$$

$$\left.-J_{ix}\Big|_{i+1/2,j,k}^{q}\right) \tag{3.50}$$

Where the constitutive parameters ϵ and σ are specified at the point $(i + 1/2, j, k)$. The equation shows that the next value of the electric field is calculated only from its previous value and orthogonal magnetic fields.

Similarly, evaluating 3.19 at $(i, j + 1/2, k + 1/2, q)$, H_x is given by equation 3.51. Finite difference equations for the rest of the fields E_y, E_z, H_y, H_z and are given in the appendix.

$$
\left. H_x \right|_{i,j+1/2,k+1/2}^{q} = \frac{1 - \frac{\sigma_m \Delta t}{2\mu}}{1 + \frac{\sigma_m \Delta t}{2\mu}} \left. H_x \right|_{i,j+1/2,k+1/2}^{q-1} + \frac{\frac{\Delta t}{\mu}}{1 + \frac{\sigma_m \Delta t}{2\mu}} \left(\frac{\left. E_y \right|_{i,j+1/2,k+1}^{q+1/2} - \left. E_y \right|_{i,j+1/2,k}^{q+1/2}}{\Delta z} \right.
$$
$$
- \frac{\left. E_z \right|_{i,j,k+1/2}^{q+1/2} - \left. E_z \right|_{i,j+1,k+1/2}^{q+1/2}}{\Delta y}
$$
$$
\left. - \left. K_{ix} \right|_{i,j+1/2,k+1/2}^{q+1/2} \right) \qquad (3.51)
$$

Where σ_m is the magnetic loss in $\Omega \, \text{m}^{-1}$ and K is the impressed magnetic current density in $\text{A} \, \text{m}^{-2}$. K is not a physical quantity as there is no equivalent single magnetic charge equivalent to the fundamental electric charge. However K is useful for defining equivalent problems. This topic is expanded later chapters.

The electric and magnetic fields are staggered in time and space by half a spatial and temporal step. Therefore a time-stepping algorithm is used to compute the temporal solution. First, all the magnetic fields components in x, y, z are updated for a set of initial current or electric field values defined at half a time step in the past. Next, at a later time step, the electric field values are calculated from the magnetic field values at the previous time step. The process is then repeated for the desired number of time steps.

Materials are placed in the lattice by modifying the local values of the constitutive parameters. No special boundary conditions are required to enforce the interface conditions. This is because the material interface always lies within the plane of the electric field and magnetic field components.

The update equations are derived from the curl equations only. However, it can be shown that the divergence equations are satisfied by the finite difference equations given the spatial organisation of the electric and magnetic components (Taflove and Hagness, 2005).

3.2.3 Numerical Stability

The central differencing of Maxwell's equations results in a set of explicit finite difference equations. Each subsequent term in the time-stepping depends explicitly on the previously calculated terms. A shortcoming of explicit methods is they often suffer from numerical instability such that the value of Δt must be appropriately bounded to prevent spurious growth of the solution.

The time step in the FDTD calculation is bounded by the Courant-Friedichs-Lewy (CFL) condition. It is derived by specifying that all the eigenmodes of the finite difference operators remain stable. A derivation of the CFL limit is given in Taflove and Brodwin (1975). An alternative treatment is given in Sarris (2011) where a condition is placed on the dispersion relation such that only solutions with real-valued frequencies allowed to propagate. The CFL condition is given by

$$\Delta t \leq \frac{c}{\sqrt{(\frac{1}{\Delta x^2} + \frac{1}{\Delta y^2} + \frac{1}{\Delta z^2})}} \tag{3.52}$$

The CFL condition states that the maximum allowable time step is bounded by the spatial discretisation. A possible physical interpretation is that the signal in FDTD cannot propagate in any direction more than a single cell per time step.

3.2.4 Numerical Errors

Numerical errors are introduced into FDTD simulations in three ways: truncation error, numerical dispersion, geometric modelling error. In this section, these sources of error and methods to reduce their impact are discussed.

The truncation error is the error introduced by the approximation of Maxwell's equations. It is measured as the difference between the analytical equations and the numerical equation for a given order of distance from the point of approximation.

The most popular variety of the FDTD method is the second-order central-difference approximation. Second-order accuracy means that the error goes up as the square of the spatial step. For instance, when the discretisation is halved, the error goes down by approximately 1/4. Greater accuracy can be achieved by using higher-order schemes. However, these schemes typically present issues at PEC boundaries. For example, in a fourth order scheme, the update of a magnetic field requires electric nodes not only adjacent to the node but also the next adjacent node. This introduces an error when

the inner electric node is a PEC, since no field from the outer node should influence the magnetic field.

The numerical dispersion error is the effect on the solution due to the truncation of the derivatives. Its effect is similar to the replacing free-space with an anisotropic frequency-dependent media such that the solution behaves differently for different frequencies and angles of propagation.

The dispersion equation in the FDTD grid is found in a similar way to the previous section where a plane wave solution was substituted into Maxwell's curl equations. Here, the discretised solution is substituted in the central difference approximation of the curl equations.

The discretised plane wave solutions are given by

$$E_z|_m^q = E_0 e^{j(\omega q \Delta t - \tilde{k} \Delta x)} \tag{3.53}$$

$$H_y|_m^q = H_0 e^{j(\omega q \Delta t - \tilde{k} \Delta x)} \tag{3.54}$$

Substituting equation 3.53 and equation 3.54 into the discretised curl equations of equation 3.19 and equation 3.20 the 1d dispersion equation can be shown to be given by

$$\sin\left(\frac{\omega \Delta t}{2}\right) = \frac{1}{\sqrt{\mu \epsilon}} \frac{\Delta t}{\Delta x} \sin\left(\frac{\tilde{k} \Delta x}{2}\right) \tag{3.55}$$

The above equation states that ω/k is not a linear proportion and therefore that the grid itself is dispersive. The equation implies that the update equations always propagate waves similar to their free space counterparts and therefore a numerical error will always exist. This is because finite spatial and temporal steps must be chosen to advance the computation. For pulsed excitation models numerical dispersion has the effect the wavefront of the pulse breaks apart and appears to ring.

This equation can be simplified by considering the Courant limit, S and the number of points per wavelength, N_λ given by equation 3.56 and equation 3.57 respectively. The Courant limit is the ratio of the distance travelled in one time step to the length of the spatial step. And the number of points per wavelength is the total number of spatial steps required to resolve the continuous wavelength.
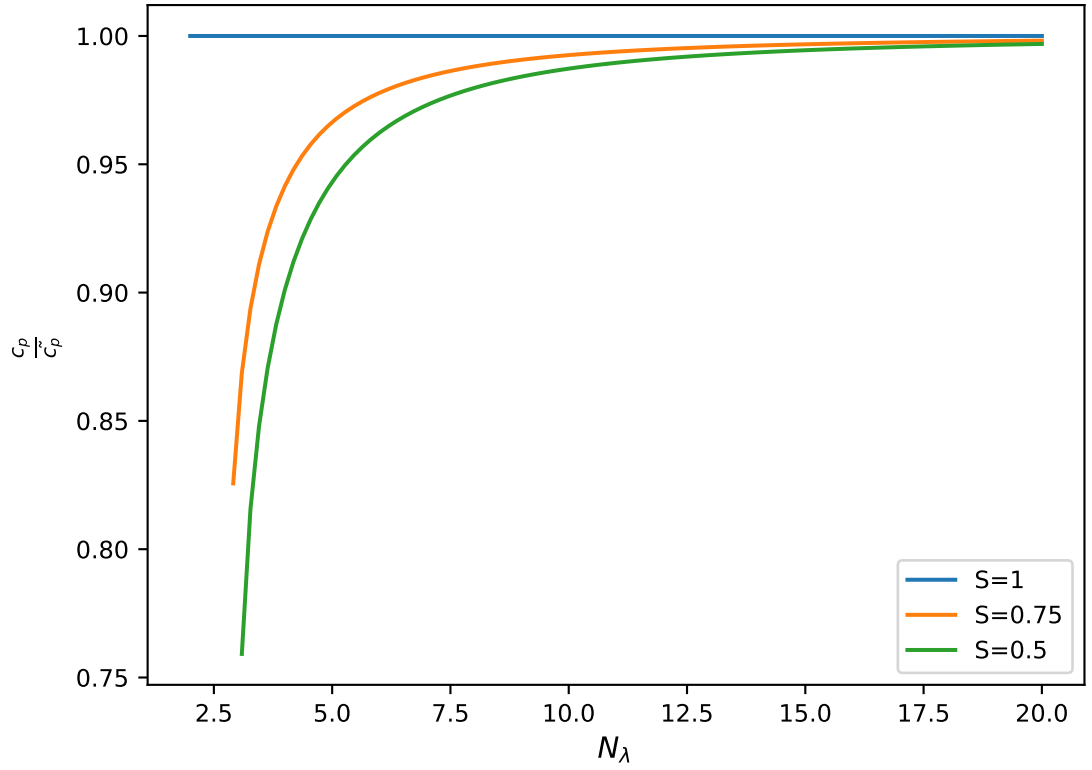
Figure 3.4: Comparison the ratio of the continuous to FDTD phase velocity $\frac{c_p}{\tilde{c}_p}$ for different Courant numbers adapted from Schneider (2010)

$$S = \frac{c\Delta t}{\Delta x} \tag{3.56}$$

$$N_\lambda = \frac{\lambda}{\Delta x} \tag{3.57}$$

For $S = 1$ light travels one spatial step per time step. In this case, the free space dispersion equation is recovered and there is no numerical dispersion. By varying S and N_λ the amount of numerical dispersion can be controlled.

Figure 3.4 shows a comparison of the phase velocity in the FDTD to the free space velocity. The figure shows large Courant numbers and a high N_λ significantly reduce the numerical phase velocity error. However, in general, a Courant number of 1 cannot be exceeded for stability reasons. Therefore the phase velocity error is controlled by the number of points per wavelength.

The 3d dispersion relation is given by

$$\sin^2\left(\frac{\omega\Delta t}{2}\right) = c^2\Delta t^2 \left[\frac{1}{\Delta x^2}\sin^2\left(\frac{\tilde{k}_x\Delta x}{2}\right) + \frac{1}{\Delta y^2}\sin^2\left(\frac{\tilde{k}_y\Delta y}{2}\right) + \frac{1}{\Delta z^2}\sin^2\left(\frac{\tilde{k}_z\Delta z}{2}\right)\right]$$

(3.58)

In the 3d case $S = 1/\sqrt{3}$ at most. A non-unity Courant number always results in dispersion and therefore numerical dispersion in the 3d case is inherent. Furthermore, the error in phase velocity in the 3d case is anisotropic. The greatest error occurs in the axial directions and the minimum dispersion is along the corner to corner diagonally. Anisotropy has the effect that a harmonic solution will radiate non-spherical wavefront from a point over a distance. Furthermore, at grid discretisations of $N_\lambda < 3$ the lattice is unable to propagate energy and acts as a low pass filter (Taflove and Hagness, 2005). In fact, Schneider and Wagner (1999) showed that $N_\lambda < 2$ waves travel faster than the speed of light.

The effects of numerical dispersion are limited by specifying that the shortest wavelength present in the simulation is resolved to $N_\lambda = 20$. Since wavelength contacts in dielectrics, the dielectric strength must be taken into account when calculated the spatial step. Many models use the rule of thumb $N_\lambda = 10$. However, in this work $N_\lambda = 20$ is generally used when the compute time is acceptable. This is because $N_\lambda = 20$ provides a relative error in phase velocity of less than 1% over all angles of propagation (Schneider, 2010). In addition, the phase error for longer propagation distances for resonances or deep penetration depths is reduced since the error is cumulative.

In order to determine the spatial step, we require the highest frequency of interest in the simulation. In GPR broadband pulses are required therefore the highest frequency of interest is always higher than the centre frequency or quoted frequency of a commercial antenna. A number of measures can be used for this which are derived from the pulse width of the pulse in the frequency domain. One common measure is electromagnetic pulses in FDTD is the $1/e$ drop in power output (Costen et al., 2009). Although this drop is mathematically convenient it does not give much physical insight into the significance of the resulting frequency in terms of GPR antennas. With this in mind Maloney and Smith (1993) state that the pulse reflected by an antenna must be $40\,\mathrm{dB}$ lower than the incident pulse in order for efficient transfer of radiation. Therefore a $40\,\mathrm{dB}$ drop in maximum power out can be seen as the noise floor of the antenna system which could, therefore, correspond to the highest frequency of interest. This is because any drop at this frequency would not be observable. It should be noted that for high-frequency antennas the condition can be relaxed. This is because frequencies in the upper range toward $10\,\mathrm{GHz}$ will be strongly attenuated by real soils.

Errors due to stair-casing arise when the geometry of objects in the FDTD grid is not well represented. The FDTD method is based on a rectangular grid method. Therefore objects which are not aligned with the grid such as curved surfaces or diagonal surfaces must be represented on a rectangular mesh. This is known as stair-casing because the edges of the geometry become stepped.

For example, Cangellaris and Wright (1991) showed that when a diagonal conducting surface is stair-cased the increased length of the stepped edge causes an increase in the time it takes for the current to propagate along the edge and that the time increases the greater the discretisation or worse the stair-casing.

Stair-casing errors can always be reduced by introducing a smaller spatial discretisation. This helps to minimise the mismatch between the real geometry and the stair-cased geometry. However, the cost of doing this is great as the time-step must be reduced due to the CFL condition and the increased number of cells to solve for. A number of techniques have been investigated to introduce local finely detailed models into the FDTD method to reduce this problem. A novel technique for GPR is discussed in the following chapter.

3.2.5 Absorbing Boundary Conditions

The FDTD equations given in the previous section provide the solution to Maxwell's equations over an infinite region. However, the real computational domain is limited by memory resources owing to the fact that the spatial discretisation must be finite in order to limit numerical dispersion (Bérenger, 2015).

The domain must be artificially truncated by some boundary. The simplest of these boundaries is to set the fields at the problem boundary to zero. This boundary condition is the equivalent of a perfect electric conductor (PEC) surrounding the domain.

In open boundary problems, we require that radiation at the boundary is only outgoing such that no reflections are directed back into the computation domain. To enforce this condition a class of boundary conditions called absorbing boundary conditions were been developed.

During the period 1970 to 1994, the most common approach to the boundary problem was the analytical boundary condition. The most well known of these techniques are the Enquist-Majda one way equations (Engquist and Majda, 1977) (and its FDTD implementation (Mur, 1981)), Higdon operators (Higdon, 1986) (Higdon, 1987) and Liao extrapolation (Liao et al., 1984).

The approach is motivated by finding a travelling wave solution which moves only outward at the boundary such that there can be no reflected wave. Therefore their solution is to find differential equations whose solutions are one-way travelling waves. And then to discretise these equations at the boundary. Numerical results for this class of method shows that reflection coefficients of up to 3.8% for second-order approximations and 1% in the Liao extrapolation (Taflove and Hagness, 2005) (33dB, 46dB respectively). It is supposed that the limitation of these methods is their failure to absorb evanescent waves as they are designed for travelling waves in particular (Bérenger, 2007a)

The introduction of the Perfectly Matched Layer (PML) eliminated the issues associated with the analytical absorbing boundary conditions. The PML approaches the problem by means of a lossy medium which attenuates incoming waves. It is perfectly matched to the surrounding medium such that it is theoretically non-reflective for plane waves of all frequencies incident at any angle (Bérenger, 1994) The PML is incredibly successful and in practice can allow the simulation of open boundary problems down to 70dB (Taflove and Hagness, 2005).

The first two formulations were the split field PML (Bérenger, 1994) and the stretched coordinate PML (Chew and Weedon, 1994) and later the uni-axial PML (Gedney, 1996). The stretched formulation replaces the curl operators with the stretched coordinate curl operators. Chew and Weedon (1994) showed that when a stretching function is a complex number the field in that direction is attenuated. The Complex Frequency Shifted PML (CFS-PML) modifies the stretching function which is known to reduce the reflections of evanescent waves close to the domain boundary (Kuzuoglu and Mittra, 1996).

CFS-PML became more popular after the advent of the convolutional PML due to its easier and more efficient implementation in FDTD (Roden and Gedney, 2000). Drossaert and Giannopoulos (2007) explored a different approach to evaluating the convolution using a recursive integration technique Recursive integration (RIPML). Giannopoulos (2008) subsequently adapted to approach to electromagnetics and offered performance improvement in comparison to the CPML. The PML used in this work is from Giannopoulos (2012). This work extends the CFS-PML to the n-order.

3.3   Summary

Maxwell's equations were discussed as a forward model for GPR. The effects of conductors, lossy-dielectrics and dispersive materials on travelling waves were considered. These findings were then discussed concerning signal propagation in GPR. Also, the requirement for approximate methods to find solutions to ground-penetrating radar problems was discussed.

Furthermore, an overview of the FDTD method was given. The method was analysed by examining its numerical stability, sources of error and techniques for mitigating these issues. In particular, attention was drawn to computational limitations imposed by the CFL condition. Also, a brief review of the common absorbing boundaries for FDTD was given.

Chapter 4

Effective Permittivities of Dispersive Half-Spaces

The free-space FDTD method is accurate to second-order. However, it has been shown that the method is only accurate to second-order at material interfaces when the constitutive parameters at the interface are averaged (Kyu-Pyung Hwang and Cangellaris, 2001).

A decrease to first-order accuracy poses a greater issue for sub-gridding in GPR problems. In many problems, we wish to preserve the high discretisation of an object, such as an antenna and reduce the discretisation of the surrounding region such as the half-space. However, reducing the discretisation creates a first-order increase in error at the interface in the main-grid. This introduces an error to the sub-gridding problem. Therefore there is a need for averaging the constitutive parameters at the half-space interface.

In particular, realistic GPR models have introduced dispersive materials to model the behaviour of soils (Giannakis et al., 2016a). Therefore it important that the averaging scheme applies to time-dependent constitutive parameters if dispersive soils are to be included within a sub-gridding scheme.

This chapter proposes a novel method for averaging constitutive parameters. It is shown that these methods result in expressions which can be cast in terms of the Debye formulation. This is useful as the materials can be implemented easily using the existing dispersive material formulations in gprMax (Warren et al., 2016a). Furthermore, the success of this approach is demonstrated by modelling dispersive soils and comparing them with an analytical solution.

4.1 Review of Averaging Techniques

4.1.1 Averaging Techniques

Several techniques have been used to treat material interfaces in the FDTD method. The contour path (CP) integral FDTD has been applied to modelling dielectric and conductive curved surfaces (Jurgens et al., 1992). The method employs a contour path approach using integral forms of Maxwell's equation to derive a set of update equations. In this way, the Faraday contour which incorporates the usual spatial part of the equation is deformed along the surface of the curved surface. This approach increases the complexity of the basic FDTD algorithm, as to evaluate the Faraday contour the electric fields on the surface must be calculated in an auxiliary update using an interpolated value of the H field or a nearest-neighbour field. The borrowing of near-by fields introduced instabilities. Later Dey and Mittra (1997) eliminated the instabilities with the locally conformal finite-difference time-domain (CFDTD) which does not borrow neighbouring fields. However, the time step was reduced to 50-70% of the Courant limit to preserve stability.

Kaneda et al. (1997) introduced the effective permittivity (EP) as a means of reducing staircasing errors resulting from curved dielectric interfaces. In the EP approach, the permittivity of the material at the usual Yee cell locations is modified to accommodate the spatial distribution of the dielectric within a single cell. This method is advantageous because only the standard FDTD update equations are required. And therefore there are no concerns about stability or increase in computation time or overall resources.

Kaneda et al. (1997) proposed the effective permittivity as a weighted sum of the dielectric material content on either side of the boundary. Additionally, a new method was reported which took into account the spatial distribution of dielectric filling. Each cell can be viewed as a stack of infinite 2d slices. On each slice, an EP is given as a weighted sum of the cross-sectional area occupied for each dielectric. The sliced EPs are then integrated and averaged along the cell length. Results comparing the results of this method using known resonances of a dielectric rod showed good agreement.

Later, Supriyo Dey and Mittra (1999) extended the CFDTD method to the dielectric case. An effective permittivity equal to the weighted volume average (V-EP) of the permittivity with a single cell was reported. Results compared favourably with those found by Kaneda et al. (1997).

Similarly to Kaneda et al. (1997), the technique was subsequently refined to account for the dielectric distribution within the cell by Wenhua Yu and Mittra (2001). The effective permittivity is introduced by weighting the permittivity by the fraction of the cell the dielectric occupies along the cell edge. In comparison with Kaneda et al. (1997), the technique is simple to implement and requires less computation processing as there is no integration required to calculate each overall cell effective permittivity during mesh generation.

The EP methods mentioned share the advantage of stability in contrast to the CFDTD methods. However, they do not necessarily ensure that the boundary conditions at the material interfaces are maintained. Furthermore, these methods describe problems in which the dielectric is distributed within a cell. For example, a dielectric cylinder whose surface cuts across the Yee cells edges. They do not provide an insight into the accuracy of modelling the interface between two dielectrics in the simplest case whereby the interface is aligned with the Yee cell edges. For example, in the half space problem where the two dielectric materials are aligned with the grid.

Kyu-Pyung Hwang and Cangellaris (2001) presented a rigorous solution to the EP problem where the integral forms of Maxwell's equations over finite volumes were applied to the dielectric interface. It was shown that for grid aligned interfaces offset from the grid, the second-order convergence of FDTD is preserved when the normal and tangential EP is determined by the harmonic and arithmetic averages weighted by the volumetric fractions of the surrounding dielectric. Additionally, it was shown that even for grid aligned interfaces the EP must be used to restore second-order convergence.

Farjadpour et al. (2006) show a generalised EP approach. In the scheme, the permittivity is represented by an inverse dielectric tensor in which harmonic and arithmetic volume averaged permittivities are projected on the normal of the dielectric interface. For grid aligned interfaces the tensor reduces to the averaging scheme as in Kyu-Pyung Hwang and Cangellaris (2001). Numerical results show that harmonic and arithmetic averaging of non-grid aligned surfaces without taking into account the surface normal reduces the accuracy below the staircasing approximation. Interestingly, performing a simple average shows better performance. The results show that the generalised scheme restores second-order convergence in all cases.

A more advanced approach to modelling curved surfaces called the Contour Path Effective Permittivity (CP-EP) was reported by Mohammadi et al. (2005). CP-EP uses a contour path approach which includes the enforcing of the boundary conditions on tilted and curved dielectric surfaces.

In this work, the radar cross-sections of dielectric cylinders were calculated using the CP-EP, V-EP and standard staircased solutions. An analytic comparison was made with results from the Mie scattering theory. The first two tests measure the radar cross-section for two dielectric cylinders, $\epsilon_r = 3, 12$ over a range of wavelengths. In both cases, the CP-EP outperforms the V-EP over the entire bandwidth of observation. Additionally, the staircased solution performs more poorly than V-EP solution. This is presumably because the V-EP does not average the permittivity over the differencing grid itself. The study did not provide details on the discretisation of the grid therefore the effect of staircasing on V-EP and the staircased solution is difficult to judge.

There is a large body of literature that is concerned with the averaging of instantaneous dielectrics at interfaces. However, there is comparatively little published on the topic of the effects of averaging at the interface between dispersive media in FDTD. And, in particular, the averaging of dispersive media at the half space interface in GPR problems.

Popovic and Okoniewski (2003) first demonstrated averaging of dispersive materials. In this study, the authors propose an averaging scheme for a grid-aligned water interface at the open end of a coaxial cable filled with Teflon. A 2d body-of-revolution code is used to simulate the setup and an auxiliary differential equation (ADE) developed by Okoniewaki et al. (1997) is used to simulate the frequency-dependent behaviour of water. Polarisation current densities are used to model the dispersive material. The averaging scheme proposed a simple averaging of the polarisation current poles by the fractional area occupied either side of the interface. The scheme has no additional computational requirements. This is because no additional dispersive poles are required to model the averaged material. The numerical simulation result is compared with reflection coefficients derived from transmission line theory. The results are in very good agreement. These results are consistent with that of Kyu-Pyung Hwang and Cangellaris (2001). They show that simple averaging as a means of modelling a grid aligned dielectric/dispersive interface is a successful approach. However, the study was limited to the TEM mode propagating at a single angle of incidence and is therefore not a complete representation of the half-space problem.

Deinega and Valuev (2007) presented a dispersive averaging scheme based on the effective permittivity scheme proposed by Farjadpour et al. (2006) and Mohammadi et al. (2005). In the study, the radar cross-section of a sphere filled with dispersive material obtained when illuminated by a plane wave source was used. The accuracy of the scheme is assessed by an analytical comparison of the results with the Mie scattering theory. The averaging scheme utilises the inverse permittivity tensor to express the

averaging. The electric field is then represented as a sum of three split field variables whose equations are solved independently. Similarly to Popovic and Okoniewski (2003), dispersion is introduced using the ADE method outlined in Okoniewaki et al. (1997). The authors evaluated four smoothing schemes against the scattering theory. The full inverse dielectric tensor, the diagonal tensor in which only the diagonal elements of the full tensor were retained, the V-EP and the staircased solution. They showed that the inverse permittivity tensor was in good agreement with the theory and it performs better than the diagonal tensor, especially for small spheres. Additionally, it was shown the V-EP always underperformed the staircased solution in agreement with Farjadpour et al. (2006).

The success of this methodology is that it allows the averaging schemes to be compared over a range of scattering angles. On the other hand, its main limitation is that the method addresses only the modelling accuracy for small spheres whose scattering can be modelled within and slightly beyond the Rayleigh scattering regime. This does not provide a sufficient basis for modelling half-spaces in GPR which are excited within their Rayleigh and Mie resonance regions. Additionally, the study introduces the use of auxiliary variables to determine the electric field which introduces additionally computational requirements.

In Liu et al. (2012) a coordinate rotation (CR) approach was presented which eliminates the need for field splitting for dielectric/dispersive material interfaces. It was shown that the inverse permittivity tensor is exactly equivalent to the application of the diagonal tensor to D in the rotated coordinate system. This reduced the non-diagonalised system to a diagonal system which can be solved directly with standard FDTD except for a few temporary variables to perform the rotations in and out of the appropriate coordinate systems. Numerical examples were presented to confirm the accuracy and efficiency of the CR approach. The scattering from a 2d cylinder in the TE mode was simulated and compared with the analytic results from the Mie scattering and the split-field approach in Deinega and Valuev (2007). A 25% reduction in CPU time was reported in comparison with the split field approach. The results are in good agreement with the Mie scattering and very good agreement with the split field approach. It should be mentioned that neither the coordinate rotation or the split field approach achieved second-order accuracy.

4.1.2 Analytical Comparisons

In the previous section, several approaches were reviewed to evaluate the accuracy of the permittivity averaging schemes. In this section, the Mie scattering approach is summarised.

Luebbers et al. (1993) showed that the accuracy of the recursive-convolution formulation for frequency-dependent and lossy materials could be evaluated against the exact results from the Mie scattering theory (Ishimaru, 2017). In this study dielectric spheres were illuminated by specifying the incident field as the sphere's surface. The scattered fields from the sphere were then radiated into the far-field using a near to far-field transformation (NTFFT) Umashankar and Taflove (1982). Once the far-fields were calculated they were expressed as radar cross-sections (RCS) and compared with the Mie scattering theory. The results were found to be in excellent agreement with the theory. The main advantage of this approach is that the interaction of homogeneous and inhomogeneous waves can be studied within a complex 3d structure. As opposed to a 1d arrangement where both the source and scattered waves are plane. Additionally, the spheres studied have resonant characteristics which can only be observed in 3d.

These scenarios provide an insight into modelling half-spaces subjected to antenna radiation. This is because the radiation from an antenna is not plane. Furthermore, the half-space is subjected to resonant behaviour since objects which resonate within the GPR bandwidth are often located close to the surface.

Following on from the success of this approach Mohammadi et al. (2005); Deinega and Valuev (2007); Liu et al. (2012) also validated their effective permittivity approaches against the Mie scattering theory. In these studies, the authors successfully validate their approaches for the scattering from small spheres where the level of staircasing is particularly high and the scattering is within and just beyond the Rayleigh scattering this can be shown as follows.

For a PEC the limit of the Rayleigh scattering is given when the wavelength of the incident field is equal to the circumference of the sphere.

$$2\pi r = \lambda \tag{4.1}$$

From this, the radius can be written in terms of N_λ for the shortest non-dispersed wavelength.

$$r = \frac{N_\lambda \Delta x}{2\pi} \qquad (4.2)$$

For a finely resolved mesh, $N_\lambda = 20$ the Rayleigh radius is

$$r = 4\Delta x \qquad (4.3)$$

Thus any sphere modelled with 4 cells or less will only be scattering radiation in the Rayleigh scattering regime. Scattering in the resonant region will certainly occur however it will be numerically dispersed. For resonance to be accurately observed the sphere should be increased in size or the spatial step should be reduced and the physical sphere radius held constant.

The analysis of dispersive dielectric smoothing in Deinega and Valuev (2007) was performed with spheres ranging from $1.5\Delta x$ and $5\Delta x$. Comparing the sphere size with equation 4.3 the majority of this analysis falls within the optical scattering regime and only partially within the resonant regime. The discretisation in Liu et al. (2012) is not given. However, it is assumed that this study is within the optical regime as authors also examine the properties of a metal sphere within the optical frequency band. These schemes do not examine the resonant region and are therefore not sufficient to describe the field behaviour in GPR. Additionally, the scattering data in Deinega and Valuev (2007) shows that the full tensor method performs well for small spheres, the diagonal tensor begins to convergence for spheres greater than $4\Delta x$. This suggests that a relaxed smoothing scheme may be used for larger spheres. This is presumably because as the sphere size increases the contribution from the off-diagonal elements of the permittivity tensor tend toward zero.

In Xu Li et al. (2005) and Robinson and Schneider (2007) the authors present radar cross-section back scatterings results for large staircased dielectric spheres with a radius of $60\Delta l$. The authors report a good agreement with the Mie scattering theory. In these numerical experiments, the spheres are far less staircased than in the previously reported studies. For example Xu Li et al. (2005) report an RMS error for the back-scattering cross-section of less than 4% for spheres with radii over 60 cells and that the RMS error decreases as the sphere size is increased. This result implies that a simple effective permittivity strategy could be used to further improve the scattering result from large spheres. And that the success of this approach can be used to show analytically that non-staircased structures such as half-spaces can be modelled more accurately with the inclusion of a simplified effective permittivity strategy.

4.2 Calculation of the RCS Back-Scatter

The RCS is calculated from the FDTD simulation using a total-field / scattered-field formulation (TF/SF) and near-field to far-field transformations (NTFFT). Once the RCS has been obtained and analytical comparison is made with RCS from the Mie Scattering Theory (Ishimaru, 2017). A review of the TF/SF formulation and the near-field to far-field transformation are reviewed in the following sections.

4.2.1 Implementation of Total-field Scattered-Field

The TF/SF is an attempt to accurately source a plane wave into the difference grid. The TF/SF was first reported in Merewether et al. (1980) which used Huygen's surfaces as a means of sourcing the plane waves. Following this several implementations have been reported. A comprehensive description of the of TF/SF is given in Taflove and Hagness (2005). However, an overview of the relevant parts of the technique is discussed as they have been implemented in this work to calculate the RCS.

TF/SF has several advantages over other plane wave formulations such as the pure scattered-field formulation. These are summarised as follows: The incident wave can be of any duration, polarisation or waveform enabling electrical structures under test to be illuminated under a range of conditions. Also, the TF/SF has a wide dynamic range in comparison with previous techniques such as the pure-scattered field formulation. This enables the response from weakly reflecting structures or cavities to be studied accurately. Furthermore, the TF/SF formulation enables the direct study of the scattered field from electrical structures.

The TF/SF divides the area of computation into two distinct regions. Their arrangement with a 2d difference grid is shown in Figure 4.1. The field in the total-field region is equal to the sum of the incident field and the scattered field. And the field in the scattered-field is equal to field reflected from the scatterer only. This superposition of fields is permitted due to the linearity of Maxwell's equations. Following from this definition the update equations for the total field and scattered field for the 1d case are given by:

$$E_{z_{total}}\Big|_i^{n+1} = E_{z_{total}}\Big|_i^n + \frac{\Delta t}{\epsilon_0 \Delta x}\left(H_{y_{total}}\Big|_{i+\frac{1}{2}}^{n+\frac{1}{2}} - H_{y_{total}}\Big|_{i-\frac{1}{2}}^{n+\frac{1}{2}}\right) \tag{4.4}$$
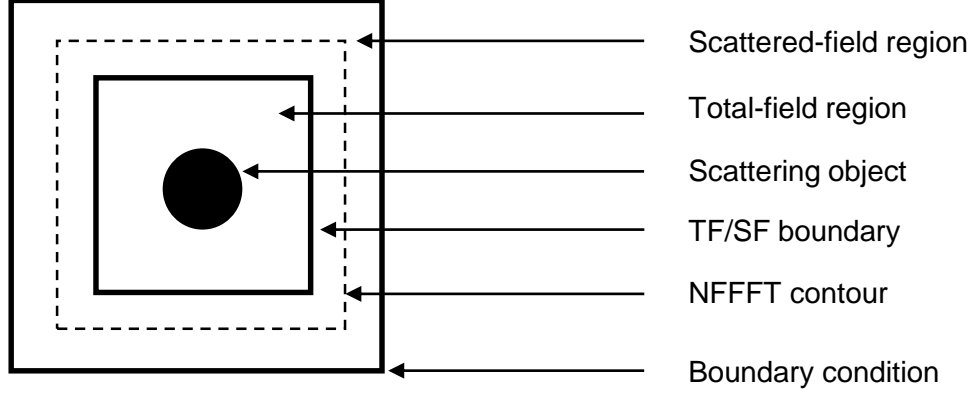
Figure 4.1: Total-field and scattered-field regions of the finite-difference time-domain grid.

$$E_{z_{Scat}}\Big|_i^{n+1} = E_{z_{scat}}\Big|_i^n + \frac{\Delta t}{\epsilon_0 \Delta x}\left(H_{y_{scat}}\Big|_{i+\frac{1}{2}}^{n+\frac{1}{2}} - H_{y_{scat}}\Big|_{i-\frac{1}{2}}^{n+\frac{1}{2}}\right) \qquad (4.5)$$

The equations can be used freely within regions of the appropriate field type. However, the equation is incorrect at the boundary as the fields to either side do not contain the same superposition of fields. For example, at the boundary the $E_{z_{total}}\Big|_{i'}^{n+1}$ field at the boundary in Figure 4.2 is a superposition of the incident field and the scattered field, however, the $H_{y_{scat}}\Big|_{i'-\frac{1}{2}}^{n+\frac{1}{2}}$ contains only the scattered field. This inconsistency is resolved by the addition of the incident field to the scattered field. This the sourcing mechanism for the incident field. For example:

$$E_{z_{total}}\Big|_{i'}^{n+1} = E_{z_{total}}\Big|_{i'}^n + \frac{\Delta t}{\epsilon_0 \Delta x}\left(H_{y_{total}}\Big|_{i'+\frac{1}{2}}^{n+\frac{1}{2}} - \left(H_{y_{scat}}\Big|_{i'-\frac{1}{2}}^{n+\frac{1}{2}} + H_{y_{inc}}\Big|_{i'-\frac{1}{2}}^{n+\frac{1}{2}}\right)\right) \qquad (4.6)$$

$$E_{z_{total}}\Big|_{i'}^{n+1} = E_{z_{total}}\Big|_{i'}^n + \frac{\Delta t}{\epsilon_0 \Delta x}\left(H_{y_{total}}\Big|_{i'+\frac{1}{2}}^{n+\frac{1}{2}} - H_{y_{scat}}\Big|_{i'-\frac{1}{2}}^{n+\frac{1}{2}}\right) - H_{y_{inc}}\Big|_{i'-\frac{1}{2}}^{n+\frac{1}{2}} \qquad (4.7)$$

The $H_{y_{scat}}\Big|_{i'-\frac{1}{2}}^{n+\frac{1}{2}}$ field also requires a correction such that the incident field is subtracted from the incoming total field.

In this 1d example, the incident field is sourced at two single points. However, in 2d the field is sourced along the edges of a rectangle as in Figure 4.1, and in 3d the field is sourced over the surface of a cuboid. Thus the incident field must be sampled at these
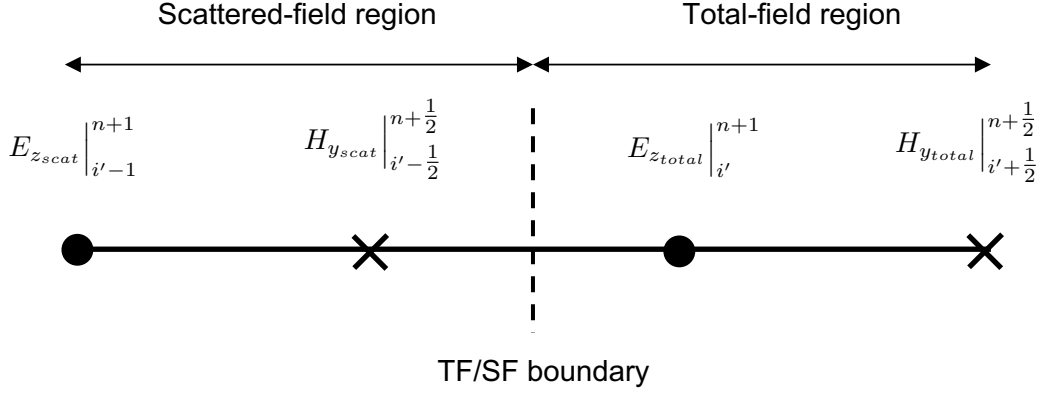
Figure 4.2: Arrangement of the E_z and H_z nodes at a 1d TF/SF boundary.

points in space and time. This can be achieved analytically by evaluating waveform at the required points. However, this method introduces leakage into the scattered-field region due to mismatch in the analytic wave and numerical dispersion present in the total-field. More commonly an auxiliary 1d simulation is used to evaluate the incident field at the required points. When the direction of propagation of the plane wave is grid-aligned the sourcing is perfect provided that the time and spatial steps in the auxiliary grid are set equal to the those in the 3d grid. This is because the phase accumulation error is matched in both grids and thus the cancellation at the TF/SF boundary is exact. For none grid-aligned propagation it has been shown that perfect sourcing can also be achieved Schneider (2004) and also using a 1d auxiliary simulation (Tan and Potter, 2007)

In addition to correcting the fields at TF/SF boundary, a boundary condition to simulate an infinite extent must be utilised in the scattered field region to prevent the reflection of fields back into the total-field region. In this study a 10 cell recursive integration PML (RIPML) has been used (Giannopoulos, 2008).

4.2.2 Near to Far-Field transformation

Once the fields scattered from the sphere have been calculated in the scattered-field region they are radiated into the far-field using a near-field to far-field transformation.

A near to far-field transformation (NTFFT) is a commonly used technique to calculate the far-field response of an antenna or the radar cross-section of a scattering object. The idea is to radiate the scattered field from the TF/SF or the pure scattered field into the far-field without simulating the intermediate space with FDTD. The ad-

52

vantages of this approach are a reduction in computational resources and an increase in accuracy. The increase in accuracy follows from the fact that wave propagation over a large region of space would suffer from the accumulation of phase errors due to the inherent numerical dispersion in an FDTD grid.

The NTFFT was first reported in Umashankar and Taflove (1982) and verified experimentally in Taflove et al. (1985). At the time this procedure commonly outstripped available computational resources for larger scatters and so an on-the-fly time-domain algorithm was developed which required less hard disk storage and only required a single Fourier transform should the frequency spectra be required (Luebbers et al., 1991). However, the original formulation has been used as it was deemed easier to implement and the computation is manageable with currently available resources.

In this method, the time history of the electric and magnetic fields tangential to an integrating surface such described in Figure 4.3 are stored to disk. After the simulation is finished the fields are then Fourier transformed for each frequency of interest and converted into electric and magnetic currents. Once these quantities have been obtained they are then radiated into the far-field region using a set of scattering integrals given by equation 4.8 and 4.9. The phasor $\vec{E}$ is then calculated from the phasor potentials according to equation 4.12. Finally, the radar cross-section is obtained using 4.13 and is normalised by the incident field.

$$\vec{A} = \frac{\mu_0 e^{-jkr_1}}{4\pi r_1}\vec{N} \tag{4.8}$$

$$\vec{F} = \frac{\epsilon_0 e^{-jkr_1}}{4\pi r_1}\vec{L} \tag{4.9}$$

$$\vec{N} = \int_S \vec{J}_s e^{jkr_2\cos\psi} d\vec{s_2} \tag{4.10}$$

$$\vec{L} = \int_S \vec{M}_s e^{jkr_2\cos\psi} d\vec{s_2} \tag{4.11}$$

$$\vec{E} = -j\omega\left[\vec{A} + \frac{1}{k^2}\nabla(\nabla\cdot\vec{A})\right] - \frac{1}{\epsilon_0}\nabla\times\vec{F} \tag{4.12}$$

where r_1 is the distance to the observation point, r_2 is the distance to a point on
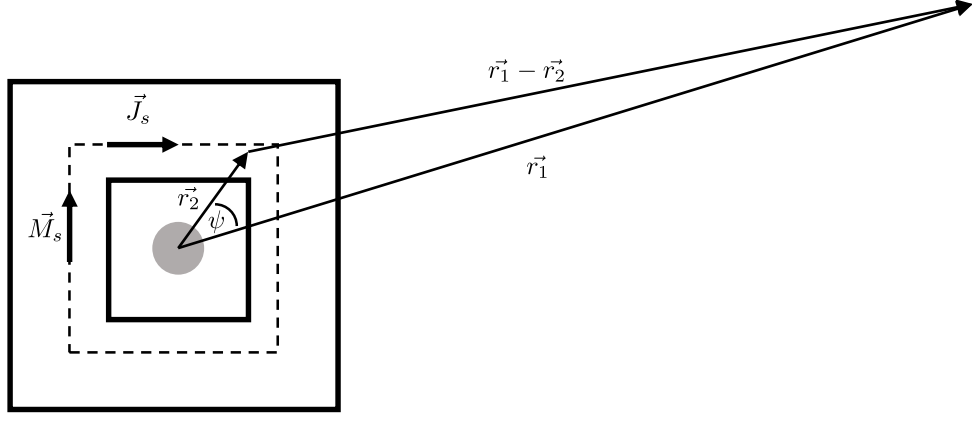
Figure 4.3: Near-field to far-field transformation schematic.

the current surface, ψ is the angle between r_1 and r_2 and J_s and M_s are the electric and magnetic surface currents on the integration surface S_2 as shown in Figure 4.3

$$RCS(\theta, \phi) = \lim_{r \to \infty} \left(4\pi r^2 \frac{|E_z(\theta, \phi)|^2}{|E_{z_{inc}}(\theta, \phi)|^2} \right) \qquad (4.13)$$

4.2.3 Implementation of the Near to Far-field transformation

The process above describes the general near-field to far-field concept. From this general theory, the RCS can be deduced for all angles and frequencies of interest from the FDTD simulation. However, the study presented here is primarily concerned with RCS in the $-\hat{i}$ direction. Whilst the total scattering across all angles is of interest as a measure of the accuracy of the effective smoothing, a good measure of the accuracy can be made by only computing the back-scattering. This due to the implicit calculation of the whole scattered field over the integrating surface. Any error generated during this calculation will propagate to the RCS back-scatter. Additionally, it has been shown by Robinson and Schneider (2007) that the error generated by the NTFFT is greatest at this angle. Therefore the back-scattering offers a measure of the accuracy of the effective permittivity in the worst possible case. A description of the FDTD NTFFT implementation follows.

First the tangential electric and magnetic fields on the integrating surface should be determined. These fields must be determined at the same position in time and space such that they are radiated to the far-field coherently. These fields in FDTD are offset by a half a spatial-step and half a time-step, therefore, they must be interpolated.
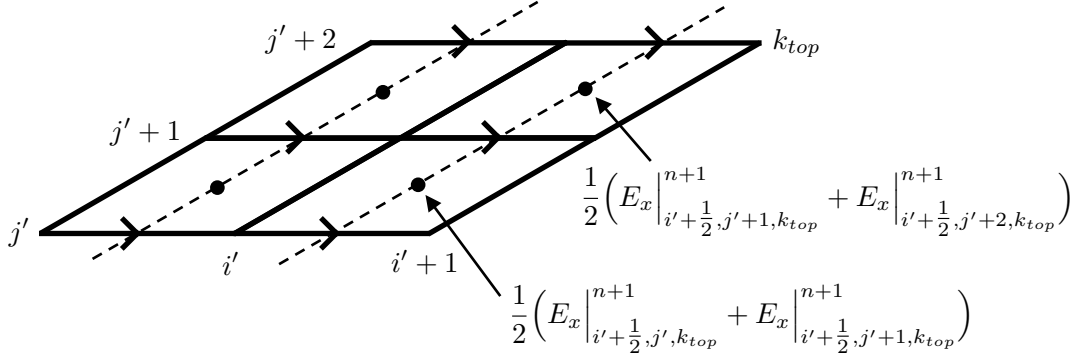
Figure 4.4: Example averaging of E_x fields on the top face of the integration surface.

The integration surface can be chosen to lie in the plane of the tangential electric fields for each of the surfaces that make up the cuboid integration surface. The tangential E fields are averaged using the arithmetic mean at the centre of each Yee cell face in the plane such that they can be integrated using a mid-point Riemann sum. An approach without averaging using the composite Simpson's rule was also investigated, however it did not yield additional accuracy. Therefore the Riemann approach was used for its ease of implementation. An example of the averaging for the E_x field on the top face of the integration surface is given in Figure 4.4.

Similarly, the tangential H fields are found at centres of Yee cell face in the integration plane. Given the plane, in the tangential E components the tangential H components are found half a cell to each side of the plane. First, the tangential components either side of the plane are averaged on to the plane and then the components at each end of the cell are averaged into the centre using an arithmetic average. An example of the averaging for the E_x field on the top face of the integration surface is given in Figure 4.5.

The evaluation of E and H is staggered in time by half a time step. The fields are calculated at the same point in time by phase-shifting the Fourier transformed magnetic fields by $e^{-j\omega \Delta t/2}$.

Once the tangential electric and magnetic fields have been calculated they are transformed into the equivalent surface currents using the standard identities.

The calculation of the back-scatter radar cross-section does not require all of the tangential fields. This is due to the angle of observation. This is shown as follows.

The spatial part of the phase angle in Equations 4.10 and 4.11 can be written using

$$\frac{1}{4}\left(H_y\Big|^{n+\frac{1}{2}}_{i'+\frac{1}{2},j',k_{top}+\frac{1}{2}} + H_y\Big|^{n+\frac{1}{2}}_{i'+\frac{1}{2},j',k_{top}-\frac{1}{2}} + H_y\Big|^{n+\frac{1}{2}}_{i'+\frac{1}{2},j'+1,k_{top}+\frac{1}{2}} + H_y\Big|^{n+\frac{1}{2}}_{i'+\frac{1}{2},j'+1,k_{top}-\frac{1}{2}}\right)$$
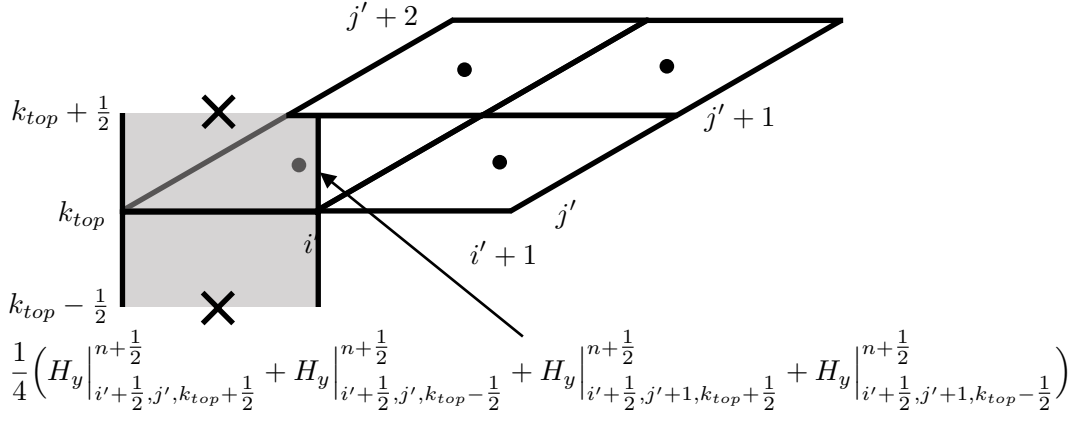
Figure 4.5: Example averaging of H_y fields on the top face of the integration surface.

the definition of the dot product

$$r_2 \cos \psi = \vec{r_2} \cdot \hat{r_1} \tag{4.14}$$

For the back-scattering RCS we are only interested in $\hat{r_1} = -\hat{j}$

Now

$$\vec{N} = \int_S \vec{J_s} e^{-jkx} d\vec{s_2} \tag{4.15}$$

$$\vec{L} = \int_S \vec{M_s} e^{-jkx} d\vec{s_2} \tag{4.16}$$

For the back-scattering we are interested in E_z component. At $\vec{r_1}(\phi,\theta)$ $E_z = E_\phi$

$$RCS|_{\theta=\frac{\pi}{2},\phi=\pi} = \frac{k^2}{4\pi} \frac{|L_\phi + \eta_0 N_\theta|^2}{|E_{z_{inc}}|^2} \tag{4.17}$$

where

$$N_\theta = \int_S -J_z e^{-jkx} ds_2 \tag{4.18}$$

$$L_\phi = \int_S -M_y e^{-jkx} ds_2 \tag{4.19}$$

56

Substituting Equations 4.18 and 4.19 gives the RCS back-scattering.

$$RCS|_{\theta=\frac{\pi}{2},\phi=\pi} = \frac{k^2}{4\pi|E_{z_{inc}}|^2}\left|\oint_S (M_y + \eta_0 J_z)e^{-jkx})ds_2\right|^2 \qquad (4.20)$$

Equation 4.20 is then evaluated over the 6 faces of the cuboid integration surface whose edges are given by $i_l, i_r, j_f, j_{ba}, k_b, k_t$. For the front, back, bottom and top surfaces x at the x coordinate corresponding to the centre of each Yee cell. For the left and right surfaces, the x coordinates are the left and right edges. The FDTD back-scatter is given by

$$RCS|_{\theta=\frac{\pi}{2},\phi=\pi} = \frac{dl^2k^2}{4\pi|E_{z_{inc}}|^2}\left|\sum_{i=i_l}^{i_r-1}\sum_{j=j_f}^{j_{ba}-1}(M_y|_{i,j,k_b} + M_y|_{i,j,k_t})e^{-jk\Delta l(-\frac{i_r-i_l}{2}+i-i_l+\frac{1}{2})}+\right.$$
$$\sum_{j=j_f}^{j_{ba}-1}\sum_{k=k_b}^{k=k_t-1}(M_y|_{i_f,j,k} + \eta_0 J_z|_{i_f,j,k})e^{jk\Delta l_l} + (M_y|_{i_{ba},j,k} + \eta_0 J_z|_{i_{ba},j,k})e^{-jk\Delta l_r}+$$
$$\left.\sum_{i=i_l}^{i_r-1}\sum_{k=k_b}^{k=k_t-1}\eta_0(J_z|_{i,j_l,k} + J_z|_{i,j_r,k})e^{-jk\Delta l(-\frac{i_r-i_l}{2}+i-i_l+\frac{1}{2})}\right|^2$$

$$(4.21)$$

4.3 Effective Smoothing for Half-Spaces

4.3.1 Constant Dielectric Smoothing

In Liu et al. (2012) is shown that the general inverse permittivity tensor is equivalent to a rotation from the tilted surface to the difference grid. The equation shows that the correct permittivity averaging for the difference in the permittivity at E_x and E_y is a linear combination of the arithmetic and harmonic averages of the permittivity in the tilted basis.

$$\begin{bmatrix} D'_x \\ D'_y \end{bmatrix} = \begin{bmatrix} \langle\epsilon'_a\rangle & 0 \\ 0 & \langle\epsilon'_h\rangle \end{bmatrix} \begin{bmatrix} E'_x \\ E'_y \end{bmatrix} \qquad (4.22)$$

where $\langle\epsilon'_a\rangle$ and $\langle\epsilon'_h\rangle$ are the arithmetic and harmonic averages of the permittivity in the dashed coordinate system.
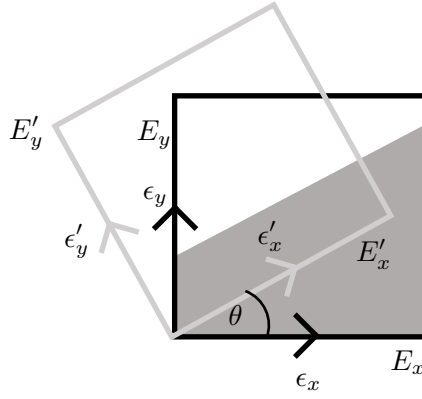
Figure 4.6: Rotated difference grid such that E'_y and E'_x are normal and perpendicular to the tilted material interface. ϵ_x and ϵ_y are the permittivities at E_x and E_y, and ϵ'_x and ϵ'_y are the permittivities at E'_x and E'_y

$$
\begin{bmatrix} D_x \\ D_y \end{bmatrix} = \begin{bmatrix} \cos\theta & \sin\theta \\ -\sin\theta & \cos\theta \end{bmatrix} \begin{bmatrix} \langle\epsilon'_a\rangle & 0 \\ 0 & \langle\epsilon'_h\rangle \end{bmatrix} \begin{bmatrix} \cos\theta & -\sin\theta \\ \sin\theta & \cos\theta \end{bmatrix} \begin{bmatrix} E_x \\ E_y \end{bmatrix} \tag{4.23}
$$

For a grid aligned surface this equation reduces to

$$
\begin{bmatrix} D_x \\ D_y \end{bmatrix} = \begin{bmatrix} \langle\epsilon'_a\rangle & 0 \\ 0 & \langle\epsilon'_h\rangle \end{bmatrix} \begin{bmatrix} E_x \\ E_y \end{bmatrix} \tag{4.24}
$$

It is shown here that a similar result for grid aligned interfaces can be obtained using a contour path approach.

The integral form of Ampere's law relates the time-varying displacement field flux to the projection of the magnetic field onto a contour.

$$
\frac{\partial}{\partial t} \int_S \vec{D} \cdot d\vec{s} = \int_C \vec{H} \cdot d\vec{l} \tag{4.25}
$$

Figure 4.7 shows the Yee cell field arrangement for the TE mode where there is a dielectric interface in the xz face at (i,j). The Amperian surface S bounded by C is shown spanning the interface. ϵ_1 is the electric permittivity assigned at the location of
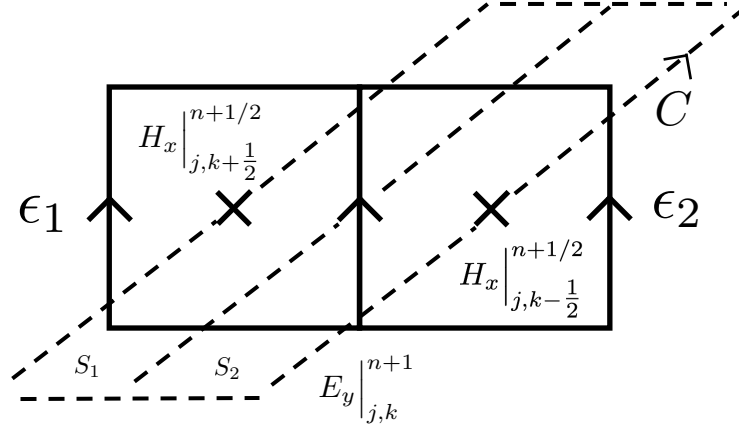
Figure 4.7: Contour paths for a material interface aligned with the FDTD grid.
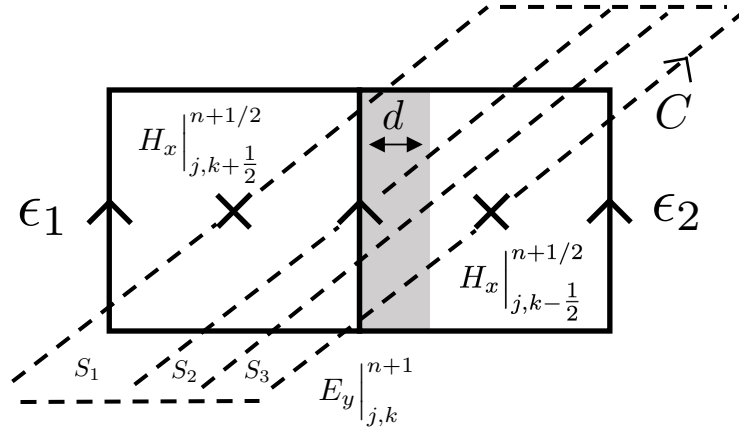
Figure 4.8: Contour paths for a material interface offset from the FDTD grid. The grey region also has a permittivity ϵ_1.

$E_y\Big|_{j,k-1}$ and ϵ_2 is the electric permittivity assigned at the location of $E_y\Big|_{j,k+1}$

When integrating over the patch S it is assumed that $\vec{D}$ is equal to the average value over the surface (Taflove and Hagness, 2005). In the case of Figure 4.7 the field value $D_y\Big|_{i,j}$. Enforcing the equality of the tangential D field at the interface allows the surface to be broken into two surfaces S_1 and S_2 such that the sum of the electric field flux through each is equal to the total through S. This is given by

$$\frac{\partial}{\partial t}\left[\epsilon_1 E_y\Big|_{i,k}^{n+1/2}\frac{1}{2}\Delta z + \epsilon_2 E_y\Big|_{i,k}^{n+1/2}\frac{1}{2}\Delta z\right] =$$
$$H_x\Big|_{i+1/2,k} - H_x\Big|_{i-1/2,k} \tag{4.26}$$

The first term is the flux of the electric field which flows through $S1$. The second terms is equal to the flux through the $S2$.

Collecting the terms gives

$$\frac{\partial}{\partial t}\epsilon^* E_y\Big|_{i,k}^{n+1/2}\Delta z = H_x\Big|_{i+1/2,k}^{n+1/2} - H_x\Big|_{i-1/2,k}^{n+1/2} \tag{4.27}$$

where

$$\epsilon^* = \frac{\epsilon_1 + \epsilon_2}{2} \tag{4.28}$$

Applying the central-difference approximation to the time derivative yields the standard 2d TE update equation with a modified permittivity.

$$E_y\Big|_{i,k}^{n+1}\Delta z = E_y\Big|_{i,k}^{n} + \frac{\Delta t}{\epsilon^*\Delta z}\left(H_x\Big|_{i+1/2,k}^{n+1/2} - H_x\Big|_{i-1/2,k}^{n+1/2}\right) \tag{4.29}$$

Equation 4.29 shows the standard second-order behaviour of the free space case is obtained when the materials either side of the half space are averaged.

The contour method used here can also derive the expression for the EP when the interface is offset from the difference grid as given in Kyu-Pyung Hwang and Cangellaris

(2001).

Figure 4.8 shows the Amperian surface S bounded by the contour C where the interface is offset from the electric field node by $0 \leq d \leq 0.5$ as a fraction of the cell width. As in the previous case, the continuity of tangential displacement field across the interface allows the computation of the flux through S as the sum of the fluxes through S_1, S_2 and S_3. The evaluation of Ampere's law over this contour is given by

$$\frac{\partial}{\partial t}\left[\epsilon_1\left(\left.E_y\right|_{i,k}^{n+1/2}\frac{1}{2}\Delta z + \left.E_y\right|_{i,k}^{n+1/2}d\Delta z\right) + \epsilon_2\left(\left.E_y\right|_{i,k}^{n+1/2}\frac{1}{2}\Delta z - \left.E_y\right|_{i,k}^{n+1/2}d\Delta z\right)\right] =$$
$$\left.H_x\right|_{i+1/2,k} - \left.H_x\right|_{i-1/2,k}$$

$$(4.30)$$

The first term is the flux of the electric field which flows through the half cell S_1. The second considers the flux through the region up to the interface, S_2. The difference in the third and fourth terms describe the flux that flows through the region on the right-hand side of the interface, S_3.

Collecting the terms gives

$$\frac{\partial}{\partial t}\epsilon^*\left.E_y\right|_{i,k}^{n+1/2}\Delta z = \left.H_x\right|_{i+1/2,k}^{n+1/2} - \left.H_x\right|_{i-1/2,k}^{n+1/2} \tag{4.31}$$

where the effective permittivity is given by

$$\epsilon^* = (\tfrac{1}{2} + d)\epsilon_1 + (\tfrac{1}{2} - d)\epsilon_2 \tag{4.32}$$

Applying the central-difference approximation to the time derivative gives equation 4.29.

The 2d contour path approach to calculating the value of the effective permittivity can be extended to the 3d case. Figure 4.9 show a diagram of four adjacent Yee cells. Each Yee cell is assigned a volumetric electric permittivity based on a physical model. The figure shows a plane through $k+1/2$ perpendicular to the z direction. The Amperian loop for the integral for the contour path approach is shown passing through the magnetic fields adjacent to the E_z node which points out of the page.

61
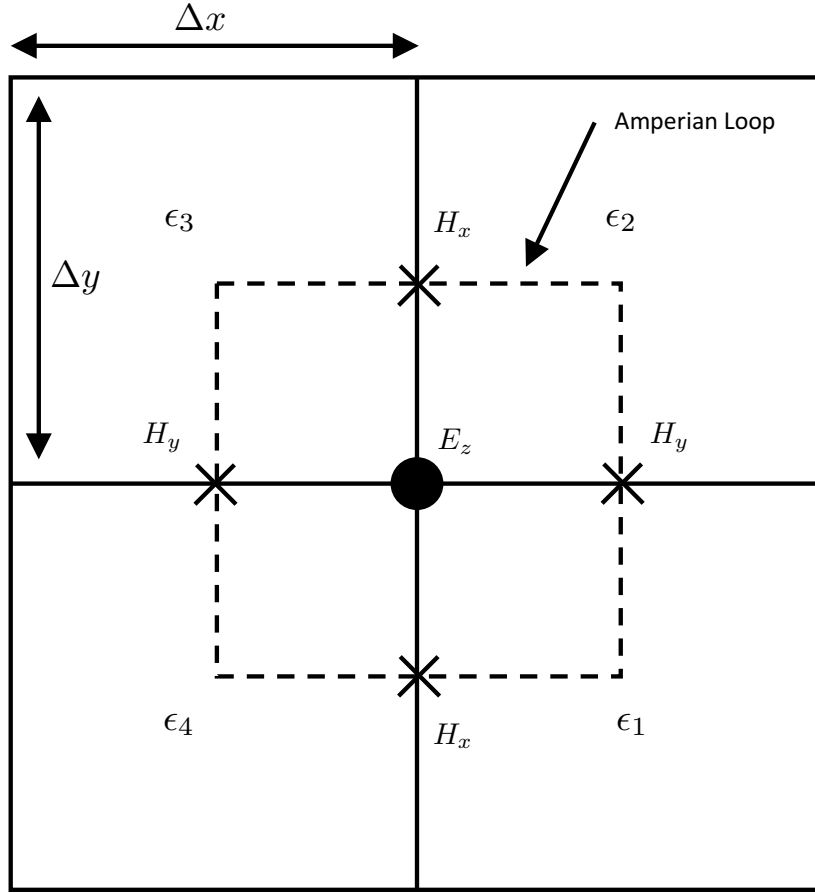
Figure 4.9: Contour paths for a 3d material interface at a surface $k + 1/2$. Four Yee cells are shown. In each Yee cell the volumetric permittivities ϵ_1, ϵ_2, ϵ_3, ϵ_4 are assigned. The EP approach calculate the effective permittivity at the location of the E_z based on the surrounding volumetric permittivity.

From Ampere law we can assume that the displacement flux through the 4 patches in each quadrant of the Amperian loop is equal to the total displacement flux through the loop. This can be written

$$\frac{\partial}{\partial t}\left[(\epsilon_1 + \epsilon_2 + \epsilon_3 + \epsilon_4)\frac{\Delta x \Delta y}{4}E_z\right] =$$

$$\Delta y\left(H_y\Big|_{i+1/2,j,k+1/2}^{n+1/2} - H_y\Big|_{i-1/2,j,k+1/2}^{n+1/2}\right) - \Delta x\left(H_x\Big|_{i,j+1/2/,k+1/2}^{n+1/2} - H_x\Big|_{i,j-1/2/,k+1/2}^{n+1/2}\right)$$

$$(4.33)$$

Collecting the terms and rearranging an expression for the update equation for E_z in terms of the effective permittivity is given

$$E_z\Big|_{i,j+1/2,k+1/2}^{n+1} = E_z\Big|_{i,j+1/2,k+1/2}^{n-1}$$

$$\frac{\Delta t}{\epsilon^* \Delta x}\left(H_y\Big|_{i+1/2,j,k+1/2}^{n+1/2} - H_y\Big|_{i-1/2,j,k+1/2}^{n+1/2}\right) - \frac{\Delta t}{\epsilon^* \Delta y}\left(H_x\Big|_{i,j+1/2/,k+1/2}^{n+1/2} - H_x\Big|_{i,j-1/2/,k+1/2}^{n+1/2}\right)$$

$$\tag{4.34}$$

where

$$\epsilon^* = \frac{\epsilon_1 + \epsilon_2 + \epsilon_3 + \epsilon_4}{4} \tag{4.35}$$

4.3.2 Dielectric/Dispersive Interfaces

The displacement field D is obtained from the constitutive relation as

$$\vec{D} = \epsilon\vec{E} \tag{4.36}$$

This can be written in terms of polarisation $\vec{P}$ which accounts for behaviour of electric dipoles within the medium.

$$\vec{D} = \epsilon_0\vec{E} + \vec{P} \tag{4.37}$$

For linear, isotropic materials P can be written in terms of a frequency-dependent susceptibility function $\chi_e(\omega)$ with the inclusion of ϵ_∞ which accounts for the permittivity at high frequencies for which the susceptibility function goes to zero.

$$\vec{D} = \epsilon_0\epsilon_\infty\vec{E} + \epsilon_0\chi_e(\omega)\vec{E} \tag{4.38}$$

The behaviour of the electric dipoles can be modelled using different susceptibility models. The Debye model is most commonly used in GPR to model soils and water. The Debye function relates the polarisation to the voltage across a capacitor in an RC circuit. It is given by

$$\chi_e(\omega) = \sum_{d=1}^{n} \frac{\epsilon_d}{1 + j\omega\tau_d} \tag{4.39}$$

where n is the number of poles, τ_d is known as the relaxation time which is the time it takes the dipole to return to equilibrium. ϵ_d in combination with ϵ_∞ defines the permittivity when the frequency is zero or the relaxation time is zero (instantaneous dielectric).

For a grid aligned air/dispersive half space modelled by a single pole dispersive medium equation 4.28 is given by

$$\langle\epsilon_a\rangle = \frac{\epsilon_1 + \epsilon_2(\omega)}{2} \tag{4.40}$$

for a single pole Debye medium this can be written

$$\langle\epsilon_a\rangle = \frac{\epsilon_1 + \epsilon_\infty + \frac{\epsilon_d}{1+j\omega\tau_d}}{2} \tag{4.41}$$

which can be written as a single Debye pole

$$\langle\epsilon_a\rangle = \epsilon_{\infty_a} + \frac{\epsilon_a}{1 + j\omega\tau_a} \tag{4.42}$$

where

$$\epsilon_{\infty_a} = \frac{\epsilon_1 + \epsilon_\infty}{2} \tag{4.43}$$

and

$$\epsilon_a = \frac{\epsilon_d}{2} \tag{4.44}$$

4.3.3 Dispersive/Dispersive Interfaces

In Liu et al. (2012) the authors report their method can only be used for a dielectric/dispersive interface. However, it is shown here that the CR approach can be extended to the dispersive/dispersive interface without using the split field approach such as

described in Deinega and Valuev (2007).

First, the arithmetic average is given in Kyu-Pyung Hwang and Cangellaris (2001) is considered

$$\langle \epsilon_a \rangle = a\epsilon_1(\omega) + b\epsilon_2(\omega) \tag{4.45}$$

where $a = \frac{1}{2} - d$ and $b = \frac{1}{2} + d$

for two single pole debye media

$$\langle \epsilon_a \rangle = \left(\epsilon_{\infty_1} + \frac{\epsilon_{d_1}}{1 + j\omega\tau_{d_1}} \right) a + \left(\epsilon_{\infty_2} + \frac{\epsilon_{d_2}}{1 + j\omega\tau_{d_2}} \right) b \tag{4.46}$$

where ϵ_{d_1} and ϵ_{d_1} account for the relative permittivity when the frequency is zero, and τ_{d_1} and τ_{d_1} are the relaxation times for each pole.

which can be written as a two pole Debye function

$$\langle \epsilon_a \rangle = \epsilon_{\infty_a} + \frac{a\epsilon_{d_1}}{1 + j\omega\tau_{d_1}} + \frac{b\epsilon_{d_2}}{1 + j\omega\tau_{d_2}} \tag{4.47}$$

where $\epsilon_{\infty_a} = a\epsilon_{\infty_1} + b\epsilon_{\infty_2}$

Next the harmonic average given in Kyu-Pyung Hwang and Cangellaris (2001) is considered

$$\frac{1}{\langle \epsilon_h \rangle} = \frac{a}{\epsilon_{d_1}} + \frac{b}{\epsilon_{d_2}} \tag{4.48}$$

where $a = 1 - d$ and $b = d$

Writing the displacement field D in terms of the static permittivity and the susceptibility $\chi_e(\omega)$

$$\vec{D}(\omega) = \epsilon_0\epsilon_\infty\vec{E}(\omega) + \epsilon_0\chi_e(\omega)\vec{E}(\omega) \tag{4.49}$$

It can be seen that the averaging can be performed by averaging the constitutive parameters separately as in Popovic and Okoniewski (2003).

A single pole expression for the harmonic averaging can be found

$$D_\perp = \epsilon_0 \langle \epsilon_{\infty_h} \rangle E_\perp + \epsilon_0 \langle \chi_e(\omega)_h \rangle E_\perp \tag{4.50}$$

where $D_\perp$ and $E_\perp$ are the field components perpendicular to the material interface. $\langle \epsilon_\infty \rangle$ is given by the harmonic average of the permittivity at very high frequency as in Liu et al. (2012).

$$\frac{1}{\langle \epsilon_{\infty_h} \rangle} = \frac{a}{\epsilon_{\infty_1}} + \frac{b}{\epsilon_{\infty_2}} \tag{4.51}$$

The harmonic average of the susceptibility function is written

$$\langle \chi_e(\omega)_h \rangle = \frac{\chi_1(\omega)\chi_2(\omega)}{a\chi_2(\omega) + b\chi_1(\omega)} \tag{4.52}$$

The numerator is given by

$$\chi_1(\omega)\chi_2(\omega) = \frac{\epsilon_{d_1}\epsilon_{d_2}}{(1 + j\omega\tau_{d_1})(1 + j\omega\tau_{d_2})} \tag{4.53}$$

The denominator is given by

$$a\chi_2(\omega) + b\chi_1(\omega) = \frac{a\epsilon_{d_2}}{1 + j\omega\tau_{d_2}} + \frac{b\epsilon_{d_1}}{1 + j\omega\tau_{d_1}} \tag{4.54}$$

Cross multiplying the fractions gives

$$a\chi_2(\omega) + b\chi_1(\omega) = \frac{a\epsilon_2(1 + j\omega\tau_1) + b\epsilon_1(1 + j\omega\tau_2)}{(1 + j\omega\tau_{d_2})(1 + j\omega\tau_{d_1})} \tag{4.55}$$

Combining the numerator and the denominator gives

$$\frac{\chi_1(\omega)\chi_2(\omega)}{a\chi_2(\omega) + b\chi_1(\omega)} = \frac{\epsilon_{d_1}\epsilon_{d_2}}{a\epsilon_{d_2}(1 + j\omega\tau_{d_1}) + b\epsilon_{d_1}(1 + j\omega\tau_{d_2})} \tag{4.56}$$

Grouping the terms and rewriting in the Debye form gives

Soil Moisture Content	ϵ_∞	σ	A_1	A_2	τ_1	τ_2
2.5%	3.2	0.397	0.75	0.3	2.71	0.108
5%	4.15	1.11	1.80	0.6	3.79	0.151
10%	6	2	2.75	0.75	3.98	0.251

Table 4.1: Debye model parameters for Puerto Rico type clay loams. Parameters fitted by Teixeira et al. (1998).

$$\langle \chi_e(\omega)_h \rangle = \frac{\epsilon_{d_h}}{1 + j\omega\tau_h} \tag{4.57}$$

where

$$\epsilon_{d_h} = \frac{\epsilon_{d_1}\epsilon_{d_2}}{a\epsilon_{d_2} + b\epsilon_{d_1}} \tag{4.58}$$

and

$$\tau_h = \frac{a\epsilon_{d_2}\tau_1 + b\epsilon_{d_1}\tau_2}{a\epsilon_{d_2} + b\epsilon_{d_1}} \tag{4.59}$$

4.4 Numerical Experiments

In the following experiments, the scattering of plane waves from spheres filled with clay soils has been investigated as a means of evaluating the effective permittivity scheme and its application to the GPR half-space problem. The soils used consists of Puerto Rico type clay loams which have a moisture content of 2.5%, 5% and 10%. The soils have been modelled using a 2-pole Debye model fitted by Teixeira et al. (1998). In this model the Debye parameters have been fitted to experimental data acquired by Hipp (1974) in which the relative permittivity and conductivity were measured over a 30 MHz - 40 GHz bandwidth. These frequencies are within the typical GPR bandwidth. Therefore they provide a good basis to test the averaging scheme. The Debye model parameters are given in Table 4.1

The soil parameters are introduced into each FDTD model using the novel piecewise linear recursive convolution (PLRC) approach reported by Giannakis and Giannopoulos (2014) called the Polarisation Density (PD) method. It has been shown that the PD method shows increased accuracy over the PLRC (Kelley and Luebbers, 1996) for reflection coefficients in 1d transmission lines. It is conjectured that the increase in

accuracy is due to the analytic evaluation of the polarisation density time derivative as opposed to a central difference approximation. This dispersion scheme was chosen for its accuracy and its use within the GPR modelling community (Giannakis et al., 2016b; Warren and Giannopoulos, 2017). Also, the formulation is particularly straightforward to use as the $\langle \epsilon_\infty \rangle$, ϵ_d and τ can be specified directly.

4.4.1   Back-Scattering from Spherical Soil Samples

The first set of numerical experiments evaluate the performance of the EP for the back-scattering radar cross-section from spheres whose properties are those of Puerto Rican soils.

In each experiment, a $200 \times 200 \times 200$ cell domain contained a sphere with a 60 cell radius illuminated by a Gaussian pulse with a centre frequency of 300MHz. A 10 cell PML was placed around the outer edges of the domain.
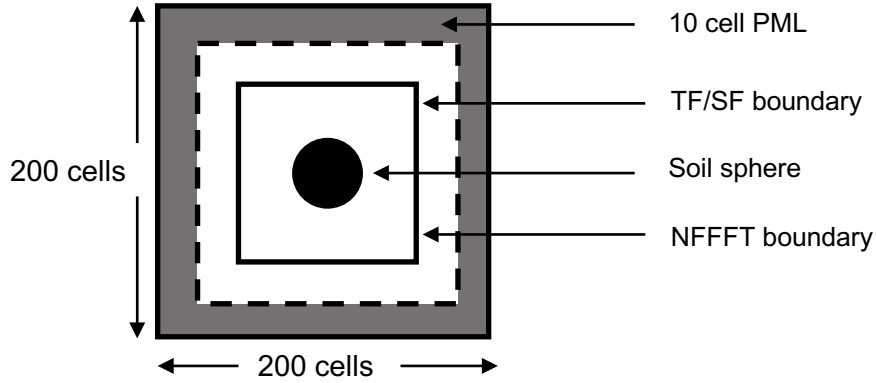
Figure 4.10: Diagram of the FDTD model for the Mie scattering from a range of soil targets.

There were three criteria for pulse selection. The first is a broadband pulse. A Gaussian pulse was selected which permitted a range of frequencies to be investigated. Secondly, 300 MHz is characteristic of a lower frequency GPR system that would be used to investigate soil structure. And thirdly, the pulse must be able to probe the frequencies for which there is a significant variation in the soils electrical properties. For the soil types used in this study the largest variation occurs within the 0 MHz-600 MHz bandwidth and therefore the 300 MHz centre frequency Gaussian pulse provided adequate resolution within this range.

The error due to staircasing should be equal for each soil type such that the errors generated by the EP can be compared. This was achieved by holding the number of

cells in the sphere radius constant for each soil type and varying the spatial step such that the wavelength at the centre frequency at the highest dielectric strength within the soil is resolved by 35 cells. This discretisation is given by

$$\Delta l = \frac{c_0}{35f\sqrt{\epsilon_{r_{max}}}} \tag{4.60}$$

The number of points used per wavelength was 35 to ensure that the higher frequency content of the pulse is correctly resolved. This scheme also ensures that the non-dispersed frequency content is the same for each experiment regardless of the dielectric strength of the medium.

The number of iterations is dependant on the desired outcome from the fast Fourier transform (FFT). When FFTs are performed to signals obtained in FDTD care should be taken to ensure that the usable part of the spectrum contains sufficient resolution to observe the physical behaviour. For instance, at the Nyquist frequency, we require two spatial steps to reconstruct the signal. This corresponds to the quantity $k\Delta x = \pi$. However, we need to take into account, from the FDTD dispersion relation, the deviation of the phase velocity in the grid to the free space phase velocity, c_0. For instance, at 20 points per wavelength we have $k\Delta x = 0.1\pi$. Thus only 10% of the spectrum is usable.

For a number of data points in the usable spectrum, the minimum iterations for each material are as follows. For each material, the maximum accurate frequency was calculated given by

$$f_{max} = \frac{c_0}{20\Delta l\sqrt{\epsilon_{r_{max}}}} \tag{4.61}$$

from this result, the minimum of iterations is given by

$$N = \frac{1}{f_0\Delta t} \tag{4.62}$$

where $f_0 = \frac{f_{max}}{100}$ for 100 data points in the usable spectrum.

For the soil samples used in this study these values are summarised in Table 4.2. In practice, the number of iterations was extended due to the long decay times associated with resonances for the soils with higher dielectric strength. Due to the increased number of iterations the Python functions which update the current surfaces were

Soil Moisture Content	$\epsilon_{r_{max}}$	Δl [mm]	Min. Iterations	f_{max} [MHz]
2.5%	3.95	14	6880	525
5%	5.95	12	8450	525
10%	8.75	9	10200	525

Table 4.2: Spatial discretisation values to model soils with varying moisture content in the Mie scattering simulation.

implemented as Cython functions to reduce the total simulation time (Behnel et al., 2011a).

The sphere was illuminated from the back-scattering angle using the TF/SF formulation described in the previous section. The TS/SF boundary was placed at $(35\Delta l, 35\Delta l, 35\Delta l)$, $(165\Delta l, 165\Delta l, 165\Delta l)$ where these points are the coordinates of the bottom left-hand corner and the top right-hand corner of a cube. The distance between the sphere and the TF/SF was 5 cells. The distance was kept small to minimise the phase error between the surfaces. The auxiliary 1d simulation grid was terminated at each end with a 10 cell PML to prevent the sourcing of non-physical reflections into the total-field region.

The near-field to far-field integration boundary was placed 2 cells outwards from the TF/SF boundary. This is the minimum number of cells the surface can be from the TF/SF without averaging the magnetic fields corrected by the TF/SF.

A 3d EP is required for the simulation of the Mie scattering in 3d. In Kyu-Pyung Hwang and Cangellaris (2001) the numerical resonance examples are 2d. In the 2d grid aligned case, the parallel components to the Yee cell are assigned a weighting of the materials in the adjacent Yee cells. In 3d there are 3 adjacent Yee cells to any component parallel to the sphere and therefore there are 3 combinations of the free space and dispersive medium. The effective permittivities for the Type-A, Type-B, Type-C soils modelled using a 2 pole Debye model are given by the following equations.

For the combination $\epsilon_2(\omega) + \epsilon_1 + \epsilon_1 + \epsilon_1$ the EP is given by

$$\langle \epsilon_a \rangle_1 = \frac{\epsilon_\infty + 3}{2} + \frac{\frac{1}{2}\epsilon_{d_1}}{1 + j\omega\tau_1} + \frac{\frac{1}{2}\epsilon_{d_2}}{1 + j\omega\tau_2} \tag{4.63}$$

For the combination $\epsilon_2(\omega) + \epsilon_2(\omega) + \epsilon_1 + \epsilon_1$ the EP is given by

Material Combination	ϵ_∞	σ	ϵ_{d_1}	ϵ_{d_2}
$\epsilon_2(\omega) + \epsilon_1 + \epsilon_1 + \epsilon_1$	1.55	9.925e-05	0.1875	0.075
$\epsilon_2(\omega) + \epsilon_2(\omega) + \epsilon_1 + \epsilon_1$	2.1	0.0001985	0.375	0.5625
$\epsilon_2(\omega) + \epsilon_2(\omega) + \epsilon_2(\omega) + \epsilon_1$	2.65	0.00029775	0.5625	0.225

Table 4.3: EP averaged values for Puerto Rico soil type A.

Material Combination	ϵ_∞	σ	ϵ_{d_1}	ϵ_{d_2}
$\epsilon_2(\omega) + \epsilon_1 + \epsilon_1 + \epsilon_1$	1.7875	0.0002775	0.45	0.15
$\epsilon_2(\omega) + \epsilon_2(\omega) + \epsilon_1 + \epsilon_1$	2.575	0.000555	0.9	0.3
$\epsilon_2(\omega) + \epsilon_2(\omega) + \epsilon_2(\omega) + \epsilon_1$	3.3625	0.0008325	1.35	0.45

Table 4.4: EP averaged values for Puerto Rico soil type B.

$$\langle\epsilon_a\rangle_2 = \frac{\epsilon_\infty + 2}{2} + \frac{\epsilon_{d_1}}{1 + j\omega\tau_1} + \frac{\epsilon_{d_2}}{1 + j\omega\tau_2} \tag{4.64}$$

For the combination $\epsilon_2(\omega) + \epsilon_2(\omega) + \epsilon_2(\omega) + \epsilon_1$ the EP is given by

$$\langle\epsilon_a\rangle_3 = \frac{\epsilon_\infty + 1}{2} + \frac{\frac{3}{2}\epsilon_{d_1}}{1 + j\omega\tau_1} + \frac{\frac{3}{2}\epsilon_{d_2}}{1 + j\omega\tau_2} \tag{4.65}$$

Additionally, the conductivity at the grid interface were also averaged arithmetically as in Popovic and Okoniewski (2003). The material parameters $\epsilon_\infty, \epsilon_{d_1}, \epsilon_{d_2}, \sigma$, are summarised in Tables 4.3, 4.4, 4.5

The analytic solution for the Mie scattering was obtained from the Python library `miepython` (Scottprahl, 2019). The Mie solution provided by the library was based on the theory and implementation given in Wiscombe (1979). In order to compare the results obtained from the FDTD simulation the complex permittivity is evaluated at the centre of each of the frequency bins given by the discrete Fourier transform (DFT)

Material Combination	ϵ_∞	σ	ϵ_{d_1}	ϵ_{d_2}
$\epsilon_2(\omega) + \epsilon_1 + \epsilon_1 + \epsilon_1$	2.25	0.0005	0.6875	0.1875
$\epsilon_2(\omega) + \epsilon_2(\omega) + \epsilon_1 + \epsilon_1$	3.5	0.001	1.375	0.375
$\epsilon_2(\omega) + \epsilon_2(\omega) + \epsilon_2(\omega) + \epsilon_1$	4.75	0.0015	2.0625	0.5625

Table 4.5: EP averaged values for Puerto Rico soil type C.

of the simulated signal for the model used in the simulation given by

$$\epsilon_2(\omega) = \epsilon_\infty + \frac{\epsilon_{d_1}}{1 + j\omega\tau_{d_1}} + \frac{\epsilon_{d_2}}{1 + j\omega\tau_{d_2}} - j\frac{\sigma}{\omega\epsilon_0} \tag{4.66}$$

Once the complex permittivity was converted to the complex refractive index, the normalised radar cross-section back-scattering was obtained directly from the library.

4.4.2 Results: Back-Scattering from Spherical Soil Samples

The results for the radar cross-section back-scattering for the 2.5%, 5%, 10% soil moisture models are shown in Figures 4.11, 4.13, 4.16 respectively. Each backscattering has been normalised by the cross-sectional area, πr^2 of the target sphere such that the accuracy of EP can be easily compared for spheres of varying size. Additionally, each figure shows the analytic solution to the Mie scattering, the FDTD solution without the effective permittivity and the FDTD solution with effective permittivities. Each figure has been plotted for frequencies up to $N_\lambda = 20$ for the wavelengths which occur within each soil.

Figures 4.11, 4.13, 4.16 show the relative error between the FDTD signal and the analytic signal. These have been provided to show quantitatively the difference between the signals. The relative error measurement is given by

$$RelativeError = \sum_{n=1}^{n} \frac{RCS_{Mie_n} - RCS_{FDTD_n}}{RCS_{Mie_n}} \tag{4.67}$$

where RCS_{Mie_n}, RCS_{FDTD_n} are the backscattering samples at each frequency bin obtained in the DFT.

Figures 4.11, 4.13, 4.16 show that the agreement between the FDTD with and without effective permittivity is reasonable. Their associated error plots show a general trend that the error worsens as the frequency increases. This is most likely due to increasing staircasing as the frequency of the incident field increases.

Figures 4.12, 4.14, 4.17 show that error below $100\,\text{MHz}$ is relatively constant. From Figures 4.11, 4.13, 4.16 this region is associated with the optical scattering or Rayleigh resonance region where the incident radiation has a wavelength larger than the circumference of the sphere. The spheres modelled with the effective permittivity show a significant improvement in modelling accuracy at optical frequencies. This finding is
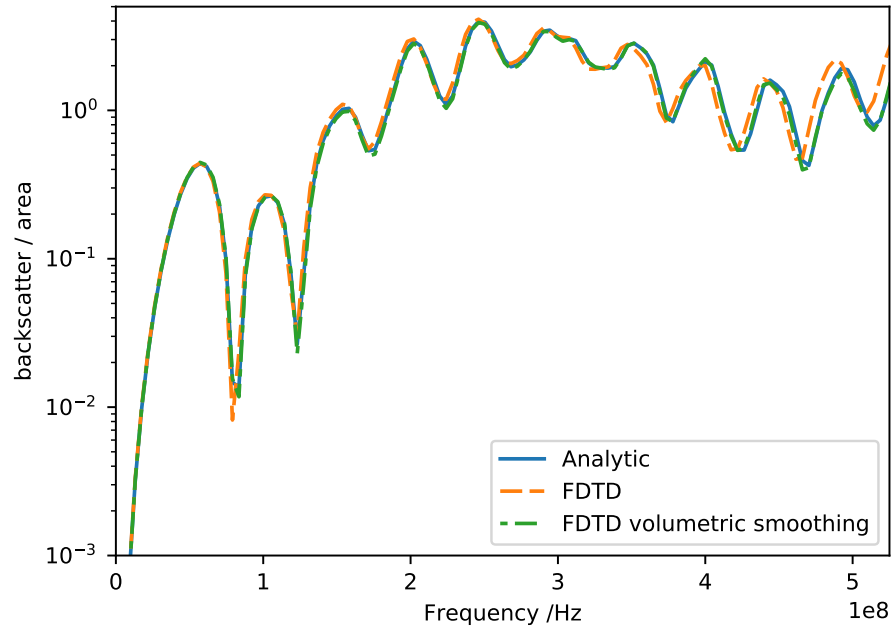
Figure 4.11: Normalised back-scatter from Puerto Rico Type A clay/loam soil sphere with a 2.5% moisture content.
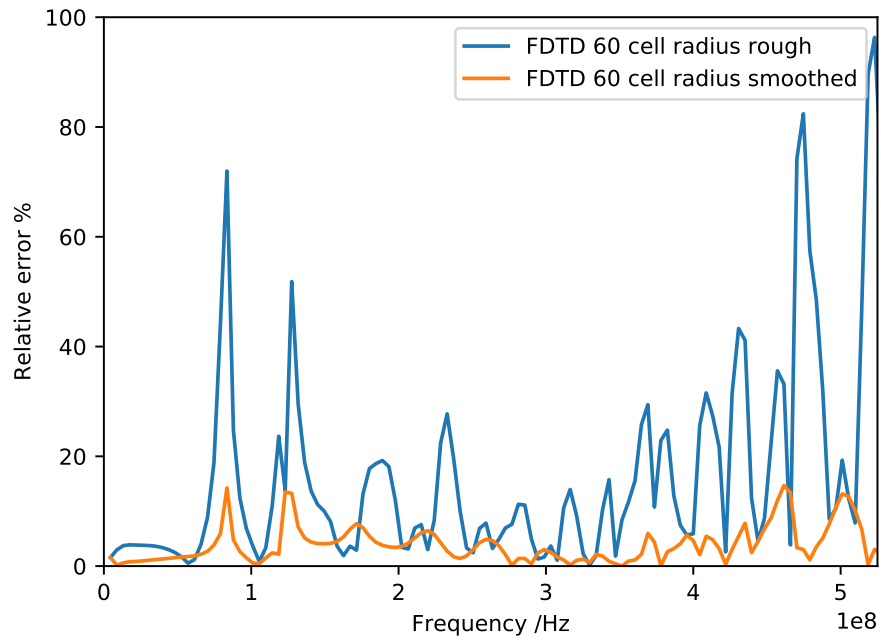
Figure 4.12: Relative error for normalised back-scatter from Puerto Rico Type A clay/loam soil sphere with a 2.5% moisture content.
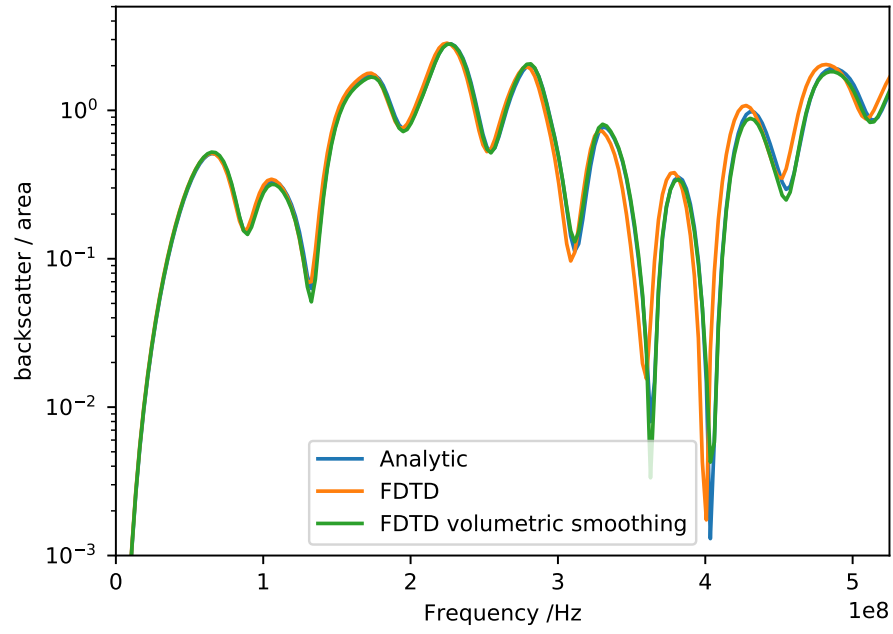
Figure 4.13: Normalised back-scatter from Puerto Rico Type B clay/loam soil sphere with a 5% moisture content.
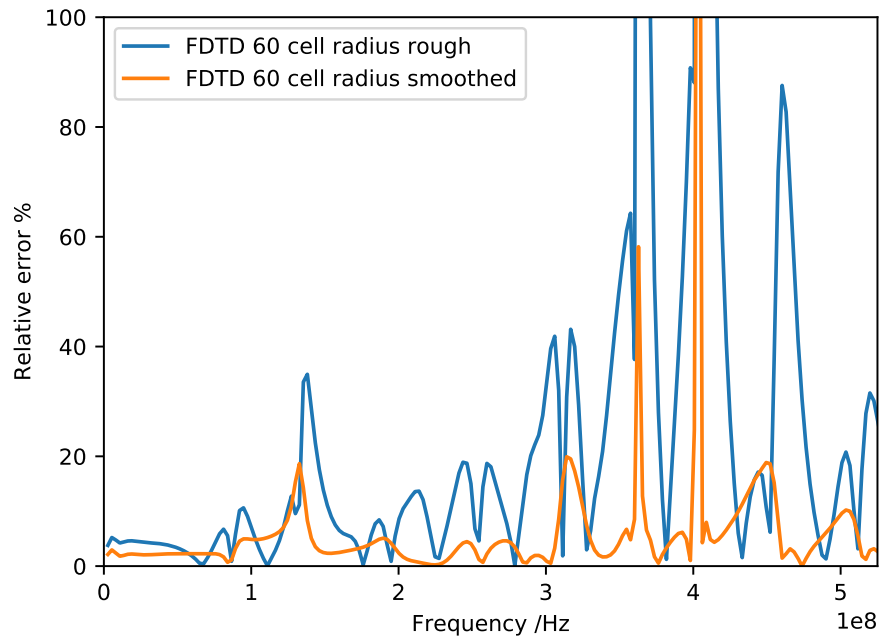
Figure 4.14: Relative error in normalised back-scatter from Puerto Rico Type B clay/loam soil sphere with a 5% moisture content.
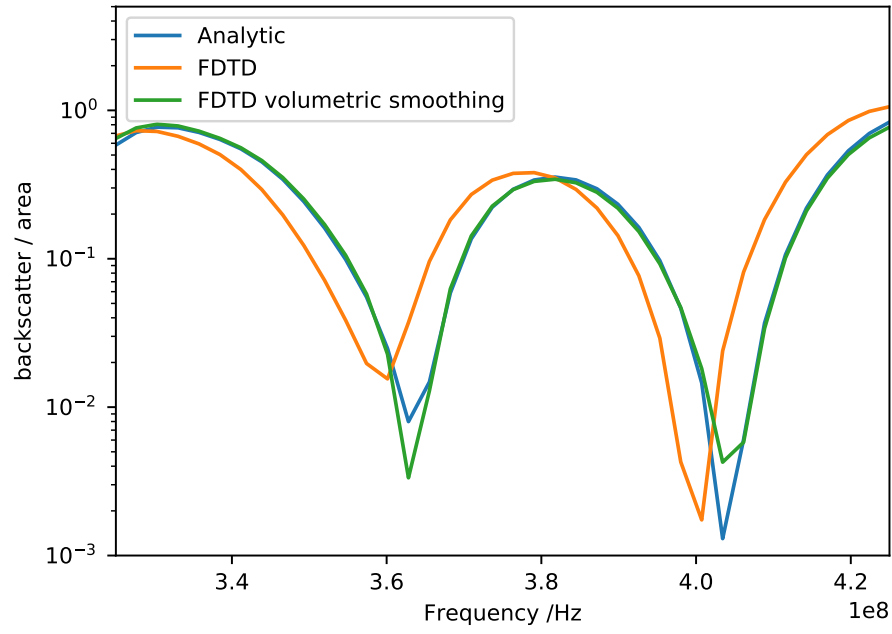
Figure 4.15: Nulls in the normalised back-scatter from Puerto Rico Type B clay/loam soil sphere with a 5% moisture content.
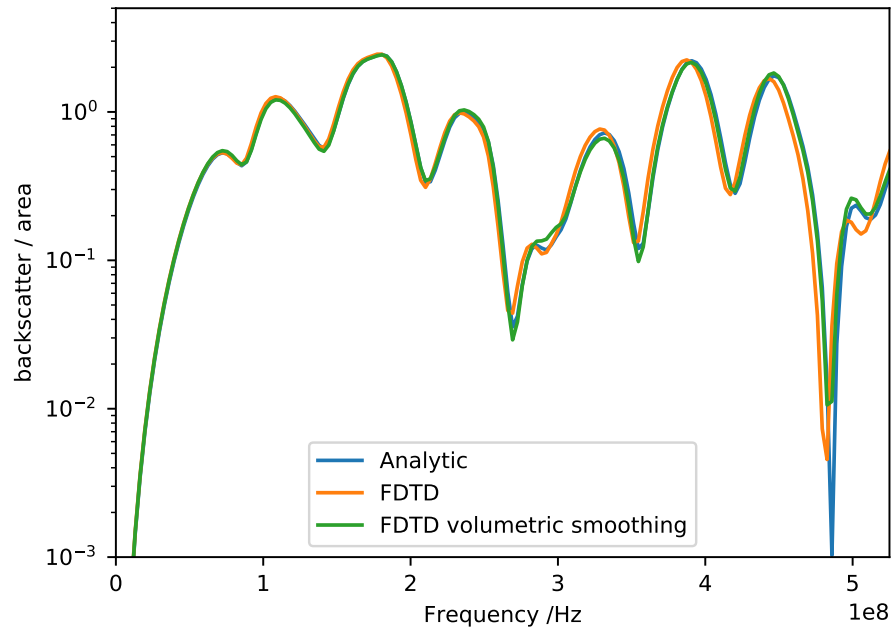
Figure 4.16: Normalised back-scatter from Puerto Rico-Type B clay/loam soil sphere with a 10% moisture content.
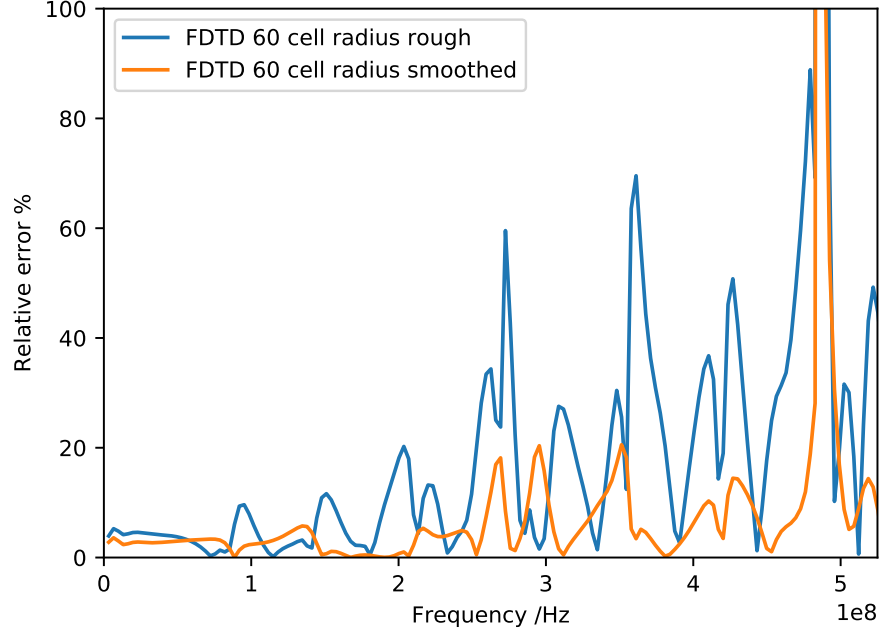
Figure 4.17: Relative error in normalised back-scatter from Puerto Rico Type C clay/loam soil with a 10% moisture content.

consistent with those of Deinega and Valuev (2007); Liu et al. (2012).

Beyond the Rayleigh resonance region, we observe the Mie resonance region where the wavelength of the incident field is less than the circumference of the sphere. In this region, we observe patterns of nulls which correspond to the destructive interference of the creeping wave around the sphere and the internal resonances within the dielectric spheres. Figure 4.12 shows that the back-scattering error in the resonant region is less than 20% and is significantly more accurate than the non-EP method throughout the region. Figures 4.14 and 4.17 show that for higher moisture content soils the EP is significantly more accurate when compared to the non-EP. The figures also show that the error at the deep nulls is significantly larger than in the 2.5% moisture soil. Figure 4.15 shows a zoomed-in image of the nulls for the soil with 5% moisture content. The EP solution shows a better phase agreement with the analytical solution in comparison to the non-EP solution. In general the Figures 4.14 and 4.17 show an increased relative error as the frequency increases in comparison to Figure 4.12. This is not a direct result of staircasing as wave propagation in each figure is equally well resolved. One possibility is that the error is larger due to the increased number of iterations required to sample the signal ring down. The increased permittivity in the higher soil samples leads to increased resonance within the sphere due to the larger reflection coefficient

at the dispersive/air boundary. Thus increased frequency of interaction with material boundary and increased wave propagation distance within the dielectric increases the numerical error.

4.4.3 Mie Scattering Conclusions

The findings of the Mie scattering numerical experiments are consistent with those by Deinega and Valuev (2007); Liu et al. (2012). They show that the dispersive/air interface can be modelled with an effective permittivity scheme for optical effects. The previous work has been extended by the finding that the arithmetic EP can be used within the resonant region to significantly reduce the modelling error for structures which are moderately staircased. In particular, it has been shown that a significant improvement in modelling these surfaces can be achieved for realistic soils in GPR.

4.4.4 Hertzian Dipole Over a Dispersive Half-Space

The second set of experiments present the responses from a Hertzian dipole over dispersive half-spaces. As per the Mie scattering approach, the boundary between the dispersive soil was smoothed using the grid aligned EP approach. The responses for each soil are compared to a fine grid solution which has not been smoothed using the EP. The comparisons are made to assess the convergence of the EP approach with a solution which is significantly accurate due to the second-order nature of the FDTD scheme. A similar approach was used by Hertel and Smith (2003) to assess the validity of common feeding models for antennas modelled using FDTD.

In each numerical experiment, the dipole is placed 5 cm above the dispersive material. This height corresponds to half of the optimum height required to achieve good directive properties of a ground-coupled antenna (Smith, 1984a). The ground coupling distance was decreased to observe a higher degree of interaction with the EP surface.

The centre frequency of the excitation pulse was retained from the Mie scattering numerical experiments as it provided a good match to the variation in the soil material parameters. However, a normalised 1st derivative Gaussian pulse was substituted for the Gaussian pulse to eliminate the introduction of static charge on the antenna (Wagner and Schneider, 1998). Additionally, a receiver was placed at a lateral distance of 20 cm from the dipole. This arrangement approximately simulates the arrangement of the antennas in a bi-static GPR system.
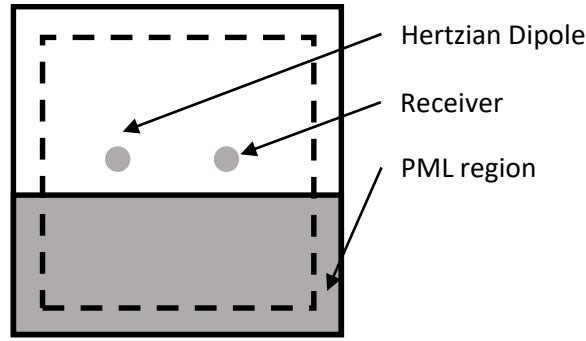
Figure 4.18: Dispersive half-space space simulation schematic

The EP used to model the soil/air interface was modelled using a 2-pole Debye model. The half-space is grid aligned therefore there is only a single material combination. The parameters for the Debye model are given in the second row of parameters in Tables 4.3, 4.4, 4.5

The size of the computational domain of the simulation was $92\Delta l \times 92\Delta l \times 92\Delta l$. The discretisation in the coarse grid was $1\,\text{cm}$ and $0.2\,\text{cm}$ in the fine grid. This corresponds to $N_\lambda = 34$ for a wave propagation within the 10% moisture soil and therefore provides a low level of numerical dispersion. A 10 cell thick PML is placed at the domain boundary. The simulation setup is shown in Figure 4.18.

Figure 4.19 shows the locations of the material parameters at the half-space interface in the non EP case. At each of the blue field node locations the half space permittivity values are assigned. At the orange field nodes the free-space parameters are specified.

Figure 4.20 show the

4.4.5   Results: Hertzian Dipole over a Dispersive Half-Space

Figures 4.27, 4.23, 4.25 show a comparison of the responses obtained from the EP, Non-EP and the Non-EP fine reference solution for soil-type A, soil-type B and soil-type C respectively. The responses are shown in the time domain as opposed to the frequency domain. The reason for this is GPR measurements are made and interpreted in the time domain and therefore error comparisons in the time domain give a better idea of the performance gains of the EP for GPR simulations. Also, the errors can be better interpreted physically by their position in time.

In all the figures the EP responses are in good agreement with the reference solution. Relative error figures are also given to provide a quantitative comparison. The relative
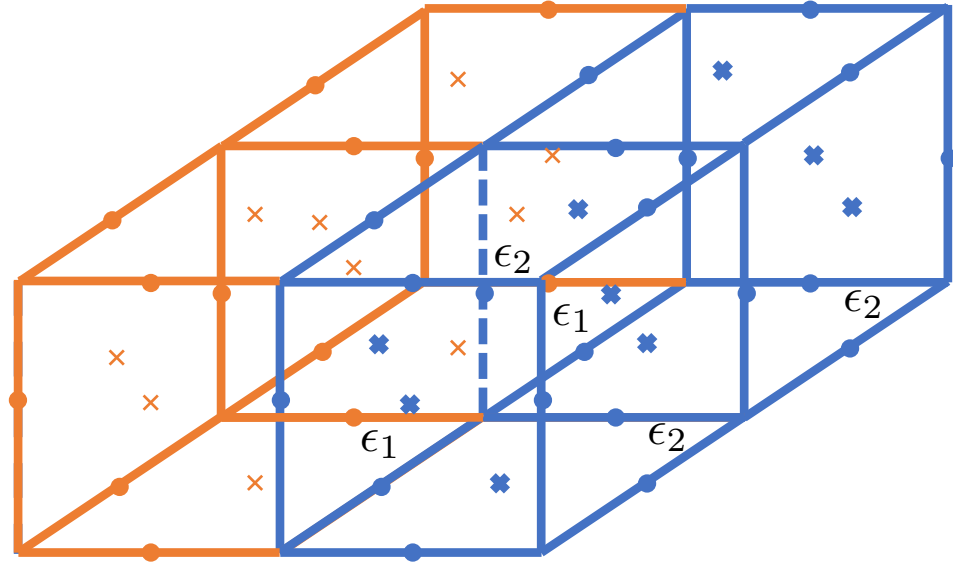
Figure 4.19: Diagram of the assignment of material parameters at the half-space interface using the standard FDTD updates. Half-space material parameters are specified at the blue nodes and free-space material parameters are specified at the orange nodes.
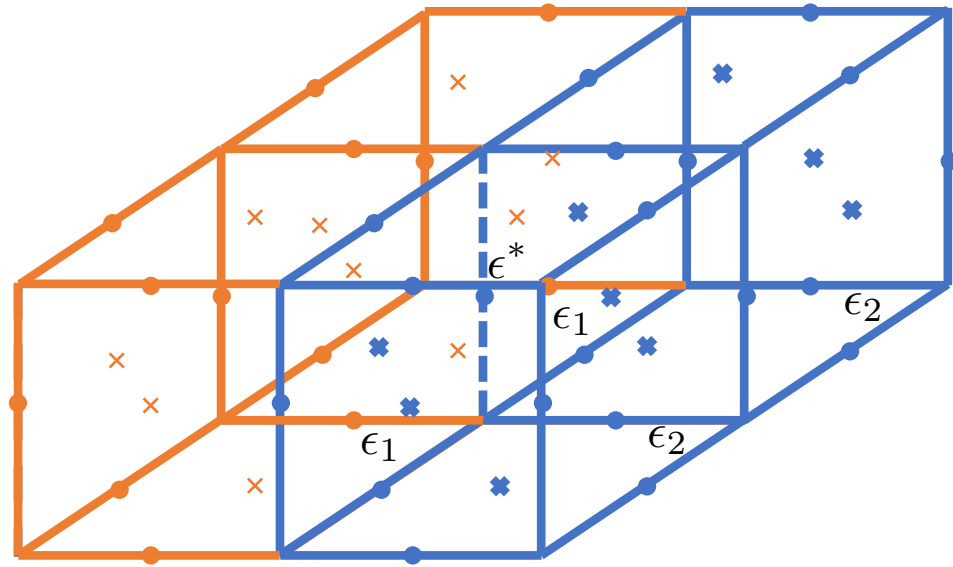
Figure 4.20: Diagram of the assignment of material parameters at the half-space interface using the EP update equations. The dotted line indicates the assignment of an EP to the E_y field location at the half-space. The value of ϵ^* is given by the average of the surrounding volumetric permittivities, ϵ_1, and ϵ_2). This averaging is repeated for at all E_y and E_x positions at the interface.

Soil Type	Non-EP Error [%]	EP Error [%]
A	7.02	1.4
B	11.6	1.2
C	15.8	1.6

Table 4.6: Summary of maximum relative error for the EP and non-EP smoothing at dispersive halfspace interfaces.

error measurement is given by

$$Error^n = \frac{|E_y^n - E_{y_{ref}}^n|^2}{|E_{y_{ref}}^n|^2} \tag{4.68}$$

This relative error measurement normalises each sample difference by the max absolute value in the reference solution. This method is preferred for time-domain measurements as finite value is obtained for zero crossings. It has been used previously to calculate the relative error for PML formulation comparisons Giannopoulos (2018a). The relative error comparisons for the EP and non-EP are show in Figures 4.22, 4.24, 4.26

Figures 4.21, 4.23, 4.25 show that the agreement between the non-EP and reference solution worsen with water moisture content and increasing permittivity. However, the relative error for the EP response remains constant for each soil type. The maximum relative errors are compared in Table 4.6. This result implies that the EP smoothing reduces the modelling error to a nominal level.

Figure 4.25 shows that the EP response for the half-space with soil type C varies significantly from the fine grid solution. The peak variation is 15.8%. This finding suggests that for soils with moisture contents higher than 10% the response obtained without EPs may not be representative of the character of the actual response.
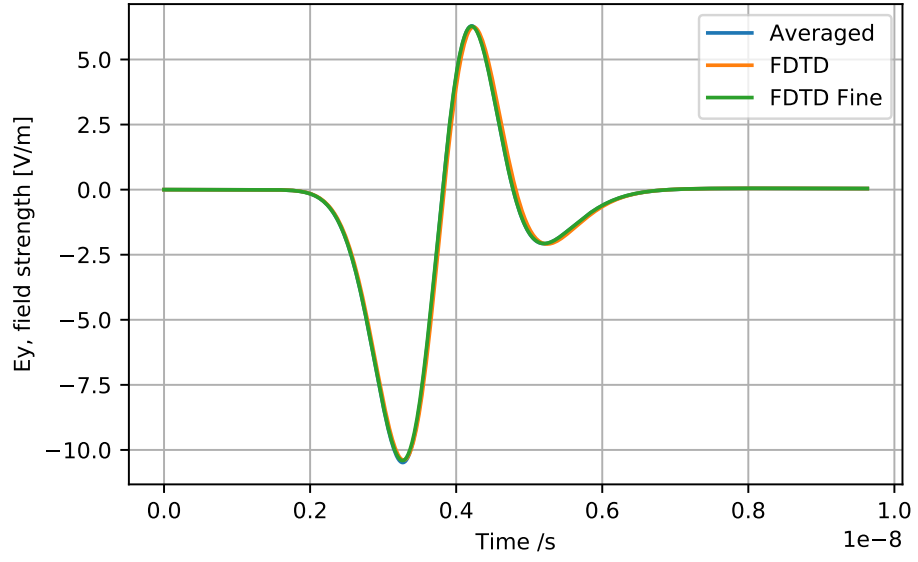
Figure 4.21: Comparison of the received signal from a Hertzian dipole over a half space containing Puerto Rico type A clay loam with 2.5% moisture for EP, Non-EP and a fine grid Non-EP solution.
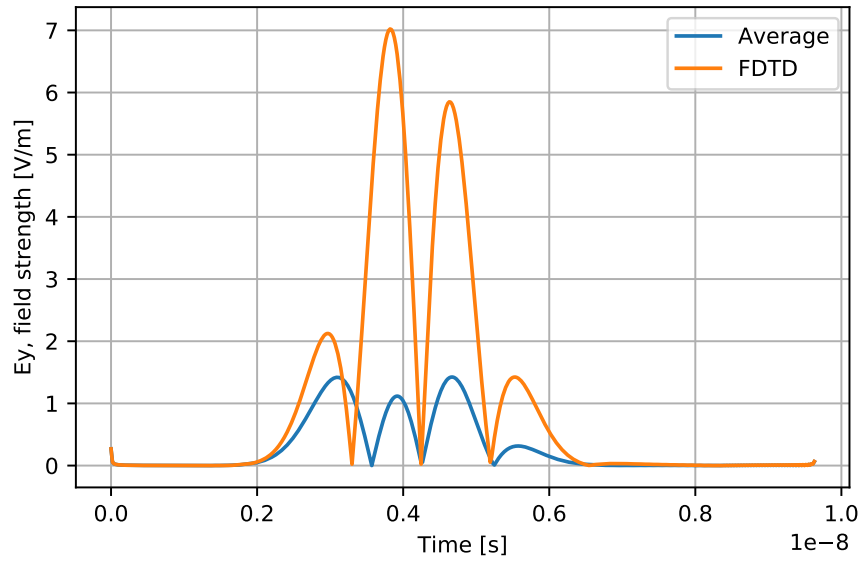
Figure 4.22: Comparison of the relative error in a signals from a herztian dipole over a half space containing Puerto Rico type A clay loam with 2.5% moisture between EP, Non-EP and a fine grid Non-EP solution.
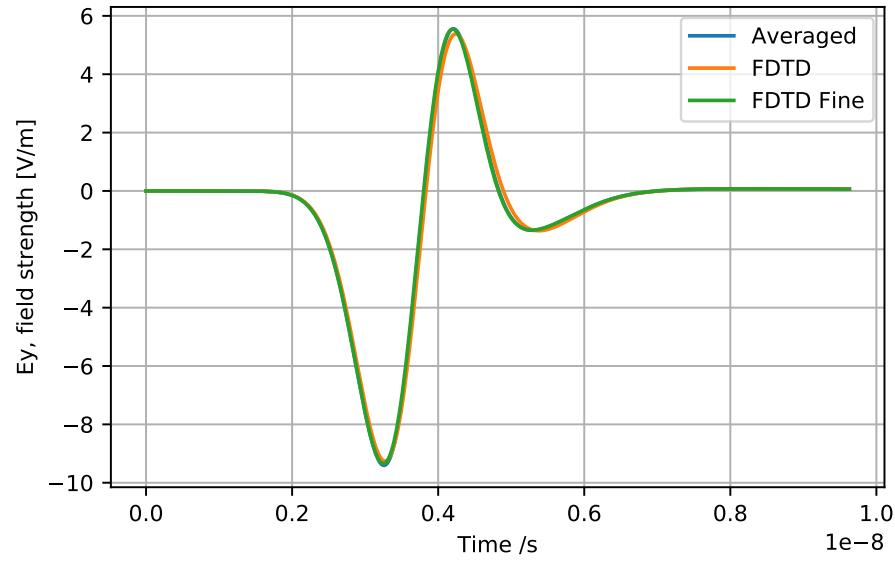
Figure 4.23: Comparison of the received signal from a herztian dipole over a half space containing Puerto Rico type B clay loam with 5% moisture for EP, Non-EP and a fine grid Non-EP solution.
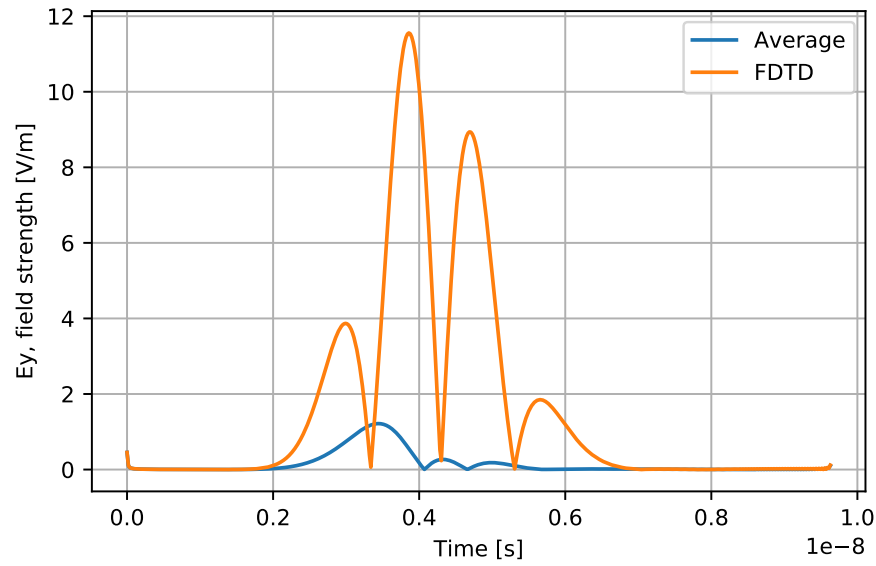
Figure 4.24: Comparison of the relative error in a signals from a herztian dipole over a half space containing Puerto Rico Type C clay loam with 5% moisture between EP, Non-EP and a fine grid Non-EP solution.
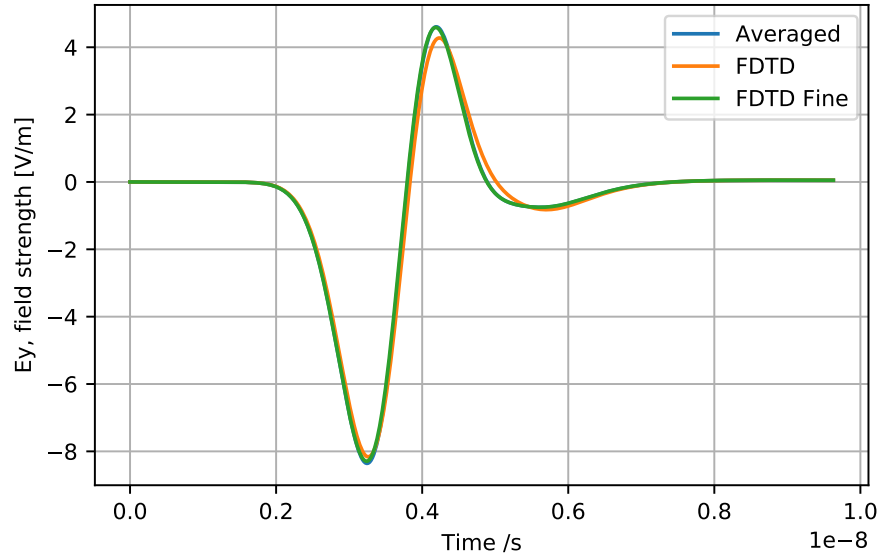
Figure 4.25: Comparison of the received signal from a herztian dipole over a half space containing Puerto Rico Type clay loam with 10% moisture for EP, Non-EP and a fine grid Non-EP solution.
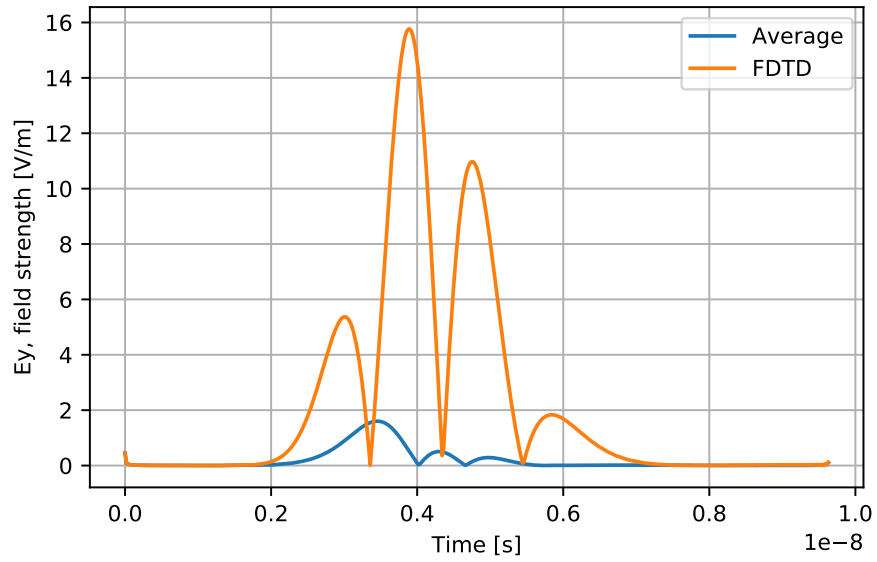
Figure 4.26: Comparison of the relative error in a signals from a hertzian dipole over a half space containing Puerto rico type C clay loam with 10% moisture between EP, Non-EP and a fine grid Non-EP solution.

4.4.6 Hertzian Dipole Over a Layered Dispersive Half-Space

The third set of numerical experiments investigate the dispersive/dispersive material interface in a layered half space. The layered half space consists of a top layer of soil-type A and a bottom layer of soil-type C. Each layer is aligned with the grid therefore arithmetic averaging was used to determine the EP. In the previous section, the arithmetic averaging was given for single-pole Debye models. This can be extended by introducing the second poles into the formulation and expanding the brackets. Hence the formula used for the tangential components at the interface of the soils is given by

$$\langle \epsilon_a \rangle = \epsilon_\infty + \frac{\frac{1}{2}\epsilon_{a1}}{1 + j\omega\tau_{a1}} + \frac{\frac{1}{2}\epsilon_{a2}}{1 + j\omega\tau_{a2}} + \frac{\frac{1}{2}\epsilon_{b1}}{1 + j\omega\tau_{b1}} + \frac{\frac{1}{2}\epsilon_{b2}}{1 + j\omega\tau_{b2}} \qquad (4.69)$$

where

$$\epsilon_\infty = \frac{\epsilon_{\infty_a} + \epsilon_{\infty_b}}{2} \qquad (4.70)$$

And ϵ_{∞_a}, ϵ_{a1}, τ_{a1}, ϵ_{a2}, τ_{a2} are the Debye parameters soil type A in the top layer and ϵ_{∞_b}, ϵ_{b1}, τ_{b1}, ϵ_{b2}, τ_{b2} are the Debye parameters for soil-type C in the bottom layer.

The arithmetic averaging for dispersive/dispersive interfaces results in a material whose number of poles is equal to the total number of poles in the averaged materials. The increased number of poles required to represent the interface carries a memory and computation overhead as the parameters for each pole must be stored in memory. A 2-pole material could be used to represent the EP provided the materials are physically similar.

The argument could be made that the EP material at the interface is another soil with different moisture content. Since all the soil models presented modelled using 2-pole Debye models it should be possible to represent the soil at the interface with a 2-pole Debye model. i.e the same soil with different moisture content.

Non-linear least-squares regression (Levenberg-Marquardt) was performed to fit a 2-pole Debye model to complex permittivity profile of the 4-pole Debye material. A non-linear scheme must be used because the Debye function is non-linear with respect to the parameters ϵ_a and τ_a. The Debye parameters were fit to the magnitude squared of the complex permittivity of the EP. The Debye parameters used in the fit are summarised in Table 4.7.

ϵ_∞	ϵ_{d_1}	τ_1	ϵ_{d_2}	τ_2
5.1	1.6	3.8	0.2	1.5

Table 4.7: Optimised 2-pole Debye model parameters for a dispersive/dispersive interface.

4.4.7 Results: Hertzian Dipole over a layered Dispersive Half-Space

Figure 4.27 shows the comparison of the signal reflected from the interface between soil-type A and soil-type B. The reflection from the air/soil interface has been omitted as it has been smoothed in the same way in each model. The figure shows that there is a good agreement between the reference solution and the Non-EP, the EP and the optimised 2-pole solution. Figure 4.27 shows the relative error between the EP, the optimised 2-pole, and the non-EP solution. The EP and the optimised solution increase the modelling accuracy by around 50%. Interestingly, the optimised 2-pole and 4-pole solutions are in good agreement. This result shows that the number of poles can be reduced effectively for soil interfaces where only the moisture content varies across the interface.
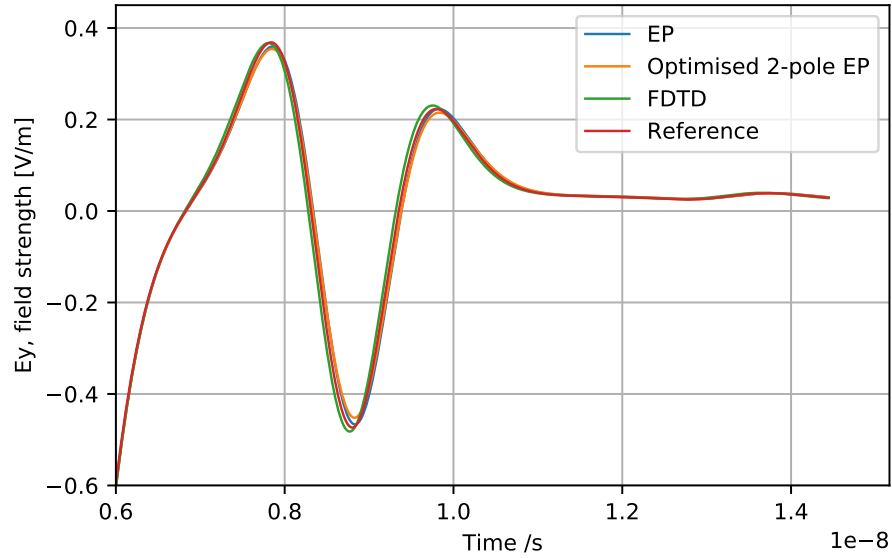
Figure 4.27: Comparison of the received signal from a Hertzian dipole over a dispersive layered half space containing Puerto Rico Type clay loam with 2.5% and 10% moisture for EP, Non-EP and a fine grid Non-EP solution.
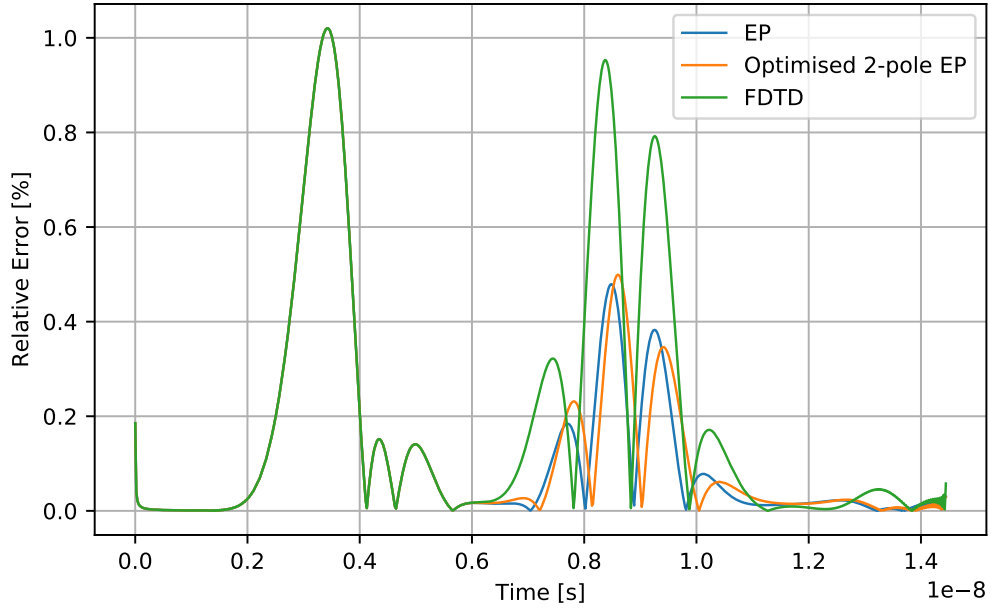
Figure 4.28: Comparison of the relative error in a signal from a Hertzian dipole over a dispersive layered half space containing Puerto Rico clay loam with 2.5% and 10% moisture for EP, Non-EP and a fine grid Non-EP solution.

4.5   Summary

In this chapter, a novel method was demonstrated which averages Debye media at grid-aligned interfaces. The method extends the CR method to dispersive/dispersive interfaces. Also, it has been shown that when the static permittivity and the polarisation of the material are considered separately, the harmonic averaging of the susceptibility function yields another Debye pole which can be utilised straightforwardly.

The accuracy of the method for the arithmetic averaging has been compared against an analytical solution. The nulls computed in the Mie scattering compare more favourably with the averaged results than the non-averaged results. The scheme was then tested in a half-space problem for dispersive/dielectric and dispersive/dispersive interfaces by comparison with a fine grid solution. The results showed that the time-domain signal was distorted when the interface was not averaged. In particular, the peak relative error was reduced from 16% to 2% for soil-type C which contained the highest moisture content. Additionally, it was shown that when the averaging results in 4 Debye poles, the number of poles can be reduced back to 2 by fitting a 2-pole Debye function to the data provided there is some underlying physical similarity in the materials.

Chapter 5

Review of FDTD Sub-Gridding Methods

The first sub-gridding algorithm for FDTD was introduced in Kunz and Simpson (1981). A fine grid was embedded within a coarse grid where the ratio of the spatial step and time step was 1:2. The field distribution is calculated in a two-step procedure. First, the fields within the main grid are computed for the duration of the time window. Subsequently, the main-grid tangential fields at the main-grid sub-grid (MSSG) boundary are introduced into the sub-grid in a secondary simulation. The main shortcoming of this technique is the outgoing field from the sub-grid are not coupled back to the main grid.

Synchronised updating of the main-grid and sub-grid was first proposed by Kim and Hoefer (1990). In this method, the electric and magnetic fields from the main-grid are interpolated in space and time at the MSSG boundary. These fields are then used to update the sub-grid until the electric or magnetic field are collocated in time. At this point, the sub-grid electric and magnetic fields are injected back into the main-grid at the MSSG boundary. This update scheme is of most interest to GPR applications as the coupling between the half-space and an antenna model can be preserved across the MSSG boundary.

The algorithm proposed in Zivanovic et al. (1991) used a similar update scheme. However, the electric fields in the sub-grid at the MSSG boundary are calculated using the discretised wave equation as opposed to linear interpolation. To advance the wave equation, electric fields are required at fine grid locations within the main grid. These fields are obtained through a quadratic interpolation of the neighbouring main grid fields. Thus an intermediate region between the main grid and the sub-grid is required.

Similarly, the algorithm developed in Prescott and Shuley (1992) utilises the wave equation to predict the tangential electric fields. However, their implementation requires less memory and CPU and demonstrates similar accuracy. Both of these methods provide a more accurate realistic field distribution. However, they can only be used to predict the fields within homogeneous media. Therefore media which traverse the MSSG, such as half-space boundaries, cannot be incorporated into the model.

A sub-gridding algorithm which allowed dielectric media to traverse the MSSG was presented in Chevalier et al. (1997). It was observed that electric field components which are tangential to the MSSG are normal to any dielectric interface which traverses the MSSG and are therefore discontinuous. To avoid the interpolation of discontinuous fields the scheme positions the MSSG over tangential magnetic fields which are continuous across dielectric interfaces. The scheme was found to be unstable. However, the instability can be delayed by reducing the Courant number in each grid. Similarly to Zivanovic et al. (1991), the scheme uses an intermediate region to weight the field near to the MSSG by the neighbouring coarse and fine grid fields. This was found to reduce spurious reflections and further increase the scheme's stability. This is presumably due to the averaging acting as a low-pass filter and attenuating unstable modes.

Another sub-gridding algorithm with material traverse was developed by Okoniewski et al. (1997). An investigation into interpolation schemes reported that the best accuracy is obtained when cubic splines are used to spatially interpolate the fields over the MSSG boundary. The accuracy is reported to be similar to Prescott and Shuley (1992). Also, this study provides new insights into how sub-gridding could be applied to complex GPR modelling. For example, the sub-gridding of the ear of a human head was also reported. Results showed that larger amounts of radiation were absorbed in the head when the sub-gridding was used. The success of the approach indicates that sub-gridding can be used to accurate sub-grid complex objects with highly non-uniform field distributions and could, therefore, be used to model antennas.

In Yu and Mittra (1999) a new scheme was presented which eliminated the need for weighted averaging of the field components near to the MSSG boundary as proposed by Chevalier et al. (1997). The approach benefits from being generalised. However, it does not permit dielectric media to traverse the MSSG boundary.

Numerical instability is reported in each of the sub-gridding schemes mentioned. A combination of averaging fields close to the sub-gridding interface and lowering the Courant number have been shown to increase the stability of these methods. Vaccari et al. (2004) claimed that instability is inherent to all sub-gridding schemes. The authors predict an infinite reflection coefficient at the sub-gridding interface gives rise

to instability. The prediction is made by considering the dispersion relation in both grids up to the spatial Nyquist limit of the sub-grid. For frequencies above the Nyquist limit in the main grid, the group velocity of the aliased wavelet is negative and thus the reflection coefficient is infinite. To reduce the instability the authors attenuated the frequencies at the cut-off using a low pass filter. The filter attenuates the frequencies in the spatial domain by process of differentiation of the magnetic fields at the interface. They report that increases the number of stable iterations.

In addition Donderici and Teixeira (2005) identified three key sources of error in sub-gridding schemes. These are improper interpolation and decimation of fields between the grids, high-frequency components in the fine grid which are not present in the main grid and the difference in impedance between the grids.

The result of incorrect interpolation at the interface is aliased copies of the signal being transferred into lower frequency components. The authors reduce aliasing by band-limiting the signal in the overlapping region using low-pass filters during the interpolation and decimation procedures. The filters also reduce frequency components which exceed the main grid Nyquist limit. This process reduces the reflection of the components at the sub-gridding interface.

High-frequency components and reflection from the interface are also reduced using an auxiliary PML. The PML is positioned beyond the MSSG boundary in each grid such that any reflections are attenuated. interestingly, it was observed that the auxiliary region also delayed the onset of numerical instability.

The mismatch in the numerical impedance of the grids gives rise to reflections at the MSSG boundary. The mismatch is a function of the difference in numerical dispersion between the grids. Physically this corresponds to discontinuity in phase velocity across the grids which implies that there is a reflection coefficient associated with the interface. The reflection coefficient increases as the ratio of the spatial steps of the grids increases. The reflection coefficient also varies with the angle of incidence due to the anisotropic nature of the grid dispersion.

Crucially, this means that accuracy is limited by the ratio for all sub-gridding methods in which the interface between the grids is a boundary condition. In this case, the authors match the impedance for a specific frequency by correcting the phase of the waves at the interface. This is achieved by inserting an anisotropic media in the grid which adjusts the propagation velocity. The weakness of the approach is that the phase velocity is incorrect in broadband scenarios such as GPR. This is because the material is non-dispersive and therefore only acts correctly at a single phase-velocity.

Stability analysis in Taflove and Hagness (2005) showed that solutions to Maxwell's equations with complex ω grow or decay exponentially and are hence unstable. Weiland (1985) showed that real values of ω can only be obtained provided that the electric and magnetic curl operators form the asymmetric product. In other words, the solution to the wave equation derived from Maxwell's equations has only real eigenvalues. The reciprocity of the curl operators implies that in a discrete system any electric fields which update a magnetic field should also be updated by that magnetic field Wang and Teixeira (2004). In Thoma and Weiland (1996) it is shown that for sub-gridding schemes this procedure is difficult due to the interpolation of fields at the sub-gridding boundary.

Subsequently, Xiao et al. (2007) presented a stable multi-grid sub-gridding scheme with consistent curl operators. Tests measuring the reflection from dielectric structures indicate the scheme is stable up to at least 5×10^5 iterations. This is achieved by the development of a novel spatial interpolation procedure. By separating the sub-gridding interface into a temporal and spatial boundary the spatial interpolation scheme could be examined independently. Consistency has been achieved by ensuring the magnetic main grid fields are always updated by the electric fields in the fine-grid which result from the original interpolation of the main grid magnetic fields on to the sub-grid. The authors go on to show that curl operators for the magnetic and electric updates form a symmetric product.

One drawback of the approach is that the sub-gridding boundary cannot be traversed by materials due to the complex interpolation procedure. However, more recently, Ye et al. (2016) presented an altered spatial interpolation scheme in which dielectric media can traverse the sub-gridding interface. The simulation was equally stable. However, it is not clear if the scheme retains stability over a pulsed signal. The tests documented only include sine wave excitations. Therefore potential issues caused by high-frequency modes around the main grid cut-off are minimised. Additionally, the scheme is only extended to 2d.

An unconditionally stable explicit FDTD algorithm has been developed in Gaffar and Jiao (2014, 2015). The solutions of the electric and magnetic fields can be computed without instability for any given time step. Additionally, unlike unconditional implicit methods, the solution does not require a matrix solution and therefore can be scaled to arbitrary grid sizes. The instability is removed by eliminating the unstable eigenvectors from the product of the electric and magnetic curl operators.

Zhou et al. (2016) used the unconditional stable explicit FDTD proposed by Gaffar and Jiao (2014) to stabilise a sub-gridding scheme. It was observed that the scheme

was stable for at least 2×10^6 iterations. The test simulations also included a material traverse. Interestingly the scheme utilises a simple interpolation procedure at the sub-gridding boundary. Whilst the underlying update scheme guarantees stability beyond the CFL it does not guarantee stability for non-symmetric curl operators as proposed in Weiland (1985) as the interpolation schemes do not respect reciprocity. Disappointingly the authors do not discuss the accuracy of the scheme.

Collino et al. (2006) were the first to observe that the sub-gridding problem could be divided into two equivalent problems. By exploiting the continuity of tangential magnetic fields at the sub-gridding interface, the authors separated the problem into two regions which are sourced by the electric current, $\vec{J}$ which runs on the sub-gridding boundary. Thus the problem is reduced to finding the electric current on the interface and solving the resulting boundary problem. Additionally, finite element (FE) techniques replace interpolation and extrapolation to solve for the unknown fields at the boundary. Similarly, Chilton and Lee (2007) uses finite elements to expand the fields on the sub-gridding interface. Matrix inversion is required to solve for the expanded fields at the interface. At higher ratios, spline interpolation is reported to outperform the method (Chilton and Lee, 2007). The drawback of these FE methods is that they do not address the critical issue of material traversal across the sub-gridding boundary.

The preceding sub-gridding schemes evaluate the fields in both grids using the same FDTD method. They are collectively known as multi-grid methods. They proceed at most at the CFL limit in both grids to reduce numerical dispersion. However, in some cases, the grids are run below the CFL limit to increase numerical stability.

Another class of methods which run different numerical schemes in each grid are known as hybrid schemes. The purpose of the second scheme is to take advantage of its numerical properties which cannot be provided by the standard FDTD method alone.

One general class of hybrid-schemes is the explicit-implicit scheme. In this class, the finite-difference equations in the sub-grid are formulated implicitly such that the scheme has no stability criteria. The time step in the sub-grid can now be synchronised with the time step in the main grid due to the relaxation of the stability criteria in the sub-grid.

Time synchronisation offers two main benefits. Firstly, the total number of time steps which are required to advance the sub-grid one main-grid step is significantly reduced. Secondly, the time synchronisation can offer stability benefits. This is due to the elimination of the time interpolation at the sub-gridding boundary which can greatly increase the complexity of the coupling (Ye et al., 2016).

One such scheme is the Alternating Direction Implicit (ADI) FDTD method coupled to FDTD (Namiki, 2000). The first formulation of this method is given by Bing-Zhong Wang et al. (2001). In general, it has been shown that the ADI method is less accurate than the standard FDTD method when the Courant numbers are equal. Additionally, it has been shown that for Courant numbers beyond the CFL limit the method suffers significantly from truncation errors (Garcia et al., 2002). However, it was subsequently shown that the accuracy is comparable to FDTD for problems where the spatial waveform is over-resolved $R \geq 20$ (Staker et al., 2003). These problems are known as ADI-class problems. Sub-gridding is an ADI-class problem because the spatial waveform is always over-resolved by the multiple of the sub-gridding ratio.

Bing-Zhong Wang et al. (2001) compared the computational efficiency of the ADI-FDTD and multi-grid schemes. It was observed that the ADI-method computed the solution faster than the multi-grid solution. However, the multi-grid scheme was more memory efficient. Additionally, the ADI-FDTD solution converges to the fine grid solution. A subsequent 3D ADI-FDTD study was performed by Ahmed and Chen (2004). It is noted that the CPU time is reduced significantly as the sub-gridding ratio increases. However, ADI-FDTD has a larger memory requirement than FDTD due to the computation of intermediate fields during the update procedure. It has also been noted that implicit methods require a matrix solution whose efficiency worsens as the grid size increases (Gaffar and Jiao, 2015). An important implication of this is that the ADI-FDTD method may be inefficient for sub-gridding larger antennas where the total grid size can be large in comparison to the domain.

More recently several sub-gridding schemes have been developed and applied to GPR problems. Diamanti and Giannopoulos (2009) developed 2d ADI-FDTD hybrid scheme which incorporated an overlapping boundary at the sub-gridding interface. In free-space was found to improve upon the accuracy demonstrated by Chevalier et al. (1997). The sub-gridding was applied to a buried plastic water-pipe located at the interface of two dielectric media. The accuracy of the sub-gridding was verified by comparison with a reference solution whose spatial step was equal to the spatial step in the sub-gridded region. The authors found that the scheme predicted the reflections from the water pipe with excellent accuracy. And also showed improvement to Chevalier et al. (1997) scheme. Results are only shown for a sub-gridding ratio of three. However, the authors claim that higher sub-gridding ratios have been tested successfully.

Diamanti et al. (2008) subsequently applied to the study of ring separation in masonry bridges. Specifically, the mortar between the layers of bricks was sub-gridded. An investigation into the detectability of deterioration in the mortar was made by sim-

ulation air voids in the mortar. The models predicted that hairline cracks in the mortar would not be detectable by GPR unless very high-frequency antennas were used. The authors did not provide any verification of the sub-gridding by reference solutions.

Wei et al. (2017) developed a novel spatially filtered FDTD hybrid method. The scheme was similar to the explicit-implicit methods in that both grids run in time synchronisation. However the sub-grid uses spatial filtering scheme to abate the unstable modes in the solution within the sub-grid. Spatial filtering was introduced by (Sarris, 2011). The time step can be extended beyond the CFL limit provided that the spatial frequencies correspond to those beyond the limit are filtered out. This method differs from the explicit unconditional stable method in that the unstable mode is attenuated and not removed. In the sub-gridding scheme, the filtering consists of Fourier transforming the fields with respect to space and imposing a hard cut-off at those frequencies above the CFL limit. Filtering only the magnetic fields is said to permit dielectric traversal across the sub-gridding boundary. However, examples demonstrating this are not given. Numerical examples detailing the sub-gridding of buried metal, plastic water-filled pipes buried inhomogeneous dispersive and non-dispersive soils. The accuracy of the method is evaluated in the same way as Diamanti and Giannopoulos (2009). The solution for the buried metal pipe buried in a dielectric is shown to vary from the absolute maximum by 5%. Results for the buried water pipe and dispersive soil are not compared with the fine grid solutions.

Wei et al. (2018) developed a hybrid scheme where FDTD method is coupled to Crank-Nicholson FDTD scheme. The authors show that the method is more accurate the spatially filtered sub-gridding scheme. This is achieved using a similar numerical test where the reflection from a buried metal pipe is measured and compared with a reference solution. Using this scheme the author observed an error of around 2%. No dielectric traversal was demonstrated using the scheme.

The studies presented thus far show that most researchers investigating sub-gridding schemes have incorporated the sub-gridding boundary as a boundary condition between the main grid and sub-grid. Subsequently many have observed spurious reflections at larger sub-gridding ratios. Although some authors have suggested that their schemes perform equally well at higher ratios they have not presented quantitative evidence for this. These observations suggest strongly that spurious reflections from the boundary between the main grid and the sub-grid are inherent in these types of schemes.

It is now well established from a variety of studies that the sub-gridding ratio can be greatly extended by the Huygens sub-gridding (HSG) scheme (Bérenger, 2006, 2009; Costen and Bérenger, 2010b; Bérenger, 2011; Abalenkovs et al., 2012). In contrast

to the other methods, the HSG utilises a physical connection to couple the grids. It has been shown that the Huygens sub-gridding performs at ratios of 99. Also, Costen and Bérenger (2010b); Abalenkovs et al. (2012) showed that the HSG permits material traversal.

5.1 Summary

This chapter has reviewed several FDTD sub-gridding schemes. Particularly it has highlighted those whose characteristics are suitable for refining objects related to GPR. Of most interest to GPR are schemes which support the traversal of dielectric materials across the sub-gridding interface and schemes which can be used with a high sub-gridding ratio without generating spurious reflections, and crucially those which offer a period of stability similar to the time scales associated with GPR. Of the methods described the HSG is most successful in these key areas.

The Huygens sub-gridding has been used extensively in this work to refine objects in GPR simulations. Therefore in the next chapter, its theoretic basis and several numerical experiments are described.

Chapter 6

The Huygen's Sub-Gridding Scheme

6.1 Sub-Gridding GPR Antennas

Chapter 5 reviewed the literature on sub-gridding schemes for the FDTD method. This chapter outlines the requirements for a sub-gridding scheme suitable for modelling GPR antennas. Also, the Huygen's Sub-Gridding method is discussed as a suitable candidate for such sub-gridding as well as for general GPR applications.

6.1.1 Extensible Sub-Gridding Ratio

Large sub-gridding ratios are required for sub-gridding finely detailed models of antennas. For instance, Wei et al. (2017) simulated a GPR antenna with a centre frequency of 200 MHz. For good dispersive properties $\Delta l_{max} = 12.5$mm when the maximum frequency of interest is 600 MHz corresponding to a drop in output power of 40 dB at $N_\lambda = 20$ and $\epsilon_r = 4$. However, finely detailed models of antennas are typically resolved by $\Delta l = 1$ mm (Warren and Giannopoulos, 2011; Stadler, 2017). Therefore, to correctly model the antenna a sub-gridding ratio of at least 12 is required. Clearly, for higher frequency antennas the ratio is lowered. However, modelling requirements for high-frequency antennas could demand cell sizes less than 1 mm if smaller components are modelled.

Many approaches reviewed in Chapter 5 support material traversal and have good stability. However, each failed to address sub-gridding ratios greater than 7. This

is because the methods treat the interface between the sub-grid and main grid as a boundary condition. The effect of which is to produce spurious reflections resulting from the difference in the numerical properties of each grid. This implies that many of these methods are not well suited to GPR since high sub-gridding ratios are required.

In contrast, the Huygen's Sub-Gridding scheme appears to support any odd number sub-gridding ratio. As opposed to other methods, the HSG is based on physical insight derived directly from Maxwell's equations. Equivalent current sources such as those described in the Near-Field to Far-Field Transformation are used to radiate fields between the grids. The elimination of the boundary condition between the two grids results in an error which is largely dependent on the leakage generated at these connecting surfaces termed "Huygen's surfaces".

Several sub-gridding studies support the view that the Huygen's Sub-Gridding can be used with arbitrarily high sub-gridding ratios. For example, Bérenger (2006) calculated the reflection coefficient of a thin conductive sheet using the 1d HSG with a large sub-gridding ratio of 99. The results were found to be in excellent agreement with reference solution over a large bandwidth. Also, Bérenger (2005) simulated the 2d scattering from a thin wire and a thin gap using the HSG. The experiments were performed with a 99 sub-gridding ratio. The results were found to be in good agreement with the fine grid reference solution. Further to this, Bérenger (2011) modelled the resonance between a thin wire and a PEC plate in 3d. Sub-Gridding ratios of 3, 5 and 15 were used, and in each case, the results were in similar agreement with the reference solution.

6.1.2 Material Traversal

GPR antennas are often placed on the ground during GPR surveys. This is primarily to increase the coupling and directivity of the antenna such that a larger reflection from the target can be obtained. From a sub-gridding point of view, this arrangement requires that a sub-grid which encompasses the antenna must also cut perpendicularly across the interface between the antenna and the ground. A possible alternative is a scheme which cuts parallel to the interface. However, this is problematic when the surface of the ground is not smooth. Also, soils are frequency-dependent lossy dielectrics. Therefore the sub-gridding scheme should support the traversal of frequency-dependent material across the sub-gridding boundary.

Several material traversals have been modelled using the HSG. For instance, Bérenger (2011) modelled PEC traversal across the sub-gridding boundary in 3d and a good

agreement was found. This was achieved with a modification to the interpolation scheme at the PEC boundary. This was required because the normal components of the electric field are discontinuous at the boundary. A straight forward interpolation would result in a smearing of the field across the boundary. Instead, the fields were specified using a nearest-neighbour interpolation.

Following the PEC traversal experiments, Abalenkovs et al. (2012) modelled the traversal of dispersive materials. In particular, the traversal of bone, fat, and muscle in human tissue crossing the sub-gridding interface was examined. In these models, no modifications to the interpolation schemes were required. The reason for this is that the displacement field was calculated at the interface as opposed to the electric field. The normal components of the displacement field are continuous across the interface. Whereas the normal components of the electric field are discontinuous across a dielectric interface. Thus the displacement field, therefore, can be averaged across dispersive media interface, and the correct interpolated electric fields are found subsequently using the auxiliary equation.

Reasonable agreement was found between the HSG and fine-grid solutions. Though a slight delay in the HSG solution was observed. It was accounted for by the variation in numerical dispersion of the grids within the coarse region of the sub-gridded solution. An important implication of this is that in addition to the dispersive properties of grids, the location of the material interfaces also varies between spatial discretisations and as such will have performance impacts upon sub-gridded solutions. This issue has not been addressed in any study.

6.1.3 Numerical Stability

Ideally, a sub-gridding scheme for modelling GRR antennas should be numerically stable. Also, the traversal of materials across the sub-gridding interface is often in competition with the stability of the sub-gridding scheme. For instance, it was shown that the electric and magnetic discretised curl operators must form asymmetric product to preserve the stability of any FDTD scheme. This criterion requires that the interpolation scheme is particularly complicated at the sub-gridding interface (Xiao et al., 2007). The consequence of which is that the Maxwellian interface conditions are not respected and thus material traverse was not permitted easily.

Other schemes have mitigated instabilities by using implicit methods. These schemes may not be suitable for sub-gridding large regions such as those occupied by commercial antennas. This is due to the increase in complexity owing to their matrix solution as

the size of the grid increases. A more viable solution appears to be band filtering the spectrum of each scheme such that the solution remains within the stable space within each grid (Donderici and Teixeira, 2005).

The main weakness of the HSG is a late-time instability. The instability occurs after several thousand iterations and presents itself as exponential growth in the solution. Although the approach is not suitable for very long-lived behaviour, it has been shown that transient behaviour can be observed during the stable period (Bérenger, 2011). An important implication of which is that the scheme is potentially stable for many GPR applications. Although other schemes offer better stability, the possibility of achieving high sub-gridding ratios is of more importance due to the increased range of applications to GPR problems.

6.1.4 Antenna Modelling

Accurate models of practice and frequently used commercial GPR antennas are key to modelling forward and inverse GPR problems that are important in everyday GPR work. As such a suitable sub-gridding scheme should be able to model non-uniform field distributions close to antennas without introducing significant numerical artefacts. Yet, sub-gridding approaches, especially those applied to GPR, have focused on the sub-gridding of targets Diamanti et al. (2008); Daniels (2009). Few studies have sub-gridded antennas.

Berenger (2009a) examined the Huygen's Sub-Gridding of a Hertzian dipole close to a small reflector. It was found that a good agreement between the solution and the fine-solution could be obtained. Interestingly, the author noted that frequencies which were not supported by the coarse grid were not reflected from the sub-grid as would be the case in the boundary-condition based schemes. The extraneous frequencies were simply absorbed by the PML used to truncate the sub-grid. In particular, this property introduces a use case for the sub-grid PML beyond attenuating the late time instability.

The success of the Hertzian dipole near to a reflector sub-gridding indicates that the Huygen's Sub-Gridding is a good candidate for sub-gridding realistic antenna designs. This is because the proximity of reflector introduces a significant variation of the field close to the source, and a similar behaviour is observed in the case of the antenna housing about the source in a realistic antenna used for practical GPR applications.

6.2 The Equivalence Theorem

Electric and magnetic fields in the HSG radiate between main-grid and sub-grid using Huygen's surfaces. The concept of Huygen's surfaces derives from the equivalence theorem which states

> "The field in one region of space can be radiated into another region by impressing the equivalent magnetic and electric currents on the surface which separates them" (Balanis, 2012).

The equivalent currents on the surfaces can be derived by considering the standard interface boundary conditions for the electric and magnetic fields at a surface where electric and magnetic currents flow.

Consider the interface between Region 2 and Region 1 shown in Figure 6.1. The electric and magnetic fields, $\vec{E_2}$, $\vec{E_1}$, $\vec{H_2}$ and $\vec{H_1}$ immediately either side of the boundary are discontinuous by magnetic and electric current densities on the separating surface. This is more formally expressed as

$$\vec{n} \times (\vec{H_1} - \vec{H_2}) = \vec{J_s} \tag{6.1}$$

$$\vec{n} \times (\vec{E_1} - \vec{E_2}) = -\vec{M_s} \tag{6.2}$$

where $\vec{n}$ is the unit vector normal to the interface in the direction away from the source and $\vec{J_s}$ and $\vec{M_s}$ are the electric and magnetic current densities on the surface S.
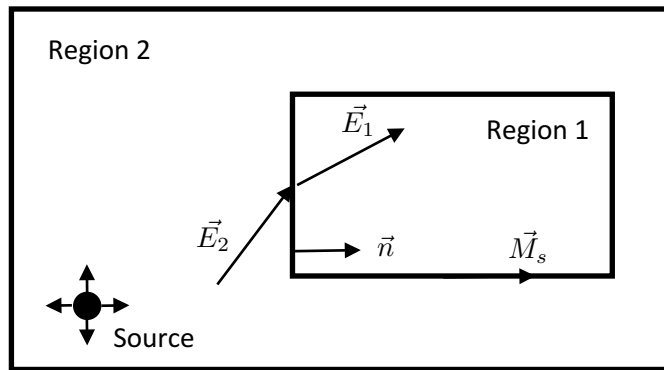
Figure 6.1: Electric fields $\vec{E_1}$ and $\vec{E_2}$ at a surface with a current density $\vec{M_s}$

In Figure 6.2 the current surface is replaced with a fictitious surface which contains no surface currents. From equation 6.2 and equation 6.1 the parallel fields either side
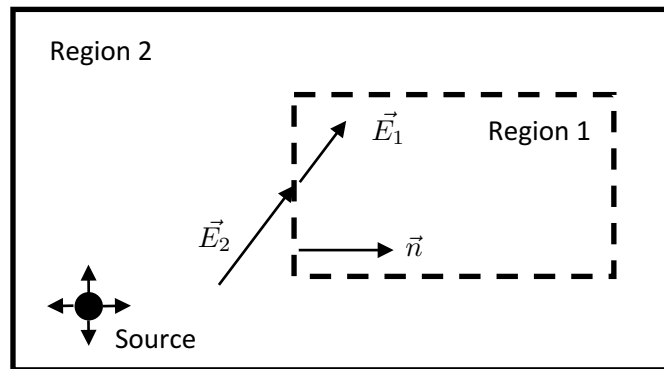
Figure 6.2: Electric fields at a fictitious surface with no current density.
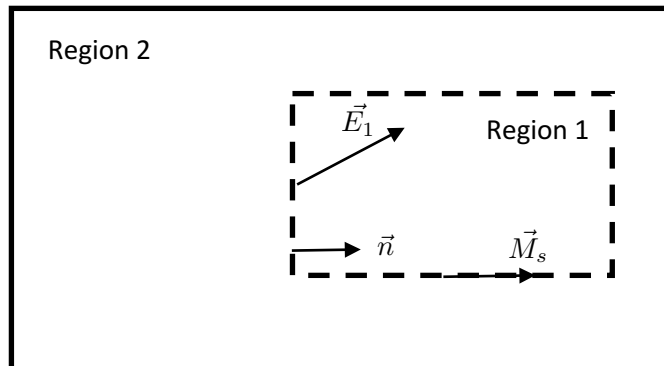
Figure 6.3: An equivalent problem showing the electric field E_1 due to a current density, M_s on a surface with unit vector $\hat{n}$.

of the boundary are now continuous. An equivalent problem the Region 1 in Figure 6.2 shown in Figure 6.3. Here, the field in Region 2 is set to zero and the fictitious surface is replaced with a Huygen's surface with the current densities $\vec{J}_s$ and $\vec{M}_s$ such that the field E_1 is equal to the field E_1 in Figure 6.2. The same principle is also similarly extended for the magnetic field to find the equivalent fields.

The equivalent current densities for the electric and magnetic fields are given by

$$\vec{n} \times \vec{H_{inc}} = \vec{J}_s \tag{6.3}$$

$$-\vec{n} \times \vec{E_{inc}} = \vec{M}_s \tag{6.4}$$

Thus the field from the source in Region 1 can be radiated into Region 2 of the equivalent problem by specifying the current densities $\vec{J}_s$ and $\vec{M}_s$ on the boundary between the regions.

Merewether et al. (1980) first implemented Huygen's surfaces in FDTD to calculate the radar cross-sections of structures and Electromagnetic Pulse (EMP) coupling to missiles. The formulation for the Huygen's surface is identical to the more common Total-Field Scattered-Field formulation with the exception that the incident field generation is not artificial. The equivalence theorem provides a physical explanation for the TF/SF. The reason for this is that the incident field in the TF/SF is expressed formally in terms of magnetic and electric current densities as opposed to the continuity of the superposition of fields in each region.

The concept of Huygen's surfaces was extended to the 1d FDTD sub-gridding FDTD by Bérenger (2006) and was extended subsequently to 2d (Berenger, 2009b) and 3d (Bérenger, 2011). Instead of radiating a field only into a total field region with a single surface, the Huygen's sub-gridding uses multiple Huygen's surfaces to source both sub-grid and main-grid by their local fields.

6.3   1d Huygen's Sub-Gridding

Figure 6.4 shows the position of a Huygen's surface in 1d discretised space. This space represents an FDTD grid and the Huygen's surface the position at which the field from the other grid is radiated. The Huygen's surface is positioned equidistantly from i'_{is}
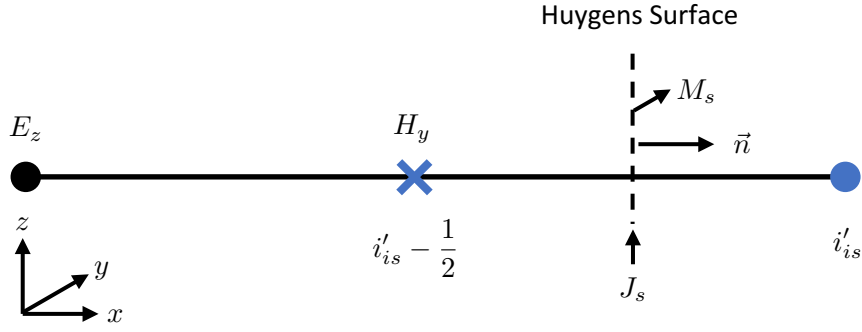
Figure 6.4: Diagram of the Huygen's Surface in 1d FDTD method. E_z is the electric field in the z-direction. H_y is the magnetic field in the y-direction J_s is the surface current density in the z-direction and M_s is the surface magnetic current in the y-direction.

and $i'_{is} - \frac{1}{2}$. The reason for this is that positioning the surface at either the E_z or H_y planes would lead to a discontinuity in one of the fields (Potter and Bérenger, 2017).

The electric and magnetic fields and the currents which run on the Huygen's surface in 6.4 are described by the Ampere's and Faraday's laws along with their associated current densities, J_z and M_y.

$$\epsilon_0 \frac{\partial E_z}{\partial t} = \frac{\partial H_y}{\partial x} - J_z \tag{6.5}$$

$$\mu_0 \frac{\partial H_y}{\partial t} = \frac{\partial E_z}{\partial x} - M_y \tag{6.6}$$

First consider the J_z current density. Discretising space and time and evaluating equation 6.5 at the space-time point $((n + \frac{1}{2})\Delta t, i\Delta x)$ gives

$$E_z\Big|_i^{n+1} = E_z\Big|_i^n + \frac{\Delta t}{\epsilon_0 \Delta x}\left(H_y\Big|_{i+\frac{1}{2}}^{n+\frac{1}{2}} - H_y\Big|_{i-\frac{1}{2}}^{n+\frac{1}{2}}\right) - \frac{\Delta t}{\epsilon_0} J_z\Big|_i^{n+\frac{1}{2}} \tag{6.7}$$

From equation 6.3 the surface current due to the incident field $H_{y_{inc}}\Big|_{i-\frac{1}{2}}^{n+\frac{1}{2}}$ is given by

$$\hat{i} \times H_{y_{inc}}\Big|_{i-\frac{1}{2}}^{n+\frac{1}{2}}\hat{j} = J_s\hat{k} \tag{6.8}$$

where $\hat{i}$ is the unit vector on the Huygen's surface in the direction away from the

source.

The current density in equation 6.7 is expressed in terms of a surface current by

$$J_z = \frac{J_s}{\Delta x} \tag{6.9}$$

Combining equation 6.8 and equation 6.9 and substituting the result into equation 6.7 gives

$$E_z\Big|_i^{n+1} = E_z\Big|_i^n + \frac{\Delta t}{\epsilon_0 \Delta x}\left(H_y\Big|_{i+\frac{1}{2}}^{n+\frac{1}{2}} - H_y\Big|_{i-\frac{1}{2}}^{n+\frac{1}{2}}\right) - \frac{\Delta t}{\epsilon_0 \Delta x} H_{y_{inc}}\Big|_i^{n+\frac{1}{2}} \tag{6.10}$$

Equation 6.10 is the update equation for the electric field at the Huygen's surface. Notice that it is consistent with the update equation for the electric field in the TF/SF.

The Huygen's sub-gridding extends the idea of Huygen's surfaces to the radiating fields between FDTD grids. Rather than specifying an incident field from some externally generated source as in the TF/SF the incident field is the incoming field from an external FDTD grid. The calculation of this field is a matter of interpolating or decimating the field in the opposing grid.

6.3.1 Propositions

Bérenger (2006) summarises with two propositions the action of the Huygen's surfaces upon the fields exchanged between the two grids.

Proposition 6.3.1. *Sources and scatterers located in the non-working region of either grid contribute no field to the working regions. The non-working regions, therefore, act as non-physical regions which do not represent the physical problem.*

Proposition 6.3.2. *The field radiated by the surfaces into the working regions is equivalent to the field in the physical problem with the addition of a common region between the IS and OS. From equation 6.6 and equation 6.5 the combination of the fields in regions labelled working is the same as if they formed a single space.*

To understand these propositions the key objects are labelled as follows: the Inner Surface (IS) - the Huygen's surface which links the main grid to the sub-grid, Outer Surface (OS) - the Huygen's surface which links the sub-grid to the main-grid, the non-working region of the main grid is the region occupied within the IS of the main

grid (positive space), the non-working region of the sub-grid is the region beyond the OS in the sub-grid (negative space), the working regions are all the other regions, the IS-OS region is the shared region in the main-grid and sub-grid which is between the IS and the OS.

The behaviour of the HSG can be derived by following the action of the Huygen's surfaces on a wavelet sourced in the working region and non-working regions. Figures 6.6 and 6.5 illustrate the propagation of a single wavelet throughout the 1d HSG. In each figure, the upper horizontal line represents the main FDTD grid and the lower line represents the sub-grid region of the FDTD. The downward and upward arrows represent Huygen's surfaces which radiate the incoming wavelets from one grid to another. The horizontal arrows represent the unit normals to the surface. The locations of the IS and OS are also shown.

Proposition 1 is proven by considering a wavelet sourced in the first non-working region of the sub-grid shown in Figure 6.5. At Surface 1 (OS) the wavelet is radiated into the main grid with negative polarity. Once the wavelet arrives at Surface 2 (IS) it is radiated back into the sub-grid. The resulting magnitude of the field in the main grid is zero due to the cancellation of the opposing fields. The negative polarity wavelet is then radiated back into the sub-grid such that the polarity is positive due to the negative direction unit vector. This field is then re-radiated back to the sub-grid. The opposing fields then cancel in the final region of the main grid. The net result is that no field from the non-working region is ever observed in a working region. Thus the field in the non-working regions represents a non-physical field.

Proposition 2 is proven by considering a wavelet sourced in the working region of the main grid shown in Figure 6.6. At Surface 1 (OS) the wavelet is not affected. This is because the surface radiates fields only from the sub-grid to the main grid. The wavelet is then radiated by the Surface 2 (IS) into the sub-grid. Where it acts as an incident field to the sub-grid. At this point, identical fields propagate through the main grid and the sub-grid. At Surface 3 (IS) the sub-grid fields act as the incident fields to the main grid. However, the direction of the unit vector is reversed. This affects that the cross product in equation 6.8 is negative. This results in an incident field with a negative polarity. At Surface 3 (IS) the field magnitude is zero due to the superposition of the opposing fields. At Surface 4 (OS) the field continues to propagate through the main grid. The net result is an equivalent problem in which the combination of the working regions represents the original physical problem.
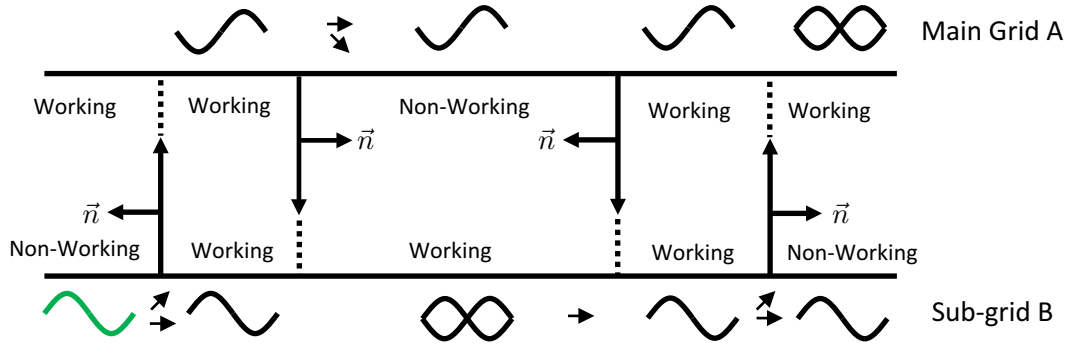
Figure 6.5: Diagram of the Huygen's surfaces connecting grid A and grid b in the HSG. A wavelet is sourced in the non-working region of grid a. It illustrates that no field is coupled to the working regions from the non-working regions.
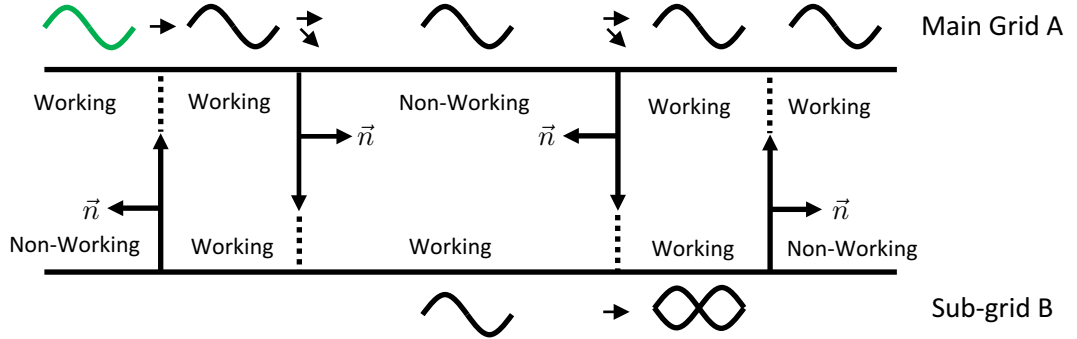
Figure 6.6: Diagram of the Huygen's surfaces connecting grid A and grid b in the HSG. A wavelet is sourced in the working region of grid a. It illustrates that the field from the working region is correctly radiated to the other working regions and that the physical field in the IS-OS gap is the sum of the fields in each grid.

6.3.2   Spatial and Temporal Interpolation

The implementation of the incident field at the Huygen's surface is straightforward for coupling grids which have equal spatial steps and Courant numbers. The exact field in time and space is implemented directly within FDTD update equation given equation 6.10 and its equivalent magnetic update. Watts and Diaz (2003) showed that the fields radiated by Huygen's surfaces in FDTD schemes are exact to numerical precision. This is known as teleportation. However, in the case of sub-gridding, spatial and temporal interpolation of the fields and an altered time-stepping of the update equations are required when the step sizes and Courant numbers are not equal.

Figure 6.7 shows an example of the location of the field nodes for the 1d HSG at the IS. The ratio of the main grid spatial step to the sub-grid spatial step is 1:3. The main grid and the sub-grid have been aligned such that the electric nodes in each grid at the IS are aligned. In this case, the main field can be used directly. However, the update of the $E_b|'_i$ requires an interpolated magnetic field value, H_p, indicated by the blue cross in the main grid. This is achieved by linear interpolation of the adjacent H fields at a single point in time.
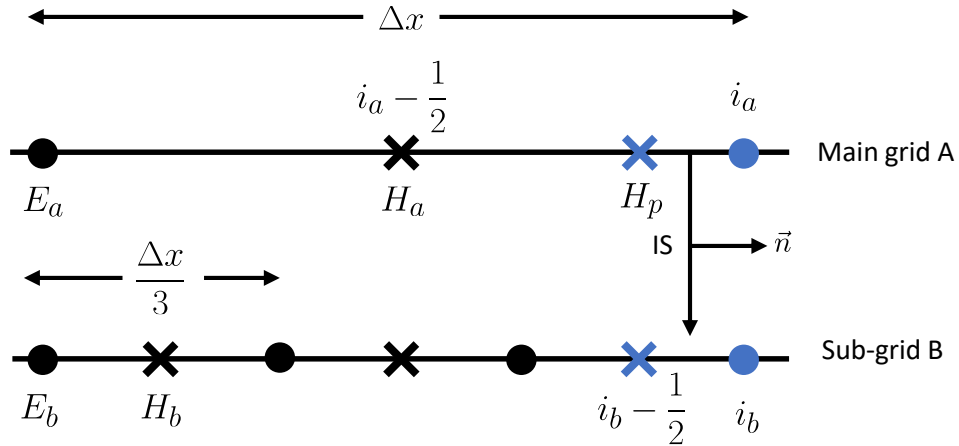
Figure 6.7: Diagram of the arrangement of the field nodes at the left IS for a 1:3 HSG. They grey cross shows the location of the interpolated magnetic field H_p.

Figure 6.8 shows the location of the field nodes for the 1d HSG at the right-hand-side OS. The OS has been positioned again such that electric field nodes are aligned. Also, the magnetic field nodes in the HSG OS are always aligned with magnetic fields in the sub-grid when a spatial step in the main grid is equal to an odd integer multiple of the spatial step in the sub-grid. And therefore do not require any spatial interpolation. Additionally, the update of the OS does not require temporal averaging. The reason for this is the main grid and sub-grid are collocated in time at every odd integer number
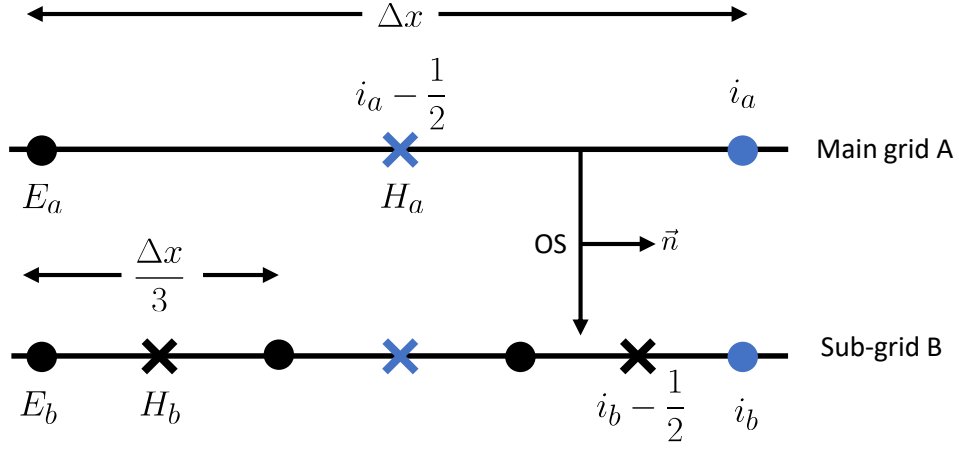
Figure 6.8: Diagram of the arrangement of the field nodes at the left OS for a 1:3 HSG. The blue field nodes indicate the fields which participate in the HSG update equations.

of time steps in the sub-grid.

Odd integer ratios are always used in the HSG. The reason for this is they simplify the HSG implementation and improve the accuracy of the HSG by eliminating spatial and temporal interpolation at the OS.

6.4   3d Huygen's Sub-Gridding

Bérenger (2009) extended the HSG to the 2d case and later to the 3d case (Bérenger, 2011). The 2d case will not be covered as it is a section of the 3d case. The 3d case is complicated by the additional tangential fields at the Huygen's surfaces. Additionally, the Huygen's surfaces which were points in the 1d scheme are surfaces in the 3d scheme. Interpolation of the fields across the surface needs a more complex spatial averaging system than in the 1d case. Additionally, a revised time-stepping algorithm has been introduced which does not require the extrapolation of fields into the future.

6.4.1   HSG Update Equations

As before the HSG update equations are derived by considering the surface currents at the IS and OS. Following the standard discretisation procedure, the FDTD update equation in a loss-free medium for the Ampere-Maxwell law E_x and E_z components are given by

$$E_{x_b}\Big|_{i+\frac{1}{2},j,k}^{ns+1} = E_{x_b}\Big|_{i+\frac{1}{2},j,k}^{ns}$$

$$+ \frac{\Delta t}{\epsilon \Delta l}\left(\left\{H_{z_b}\Big|_{i+\frac{1}{2},j+\frac{1}{2},k}^{ns+\frac{1}{2}} - H_{z_b}\Big|_{i+\frac{1}{2},j-\frac{1}{2},k}^{ns+\frac{1}{2}}\right\} - \left\{H_{y_b}\Big|_{i+\frac{1}{2},j,k+\frac{1}{2}}^{ns+\frac{1}{2}} - H_{y_b}\Big|_{i+\frac{1}{2},j,k}^{ns+\frac{1}{2}}\right\}\right)$$

$$- \frac{\Delta t}{\epsilon}J_{x_b}\Big|_{i+\frac{1}{2},j,k}^{ns+\frac{1}{2}} \quad (6.11)$$

The only contribution to the electric surface current in the x-direction from H_z. The surface current in the x-direction is given by

$$J_{sx_b}\hat{i} = \hat{j} \times H_{z_a}\Big|_{i+\frac{1}{2},j_{is}-\frac{1}{2},k}^{ns+\frac{1}{2}} \hat{k} \quad (6.12)$$

$$J_{sx_b} = H_{z_a}\Big|_{i+\frac{1}{2},j_{is}-\frac{1}{2},k}^{ns+\frac{1}{2}} \quad (6.13)$$

Dividing equation 6.13 through by Δl to obtain the volumetric current density and then substituting the result into equation 6.11 yields the update equation for E_{b_x} on the front face. Hence, the HSG correction to the standard update equation is given by

$$E_{x_b}\Big|_{i+\frac{1}{2},j,k}^{ns+1} - = \frac{\Delta t}{\epsilon \Delta l}H_{z_a}\Big|_{i+\frac{1}{2},j_{is}-\frac{1}{2},k}^{ns+\frac{1}{2}} \quad (6.14)$$

This correction is applied to all the E_{x_a} nodes on the front face of the Huygen's surface.

A similar procedure can be carried out for the update of the H_{z_b} nodes. Consider the standard discretisation of the Ampere-Maxwell equation for H_{z_b} given by

$$H_{z_b}\Big|_{i,j+\frac{1}{2},k+\frac{1}{2}}^{ns+\frac{1}{2}} = H_{z_b}\Big|_{i,j+\frac{1}{2},k+\frac{1}{2}}^{ns-\frac{1}{2}}$$

$$+ \frac{\Delta t}{\mu \Delta l}\left(\left\{E_{x_b}\Big|_{i+\frac{1}{2},j+1,k}^{ns} - E_{x_b}\Big|_{i+\frac{1}{2},j,k}^{ns}\right\} - \left\{E_{y_b}\Big|_{i+1,j,k+\frac{1}{2}}^{ns} - E_{y_b}\Big|_{i,j,k+\frac{1}{2}}^{ns}\right\}\right)$$

$$- \frac{\Delta t}{\mu}M_{z_b}\Big|_{i,j+\frac{1}{2},k+\frac{1}{2}}^{ns} \quad (6.15)$$

From equation 6.4 the magnetic surface current is given by

$$M_{sz_b}\hat{k} = -\hat{j} \times E_{x_a}\Big|_{i+\frac{1}{2},j_{is},k}^{ns} \hat{i} \tag{6.16}$$

$$M_{sz_b} = E_{x_a}\Big|_{i+\frac{1}{2},j_{is},k}^{ns} \tag{6.17}$$

Dividing equation 6.17 through by Δl to obtain the magnetic volumetric current density and then substituting the result into equation 6.15 yields the update equation for H_{b_z} on the front face. Hence, the HSG correction is given by

$$H_{z_b}\Big|_{i,j+\frac{1}{2},k+\frac{1}{2}}^{ns+\frac{1}{2}} - = \frac{\Delta t}{\mu \Delta l} E_{x_a}\Big|_{i+\frac{1}{2},j_{is},k}^{ns} \tag{6.18}$$

The corrections for the E_{z_b} and H_{x_b} can be derived following the same logic. The other faces of the IS cube are rotations of the front face and can also be derived similarly. The correction factors for the IS are given in Appendix A.

The OS is a Huygen's surface which has unit vectors pointing in the opposite direction to the IS unit vectors. Therefore the correction factors are the same as the IS, with additions and subtraction multiplied by -1. The OS correction factors are given in Appendix A.

6.4.2 Spatial Interpolation

In comparison to the 1d arrangement, the 3d arrangement requires addition spatial interpolation of the fields. This is because there are non-collocated electric fields and the magnetic fields do not lie in the same plane.

In 3d the IS and the OS are cubic surfaces though any closed shape is permitted. Figure 6.9 shows an example of a Yee cell in the main grid which is located in the front face of the IS cube. The figure shows the projection of the Yee surface in the main grid on to the Yee surface in the sub-grid where the two planes are collocated in the xz plane. Only the E_z fields are shown. However, the E_x fields are also present in their usual positions. From the equivalence relations, only the fields parallel to the Huygen's surface generate surface currents. Therefore in the front face only $E_{x_b}, E_{z_b}, H_{x_b}, H_{z_b}$ are updated using the Huygen's update equations. The remaining fields are updated with the standard FDTD update equations.

In order to update the H_{x_b}, E_{z_a} must be evaluated at all the points shown in 6.9.

This is accomplished via a 2d interpolation of the collocated main grid electric fields shown in orange with the adjacent Yee cells. Eventually at the edges of the front IS surface the electric fields must be interpolated from fields which are not on the IS. The spatial interpolation for the E_{x_a} nodes proceeds in the same way. At the edges of the IS, the fields must be corrected twice. This is because these fields lie in the perpendicular planes of the other faces of the cube. For instance, E_{z_b} is also updated by $H_{y_{inc}}$ from the left face of the IS.

The interpolation procedure for the magnetic fields at the IS is more complex. This is because there are no magnetic fields which are straightforwardly collocated. Figure 6.10 shows the positions of the magnetic fields involved in the E_{x_a} update at the IS. Again the required fields have been projected onto the sub-grid Yee surface. Additionally, the Yee cell grid has been shifted onto the H_z field plane to show the fields more clearly. The diagram shows the planes containing the H_{z_a} fields transverse and adjacent to the IS. The magnetic fields in the $j' = is' - \frac{1}{2}$ plane are evaluated as follows. The yellow nodes in the sub-grid plane are linearly interpolated in the transverse direction to the plane using the adjacent nodes shown. Then these nodes are interpolated across the $j' = is' - \frac{1}{2}$ plane.
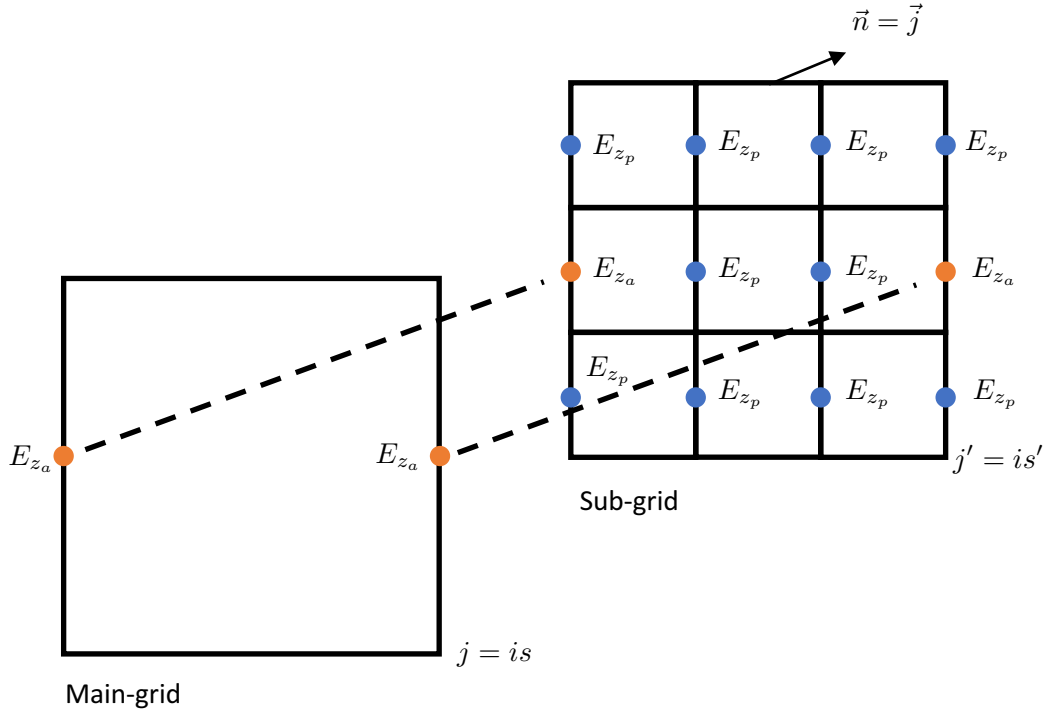
Figure 6.9: Diagram of a 3:1 spatial interpolation at the IS. Orange dots represent to collocated E_z fields and the blue dots represent the precursor node which must be obtained via interpolation.
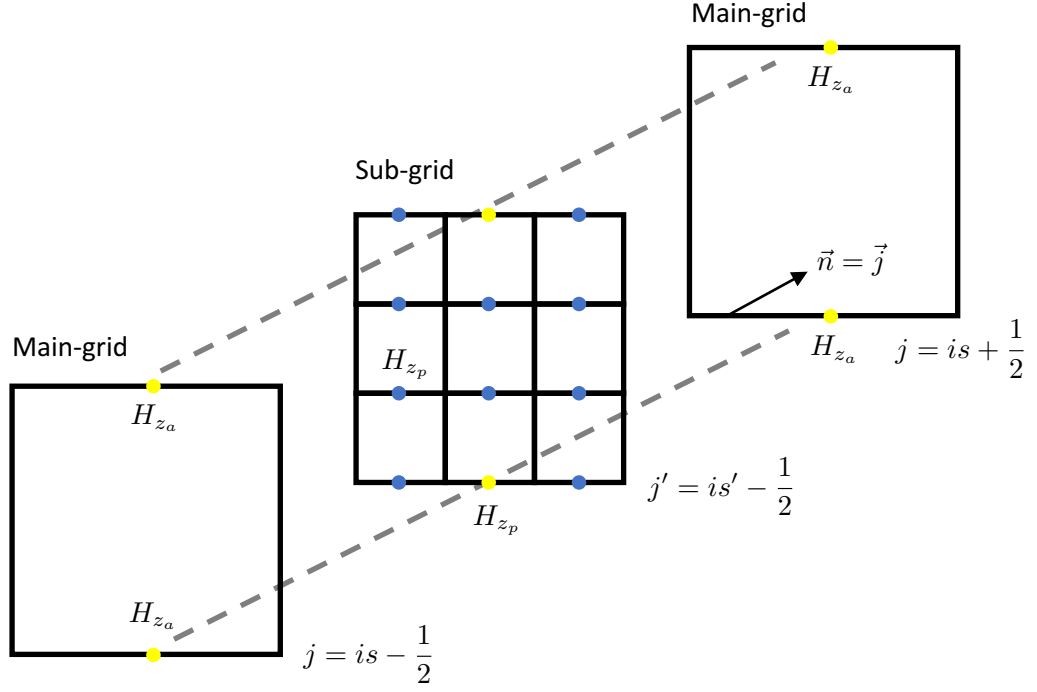
Figure 6.10: Diagram of a 3:1 spatial interpolation at the IS. Yellow dots represent the magnetic fields which are linearly interpolated in the direction perpendicular to the surface. The magnetic fields in the $j' = is' - \frac{1}{2}$ plane are interpolated from the resulting fields.

At the OS spatial interpolations are not required. This is because the main grid nodes are always collocated with sub-grid nodes when odd integer ratios are used.

6.4.3 Time-stepping and Time Interpolation

The HSG updates, equation 6.14 and equation 6.18, evaluate the surface currents at sub-grid temporal index ns, and $ns + \frac{1}{2}$. However, the field values in the main grid which are incident to the sub-grid are available for all the indexes with a single time-step. Therefore, an altered time-stepping algorithm and time interpolation scheme is required to obtain these fields at the correct times.

The HSG updates are split into two separate algorithms. The first, HSG 1, proceeds after the electric update in the main grid. And the second, HSG 2, proceeds after the magnetic update in the main grid. The advantage of the two algorithms is they can be incorporated into most FDTD codes without modification to the core FDTD algorithm. An illustrative example is given in Figure 6.11. It shows a timeline of the field updates for a single loop of the HSG during a 1:3 sub-gridding. It is assumed that magnetic fields at $n + \frac{1}{2}$ in the main grid are already known or equal to zero. The updates for the HSG 1, and HSG 2 are given as follows:

Time-stepping for the HSG 1

1. Update E_a. And then update the electric precursor nodes E_p to $(n + 1)$.

2. Update E_b to $ns + 1$. Interpolate H_p to $(ns + \frac{1}{2})$ and then apply correction to E_b at the IS.

3. Update H_b to $(ns + \frac{3}{2})$. Interpolate E_p to $(ns + 1)$ and then apply the correction to H_b at the IS.

4. Update E_b to $(ns + 2)$. Use exact value of H_a at $(n + \frac{1}{2})$ to the correction to E_b at the IS.

5. Update E_a at the OS now that $H_b|^{ns+\frac{3}{2}}$ is known.

Time-stepping for the HSG 2

1. Update H_a to $n + \frac{3}{2}$. And then update the magnetic precursor nodes to $n + \frac{3}{2}$

2. Update H_b to $ns + \frac{5}{2}$. Interpolate E_p to $ns + 2$ and then apply the correction H_b at the IS.

3. Update E_b to $ns + 3$. Interpolate H_p to $ns + \frac{5}{2}$ and then apply the correction to E_b at the IS.

4. Update H_b to $ns + \frac{7}{2}$. Use exact value of E_a at $n + 1$ to the correction to H_b at the IS.

5. Update H_a at the OS for $n + \frac{3}{2}$ now that $E_b|^{ns+3}$ is known.

The initial updates of E_a and H_a are incorrect at the OS. This is because the incident fields in the sub-grid have not yet been calculated. The fields at the OS are subsequently corrected in step when the correct fields are available. This places the condition that the IS is at least one main grid cell from the OS. This is such that within the one main grid time step information can not travel between the surfaces and radiate back into the sub-grid. A gap of less than one cell results in a feedback effect which leads to numerical instability (Bérenger, 2007b).

Also, the algorithm can be easily extended to greater sub-gridding ratios. In general the HSG 1 leap-frog algorithm updates E_b $r/2 + 1$ times and the H_b $r/2$ times where r is the sub-gridding ratio. The HSG 2 performs the same number of update per each field vice versa.
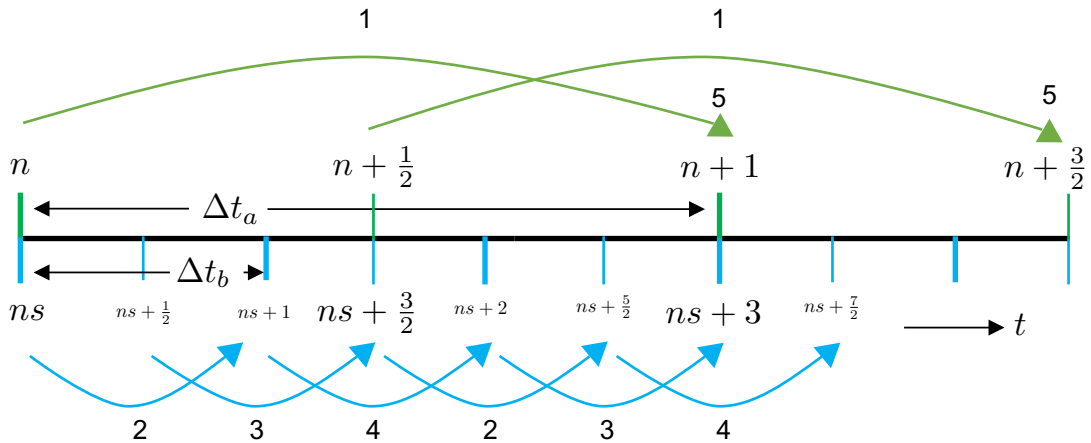
Figure 6.11: Diagram of a 3:1 HSG time-stepping algorithm. The green arrows indicate updates of the fields in the main grid and the blue arrows indicate updates in the sub-grid. (n) is the time index in the main grid and (ns) is the time index in the sub-grid.

6.5 Late-Time Instability

One major drawback of the HSG is the presence of a late-time instability. The onset of the instability is not generally predictable. It is thought that the instability depends on

several free parameters such as the sub-gridding ratio, the time-step and the distribution of objects within the grids (Bérenger, 2006). Additionally, the instability arises within a large margin of error of 1000-10000 time-steps. These uncertainties contribute to a lack of confidence in the approach for the application to general problems. This is presumably the reason that the approach has not been widely adopted. Several methods have been proposed to delay the onset of numerical instability.

6.5.1 PML

It was found that the late-time instability was delayed by the introduction of a PML in the non-working regions of the sub-grid (Bérenger, 2006; Berenger, 2009b; Bérenger, 2011). The attenuation of unstable energy is the reason for the reduction in the growth of the instability. It was also observed that the PML bounding the main grid reduced the onset of the instability. However, the introduction of a PML in the non-working region of the main grid had only a slight effect on the growth of the instability. This is thought to be because the unstable energy is reflected completely at the interface at the cut-off frequency and therefore there is no unstable energy within the PML.

Several numerical experiments give an insight into the period of stability. For example, Bérenger (2011) modelled the resonance between a wire and a metal plate. Without the PML, the instability presents before 2000 iterations. However, with the PML, the instability was delayed for a further 3000 iterations. For 3d implementations a 6 cell PML placed 2 sub-grid cells away from the magnetic OS field node was used for the numerical experiments (Bérenger, 2011).

6.5.2 Filter

The numerical instability has been shown to oscillate at the cut-off frequency (Bérenger, 2006). Bérenger (2006) decreased the onset of the instability by attenuating the spatial frequencies at the cut-off. This is possible without a substantial loss inaccuracy in the solution. This is because the cut-off frequency corresponds to $k\Delta x = \pi$ whereas the limit off acceptable dispersion is $k\Delta x = 0.2\pi$ (Sarris, 2011). Therefore, provided the filter slope does not cut across the non-dispersed spatial frequencies, the filter should preserve the simulation accuracy.

The filter was implemented in the spatial frequency domain. This is because the fields' values at a future times are not known. Bérenger (2006) tested several filters and it was found that a 3-node Finite Impulse Response (FIR) filter at the IS was found

to eliminate the instability for free-space problems in 1d. The 3-node filter is a low pass filter with a cut-off at the FDTD cut-off frequency and is therefore presumed to attenuate frequencies above the cut-off.

The 3-node filter is implemented by taking a weighted average of the electric and magnetic fields adjacent to the field used in the IS HSG update. The outer fields are weighted by 0.25 and the central field is weighted by 0.5. Each of the magnetic fields which contribute to the transverse interpolation is also filtered using the same weighted sum.

The filter can increase the number of stable iterations by 30000. This was shown in a calculation of the resonance between a PEC plate and a wire (Bérenger, 2011)

6.5.3 Implicit Schemes

Huang et al. (2013) suggested the instability results from temporal interpolation of the fields. The implication of this is the discretised curl operators in the HSG form asymmetric product. In terms of consistency, this follows. The fields which are updated at each surface do not directly update the fields in the opposing grid. i.e. there is no issue with consistency as in the boundary condition methods. The only inconsistency is that the fields in the sub-grid are not updated using the same temporal field as the updates in the main grid.

Huang et al. (2013) hybridised the HSG by discretising the sub-grid space using a Crank-Nicholson (CN) approach. No instability was observed within 1×10^6 iterations. However, the excitation appears to have a period of approximately the iteration order. Therefore, in this case, the upper frequencies near to the cut-off may experience very little excitation.

6.5.4 Artificial Loss

Costen and Bérenger (2010a); Abalenkovs et al. (2012) observed that the late time instability was not present when the sub-grid was embedded within human tissue. It is thought that the loss experienced through the complex permittivity in the tissue absorbed the unstable energy and therefore prevented the growth of the solution. An implication of this for GPR is that the scheme is stable for applications where objects are embedded within dispersive soils such as buried water pipes. In these scenarios, the additional stability measures such as the PML and filter are likely not to be required.

Following on from this work Zhou et al. (2010) experimented by adding regions of artificial loss to the sub-grid and main grid at the IS and OS to absorb the unstable energy. The authors were successful in eliminating the instability for 40000 iterations. However, the artificial loss caused the solution to rapidly attenuate. Dispersive losses and dispersive gains were also tested in an attempt to apply a frequency-dependent loss targeted at the cut-off frequency. This approach was successful in 1d. However, when the scheme was applied to the 3d HSG instabilities were still observed. These methods all lead to a rapidly decaying solution even when the loss is very small. This results from the fact that the equivalent problem no longer represents the physical problem; the physical problem has no loss in the working region.

6.5.5 Stability Estimate

Whilst the wire-plate resonance problems are not equivalent to GPR half-space problems they do provide some insight into the region of stability which could be expected for such problems. Such problems could be more stable if the sub-grid is embedded in lossy soils.

The stability is also related to the distance from objects in free space to the main grid PML. The greater this distance the larger the unstable field flux through the PML and presumably greater the attenuation. For the wire resonance problem, a single Yee cell is used between the source and PML. In comparison, for GPR problems this distance would be considerably larger due to the physical dimensions of a real antenna. This suggests the stability could be improved upon for the antenna over a half-space problem.

For sub-grids embedded in free-space, an approximate argument for the stability of the HSG over GPR timescales can be made by considering the depths that GPR systems can probe and whether the travel times for these distances are within the algorithms stable period.

Cook (1975b) examined penetration depths of GPR in the sub-surface for a range of materials. The signal losses in samples of rock were measured and penetrating depths were calculated using the radar equation over a frequency range 25 MHz to 100 MHz. Figure 6.12 shows the expected penetration depths for a range of rock types. For clay type materials such as soils the estimated penetration depth is 10 m or less. In rocks such as limestone and granite probing depths of 100 m and 500 m are expected. At higher frequencies, the attenuation is expected to be greater due to the dielectric loss associated with water content or other lossy dielectrics (Daniels, 2007a).
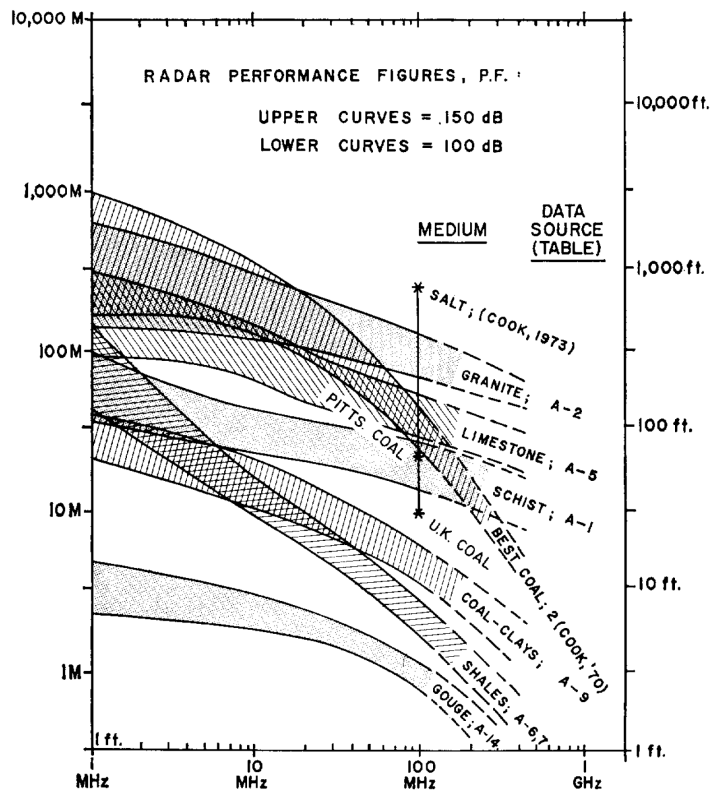
Figure 6.12: Estimated penetration depths for GPR for a range of rock types over a frequency range 25 MHz to 100 MHz. Figure taken from Cook (1975b)

118

In comparison Figure 6.13 shows the depths for which a signal can penetrate a loss-free dielectric and return to surface within a stable time-window. The calculation is based on the assumption that the stability of the wire/plate resonance is equal or worse than the half-space problem. The equation for the depth is based on the travel time for a signal to propagate through a material ϵ_r to a target and return to a receiver in FDTD simulation at the 3d CFL limit. A 1:5 sub-gridding is used as in Bérenger (2011). However, the sub-grid resolution has been set to 1 mm to reflect more accurately a common discretisation used to model GPR systems.

The estimated stable depth is given by

$$d = \frac{vn\Delta t}{2} \tag{6.19}$$

where n is the number of iterations and v is the velocity in the dielectric given by

$$v = \frac{c_0}{\sqrt{\epsilon_r}} \tag{6.20}$$

and Δt at the 3d Courant limit given by

$$\Delta t = \frac{1}{\sqrt{3}}\frac{\Delta x}{c_0} \tag{6.21}$$

Therefore the stable depth penetration is given by

$$d = \frac{n\Delta x}{2\sqrt{3\epsilon_r}} \tag{6.22}$$

From Figure 6.13 the maximum depth of penetration given with the 3-node filter is 13 m. For a typical wet clay/loam soil $\epsilon_r = 10 - 30$ (Daniels, 2007a), a penetration depth of around 10 m is possible. However, the clay curve in Figure 6.12 shows that in reality a penetration depth of less than 5 m is expected. Therefore, the HSG should be able to model the full range of behaviour of a wet clay/loam soil. However, the HSG with only the PML used as a stability mechanism is predicted to support a penetration depth of 2 m only.

Another instability problem is a slight drift in the field after around 8000 iterations have passed. It is conjectured that parasitic charge is left on the Huygen's surfaces in the 3d case only (Zhou et al., 2010). It was shown in Bérenger (2011) that offsetting
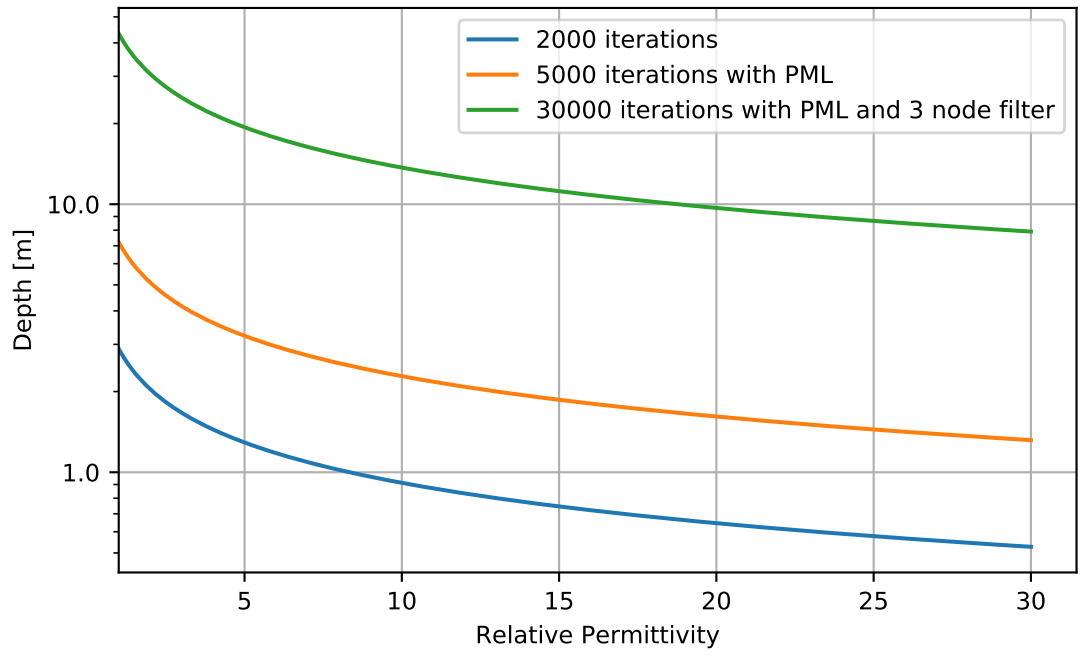
Figure 6.13: Depth to which the HSG is stable based on a number of the number of stable iterations for a 1:5 sub-gridding for various stability mechanisms given in Bérenger (2011). The discretistion in the sub-grid is 1 mm based on a common fine grid solution often used to model GPR systems (Warren and Giannopoulos, 2011; Stadler, 2017).

the IS and OS surfaces by 3 main grid cells that the shift is reduced to $\frac{1}{400}$ of the peak value. Therefore each of the numerical experiment is performed with a 3 cell gap unless indicated otherwise.

6.6   Summary

This chapter reviewed the theoretical background of the Huygen's Sub-Gridding. The suitability of the scheme for GPR half-space problems was also assessed. Also, the estimated stable penetration depths for modelling antennas with a resolution of $1\,\mathrm{mm}$ were suggested from the available data. In the next chapter, the implementation of the Huygen's Sub-Gridding is described in detail and numerical examples are given.

Chapter 7

gprMax Implementation

7.1   Introduction

A wider aim of HSG implementation is to produce a generic sub-gridding code and release it to the GPR community through the Python package gprMax. This chapter discusses the implementation of the HSG as an extension module to the package. It also describes optimisations that have been made to the code to make it run as fast as possible. And the reasons for releasing the code under an open-source license.

7.2   gprMax

gprMax is an open-source FDTD simulation tool designed primarily used for modelling GPR, although it can be used to model many electromagnetic phenomena. It was first developed by Giannopoulos (2005) and has since undergone many novel developments (Warren et al., 2016a).

The package has been used to perform all of the 3d forward modellings in this work. This is due to its advanced feature set. For example, the package implements a new multi-pole perfectly matched layer (MPML) formulation (Giannopoulos, 2018b), dispersive material modelling (Giannakis and Giannopoulos, 2014), tools for modelling soil distributions (Giannakis et al., 2016a), libraries of calibrated antenna models (Warren and Giannopoulos, 2011; Giannakis et al., 2019b) and a GPU solver (Warren et al., 2019).

Also, gprMax has been used by many GPR researchers to perform advanced anal-

ysis, and therefore there is a precedent for using it for sub-gridding. For example, Giannakis et al. (2019a) used the software to generate labelled data for supervised training of a deep neural network. The network was used to predict re-bar heights in concrete. gprMax was used to model complex reflection patterns in tree trunks from GPR antenna (Giannakis et al., 2019c). Klotzsche et al. (2019) modelled realistic boreholes and borehole fillings in 3d using gprMax.

Furthermore, the software is open source and therefore permits new formulations to be tested. Also, there is a great deal of existing knowledge within the research group. The supervisor of this work, Dr Antonis Giannopoulos, is the original author and author of the PML formulations, and Dr Craig Warren is a collaborator.

7.3 Implementation

Implementing the sub-gridding code as an extension module to gprMax is considerably more time consuming than producing a standalone code. However, there are still good reasons for doing so.

It is hoped that the sub-gridding code will be actively maintained and developed once it is released as a component of the gprMax package. The sub-gridding algorithms in chapter 5 have not been distributed. This is most likely because these codes are non-trivial to implement and or have not been designed to be applied generally and documentation is time-consuming to produce. This approach has resulted in codes and formulations which have not been developed further by other authors. This is problematic for two reasons. Firstly, the scope for improvement is limited. Secondly, their use and application to engineering problems in other areas are reduced.

Releasing the implementation will increase the number of tools available to GPR practitioners who wish to embed fine structures within large regions without fine discretisation requirements. Currently, the options for this are reasonably limited. For example, Meep is a widely used, powerful open source FDTD solver which implements a non-grid aligned EP (Oskooi et al., 2010). The EP only restores second-order convergence at non-grid aligned material interfaces. It does not reduce numerical dispersion in regions of high-dielectric strength. Therefore, gprMax will add to the existing toolset, a mesh refinement capability for generic objects and the ability to correctly model region of high dielectric strength.

Another advantage is that practitioners and modellers using the sub-gridding capability will also have access to the gprMax's existing modelling features. Users will

be able to include models of antennas within sub-gridded regions without requiring technical knowledge of the underlying algorithms. This increases the number of use cases greatly.

7.3.1 Architecture

gprMax is written in Python. Therefore the implementation has also been written in Python. Python modules have been created for each of the core components of the algorithm. Each module contains reusable classes that have been programmed in an Object-Orientated Programming (OOP) style. Each object has an interface which can contain any implementation. This enables polymorphism whereby different implementations can be easily substituted for each other. For instance, a GPU sub-gridding solver could be added to the package only by changing the underlying implementation of a few classes. Also, it is trivial to add multiple sub-grids to a given simulation using the OOP style.

There are four primary modules to the sub-gridding implementation.

- `subgrid3d.py`

- `precursor_nodes.py`

- `solver.py`

- `fields_updates.pyx`

`subgrid3d.py` handles the creation of the sub-grid and the radiation of fields into the sub-grid and main grid. The main grid updates are decoupled from the main grid class to encourage separation of concerns. Next `precursor_nodes.py` handles the updates of the precursor nodes and their spatial and temporal interpolation. `solver.py` is a generic solver which updates all sub-grids. It is called by the general FDTD solver. `fields_updates.pyx` contains the optimised functions which handle core updates to the main grid and sub-grid data structures.

7.3.2 Optimising Performance

In comparison to typed languages, C and C++, Python is relatively slow and memory intensive. The dynamic nature of Python results in a substantial overhead due to type-checking and also memory management, particularly when utilising language constructs

such as for-loops and iterators over large data structures. This is an issue in sub-gridding algorithms as repeated iteration over the IS and OS surfaces are required. These issues have been addressed in the main grid update functions and geometry building functions in gprMax. Slow parts of the Python implementation have been replaced with Numpy matrix operations and bespoke Cython modules.

Numpy is a Python library which provides a multi-dimensional array object and vectorised routines for performing common array manipulations such as slicing, indexing and sorting. The library also contains a range of scientific tools such as interpolation algorithms which are useful for implementing the HSG. The increase in computational speed derives from pre-compiled C code which Numpy executes at run-time. The binaries allow Numpy to execute array operations at near C speed (The SciPy community, 2019; van der Walt et al., 2011). Whilst speed improvements could be achieved by writing C extensions, Numpy is a Python library therefore the complexity of coding in C is avoided. Additionally, the libraries are well optimised and packaged with Intel Math Kernel Library (MKL) or openBLAS.

Cython has been used to increase the performance of sub-gridding routines which cannot be easily vectorised using Numpy (Behnel et al., 2011b). Cython is a static optimising compiler. It can be used to compile pure Python code or Cython language code to C code which is then compiled into machine code. The resulting Python extension can then be called directly from Python.

The Cython language is a superset of Python. Therefore any Python can be used within Cython modules and compiled to C code. However, the best performance gains are achieved by taking advantage of the Cython language. In Cython type declarations can be given to variables. This significantly increases the performance of the resulting code. In addition to types, Cython provides access to multi-threading via OpenMP. The HSG routines which update the main grid and sub-grid have been optimised using OpenMP. The Cython sub-routines are given in Appendix B.

7.3.3 Extension Modules

The `precursor_nodes.py` module implements the precursor nodes that result from the interpolation of the fields at the IS. Each surface of the IS contains four field components. These are the parallel components of the electric and magnetic field to the surface. The precursor nodes are stored in memory as 2d 64-bit Numpy arrays. Each precursor field is stored at the current main grid time-step and at the previous main grid time-step. The time-interpolated fields are calculated using a linear interpolation

during the time stepping.

Upon instantiating of the `PrecursorNode` object the Numpy arrays are pre-allocated according to the size of the sub-grid. During Step 1 of the time-stepping, the main grid is sliced at the IS surface locations and the surfaces are allocated to the 2d arrays. The surfaces are then spatially interpolated to correct projection onto the sub-grid.

`subgrid3d.py` is essentially a wrapper module for the `fields_updates.pyx` module. `fields_updates.pyx` contains 3 Cython routines `update_electric_os`, `update_magnetic_os` and `update_is`. Each of these routines updates the field components at the surface of the Huygen's surfaces. The updates take place within a 2d loop. These loops have been parallelised for multi-processor shared memory machines using Cython built-in method `cython.parallel.prange`. This markup instructs Cython to create multiple threads and to distribute the loop amongst the pool using OpenMPI.

7.3.4 Dispersive Materials Traversing the IS and OS

The traversal of dispersive materials across the OS is directly supported by the HSG (Costen and Bérenger, 2010a; Abalenkovs et al., 2012). This is because the equivalence theorem is valid within any media (Costen and Bérenger, 2010a). However, at the IS material traversal is supported only when the displacement field is calculated. Each of the preceding Huygen's sub-gridding implementations has used the auxiliary differential equation (ADE) method to implement dispersive materials. In practice, gprMax implements dispersive materials using a novel Piecewise-Linear-Recursive-Convolution (PLRC) method (Giannakis and Giannopoulos, 2014). The formulation offers increase performance to the formulation proposed by Kelley and Luebbers (1996). The approach uses an analytic time derivative of the polarisation current as opposed to a finite-difference approximation. As the HSG has been developed within gprMax a derivation of the IS update for the E_x field specific to the novel PLRC is given. The remaining field components follow the same logic.

First, consider the Ampere-Maxwell law for the displacement field $\vec{D}$.

$$\frac{\partial \vec{D}}{\partial t} = \nabla \times \vec{H} + \vec{J} \tag{7.1}$$

In general, the $\vec{D}$ can be written in terms of $\vec{E}$ and the polarisation, $\vec{P}$. The

polarisation vector is a measure of the macroscopic shift of the bound charge within the material under the influence of an electric field.

$$\vec{D} = \epsilon_0 \vec{E} + \vec{P} \tag{7.2}$$

Substituting equation 7.2 into equation 7.1 the Ampere-Maxwell law is written in terms of the polarisation current density given by

$$\nabla \times \vec{H} = \epsilon_0 \epsilon_\infty \frac{\partial \vec{E}}{\partial t} + \epsilon_0 \sum_{s=1}^{n} \frac{\partial \vec{P}_s(t)}{\partial t} + \vec{J} \tag{7.3}$$

Where the sum over s describes the effect of multiple polarisation currents within the material. We are free to do this since every $\frac{\partial \vec{P}}{\partial t}$ term is formally another current density $\vec{J}_p$.

For linear, isotropic materials the polarisation $\vec{P}(t)$ is given by

$$\vec{P}_s(t) = \epsilon_0 \chi_s(t) * \vec{E} \tag{7.4}$$

where $\chi_e(t)$ is the electric susceptibility and ϵ_∞ is the relative permittivity at a high-frequency where the susceptibility vanishes. The convolution in the time domain is equivalent to a multiplication of a complex frequency-dependent susceptibility function and the electric field phasor in the frequency domain. In this way, the material is frequency-dependent.

In this work, dispersive soils are modelled using Debye media. The susceptibility of a Debye medium is modelled by the following function

$$\chi_s(t) = \frac{\epsilon_s}{\tau_s} e^{-\frac{t}{\tau_s}} = W_s e^{Q_s t} \tag{7.5}$$

where τ_s is the relaxation time and $\epsilon_s = \epsilon_{dc} - \epsilon_\infty$ where ϵ_{dc} is the dc relative permittivity

Equation 7.3 is discretised following the procedure by Giannakis and Giannopoulos (2014). The resulting finite-difference equation for the E_x field in a Debye material is given by

$$
\begin{aligned}
E_{x_b}\Big|_{i+\frac{1}{2},j,k}^{ns+1} &= \frac{CB}{CA}E_{x_b}\Big|_{i+\frac{1}{2},j,k}^{ns} - \frac{1}{CA}\phi\Big|_{i+\frac{1}{2},j,k}^{ns} \\
&+ \frac{1}{CA\Delta l}\left(\left\{H_{z_b}\Big|_{i+\frac{1}{2},j+\frac{1}{2},k}^{ns+\frac{1}{2}} - H_{z_b}\Big|_{i+\frac{1}{2},j-\frac{1}{2},k}^{ns+\frac{1}{2}}\right\} - \left\{H_{y_b}\Big|_{i+\frac{1}{2},j,k+\frac{1}{2}}^{ns+\frac{1}{2}} - H_{y_b}\Big|_{i+\frac{1}{2},j,k}^{ns+\frac{1}{2}}\right\}\right) \\
&\qquad\qquad - \frac{1}{CA}J_{x_b}\Big|_{i+\frac{1}{2},j,k}^{ns+\frac{1}{2}} \quad (7.6)
\end{aligned}
$$

where

$$
\phi\Big|_{i+\frac{1}{2},j,k}^{ns} = \epsilon_0 \sum_{s=1}^{n} Q_s e^{\frac{\Delta t}{2}} P\Big|_{i+\frac{1}{2},j,k}^{ns} \tag{7.7}
$$

$$
CA = \frac{\epsilon_0 \epsilon_\infty}{\Delta t} + \frac{\epsilon_0}{\Delta t}\sum_{s=1}^{n} L_s + \frac{\sigma}{2} \tag{7.8}
$$

$$
CB = \frac{\epsilon_0 \epsilon_\infty}{\Delta t} + \frac{\epsilon_0}{\Delta t}\sum_{s=1}^{n} K_s - \frac{\sigma}{2} \tag{7.9}
$$

and

$$
L_s = \frac{W_s}{Q_s}\left(e^{Q_s \frac{\Delta t}{2}} - 1\right) \tag{7.10}
$$

$$
K_s = \frac{W_s}{Q_s}\left(1 - e^{Q_s \frac{\Delta t}{2}}\right) + \Delta t W_s e^{Q_s \frac{\Delta t}{2}} \tag{7.11}
$$

The surface current depends only on the magnetic field, therefore, its value is unchanged from the Electric field HSG value

$$
J_{sx_b} = H_{z_a}\Big|_{i+\frac{1}{2},j_{is}-\frac{1}{2},k}^{ns+\frac{1}{2}} \tag{7.12}
$$

Dividing equation 7.12 by the Δl to obtain the volumetric current density and substituting the result in to equation 7.6 gives the update equation at the IS for the E_x field in the sub-grid.

$$
\begin{aligned}
E_{x_b}\Big|_{i+\frac{1}{2},j,k}^{ns+1} = {} & \frac{CB}{CA} E_{x_b}\Big|_{i+\frac{1}{2},j,k}^{ns} - \frac{1}{CA}\phi\Big|_{i+\frac{1}{2},j,k}^{ns} \\
& + \frac{1}{CA\Delta l}\left(\left\{ H_{z_b}\Big|_{i+\frac{1}{2},j+\frac{1}{2},k}^{ns+\frac{1}{2}} - H_{z_b}\Big|_{i+\frac{1}{2},j-\frac{1}{2},k}^{ns+\frac{1}{2}} \right\} - \left\{ H_{y_b}\Big|_{i+\frac{1}{2},j,k+\frac{1}{2}}^{ns+\frac{1}{2}} - H_{y_b}\Big|_{i+\frac{1}{2},j,k}^{ns+\frac{1}{2}} \right\} \right) \\
& \hspace{6cm} - \frac{1}{CA\Delta l} H_{z_a}\Big|_{i+\frac{1}{2},j_{is}-\frac{1}{2},k}^{ns+\frac{1}{2}} \quad (7.13)
\end{aligned}
$$

The equations for the magnetic update are unchanged from the non-dispersive case. This is because the magnetic field depends only on the electric field.

7.4 Summary

The HSG algorithm has been implemented as an extension module to the open-source Python package gprMax. This implementation increases the number of use cases of the algorithm as it extends its use out to GPR practitioners without knowledge of the underlying algorithm. Additionally, is it hoped the algorithm can be advanced by members of the open-source community. The implementation contains Cython and OpenMP optimisations that speed up the implementation considerably. Another advantage of this implementation is that numerous sub-grids can be easily included in the model and that materials within the sub-grid are automatically positioned from their global position data.

Chapter 8

Application of the Huygens Sub-Gridding to the GPR Half-Space Problem

Chapter 6 reviewed the theoretical basis of the HSG. Specific aspects of the HSG such as material traversal, the sub-gridding ratio and accuracy of antenna modelling were discussed concerning sub-gridding GPR antennas in half-space problems. This chapter explains the HSG implementation used in this work. Numerical examples are given which demonstrate the accuracy and efficiency of the HSG as an approach to modelling commercial GPR antennas.

8.1   Preliminary Numerical Experiments

One of the primary advantages of the HSG is that any odd integer sub-gridding ratios can be used without spurious reflections even when the numerical dispersion in each grid is significantly different. Although qualitative comparisons of accuracy resulting from various sub-gridding ratios have been made in the literature, a quantitative comparison with an analytical result has not been made. The following numerical examples motivate the idea that the HSG can be used with any sub-gridding ratio.

8.1.1 Sub-gridded Hertzian dipole

The first numerical experiment tests the modelling accuracy of sub-gridding a Hertzian dipole at a range of sub-gridding ratios. The sub-grid is placed at the centre of the domain. The Hertzian dipole source is placed at the centre of the sub-grid. The experiment is repeated for all sub-gridding ratios, r, between 1-17. Higher ratios could not be tested due to the available memory of the computer. The coarse solution in which the dipole is modelled at the main grid resolution is also plotted. For comparison, the analytic solution is also given.

The extent of computation domain is $(76\Delta l \times 76\Delta l \times 76\Delta l)$. The sub-grid comprises 14 main grid cells and is positioned at $(31\Delta l \times 31\Delta l \times 31\Delta l)$, $(45\Delta l \times 45\Delta l \times 45\Delta l)$ with $\Delta l = 1\,\text{cm}$. The dipole is excited with a first derivative Gaussian waveform with a centre frequency $428\,\text{MHz}$. This corresponds to $N_\lambda = 21$ at a $-40\,\text{dB}$ drop in power. The domain is truncated with a 10 cell PML. The receiver is placed 15 cells from the right hand side PML. To help mitigate the instability the sub-grid domain is truncated with a 6 cell PML (Bérenger, 2006). The distance between the sub-grid PML and the OS is $r/2 + 2$. Figure 8.1 shows a diagram of the arrangement.

Figure 8.2 shows the E_y signal at the receiver for each sub-gridding. The convergence of the results shows clearly that the sub-gridding ratios produce very similar results. Also, no spurious reflection is observed in the main grid. This strongly suggests that increasing the sub-gridding ratio does not increase the reflection from the sub-grid interface for outgoing waves.

The largest error in the simulated E_y field occurs at the first peak shown in Figure 8.3. The relative error between the coarse grid solution and the analytical result is approximately 1%. The sub-gridded solutions converge to the coarse grid solution as the ratio increases. This suggests that decimation of the fields at the OS is improved by increasing the sub-gridding ratio.

8.1.2 Sub-Gridded Free-space

This experiment is designed to test the accuracy of the Huygen's sub-gridding for a wavelet which propagates across the IS and OS. A similar result to the previous example is obtained when the IS is switched off. This is because the outgoing wave passes only through the OS. In this experiment, the wave must traverse both Huygen's surfaces therefore a more general measure of the accuracy is provided.
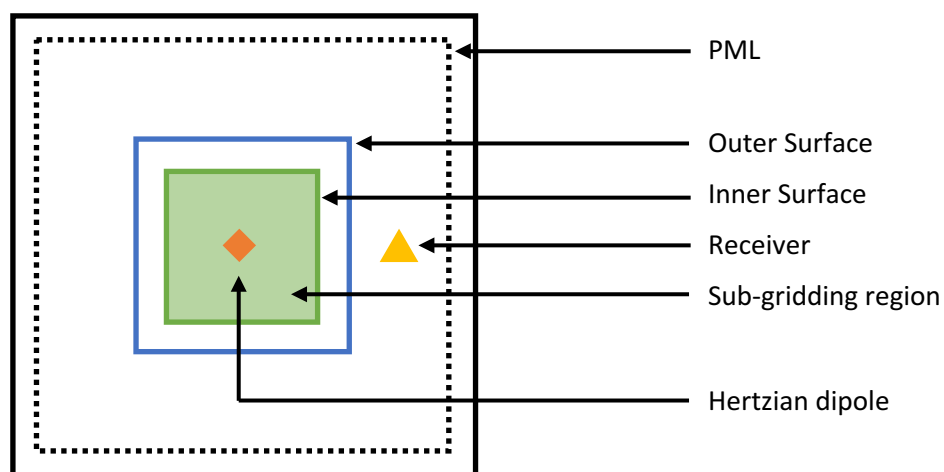
Figure 8.1: Diagram of the free-space ratio test showing the position of the sub-grid and the source and receiver.
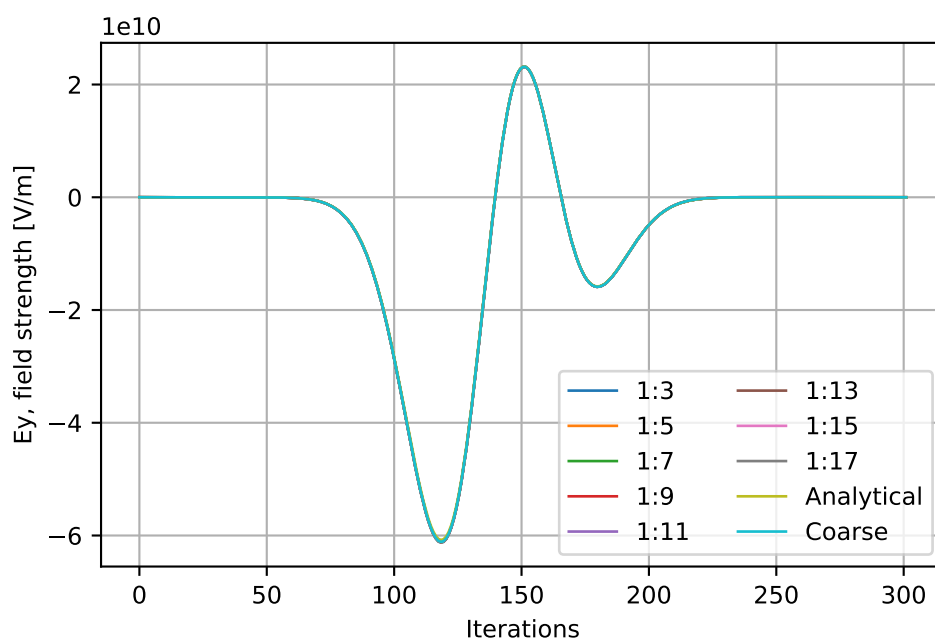
Figure 8.2: E_y field at the receiver point for the free-space hertzian dipole.
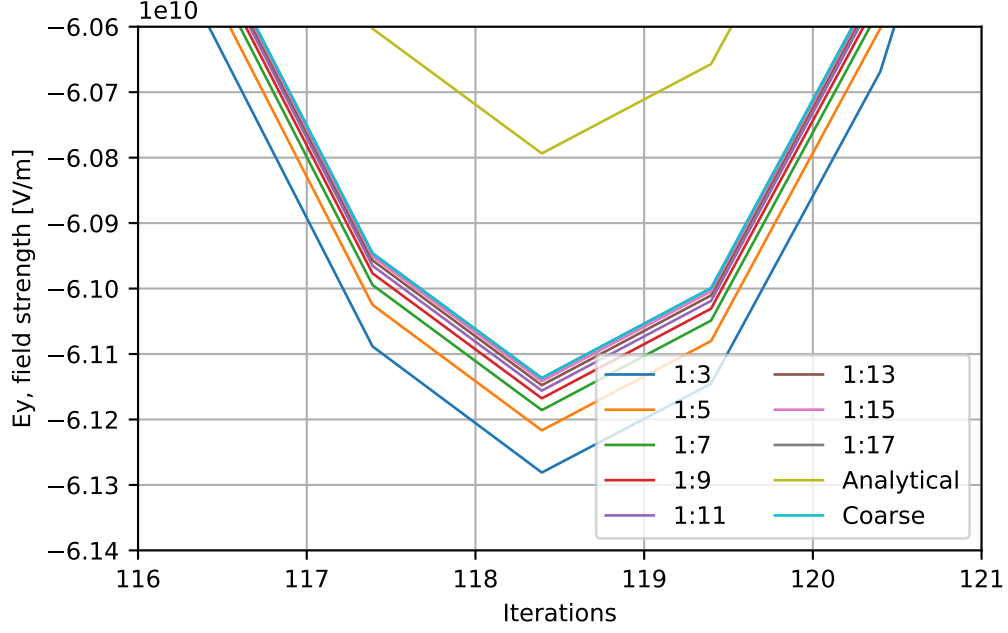
Figure 8.3: Comparison of an analytical Hertzian dipole solution with HSG sub-gridding for ratios 3-17.

Previous sub-griddings have dealt with fields which are far from the antenna or were planar fields introduced by TF/SF boundaries (Wei et al., 2017; Bérenger, 2011). These scenarios place a lower demand on the sub-gridding algorithm than if the antenna were close to the sub-grid. This is because the field is more uniform and hence easier to interpolate. Additionally, the spurious effects of anisotropic numerical dispersion in the grid are reduced because the wavefront has a lower curvature at the sub-gridding boundary.

In this experiment, the dipole is positioned very close to the sub-gridding boundary. This ensures that the field is highly non-uniform and more representative of the field distribution surrounding a real GPR antenna.

The model is identical to the sub-gridded Hertzian dipole. With the exception that the Hertzian dipole is positioned three cells from the left-facing OS and the receiver is placed three cells out from the right-facing OS. In this configuration, the travelling wave must cross both the IS and OS surface on each face of the sub-grid. The arrangement of the source, receivers and sub-grid is shown in Figure 8.4.

Figure 8.5 shows the E_y field at the receiver for a range of sub-gridding ratios. The results are in good agreement with the analytical solution and no-spurious reflections are directly observed. Three conclusions can be made.
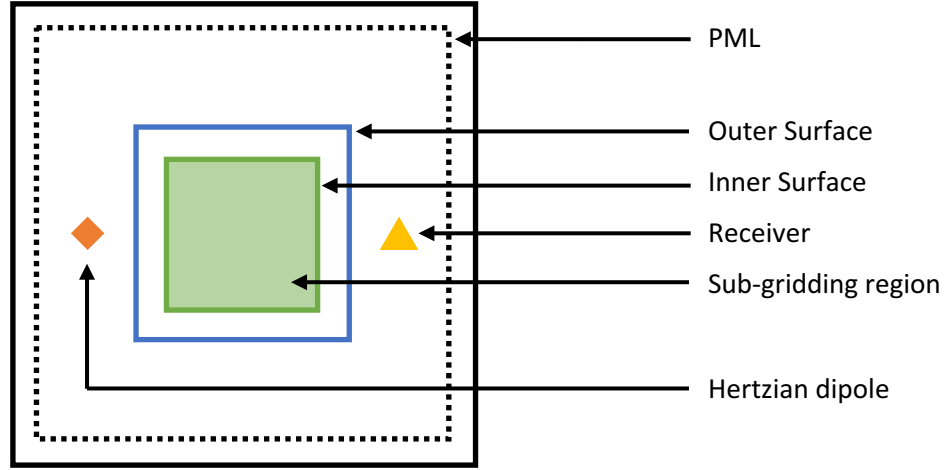
Figure 8.4: Model setup for the free-space sub-gridding.

- First the cancellation of the fields at the IS and OS is accurate for the range of significant frequencies in the pulse.

- Secondly, higher sub-gridding ratios do not introduce significant reflections.

- Thirdly, the HSG produces accurate results even when the fields are non-uniform and close to the Huygens surfaces.

Figure 8.6 shows the received pulse over the period 200-400 iterations. The scale has been adjusted to view the pulse error more clearly.

Clearly, the pulses converge. However, a spurious wave is observed when the sub-gridding ratio is equal to five. These spurious waves are also present in the other signals. However, they are of similar and lower magnitude. Although the error is large in comparison to the other sub-griddings the relative error is still low approximately 2/1000.

The experiment is repeated without the PML in the sub-grid non-working regions to assess whether the PML affects the magnitude of the spurious wave. The E_y fields for sub-gridding ratio 3, 5 and 7 are plotted in Figure 8.7. The results now show that the wave is present. Additionally, the magnitude of the wave increases as the sub-gridding ratio is increased.

Therefore the previous experiment demonstrates that the PML attenuates the spurious wave. However, it appears in the case of the 1:5 sub-gridding the PML attenuates the wave only slightly.
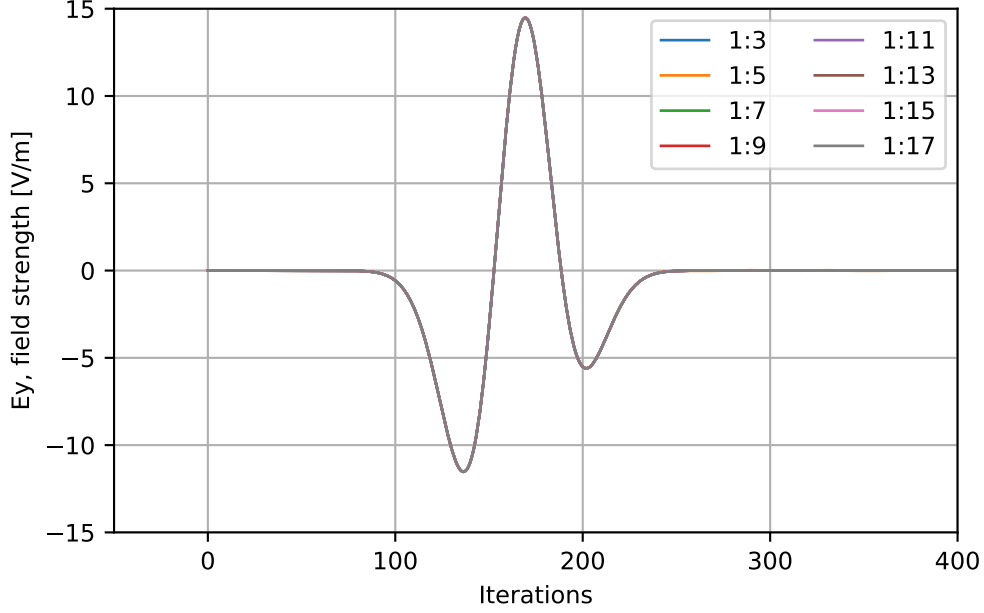
Figure 8.5: Comparison of E_y signal which passes through a region of space sub-gridded with a range of ratios of the main grid sub-grid spatial step.

The waves in Figure 8.7 are caused by leakage across the Huygen's surface. Normally, leakage is usually observed in the Total-Field Scattered-Field formulation where the continuous analytical incident field does not cancel correctly with the finite-difference solution along the TF/SF boundary. A similar effect is seen in the HSG and is described as follows.

The incident wavelet is present in the working region of both grids once it is transferred by the left IS into the sub-grid. At the right IS the main grid wavelet is flipped and summed with the sub-grid wavelet. In theory, the wavelets should cancel exactly. However, each wavelet is distorted by the grid dispersion over the propagation distance of the working region. Since the dispersion relations in the two grids are different the summation of the wavelets results in a residual field. This effect is stronger at higher frequencies as the grid dispersion vary more greatly. This is why the frequency of the leakage field observed is higher than the centre frequency of the initial pulse. This effect should converge as the sub-gridding ratio increases. This is because the fine grid dispersion relations converge below the cut-off frequency in the coarse grid.

The E_y field distributions of a slice through the sub-grid are shown for three sub-gridding ratios in Figure 8.9 and Figure 8.8 where the PML has been included and removed respectively. The central square region represents the working region of the sub-grid shown in green in Figure 8.4.
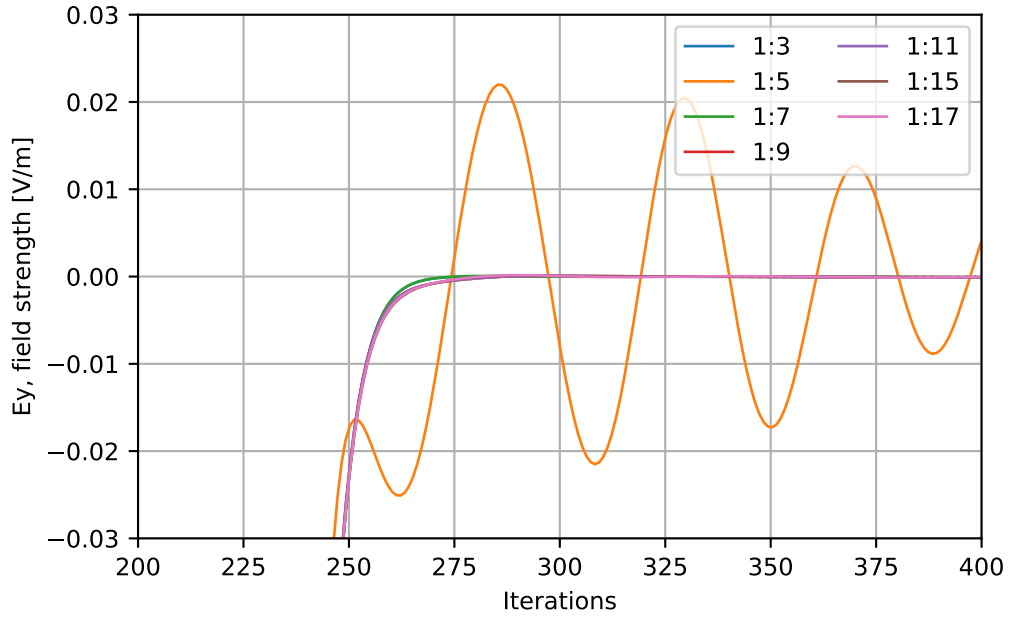
Figure 8.6: Comparison of E_y signal which passes through a region of space sub-gridded with a range of ratios of the main grid sub-grid spatial step.
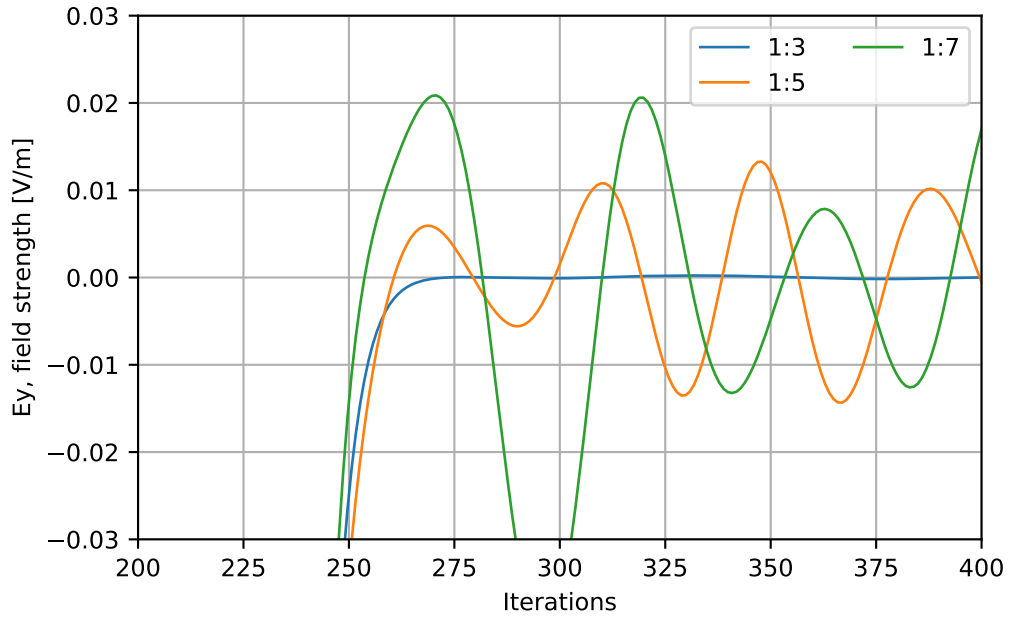
Figure 8.7: Comparison of E_y signal which passes through a region of space sub-gridded with three of ratios of the main grid sub-grid spatial step when the PML in the non-working region is switched off.

In Figure 8.8 the first row of field snapshots show the field within the range of magnitudes shown in Figure 8.5 for a sub-gridding ratio of 3. The field proceeds through the working region of the sub-grid without any significant reflection. The remaining three rows are scaled to display the errors in the fields more clearly.

The first snapshot at each ratio shows that the field to the left of IS in each sub-grid. This field is erroneous as violates the first proposition that the fields in the IS-OS regions should sum to the fields in the equivalent problem.

The leakage is most pronounced along the x-axis this is because the FDTD grid is most dispersive along the grid axes and best along the diagonals. The leakage is increased but of a similar level for the sub-gridding ratio 5 and 7. The final snapshot for sub-gridding ratio 5 shows the electric field within the working region of the sub-grid. This is not the case for the other sub-gridding ratios. Additionally, the field in the final snapshot of Figure 7 is very dispersed.

In Figure 8.9 the fields are shown with the inclusion of the PML in the non-working region. The leakage in the non-working region of the sub-grid is reduced to a similar level as the 1:3 sub-gridding in Figure 8.8. Additionally, the highly dispersed field present in Figure 8.8 has been attenuated such that the snapshots show similar smooth field distributions in the non-working regions for each sub-gridding ratio. The field in the non-working region for sub-gridding ratio 5 has not been affected by the presence of the PML.

These observations indicate that the PML can be used to regulate the leakage and thus improve the solution at higher sub-gridding ratios. Therefore it is not only required to reduce the late time instability as stated by (Bérenger, 2006).

8.1.3 Inner Surface Outer Surface Gap

In the previous section, a slow drift in the signal output from the HSG was described for cases where the gap between the IS and OS was less than or equal to 2 cells. This is problematic in terms of the computational efficiency of the sub-gridding. This is because the region between the IS and the OS is a shared region within the equivalent problem. Hence a 3 cell gap in the main grid incurs an overhead of three times the sub-gridding ratio cells in the sub-grid. For large sub-gridding ratios, this increases the number of cells in the sub-grid substantially.

Better computation performance would be obtained from a smaller gap provided that the drift in the solution is sufficiently small. Bérenger (2011) stated that a 3 cell
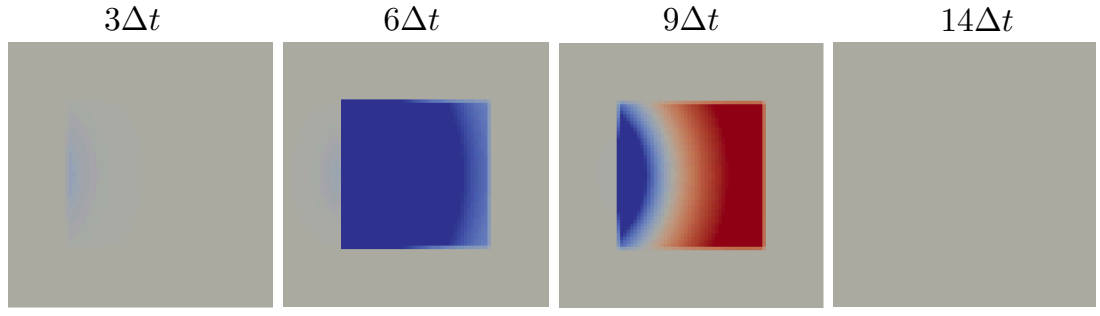
| $3\Delta t$ | $6\Delta t$ | $9\Delta t$ | $14\Delta t$ |
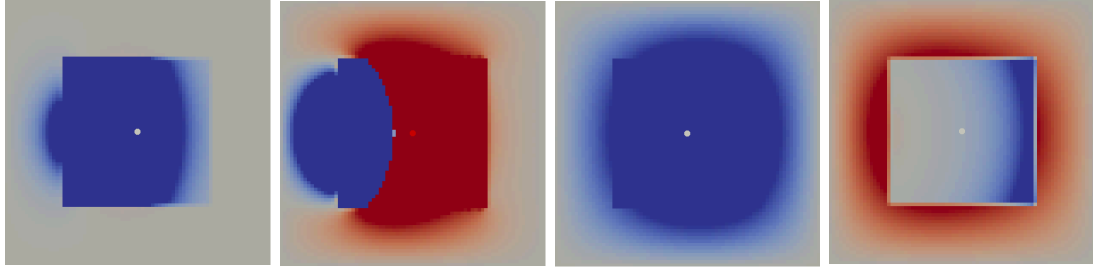
a) 1:3 without PML

b) 1:3 without PML
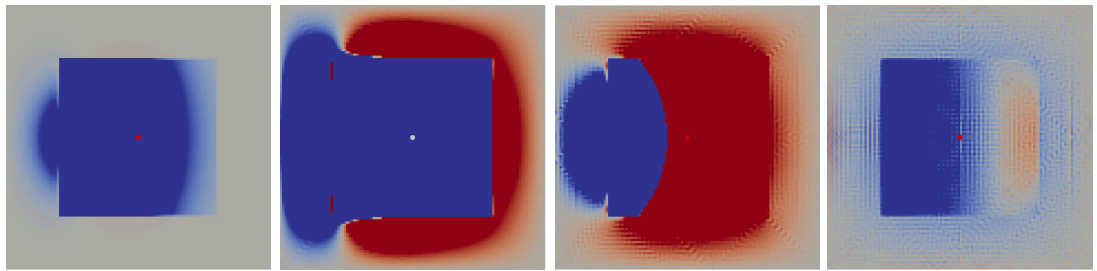
c) 1:5 without PML
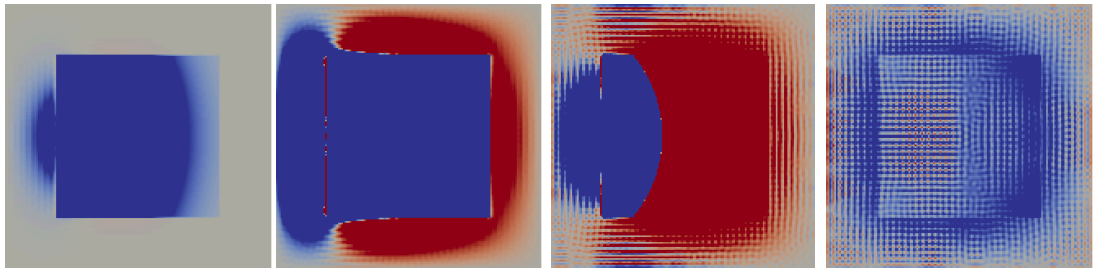
d) 1:7 without PML

Figure 8.8: E_y field in free space subgrids where the sub-gridding ratio is 1:3, 1:5, 1:7. At time steps $3\Delta t$, $6\Delta t$, $9\Delta t$, $12\Delta t$ where $\Delta t = 3.3 \times 10^{-10}\,\text{s}$
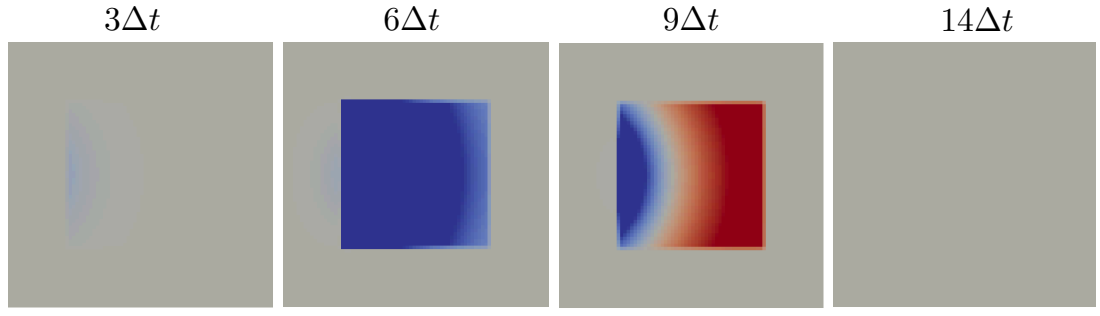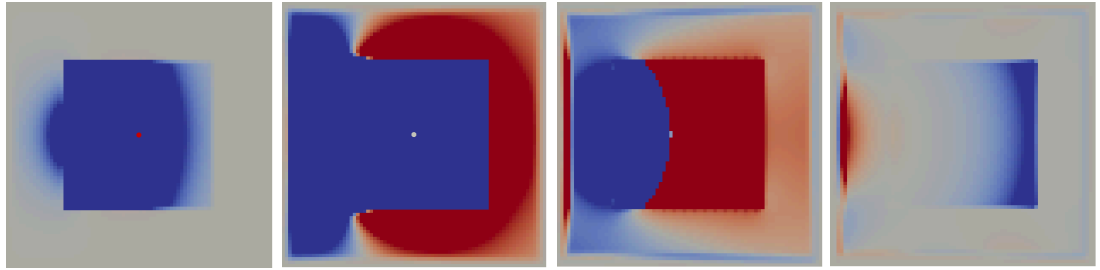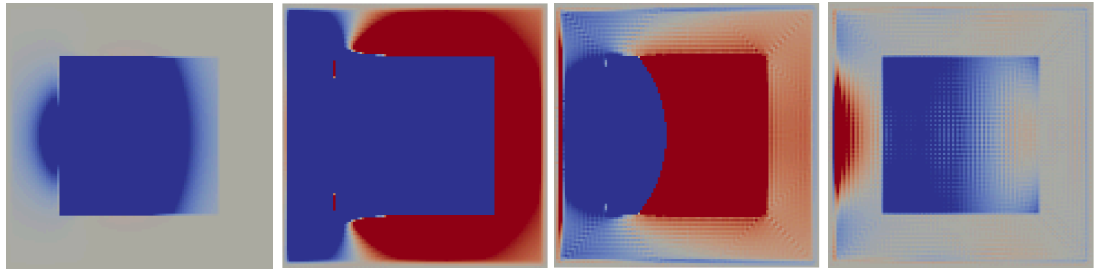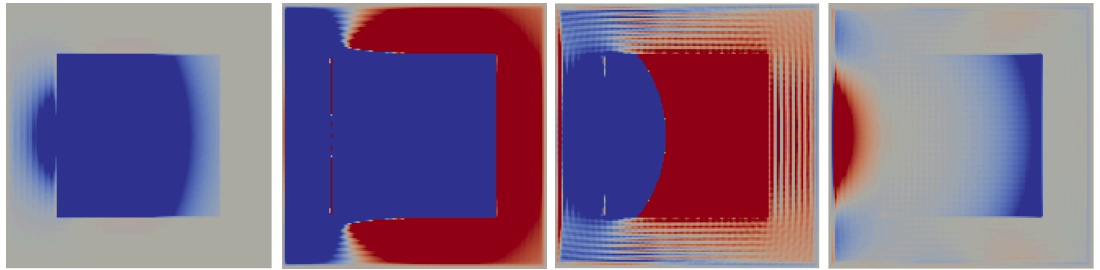
Figure 8.9: E_y field in free space subgrids where the sub-gridding ratio is 1:3, 1:5, 1:7. At time steps $3\Delta t$, $6\Delta t$, $9\Delta t$, $12\Delta t$ where $\Delta t = 3.3 \times 10^{-10}$ s

gap reduced the error in the peak amplitude of the signal to 1/400. However previous GPR sub-gridding codes produced a relative error between 1-5% (Wei et al., 2017). The peak HSG error due to drift is not significant within this range. Therefore reducing the gap may still provide an acceptably accurate result. The following experiment determines whether the solution when the gap is 2 cells is tolerable in comparison to previous results.

The main computational domain is $36 \times 36 \times 36$ cells. A sub-grid is placed with IS collocated at the main grid $(13\Delta l, 13\Delta l, 13\Delta l)$, $(23\Delta l, 23\Delta l, 23\Delta l)$. A sub-gridded ratio of 1:3 is used in sub-grid. Therefore there are 30 cells within the IS working-region. The sub-grid is truncated with a 6 cell PML as recommended by Bérenger (2011). A 3 cell gap is placed between the PML and the OS. The total number of cells in the sub-grid is $60 \times 60 \times 60$ cells. In the main grid $\Delta L = 1\,\mathrm{cm}$. A Hertzian dipole at the centre of the sub-grid is used as an excitation source. The dipole is excited by a first derivative normalised Gaussian waveform with a centre frequency $100\,\mathrm{MHz}$. $N_\lambda = 23$ in the main grid at the frequency corresponding to a $40\,\mathrm{dB}$ drop in power.

Figure 8.10 shows E_y at $(1\Delta l, 18\Delta l, 18\Delta l)$ for a solutions computed with 1, 2 and 3 cell gaps.

The 1 cell solution is unstable. The reason for this is the distance between the H nodes at the IS and the E nodes at the OS is the physical dimension of a single Yee cell. This is due to the placement of the Huygen's surface mid-way between positions of the fields within the sub-grid Yee cell. This arrangement allows energy to propagate further than a single cell in the main grid within a single time step. This is a violation of the Courant limit and subsequently leads to numerical instability. This feedback effect has been observed when the HSG is used as an absorbing boundary condition (Bérenger, 2007b).

The 2 cell solution illustrates the drift in the solution. Whereas the 3 cell gap solution does not appear to drift significantly. However, each solution is corrupted by the late-time instability. The 3 cell solution appears to be slightly more stable. This is most likely because the PML's surface area within the sub-grid is increased as the IS-OS gap increases.

Figure 8.11 shows the relative error between the solutions for the 2 cell and 3 cell gap setups. The normalising value was chosen as the absolute maximum value from the 3 cell solution between 0-5000 iterations. This corresponds to a value from the stable part of the solution. The relative error is larger the 4% after 10000 iterations. Up to 5000 iterations the solutions are in excellent agreement. This suggests that a 2 cell gap

can be used for simulations within this time-window.

8.2   GPR Numerical Experiments

A few studies have investigated sub-gridding techniques in GPR. Primarily, these studies have used these methods to sub-grid sub-surface targets whose geometry is insufficiently resolved by the spatial step required by the numerical dispersion criteria, or where regions of high dielectric strength exist whose spatial step does not adequately resolve the highest wavelength according to the numerical dispersion criteria in dielectrics.

The following set of numerical experiments are designed to compare the accuracy of the HSG with the accuracy of the techniques in the literature for typical GPR problems. Although the other schemes have not been implemented the experiments are similar such that the accuracy can be compared approximately.

It should be noted that implementation of the spatially filtered sub-gridding algorithm was obtained from the authors. However, it was not possible to replicate the results for the buried metal pipe experiment found by Wei et al. (2017). This was due to uncertainty in the positioning of the pipe. Therefore it was decided that new models of the buried metal pipe and buried plastic water pipe numerical experiments would be constructed and the results compared with the literature based on the similarity of the underlying physical processes.

In each of the experiments, a PML is used to truncate the sub-grid. A 6 cell PML is used. The number of cells between the Outer Surface and the PML is $ratio/2 + 2$. This corresponds to 4 cells for sub-gridding ratios of 5. The 3-node filter is also turned on to increase stability. In the next chapter, the effects of these stabilisation methods are assessed.

8.2.1   Hertzian Dipole Over a Sub-Gridded Buried Metal Pipe

A typical sub-gridding problem in GPR is modelling the response of a metal pipe buried in a dielectric (Wei et al., 2017; Diamanti and Giannopoulos, 2009). This numerical experiment demonstrates the accuracy of the Huygen's Sub-Gridding for this application.

A metal rod of radius 2.5 cm is buried at a depth of 50 cm in a dielectric medium
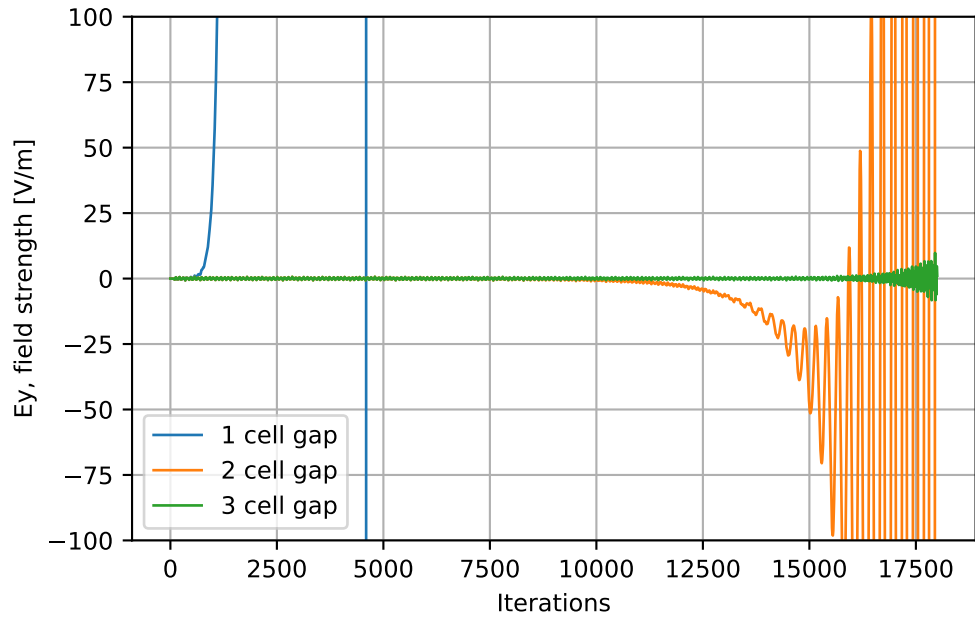
Figure 8.10: Comparison of E_y signal in a sub-gridded resonator for 1, 2 and 3 cell separation between the IS and OS
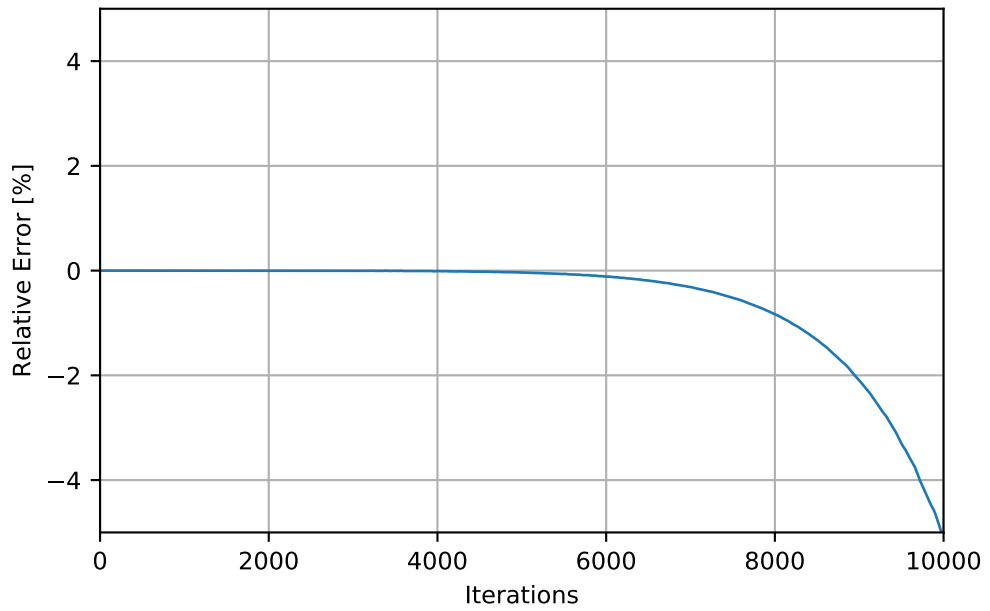
Figure 8.11: The relative error between sub-gridded resonator solutions a 2 cell gaps between the IS and OS

$\epsilon_r = 4$. A Hertzian dipole source is used as an approximate excitation source to a real GPR antenna. The dipole is positioned 5 cm above the half space. This is close to the distance of maximum directivity proposed by Smith (1984b). The dipole is excited with a normalised Gaussian derivative pulse with a centre frequency of 300 MHz. Figure 8.12 shows the shape of the pulse and Figure 8.13 shows its frequency content. The highest frequency of interest is approximately 1 GHz. This corresponds to $N_\lambda = 15$ within the dielectric material. The dielectric material interface is averaged arithmetically. The sub-grid dimensions are $9\Delta l \times 9\Delta l \times 9\Delta l$. The sub-gridding ratio is 5. This ratio is also used in Wei et al. (2017). The positions of the dielectric and PEC materials in the finite-difference grid around the sub-gridded region is shown in Figure 8.14. The diagram shows that the rod is better resolved in x, z directions than the equivalent coarse grid meshing.

The response from the coarse meshing suffers from the stair-casing of the fields about the rod. This is due to the slowing of the wave which travels about rod in the transverse direction (Cangellaris and Wright, 1991). The velocity of the wave converges to the continuous space velocity as the spatial step is reduced. Therefore the resonance of the rod should be observed more accurately when it is positioned within the sub-grid.
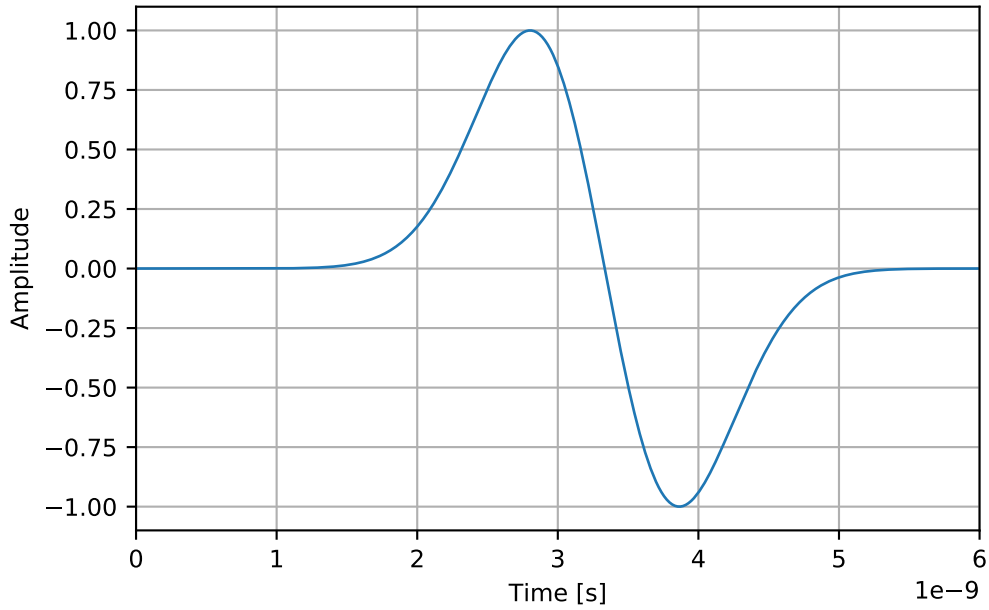
Figure 8.12: 300 MHz normalised Gaussian waveform

Figure 8.15 shows the E_y signal which is received at a point 10 cm in the x direction of the dipole. The solution to the fine grid problem is also shown. The agreement between the sub-gridded solution and the fine grid solution is very good. No spurious

143
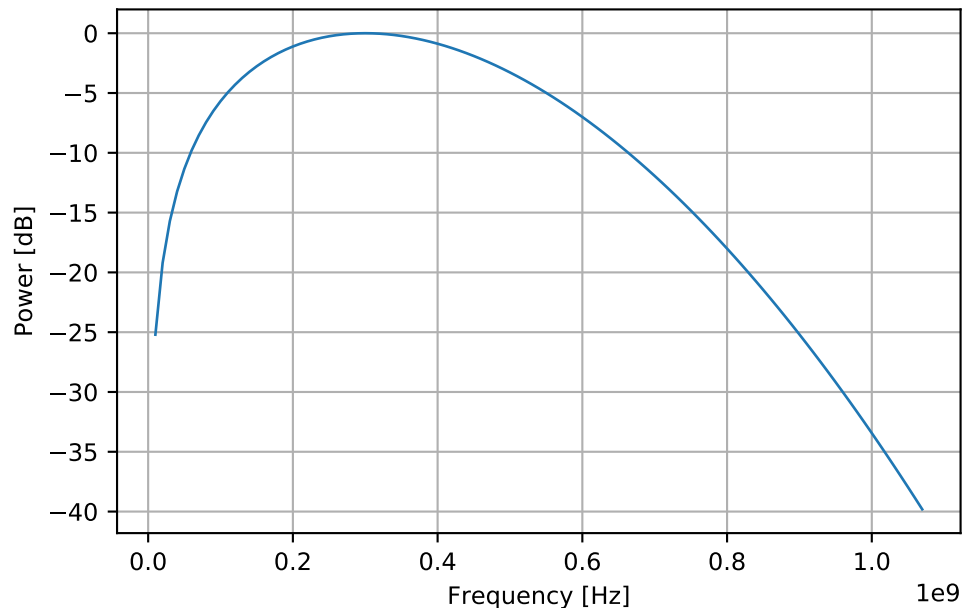
Figure 8.13: 300 MHz normalised Gaussian waveform FFT frequencies of interest
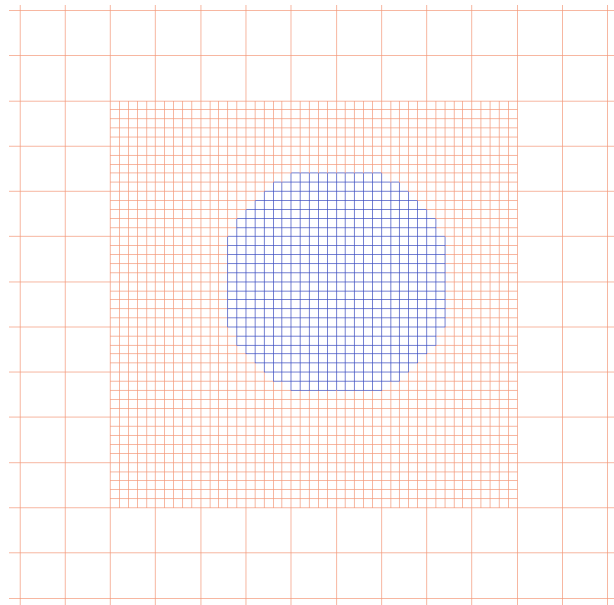
Figure 8.14: Zoomed fine grid view of the buried metal pipe within a 1:5 Huygens sub-grid.

reflection from the sub-grid is observed. Also, there are no significant phase differences between the solutions. Additionally, the magnitudes are also in very good agreement.

A measure of the relative error introduced by the sub-gridding is given in Figure 8.16. The error associated with the reflection from the pipe is approximately 0.5%. This is a large improvement from the 5% error introduced by the spatially filtered scheme. A smaller increase in accuracy is achieved in comparison with the 1.5% error introduced by Xiao et al. (2007).
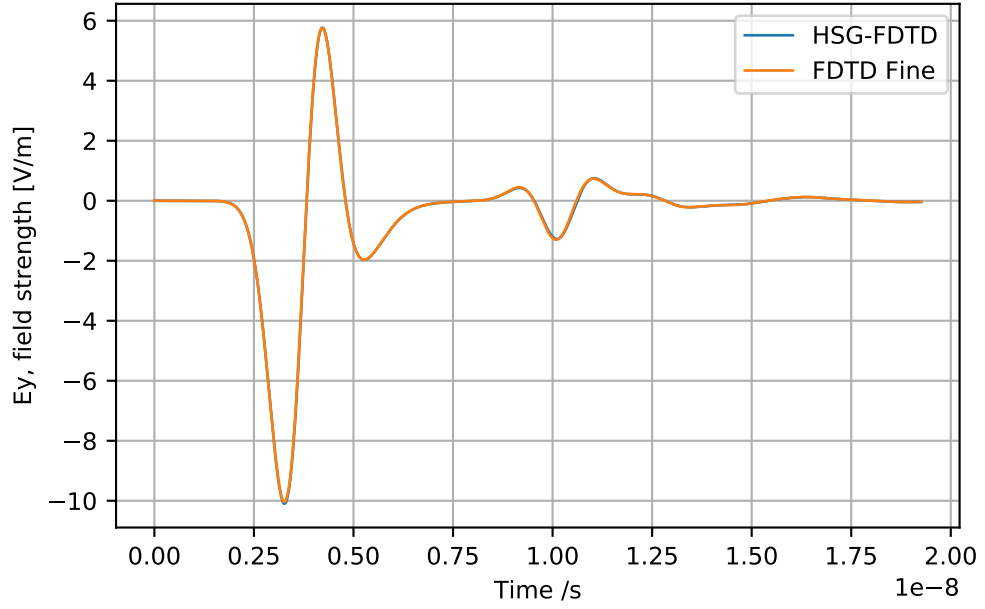
Figure 8.15: E_y response from the buried metal pipe in $\epsilon_r = 4$ subgridded using a 1:5 Huygen's sub-grid in comparison with a 1:5 fine-grid solution

Statistics on the run-time and memory allocation for the sub-gridding and the fine grid solution are given in Table 8.1. The results show that the HSG run time is 17 times faster than the fine grid solution. Also, the reduction in memory is 28 times. The speed-up factor is less than memory improvement due to extra overhead in updating and interpolation the fields at the interface. Nevertheless, the HSG improves on the computation time significantly.

Model	Solve time [s]	Speed up factor	Memory [GB]	Memory reduction
FDTD Reference	178.3	1	14.7	1
HSG-FDTD	10.8	17	0.529	28

Table 8.1: Simulation statistics for the sub-gridding of the buried metal pipe.
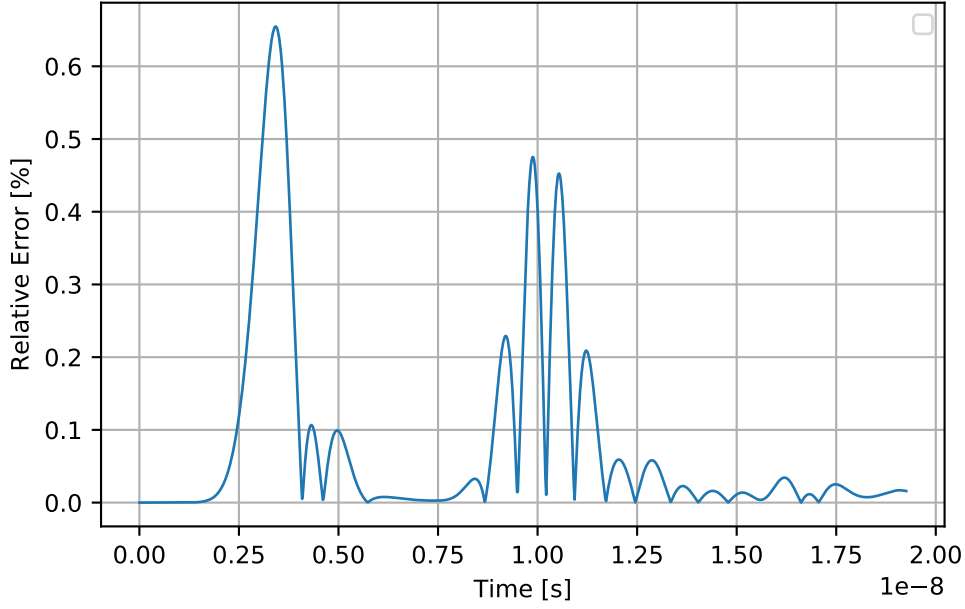
Figure 8.16: Relative error on the E_y measurement from the buried metal pipe in in $\epsilon_r = 4$ sub-gridded using a 1:5 Huygen's sub-grid

8.2.2 Buried Metal Pipe over half-space with large permittivity

The buried pipe experiment is repeated with the inclusion of a higher dielectric constant of $\epsilon_r = 11$ for the half-space material. This dielectric constant is representative of wet clay, sand or loamy soil. Since the permittivity has increased the pulse within the dielectric is excessively dispersed when the centre frequency is 300 MHz. Therefore the centre frequency of the pulse is reduced to 180 MHz. This corresponds to $N_\lambda = 14$ for the highest frequency of interest within the dielectric.

Figure 8.17 shows E_y at the receiver for the sub-gridding and the reference solution. The most significant difference between the solutions $\epsilon_r = 4$ and the $\epsilon_r = 11$ is the variation in the direct wave. The direct wave in the latter case is reduced. This is due to the increased directivity resulting from the higher permittivity of the half-space which causes the incident field to bend toward the surface normal. The reflection from the pipe, however, appears very similar.

The relative error is shown in Figure 8.18. The relative error at a time position corresponding to the reflection from the pipe is in good agreement with the experiment containing the dielectric $\epsilon_r = 4$. This indicates the sub-gridding is not affected by the change in dielectric strength. This is expected as the spatial resolution of the field at the sub-grid is near equal to the previous experiment. The peak relative error in the

146

direct wave is 1%. This is an increase of 67%. The increase is not a direct result of the sub-gridding as it occurs before the travelling wave has reached the sub-grid. It is a result of the larger spatial step used to discretise the half-space interface. The problem can be resolved by sub-gridding the interface.

8.2.3   Buried Water Pipe

In this experiment a buried water-pipe is sub-gridded. The purpose of the experiment is to show how sub-gridding reduces the global requirement for small spatial steps when there are local regions of high electric permittivity.

Water has a very high relative permittivity of approximately $\epsilon_r = 81$ over the GPR bandwidth. This introduces the requirement that the spatial step must be reduced by 9 times relative to the free-space spatial step. This implies the sub-gridding ratio can be set to 9. However, the geometry of the water object must also be well represented. This tends to reduce the actual sub-gridding ratio that can be used. This experiment was first carried out in 2d by Diamanti (2008). It was shown that the coarse grid solution introduced significant dispersion to the pulse and was resolved using sub-gridding.

In this experiment a 30 cm water pipe is buried within a dielectric medium with a relative permittivity $\epsilon_r = 4$. The geometry and positions of the water pipe and the half-space are equal to the those in the buried metal pipe experiment. The ratio of the spatial steps is 5. The pulse is a normalised Gaussian derivative with a centre frequency of 300 MHz. At the highest significant frequency, this results in $N_\lambda = 16$ within the sub-gridded water pipe. When the water pipe is resolved by the coarse grid spatial step $N_\lambda = 3$. At this resolution, the pulse is highly dispersed and thus the solution is inaccurate.

Figure 8.19 shows a comparison of E_y signals at the receiver for the reflection from the water pipe. The first signal is from the sub-gridding experiment. The second and third signals are from solutions discretised entirely with the coarse spatial step and the fine spatial step respectively. Each signal appears to be dispersed by the water pipe. The ringing actually corresponds to the field resonating within the water pipe as it is bounded by the half-space material. From the figure, the period of the oscillation in the fine grid is 3 ns. This corresponds to a half wavelength of 0.05 m within the dielectric which is the diameter of the pipe. The oscillation, therefore, corresponds to the first harmonic within the water pipe.

The figure also shows there are significant phase and magnitude differences between
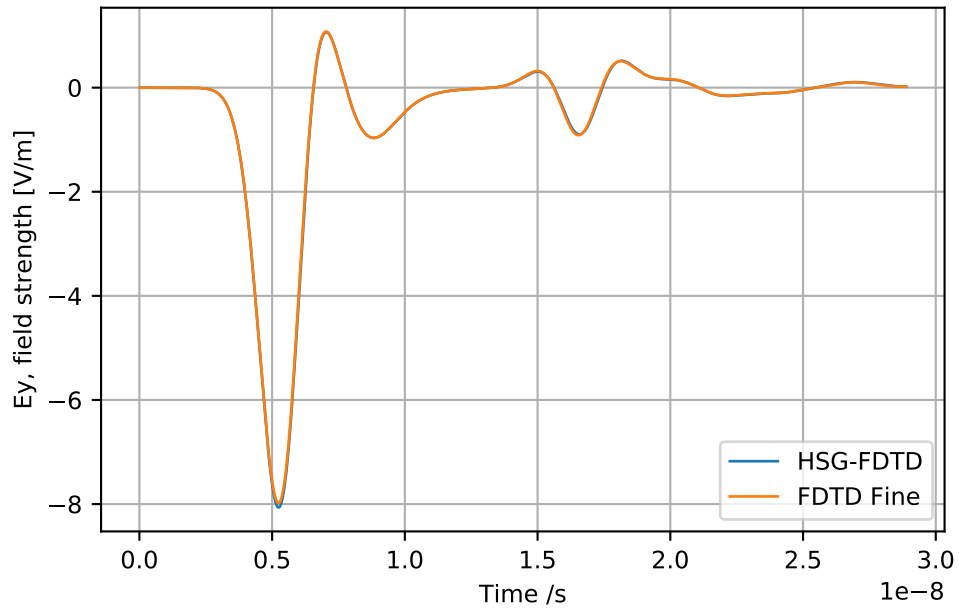
Figure 8.17: E_y response from the buried metal pipe sub-gridded using a 1:5 Huygen's sub-grid in comparison with a 1:5 fine-grid solution $\epsilon_r = 11$
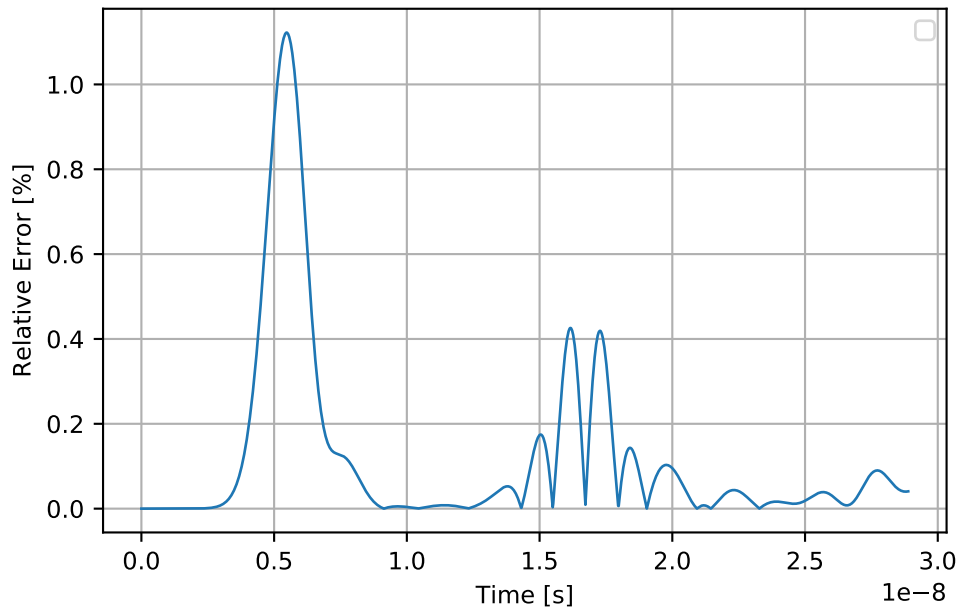
Figure 8.18: Relative error on the E_y measurement from the buried metal pipe sub-gridded using a 1:5 Huygen's sub-grid $\epsilon_r = 11$

the coarse grid and fine grid solutions. This illustrates the numerical dispersion in the coarse grid resulting from the extremely low spatial sampling of the field within the water region. The figure also shows that there is a very good agreement between the sub-gridded solution and the fine grid solution.

Figure 8.20 shows the relative error between the sub-gridded solution and the fine grid solution. The peak error in the signal reflected from the water pipe is approximately 0.25%. Unfortunately, no relative error measurements were given by Wei et al. (2017); Diamanti (2008). Therefore a direct comparison cannot be made.
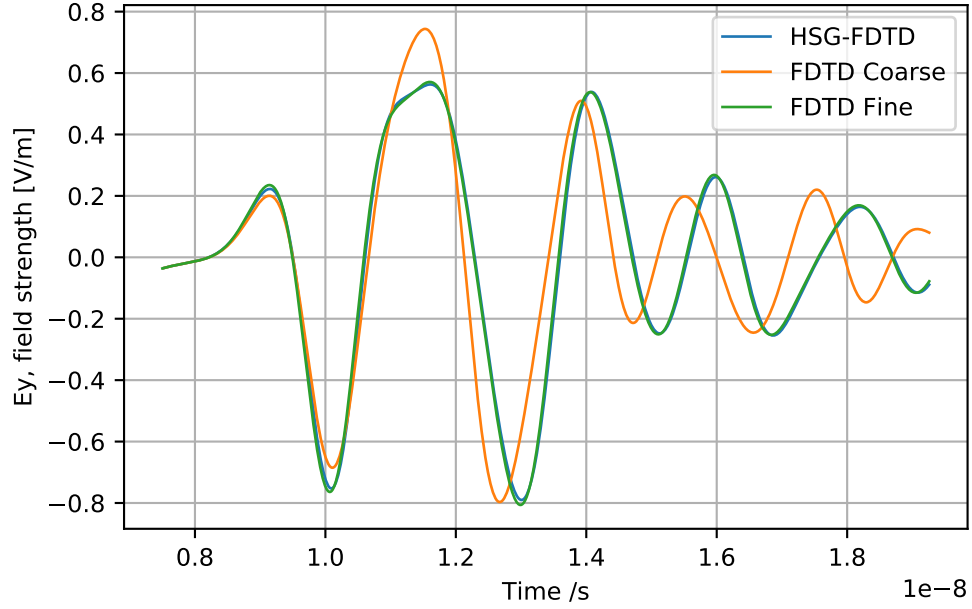
Figure 8.19: E_y reflection from the buried water pipe sub-gridded using a 1:5 Huygen's sub-grid in comparison with a 1:5 fine-grid solution and a coarse grid at 5:1

8.2.4 Buried Water Filled Plastic Pipe with Dispersive Materials

The purpose of the model is to introduce realistic physical dispersion and attenuation to the propagating fields in the half-space. And consequently, to observe its effect on the accuracy of the Huygen's sub-gridding.

A dispersive homogeneous soil model is introduced to the half-space model. The soil is Type-A Puerto-Rico clay-loam (Teixeira et al., 1998). This soil was modelled in Chapter 4. To recap, the soil's moisture content is 2.5% and it is modelled using a 2-pole Debye function with parameters $\epsilon_\infty = 3.2$, $\sigma = 0.397 \times 10^{-3}\,\mathrm{S\,m^{-1}}$, $\epsilon_{d_1} = 0.72$, $\epsilon_{d_2} = 0.3$, $\tau_1 = 2.71 \times 10^{-9}\,\mathrm{s}$, $\tau_2 = 0.108 \times 10^{-9}\,\mathrm{s}$.
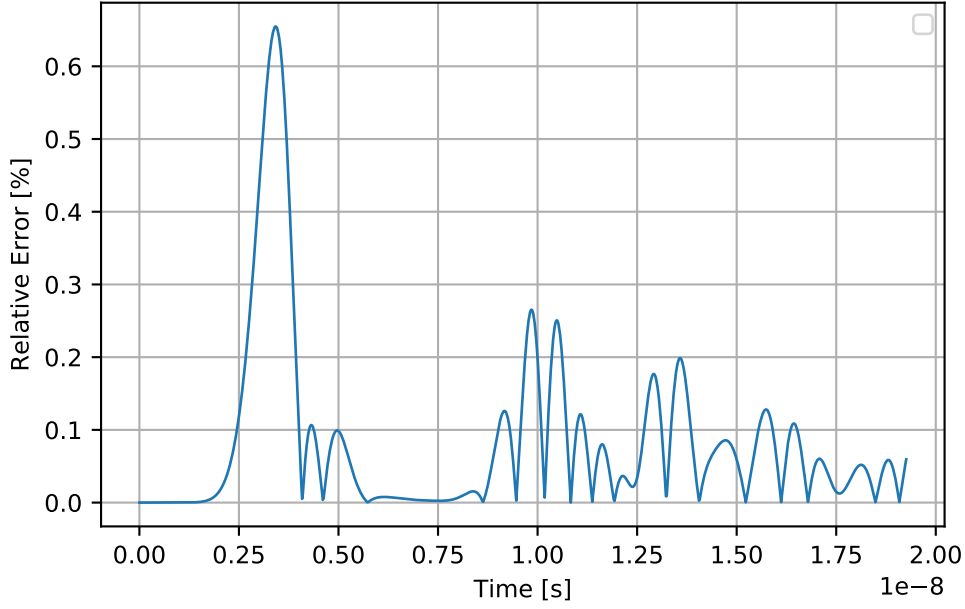
Figure 8.20: Relative error on the E_y measurement from the buried water pipe sub-gridded using a 1:5 Huygen's sub-grid

The half-space problem is simulated using two models. The first does not use any kind of averaging at the half-space interface. This approach is similar to the existing sub-gridding literature and to the GPR modelling literature in general. The second model introduces the averaging procedure outlined in Chapter 4. There are two possibilities for averaging which depend on the alignment of the interface with the difference-grid. In this model, the interface is grid aligned. Therefore an arithmetic averaging of tangential components of the dispersive poles and the relative permittivity is used. A diagram of the simulation setup in shown in Figure 8.21. The diagram shows the material properties assigned at the locations of the E_x and E_y field locations. A detailed view of the materials assigned for the sub-gridded pipe is shown in Figure 8.22.

In the previous experiment, the water pipe material is approximated using a static permittivity. In this model, a dispersive model of water is introduced. The water is modelled with a single-pole Debye material with parameters $\epsilon_\infty = 4.9$, $\epsilon_d = 75.2$, $\tau = 9.231 \times 10^{-12}$ s. The water introduces a grid-aligned dielectric/dispersive interface between the plastic and the water. This interface is also averaged using an arithmetic average of the tangential components.

Except for the pipe and half-space, the other simulation parameters are the same as in the previous experiment. The radius of the plastic pipe is 25 mm and its thickness is 8 mm. It is positioned 50 cm below the surface. At the ends of the pipe, there

150

is a dispersive/dispersive interface between the water and the soil. The accuracy of dispersive averaging between two dispersive materials has not been verified using the Mie scattering. Therefore the ends of the pipe are capped with plastic to eliminate the interaction.

Figure 8.23 shows a comparison of the E_y field at the receiver for the non-averaged, effective permittivity and fine-grid cases. The data shows that there is a good agreement between the non-averaged, and the effective permittivity and the fine grid solution. These findings indicate that the HSG is successful in modelling the dispersive media present in the simulation. Similar results were obtained the first study of the HSG in homogeneous dispersive media (Abalenkovs et al., 2012).

Interestingly, the comparison shows a phase difference between the EP and the non-EP solutions. Figure 8.24 provides a more detailed comparison of the section of the solutions corresponding to the reflection from the pipe. The comparison shows the resonance of the field within the sub-gridded pipe. In contrast with Figure 8.19 the resonance is attenuated more rapidly due to dispersive effects of the water. The data also shows that the phase difference increases between the EP and non-EP solution. This is due to inaccuracy in the positioning of the material boundary in the non-EP case. Similar results were presented by Abalenkovs et al. (2012). However, the difference in the signals was attributed to the error in propagation within the coarse region and the equivalent region in the fine grid solution. The significant variation is shown in Figure 8.24 indicates it is possibly more likely that the error is due to the improper treatment of the material interface.

The argument could be that the averaging of the half-space at the interface, in the fine and coarse spaces, produces solutions which are in better agreement but are just equally incorrect in comparison with reality. However, this is most likely not the case. Since it was shown from the Mie scattering comparison in Chapter 2 that the averaged solutions are in fact in better agreement for a range of realistic grid discretisations.

In previous experiments, the dispersive averaging was performed at free-space / dispersive interfaces. In this experiment, the averaging occurs also at the plastic/water interface where the plastic has a static permittivity.

Figure 8.25 presents a comparison of the relative errors between the non-EP and EP sub-griddings with the fine grid solutions. Turning to the reflection from half-space, the magnitude of the non-EP error is significantly larger error than the EP case. There is also a difference in phase between the two error measurements. These errors occur independently of the sub-gridding. However, there is a contribution to the error shown

in the reflection from the sub-gridded pipe. This is because the phase and magnitudes of the wavelet are incorrect when they reach the sub-grid.

Interestingly, when the EP is introduced the relative error level falls to a level similar shown in the static permittivity tests. This shows that adding dispersive materials to the sub-gridding introduces no additional error provided the material boundaries are properly treated.

8.3   Sub-gridding Realistic Antennas

All studies of sub-gridding for GPR problems have focused on refining the sub-grid resolution for embedded targets. No previous study has investigated the sub-gridding of GPR antennas.

The importance of including detailed GPR antennas in forward-models, in general, is expressed here in terms of the differences between the Hertzian dipole and antennas which have finite size and in particular when they are ground-coupled.

The Hertzian dipole radiates all frequencies equally. Consequently, the transmission of the input current pulse to the free-space field is a faithful representation. This is not the case for finite antennas. The finite nature of the GPR antenna gives rise to resonances which result in a distortion of the pulse when it is radiated. Although a range of broadband antenna designs can be found in the literature, (Balanis, 2016), in practice they will suffer some pulse distortion. This is due to the truncation of the infinite design parameters on which they are based (Vickers, 1991). Modelling the correct distortion can be achieved by modelling the fine detail of the antenna.

The transmission of the input pulse and the reception of the resulting field occurs across the entire surface of the finite antennas (Annan, 2005). This means that the exact position of the transmitter and receiver are not well defined. Therefore modelling the antenna/transmitter at single points does not give an accurate representation of the finite antenna. Addition, the vector character of the field is smeared as the field generation is distributed across the antenna. This makes it more difficult to detect the change in a single vector component at the receiver.

Initially, Maloney et al. (1990) modelled finite antennas in free-space. Cylindrical and biconical monopoles were analysed and excellent agreement with the measured data was found. These models also illustrated in real-time the reflections of the pulse from the coaxial cable and the antenna ends that result in pulse distortion. Subsequently,

several studies included a more realistic description of antennas. Shlager et al. (1994) investigated the effects of resistive loading on planar bow-tie antennas. Resistive loading and capacitive loading using slots in planar bowties antennas were modelled by Lestari et al. (2004). Uduwawala and Norgren (2006) used FDTD modelling to assess the impact of the shape of planar bow-ties on GPR applications.

Warren and Giannopoulos (2011) was the first to incorporate geometrically complex models of commercially available antennas into real GPR type environments. The fine geometry of two commercial antennas, the GSSI 1.5 GHz and the MALÅ 1.2 GHz were modelled by placing the constitutive parameters of the antenna in a finite-difference grid with a spatial step of 1 mm. A number of the constitutive parameters were unknown as they were not provided by the manufacturer. Estimates of these parameters were obtained using a Taguchi optimisation procedure in which the cost function was the error in the free-space cross-talk response. The models were validated against real antenna responses for antennas positioned over oil-water emulsions with different electrical permittivities. The models predicted the arrival times of the wavelets fairly well. The models were also compared with Hertzian dipole approximations. The results showed that the dipole model predicted the arrival times of the real reflections very poorly. Subsequently, Giannakis et al. (2015) included these models in a highly realistic half-space modelling framework. The results showed that the resulting field distributions cannot be modelled with Hertzian dipoles. Following on from these works, Stadler and Igel (2018b) produced a model of the GSSI 400 MHz using the same procedure.

More recently, a novel optimisation method was used to further improve realistic antenna modelling in FDTD (Giannakis et al., 2018). The study puts forward the idea that the real antenna signal is obtained from the convolution of the FDTD signal and a correction factor. Or by applying a filter to the frequency domain signal. The correction factor is said to compensate for the effects of the transmitter and receiver which are difficult to model directly. First, the model parameters are determined using a non-linear least-squares minimisation (Levenberg-Marquardt) where the overdetermined system is generated from the antenna over a PEC and in free space. The filter is obtained using a linear least-squares method. The method improves agreement with the real antenna signal in comparison to the Taguchi optimisation.

The GSSI 1.5 GHz, GSSI 400 MHz and the MALÅ 1.2 GHz models have been implemented in gprMax and have been used for several near-field applications (Warren and Giannopoulos, 2011). However, few studies have utilised the models in large scale simulations. For example, full-waveform inversion of cross-hole GPR data has not leveraged detailed antenna models. This primarily due to large the computational overhead

invoked by large fine grid solutions.

Sub-gridding can reduce the computational overhead associated with solving large scale problems. For instance, a full waveform-inversion (FWI) was performed on GPR data obtained from a GPR cross-hole survey in van der Kruk et al. (2015). The FWI is determined over a 10×6 m 2d slice. The most important physical parameters for an FDTD simulation are the centre frequency of the antenna and the largest permittivity. These were 200 Hz and $\epsilon_r = 25$ respectively. Using these parameters, a 3d antenna model would result in a computational volume of approximately $10 \times 6 \times 0.75$ m where the z-dimension is taken to be the length of a half-wave dipole antenna with centre frequency 200 MHz. The memory requirement for such a model using a spatial step of $\Delta x = 1$ mm is a staggering ~ 5 TB of RAM. This is beyond the memory of a single node in an HPC typically 64-128 GB (University of Edinburgh, 2019). Although techniques exist to leverage shared memory such as domain decomposition, they are architecture-specific. Thus sub-gridding can be used to improve computational performance regardless of the underlying architecture.

Using a sub-gridding approach the dielectric can be modelled in the main grid $\Delta x = 6$ mm and the antenna contained within a sub-grid. This calculation is based on $\epsilon_r = 25$, $f_{max} = 700$ MHz at a 40 dB drop and $N_\lambda = 14$. This corresponds to a main grid memory requirement of 24.9 GB using gprMax. Clearly sub-gridding offers a large performance gain.

8.3.1 Sub-gridded GSSI 1.5 MHz Over Buried Plastic Water Pipe in Dispersive Soil

In this example, the GSSI 1.5 MHz antenna is positioned over a dispersive half-space containing a buried water-filled plastic pipe. The half-space is modelled using the Type-A soil and the water is modelled using the same parameters as in the previous experiment.

The antenna is represented by the model calibrated with the Taguchi optimisation process. Although the hybrid linear/non-linear approach yields a model which is more accurate in comparison with the real data, the success of the HSG needs only to be evaluated against the fine-grid solution. This is true provided that the antenna model is reasonably accurate. Therefore the original model represents simply another physically realisable antenna in the parameter space which can be used to evaluate the sub-gridding scheme.

The antenna introduces two requirements to the model. The first is a spatial sampling of 1 mm and the second is a pulse with centre frequency 1.71 GHz. This corresponds to the highest significant frequency of 5.20 GHz which in turn corresponds to $N_\lambda = 10$ within the half-space.

The antenna is excited using a similar approach to the transmission line model (Maloney et al., 1994) in which the voltage drop across the antenna terminal is specified for the duration of the simulation. The drop is calculated by an external FDTD simulation of the current and voltage propagation in a TEM transmission line. The model couples the voltage drop via the electric field across the terminal. The current in the antenna is coupled back to the external FDTD using the displacement current between the terminals. This is calculated from the integral of the curl about the terminal. The advantage of this method is the reflected current at the terminal can be calculated using a single FDTD run.

A diagram of the antenna is shown in Figure 8.26. The antenna is comprised of an High-density polyethylene HDPE case with dimensions $0.170 \times 0.108 \times 0.043$ m. The antennas transmitting/receiving elements are of a bow-tie design etched in copper on PCB. A wide bandwidth is obtained by the flaring of the bow-tie edges. Additionally, reflections from the ends of the bow-tie are reduced by the addition of parallel endplates. The antennas are isolated from each other by surrounding PEC shields. The shield reduces the antennas performance by the increased reflections of the radiated field within the cavity. These effects are mitigated by including an absorbing material within each cavity.

Figure 8.16 shows a slice in the normal y direction through the materials in the FDTD grid. Each cell edge represents a material at the locations of the E_x and E_z components of a Yee cell. The antenna is embedded within the sub-grid two main grid cells from IS. Although the skid plate of the antenna is grid aligned the other faces are not. This illustrates the useful property that the sub-grid can be used to position any interface at a non-grid aligned location. For example, the half-space interface itself could also be sub-gridded.

The parameters of the models are as follows. The computational domain is $600\Delta l \times 600\Delta l \times 600\Delta l$ where $\Delta l = 3$ mm. The antenna is positioned close to the half space at a distance of 39 mm. It is positioned within the sub-grid two main grid cells from the IS. A diagram of the material parameters for the antenna is the sub-grid is given in Figure 8.27. The water-filled plastic pipe's radius is 45 mm and has a thickness of 6 mm. It is positioned 261 mm below the surface. The domain is truncated by a 10 cell PML. A diagram of the the sub-gridded setup is shown in Figure 8.28

Figure 8.29 shows a comparison of the E_y field at the terminal of the receiving antenna in the sub-gridded and fine grid solutions. The variation at the y-component of the electric field is used as a proxy measurement for the voltage drop across the antenna terminal. The voltage drop can also be measured using a transmission line model. However, there are several free parameters associated with this method. The most important of these is the location of the Ampere loop which is used to derive the current flowing through the antenna. These issues are avoided by considering the received voltage as the integral of the electric field across a single Yee cell at the terminal.

The results show good agreement between the sub-gridded and fine grid solutions. In particular, the sub-gridding of antenna shows a good agreement. This is seen in the agreement in the first set of peaks within the time-frame 0-2.5 ns which correspond to the direct waves and the coupling between the antenna and the ground. The wavelets in the time-frame after this period show the interaction of the antenna with the water-filled pipe. There is a good agreement in the signals over this period. This indicates that multiple sub-griddings of the antenna and the target perform well.

Figure 8.30 shows the relative error between the sub-gridded and fine grid solutions. The data shows that the peak relative error is $\approx 1.2\%$. This improves on the result in the literature for many of the single sub-griddings. However, the results are more inaccurate in comparison with the relative error Hertzian dipole with sub-gridded targets of the single sub-gridding using the HSG. For instance, from Figure 8.25 the peak relative error is $\approx 0.6\%$. Whereas the result shown here has a peak error of $\approx 1.2\%$. These findings suggest that the error doubles with the addition of each sub-grid.

The highest significant frequency is a limiting factor in the choice of sub-gridding ratio. The spatial step requirement shows that a higher permittivity of the soil would require $N_\lambda < 10$. This discretisation is not recommended as the phase speed of the discretised wave begins to differ significantly from the free-space/half-space wave. Consequently, for GSSI 1.5 GHz half-space models, the sub-gridding ratio is limited to 3, and $\epsilon_r = 3$. For lower frequency antennas these criteria can be relaxed. This is because the ratio of the numerical discretisation requirement to the geometric resolution requirement is larger than in the high-frequency case. These findings are not specific to the choice of sub-gridding scheme. They are relevant to all schemes and particular to sub-gridding high-frequency antennas.

Table 8.2 shows are summary of the computational requirements for each simulation. The results show that the solve time is reduced by a factor of 17 and the memory requirement is reduced by a factor of 16. These results show a significant increase in

performance for the sub-gridding. However, the performance will vary depending on the fractional volume of the sub-grids to the main-grid and the sub-gridding ratio.

Model	Solve time [s]	Speed up factor	Memory [GB]	Memory reduction
FDTD Reference	59806	1	33.7	1
HSG-FDTD	3570	17	2.2	16

Table 8.2: Simulation statistics Simulation time and RAM used in the GSSI 1.5 MHz over a buried water filled pipe.

8.3.2 Sub-gridded GSSI 1.5 GHz with material traverse in contact with dispersive soil over a buried water-filled pipe.

Commonly the antenna is placed on the ground in GPR surveys. The reason for this is the coupling and directivity of the antenna are increased when in contact with the ground. This results in greater efficiency and focusing of the antenna's beam.

Modelling this scenario with the HSG requires that the half-space interface traverses the left, right, front and back faces of the sub-grid. This is because the HSG has two boundaries which cannot both be aligned with the antenna casing. Sub-gridding methods which utilise a single boundary can be applied to this case without material traversal. Nonetheless, sub-gridding the interface with any scheme is beneficial as the second-order accuracy of the fine grid solution can be retained at the boundary.

The purpose of this experiment is to illustrate the HSG material traversal and how it can be applied to the finite-sized antenna half-space problem.

Figure 8.31 shows a diagram of the sub-gridded antenna in contact with the half-space where the main grid and sub-grid have been merged at the IS boundary. In contrast to the previous experiment, the sub-grid interface extends beyond the half-space interface. Notice the half-space crosses the left and right Inner Surface boundaries.

Figure 8.32 shows a diagram of the sub-grid domain only. The Outer Surface is shown 8 cells from the edge of the domain. Notice that the interface crosses the OS boundary. This is required such that the update equations in the sub-grid are consistent with those in the main grid at the points where the interface exists in the physical problem.

Materials can freely traverse the OS. This is because the fields are injected directly. Consequently, interpolation of discontinuous fields is not required. However, at the IS,

interpolation across the discontinuous interface is more complex and has been treated differently depending on the material type. For example, PEC traversal has been treated with a nearest neighbour approach and dielectric have been treated using the continuity of the displacement field at the interface.

Material traverse of dispersive materials using the ADE scheme is straightforward. The exact local electric field at the interface is recovered from the displacement field. However, the PLRC scheme used to implement dispersive materials in this work requires a different approach. The key difference between the PLRC and ADE schemes is the former computes the electric field directly. Consequently, the exact electric fields at the fine grid positions cannot be obtained exactly from the displacement field. Therefore the nearest neighbour approach is necessary as in the PEC case.

A preliminary experiment is conducted to show the accuracy of the nearest neighbour interpolation for the worst-case scenario. This is then used to justify the interpolation procedure for half space with high dielectric strength.

Additionally, the PEC half-space is chosen as a stringent test because the fields must traverse boundary many times during the antenna ringing. This increases the sensitivity of the antenna to the interpolation procedure. Furthermore, the experiment is repeated using increasing sub-gridding ratios of 3 and 5. The purpose of which is to increase the number of nearest neighbour nodes and thus gives an indication of the accuracy as the sub-gridding ratio increases.

The increase in the number of nearest neighbour nodes is demonstrated in Figure 8.33. The figure shows the precursor nodes at the front face the IS for the 5:1 sub-gridding where the two rows of nearest neighbour nodes are shown in green. In contrast, the 3:1 sub-gridding would require only a single row of nearest neighbour nodes. The blue and yellow nodes represent E_{z_p} field values which are interpolated from the main grid E_{z_b} shown in black. The nearest neighbour nodes and are calculated using equation 8.1, 8.2, 8.3, 8.4 for all i belonging to each of the front, back, left, right IS surfaces. The top and bottom surfaces are unaffected as they are not traversed by the half-space.

$$E_{z_p}\Big|_{i,k'} = E_{z_p}\Big|_{i,k'+2} \tag{8.1}$$

$$E_{z_p}\Big|_{i,k'+1} = E_{z_p}\Big|_{i,k'+2} \tag{8.2}$$

$$E_{z_p}\Big|_{i,k'-1} = E_{z_p}\Big|_{i,k'-3} \tag{8.3}$$

$$E_{z_p}\Big|_{i,k'-2} = E_{z_p}\Big|_{i,k'-3} \tag{8.4}$$

Figure 8.34 shows a comparison of the sub-gridding solutions for each sub-gridding ratio and interpolation approach. The fine grid solution is not computed in this case as we are interested only the variation of the sub-gridded solutions. The solutions are superimposed which shows clearly that the nearest neighbour approach has no effect. This result indicates that the standard interpolation approach is effective in modelling half-spaces with high dielectric strengths.

Following these results, the PEC half-space is replaced with the type-A soil and the buried plastic water pipe is returned. The half-space interface is averaged with the free space and the antenna skid plate using the grid-aligned procedure outlined previously. Also, the sub-gridding ratio is returned to 3. The experiment is run with the nearest neighbour approach and the standard interpolation procedure to improve the validation. A fine grid solution also computed for comparison.

A comparison of the E_y field at the antenna terminal for the three solutions is shown in Figure 8.35. The three solutions are in very good agreement. Additionally, the wavelet reflected from the pipe is larger in magnitude than the wavelet shown in Figure 8.29. This result shows the improved coupling and directivity of the antenna in contact with the half-space. Also, the direct wave is less distorted. This shows the antenna is better matched to the ground.

The relative error between the sub-gridded and fine grid solutions is shown in Figure 8.36. The first observation is the error in interpolation procedures is perfect. This result combined with the PEC half-space results strongly indicate that the standard interpolation procedure is suitable for half-space problems. The second observation is the relative error in the direct wave is $\approx 1.2\%$. This result is very similar to the result shown in Figure 8.30. Therefore, it can be assumed that the sub-gridding of the interface does not introduce additional errors into the sub-gridding procedure. This is an important finding as the sub-gridding of the interface will be a common application of the HSG for GPR problems. The third observation is the increase in the relative error of the reflection from the pipe. This is accounted for by the scaling of the solution by the peak magnitude in the relative error metric. Figure 8.37 shows a comparison of the difference in the fields for the traverse and non-traverse case. The errors are in

good agreement within the 3 to 4 ns range corresponding to the pipe reflection. The phase error between the solutions is due to the variation in the pipe-antenna distance in the experiments.
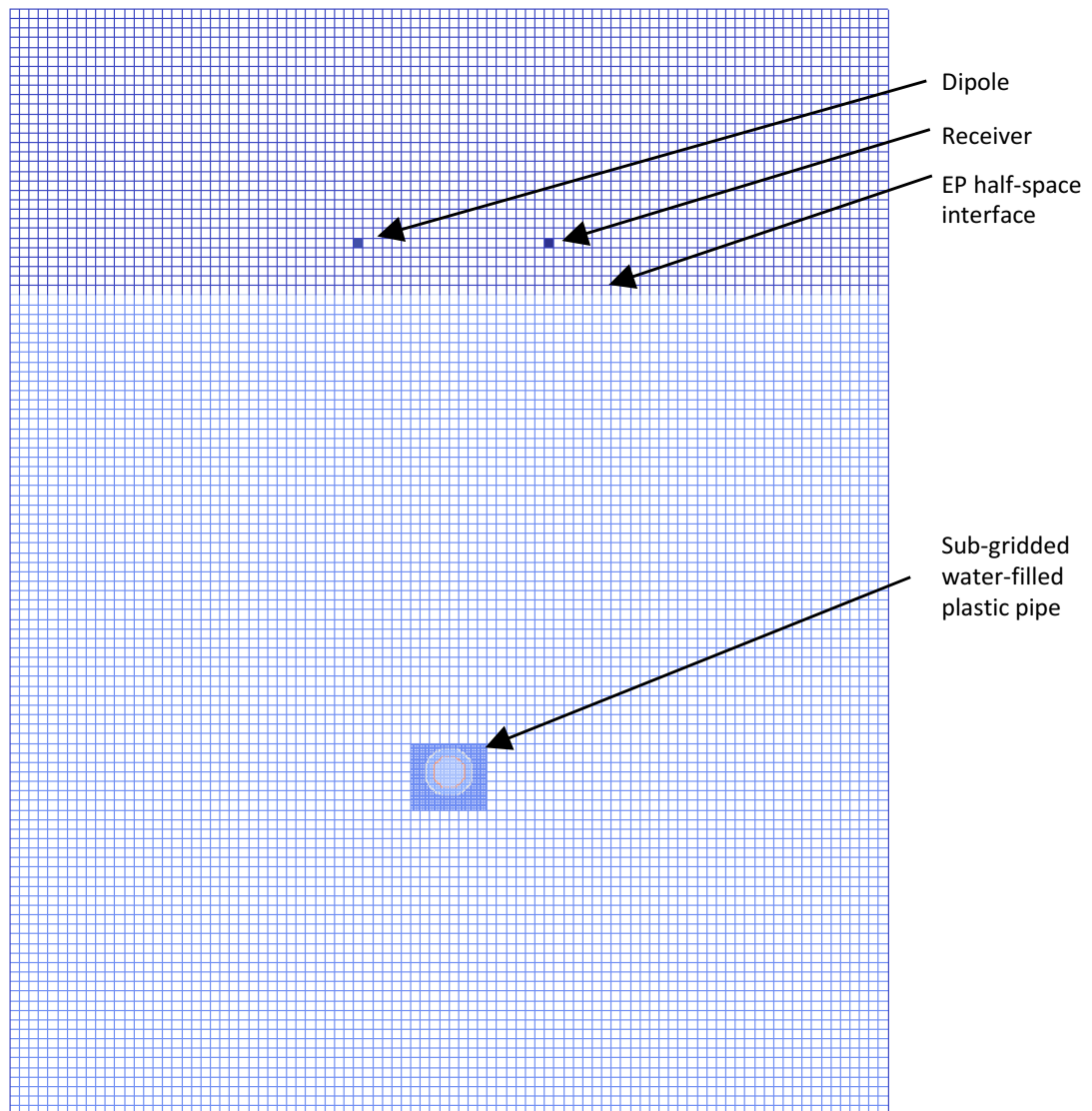
Figure 8.21: Diagram of a buried water filled plastic pipe buried in a dispersive soil. The boundaries of the dispersive materials are averaged using the effective permittivity scheme.
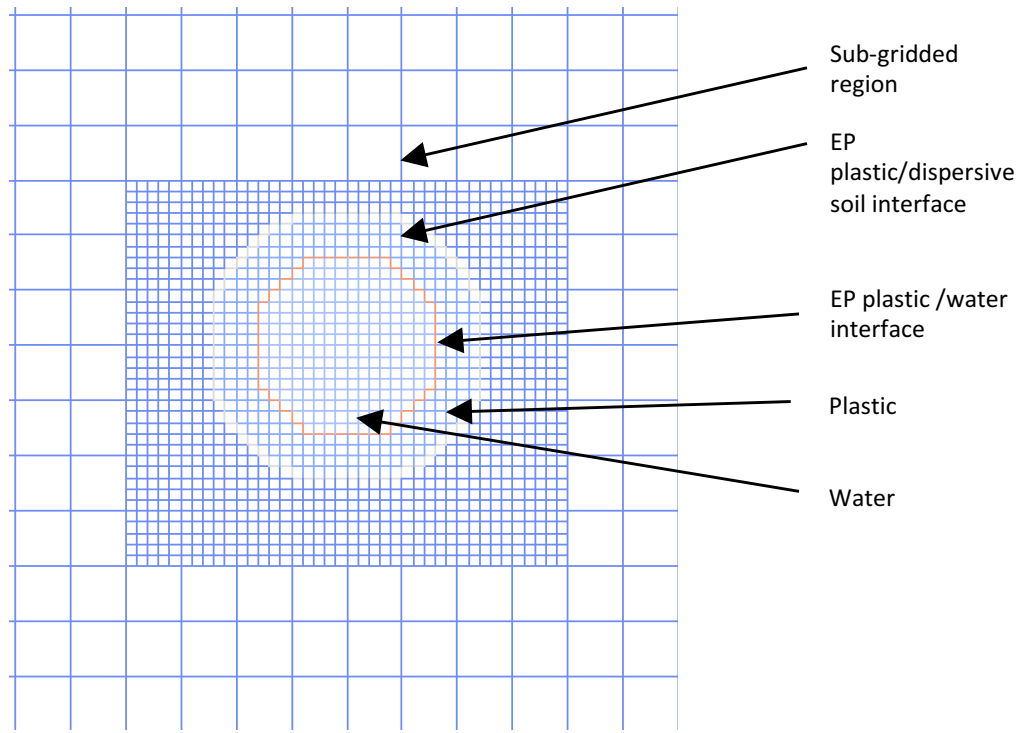
Figure 8.22: Diagram of the material parameters for a sub-gridded buried water filled plastic pipe buried in a dispersive soil. The boundaries of the dispersive materials are averaged using the effective permittivity scheme.
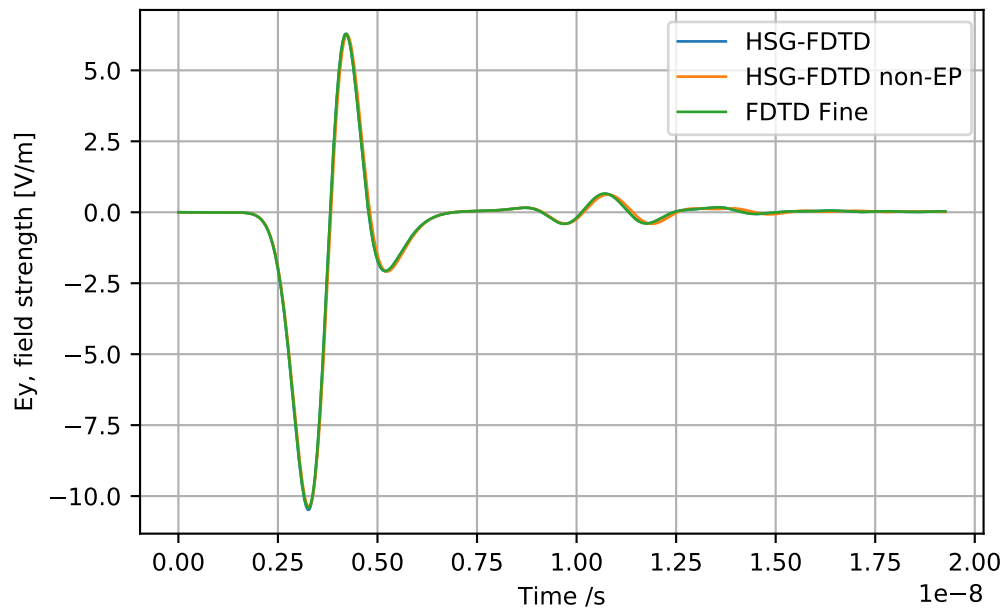
Figure 8.23: E_y reflection from the water pipe buried in soil type a subgridded using a 1:5 Huygen's sub-grid in comparison with a 1:5 fine-grid solution and a coarse grid at 5:1
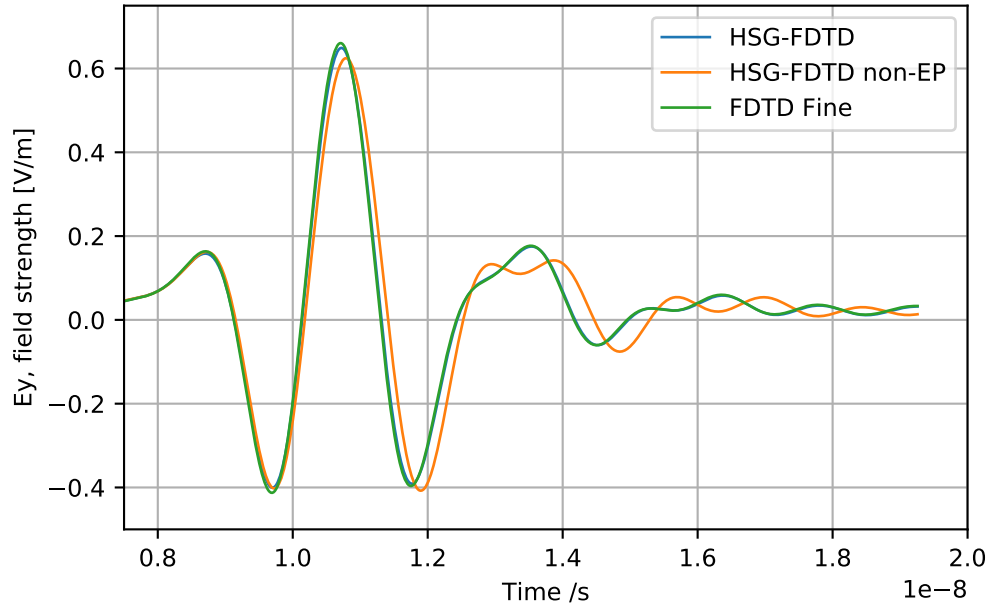
Figure 8.24: E_y reflection from the water pipe buried in soil type a subgridded using a 1:5 Huygen's sub-grid in comparison with a 1:5 fine-grid solution and a coarse grid at 5:1
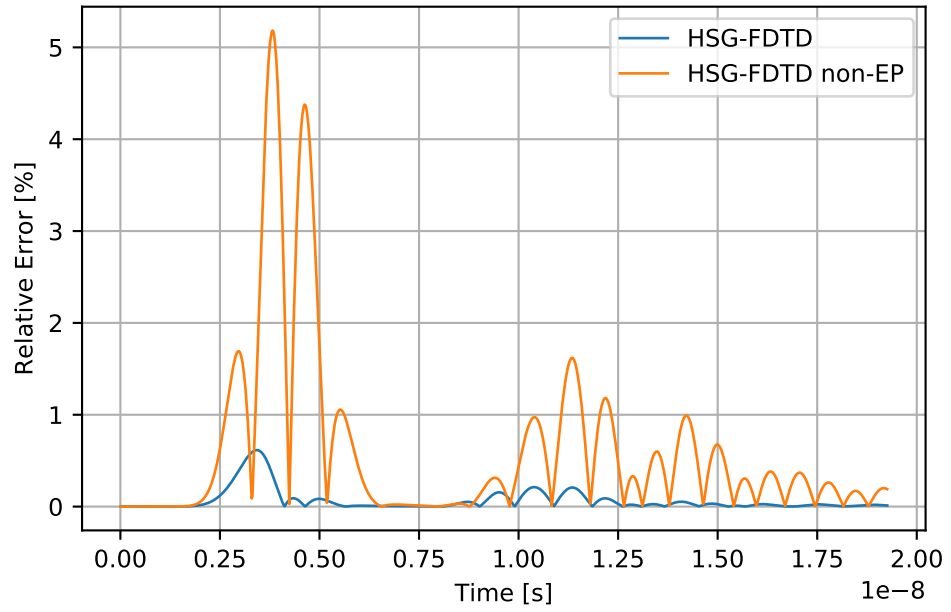
Figure 8.25: Relative error on the E_y measurement from the water pipe buried in dispersive Type-A Puerta Rico soil. The pipe is sub-gridded using a sub-gridded using a 1:5 Huygen's sub-grid without and without EP at the dielectric/dispersive interfaces.
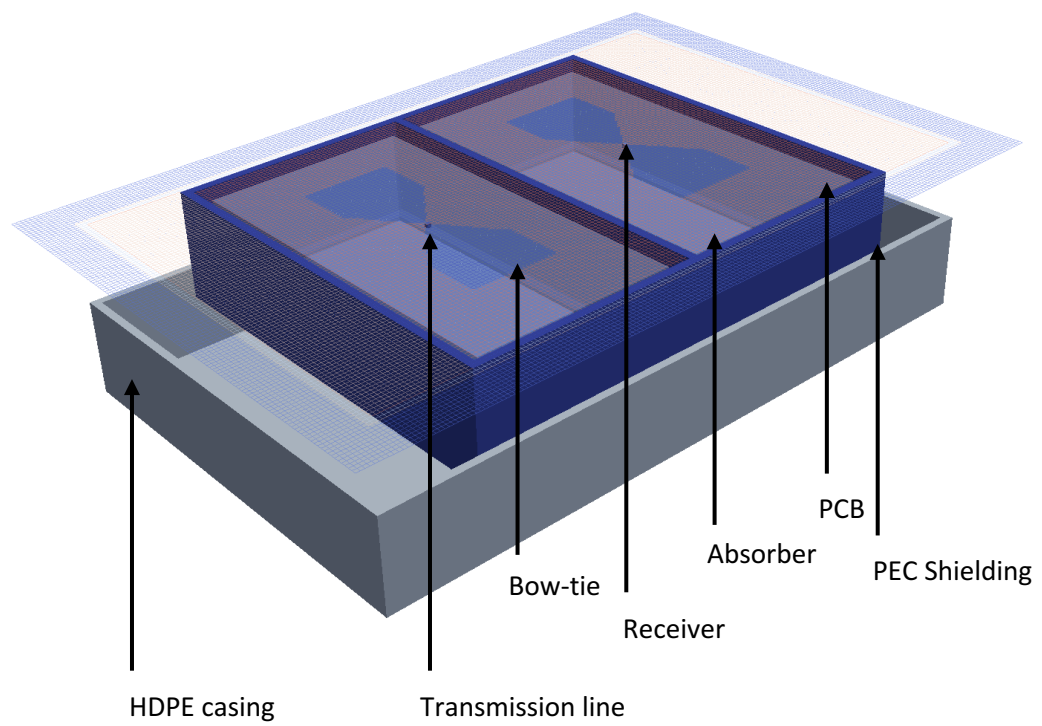
Figure 8.26: Model of the GSSI 1.5 GHz
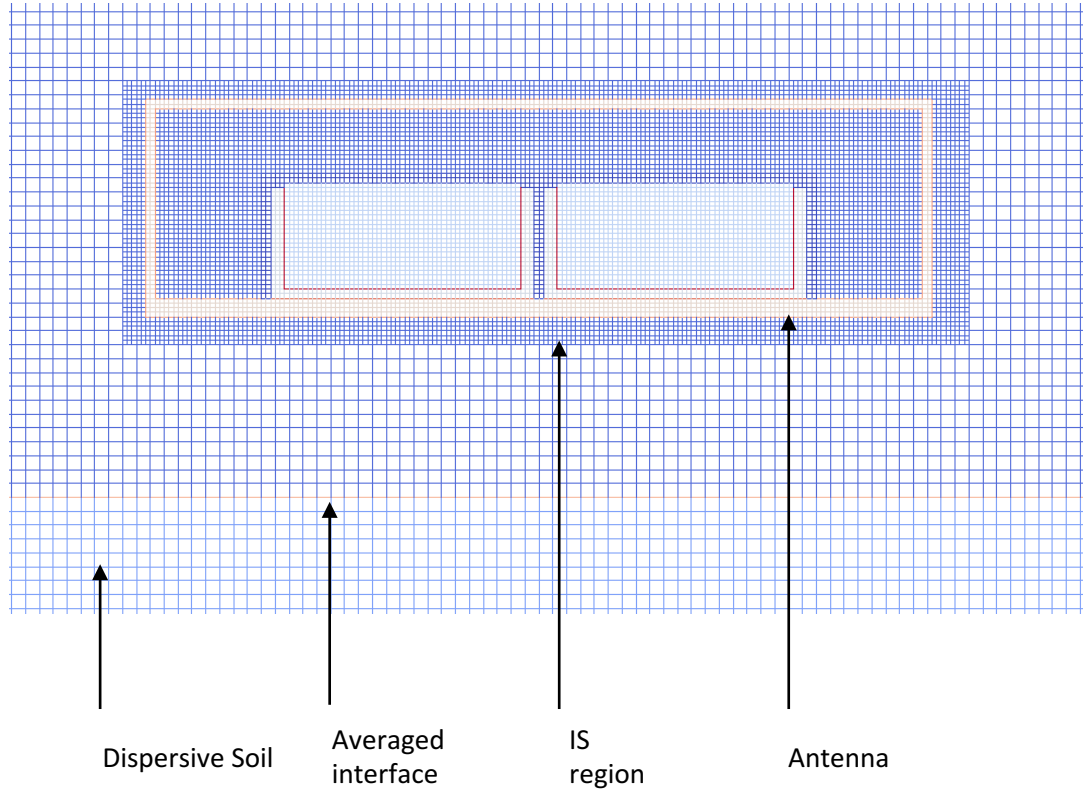
Figure 8.27: Diagram of the GSSI 1.5 GHz antenna over the dispersive half-space. Each edge represents the material at the E_x and E_z positions of a Yee cell.
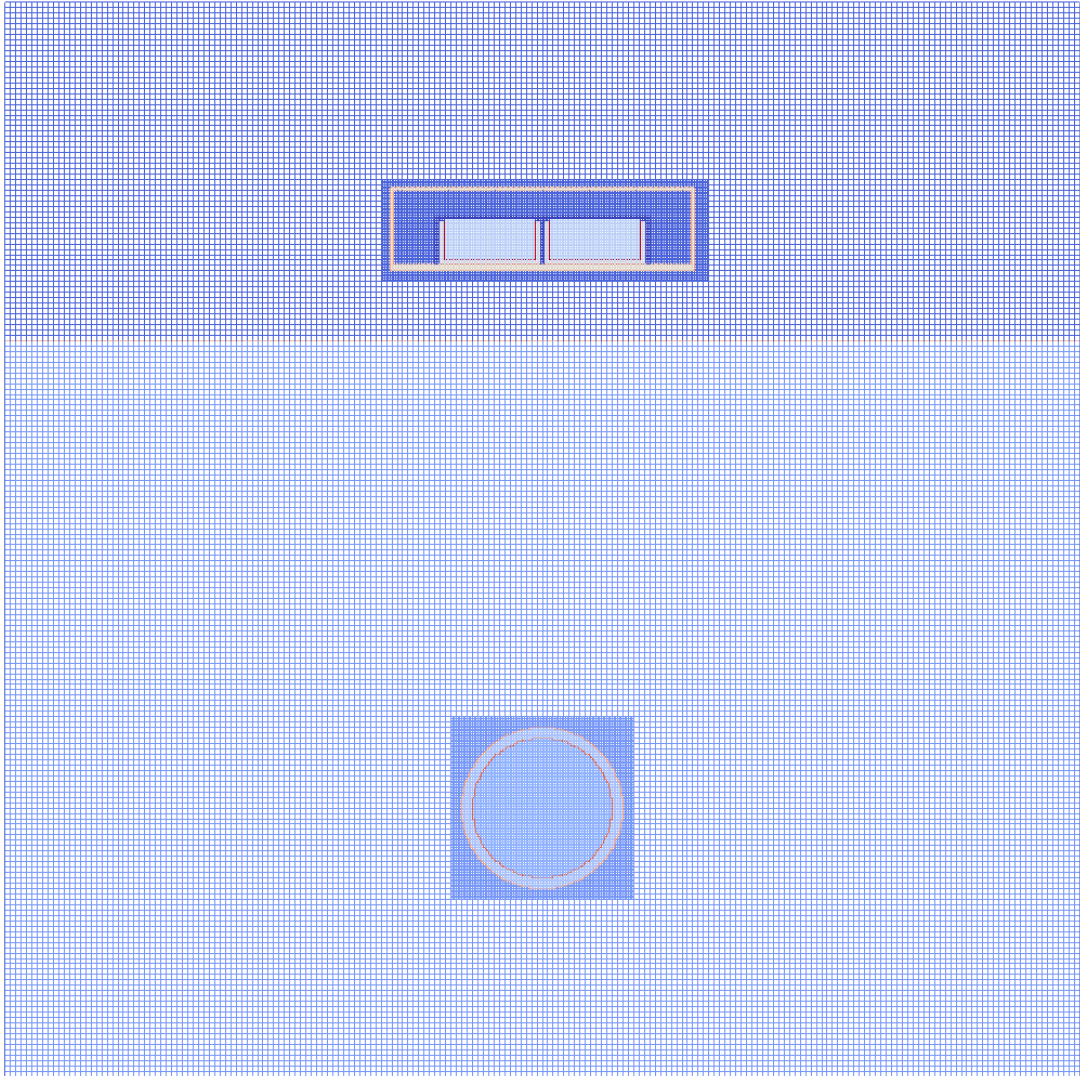
Figure 8.28: Sub-gridded GSSI 1.5 MHz antenna over a dispersive soil containing a sub-gridded water-filled plastic pipe. The boundaries between the dispersive media have been averaged using the EP scheme.
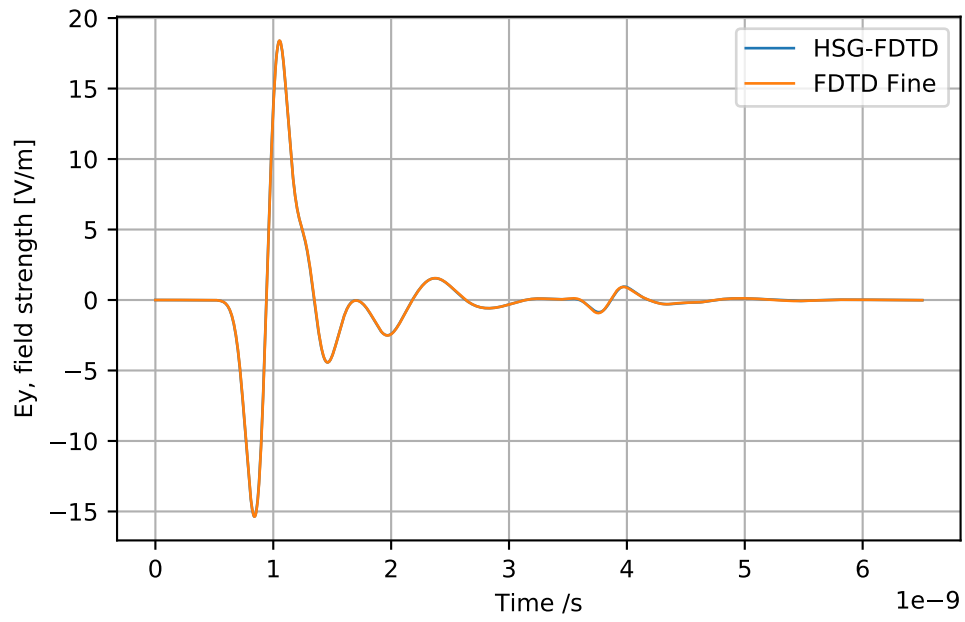
Figure 8.29: E_y signal recorded at the GSSI 1.5 MHz receiver for the HSG and the fine grid simulations.
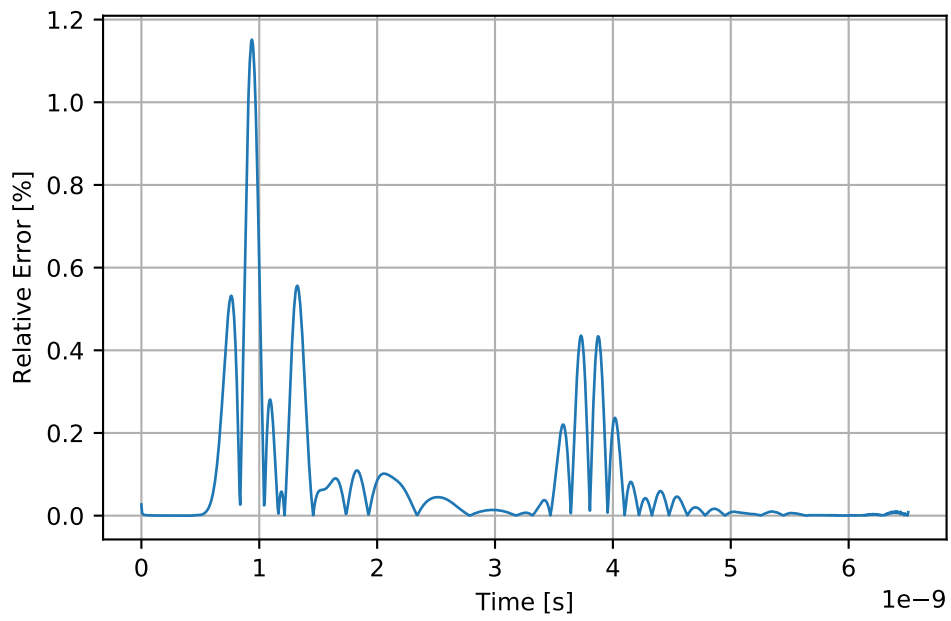
Figure 8.30: Relative error in the E_y signal recorded at the GSSI 1.5 MHz receiver for the HSG and the fine grid simulations.

Material traversal
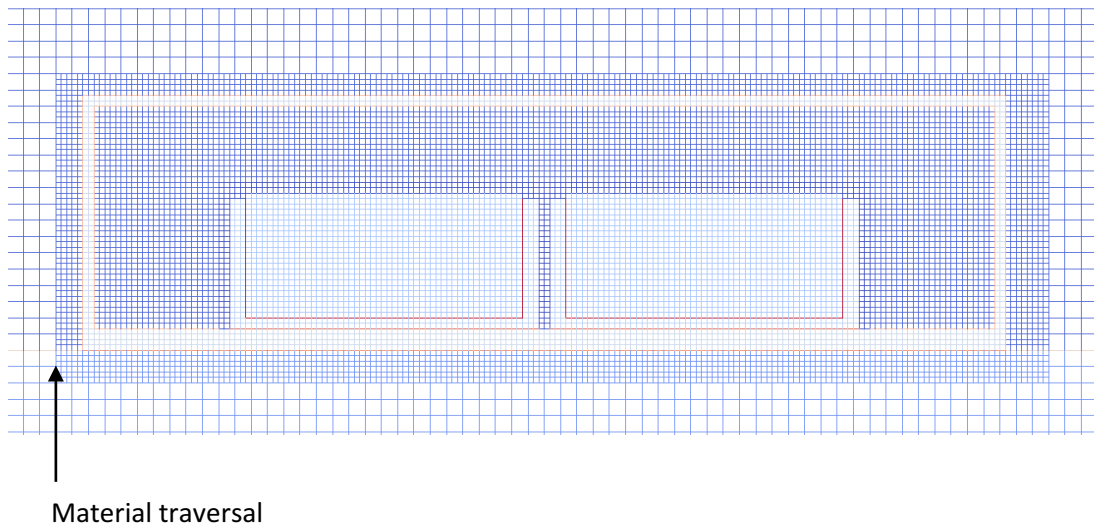
Figure 8.31: Diagram of the GSSI 1.5 GHz antenna in contact with the dispersive half-space. The half-space traverses at the left, right, front and back faces of the IS and OS.

Material traversal   6 Cell PML   Outer Surface
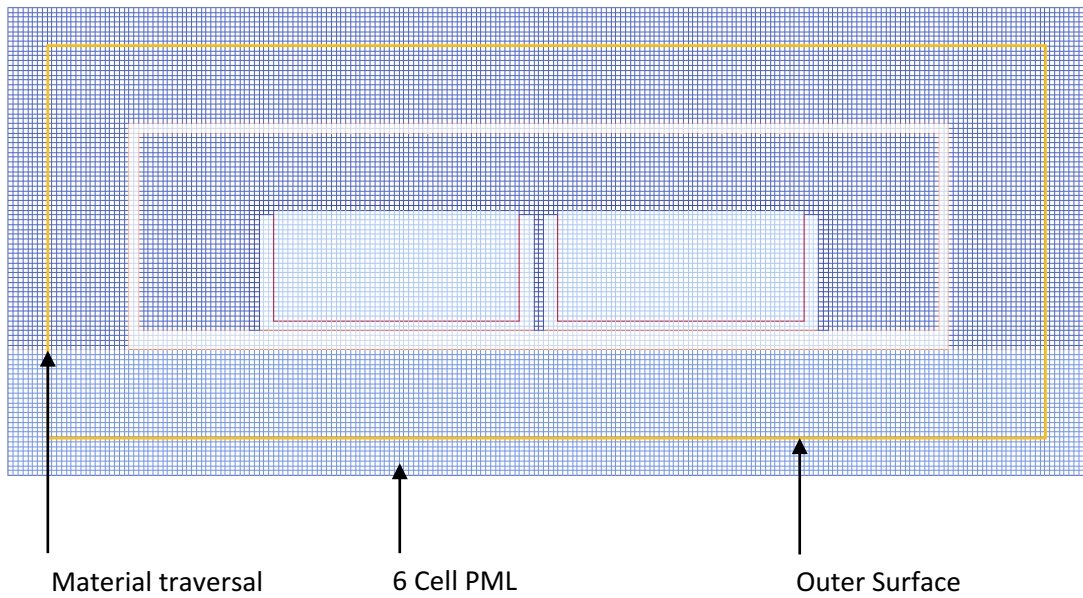
Figure 8.32: Diagram of the antenna sub-grid showing the GSSI 1.5 GHz antenna in contact with the dispersive half-space. The half-space traverses at the Outer Surface.
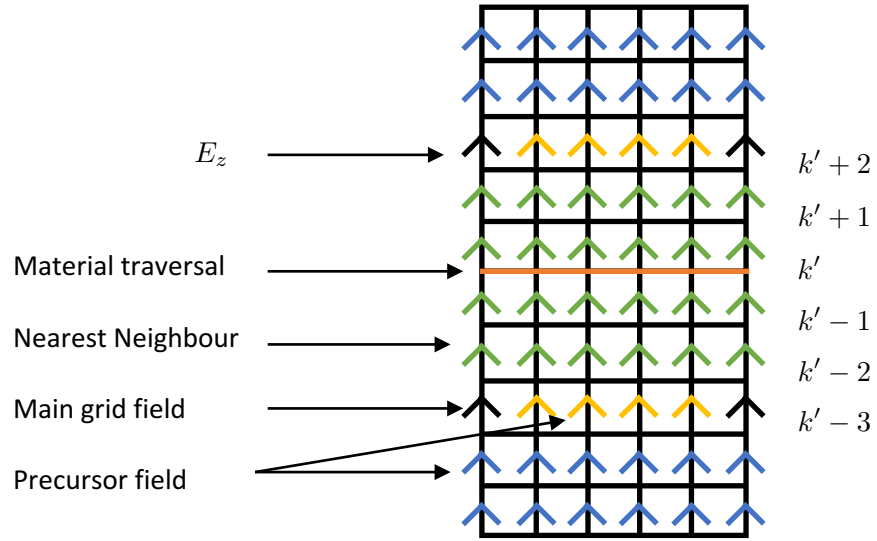
Figure 8.33: Nearest neighbour interpolation.
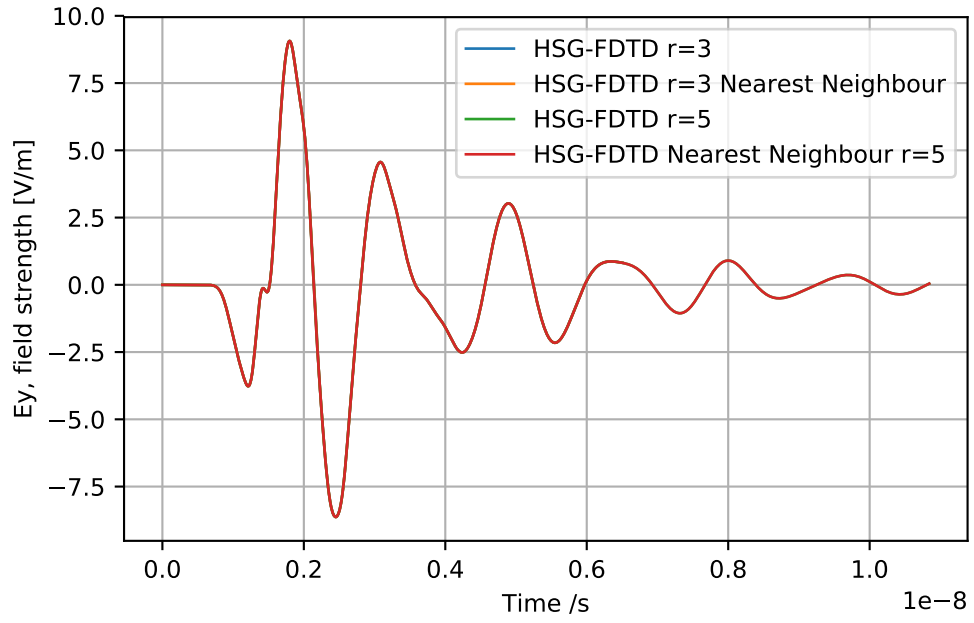
Figure 8.34: GSSI 1.5 GHz in contact with PEC half-space
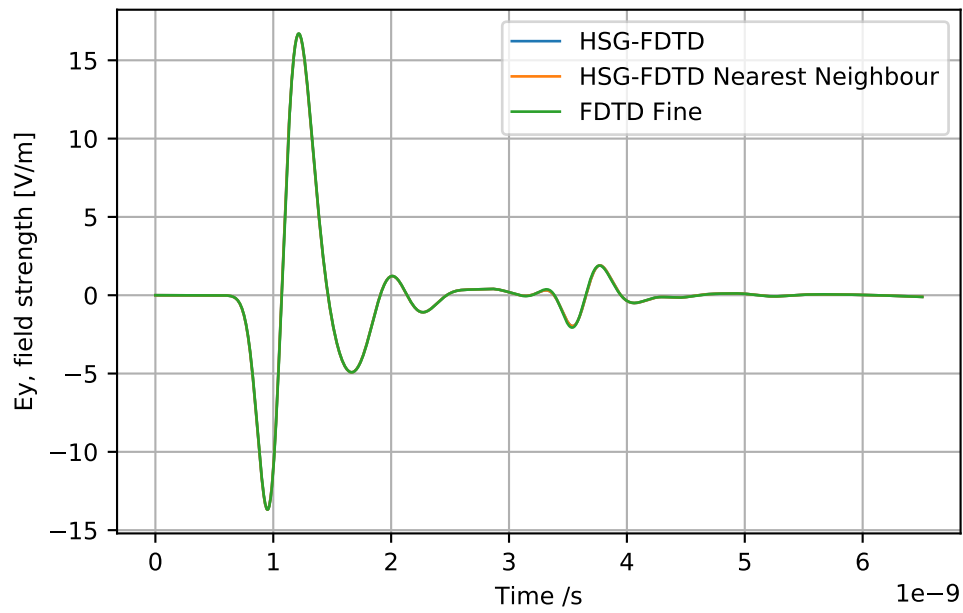
Figure 8.35: GSSI 1.5 GHz in contact with dispersive soil over buried water filled pipe. material traverse
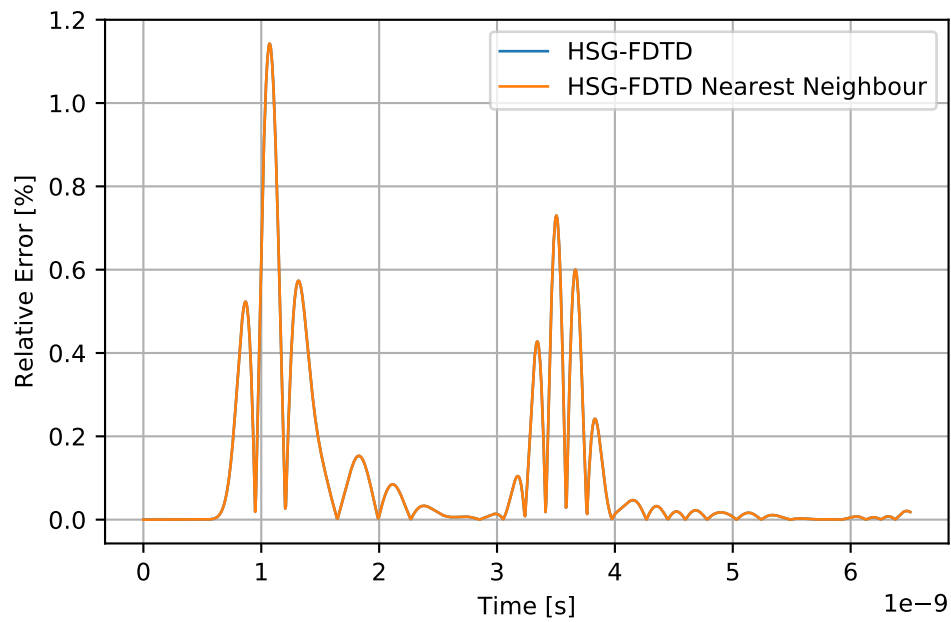
Figure 8.36: GSSI 1.5 GHz in contact with dispersive soil over buried water filled pipe. material traverse

170
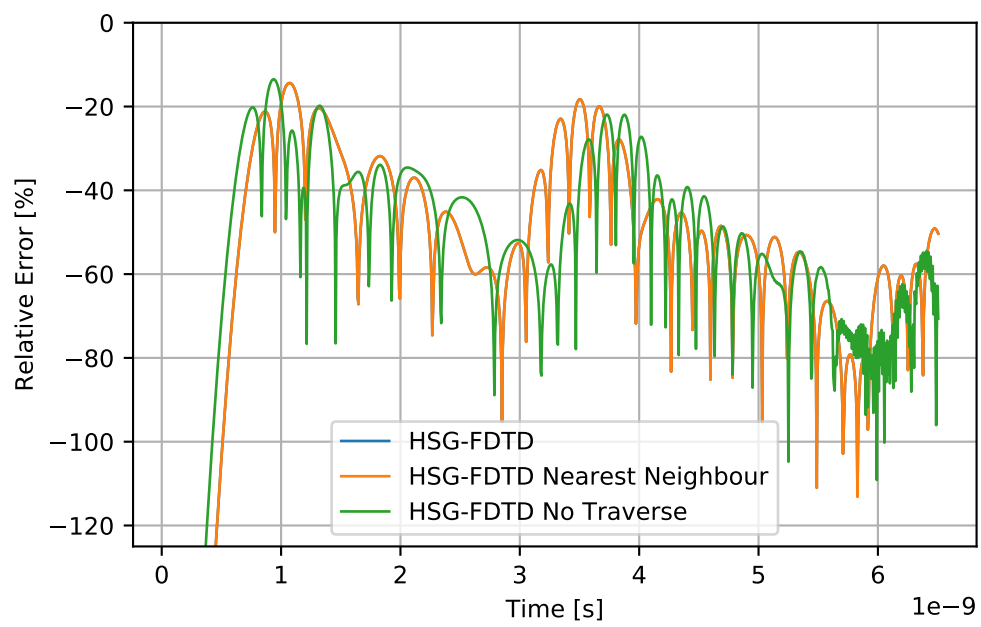
Figure 8.37: GSSI 1.5 GHz in contact with dispersive soil over buried water filled pipe.
material traverse

8.3.3 GSSI $400\,\mathrm{MHz}$ antenna over a PEC plate buried in dispersive soil

The GSSI $400\,\mathrm{MHz}$ antenna is intended for detection of utility pipes up to a depth of $5\,\mathrm{m}$ where the permittivity of the ground is around $\epsilon_r = 9$. Stadler and Igel (2018a) modelled this transducer using gprMax. The antenna was used to perform permittivity soundings using a guided wave technique where waves couple to a waveguide in a borehole. The model was calibrated using the Taguchi method. The model parameters were the unknown material parameters, the centre frequency of the pulse, and the input resistance. Similarly to the GSSI $1.5\,\mathrm{GHz}$, the model was implemented using a spatial step $\Delta l = 1\,\mathrm{mm}$.

The GSSI $400\,\mathrm{MHz}$ model requires more computational resource than the GSSI $1.5\,\mathrm{GHz}$. This requirement is exacerbated in half-space problems. This is due to the antenna's large physical dimension $0.3 \times 0.3 \times 0.178\,\mathrm{m}$ and the small spatial step required to resolve its geometry. For instance, the volume required to model the antenna within the usage range defined by the manufacturer is approximately $0.35 \times 0.35 \times 5.05\,\mathrm{m}$. The RAM usage for the volume as estimated by gprMax is $74\,\mathrm{GB}$.

The HSG sub-gridding can be used to significantly reduce the memory footprint and number of iterations. In particular, the sub-gridding ratio can be extended beyond 3 due to the lower operational frequency. Also, soils with higher dielectric strengths can be modelled. For instance, the centre frequency of the antenna is $0.39\,\mathrm{GHz}$. This corresponds to the highest frequency of interest of $1.2\,\mathrm{GHz}$ for a $40\,\mathrm{dB}$ drop in power. For Puerto Rico type-C soil, $\epsilon_{r_{max}} = 8.75$, the highest frequency of interest must be resolved by $9\,\mathrm{mm}$ for $N_\lambda = 10$. Given that the antenna model resolution is $\Delta l = 1\,\mathrm{mm}$ a sub-gridding ratio of 9 can be used.

In this example, the antenna is simulated over a dispersive half-space containing a buried PEC plate. The half-space consists of Puerto Rico type-C soil. The plate is buried $0.495\,\mathrm{m}$ below the half-space surface. The extent of the computational domain is $0.9 \times 0.9 \times 1.278\,\mathrm{m}$. The spatial step is $9\,\mathrm{mm}$ and the sub-gridding ratio is 9 such that the discretisation in the sub-grid is $1\,\mathrm{mm}$. The antenna is placed in contact with the ground such that the half-space traverses the grid. The dielectric/dielectric and dispersive/dielectric interfaces have been smoothed using the grid-aligned EP method. The PEC plate has not been treated with any refinement. Therefore, it should be expected that there is a phase difference between the reflected wave in the coarse grid and fine grid solutions. Also, the standard interpolation procedure is used where the sub-grid traverses the half-space interface. A diagram of the sub-gridded antenna is

shown in Figure 8.38.
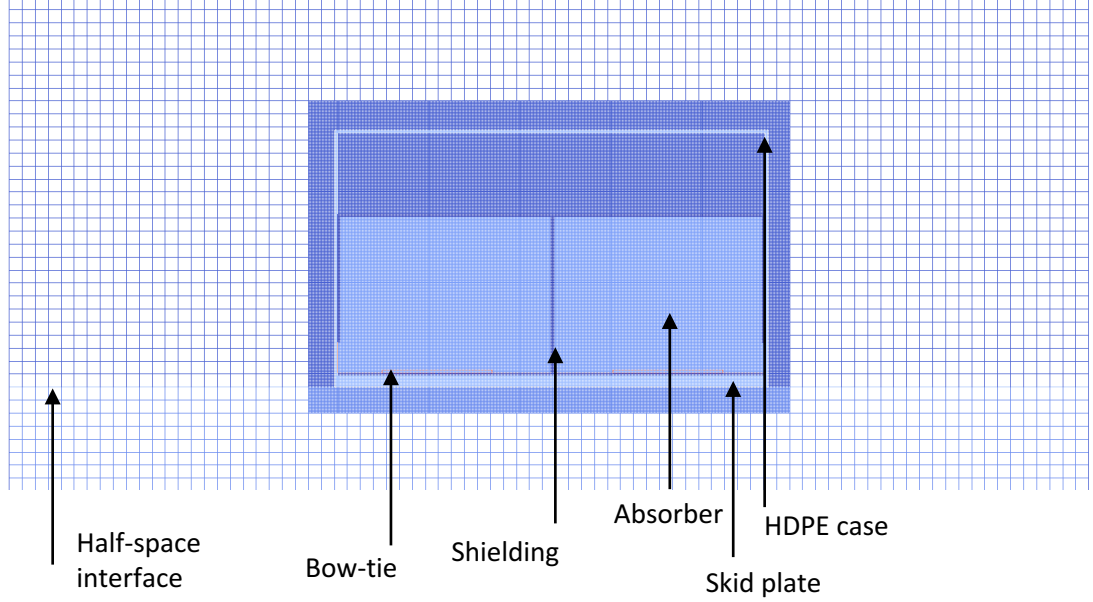
Figure 8.38: Diagram of the material parameters for the GSSI 400 MHz in contact with a half-space.

The response of the antenna is shown in Figure 8.39. The figure shows clearly the direct wave and the subsequent reflection from the PEC sheet. At 2.5 ns follows the resonance between half-space surface / antenna. Each of these features is found in the sub-gridded and the fine grid solution. The features are in good agreement. However, there is a small phase error between the reflected wavelet solutions as expected. This could be rectified by sub-gridding the plate. Crucially, no spurious reflections are visible in the HSG solution. This strongly suggests that the HSG can be used with large sub-gridding ratios for finely detailed modelling. This result is the first GPR sub-gridding which has used a sub-gridding ratio of 9. Wei et al. (2017) used a maximum sub-gridding ratio of 7.

Figure 8.40 shows the relative error between the HSG solution and the fine-grid solution. The relative error in the direct wave is very low. This indicates that using the standard interpolation procedure for the grid-traversal works well. The region 1-2 ns corresponds to the reflection from the PEC sheet. The error is $\approx 7\times$ greater than the direct wave error. This error is due to the difference is the position of the PEC sheet in the fine and coarse grids. Nevertheless for the error is still lower than the result for buried metal pipe found by Wei et al. (2017).

Table 8.3 shows the simulation statistics. The HSG solution is computed 20 times faster than the reference solution and utilises 19 times less memory. Although greater

gains in speed would be expected with a higher sub-gridding ratio, the model size is relatively small for an antenna of this frequency. Greater gains are possible for larger models. However, a more powerful computer system is required to compute a reference solution.

Model	Process time [s]	Real Time [h/cpu]	Speed up factor	Memory [GB]	Memory factor
FDTD Ref.	2396504	33.3	1	123	1
HSG with PML	119365	1.7	20	6.5	19

Table 8.3: Simulation statistics. Process time and RAM allocated in the GSSI 400 MHz over a PEC sheet experiment. Results computed on a Supermicro SYS-7048GR-TR system with 2 x Xeon E5-2640 v4 (2.4 GHz, 20 cores) CPU.
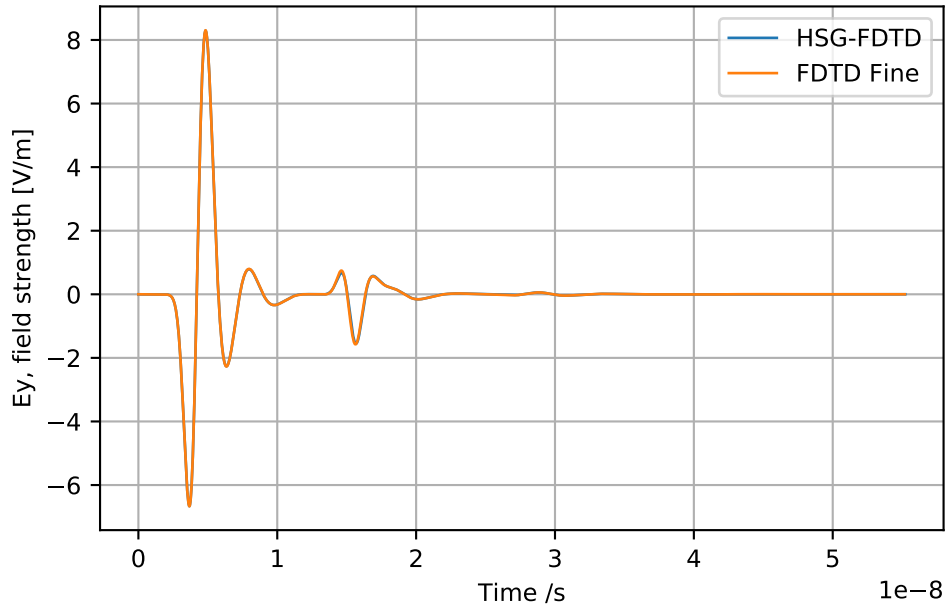
Figure 8.39: E_y received by a GSSI 400 MHz in contact with a dispersive half-space over a PEC sheet. Solutions are shown for the antenna sub-gridded using the HSG and a uniform fine grid.
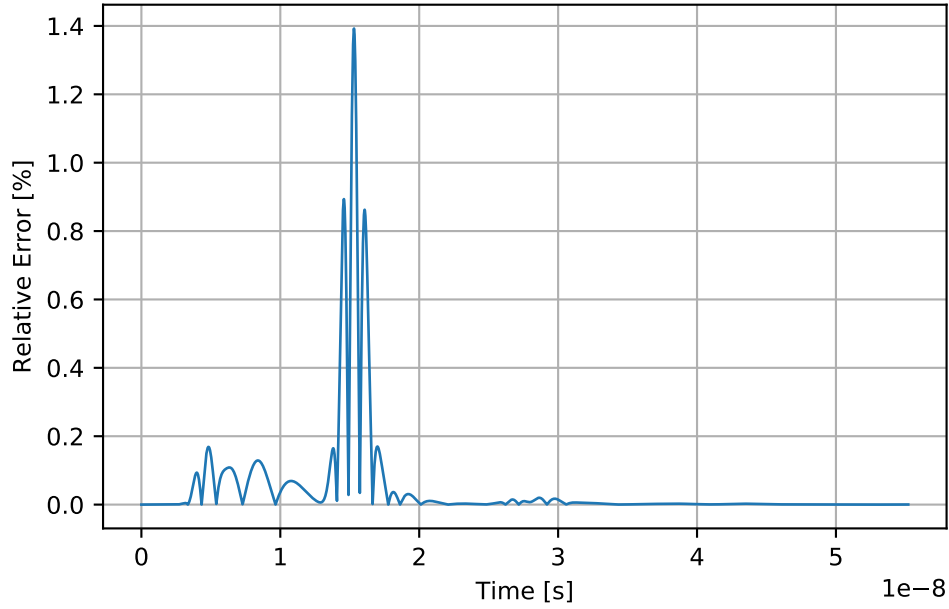
Figure 8.40: Relative error in the sub-gridded solution for E_y received by a GSSI 400 MHz in contact with a dispersive half-space over a PEC sheet.

8.4 Summary

The HSG was used to sub-grid a Hertzian dipole. The results showed that sub-gridding provided accurate results for sub-gridding ratios 3-17. Interestingly the results showed that in addition to stabilising the solution, the PML absorbs the leakage generated by the Huygen's surfaces. This implies that the PML should always be used regardless of stability.

A series of half-space experiments with Hertzian dipoles and buried sub-gridded targets showed increased performance over the sub-griddings performed in the literature. In particular, the maximum relative error observed was $\approx 1\%$. This compares favourably with the sub-griddings performed by Wei et al. (2017). Another important outcome was that the EP significantly improves the performance of the sub-gridding when the antenna field crosses the half-space.

Novel sub-griddings of commercial antenna models above half-spaces were performed. The results demonstrated that the antenna models could be sub-gridded with a relative error increase of $\approx 1\%$. Also, these models were up to 17 times faster to compute and required 16 times less memory. Furthermore, it was demonstrated that the nearest neighbour approach to interpolating fields at material traversals can be

used without detrimental effects on the solution.

Chapter 9

Late Time Instability and the Switched Huygen's Sub-Gridding (SHSG)

The main weakness of the Huygen's Sub-Gridding is the presence of a late time instability. The instability has been mitigated by several approaches. Firstly, a PML placed in the non-working regions of the sub-grid was found to reduce the onset of the instabilities. A six-cell PML yielded an additional 3000 iterations of stable performance. Secondly, a low pass filter at the IS was found to significantly increase the stability. The 3-node filter increased the stability to 30000 iterations in a simulation modelling the resonant field between a thin wire and a plate. Thirdly, an implicit scheme in the sub-grid was used to control the instability indefinitely. Fourthly, artificial losses were placed at the IS and OS to attenuate the instability. The fourth scheme is of great interest as it does not require any additional computation resources. Unfortunately, it was found that the artificial loss attenuated the solution rapidly.

In this thesis, a proposition is put forward that the key reason for the unacceptable attenuation, when the artificial loss is introduced, is that the artificial loss was always applied to fields which contribute to the solution of the physical problem.

In this chapter, a new and novel Huygen's Sub-Gridding algorithm is proposed. The scheme is called the Switched Huygen's sub-gridding (SHSG). It has the property that the inner nodes of the IS and OS have fields of theoretically zero magnitudes and thus should contribute nothing to the physical solution. Therefore, it is proposed that at these nodes it should be possible, in theory, to strongly attenuate the instability using

an artificial loss without affecting the physical solution.

The SHSG has several advantages over the HSG.

- The SHSG is more computationally efficient than the HSG. This is because the SHSG does not require a PML for stability, and therefore the additional update equations for the PML are not required and the standard update equations can be used. The second reason is that the loss is so great the skin depth is very small and therefore fewer nodes are required in the none-working region for the same attenuation using a PML.

- The fields are correct in all the location of the SHSG scheme. This means that the fields in the IS-OS can be sampled directly without additional interpolation.

- The SHSG is simpler to implement since it can be implemented with the standard update equations.

9.1 The 1D Switched Huygen's Sub-gridding

9.1.1 SHSG Propositions

The HSG propositions state that sources in the non-working regions contribute no field to the working regions. This is not strictly true. Although a source placed somewhere within the non-working region contributes no field, it is not true for the electric field at the Inner Surface and the magnetic field at the Outer Surface.

Figure 9.1 illustrates this problem. The figure shows the IS in the HSG connecting two grids A and B where grid B has sub-gridding ratio 1:3. The field $H_{y_p}[is - \frac{1}{6}]$ is obtained via a transverse interpolation of the fields $H_{y_a}[is - \frac{1}{2}]$, $H_{y_a}[is + \frac{1}{2}]$. In addition, the introduction of a 3-node filter requires that $H_{y_a}[is - \frac{1}{2}]$, $H_{y_a}[is + \frac{1}{2}]$ are obtained by a weighted average of their nearest neighbours Bérenger (2006). Since these working region fields depend on non-working region fields any attenuation in $E_{z_a}[is]$, or magnetic fields in the non-working region results in an error in $H_{y_p}[is - \frac{1}{6}]$. Zhou et al. (2010) showed that it was not possible to alter the field values at the inner nodes of the non-working regions without attenuating the solution in the working region.

However, it is possible to ensure the magnetic or electric fields in the non-working regions are equal to zero by modifying the HSG Huygen's surfaces. Figure 9.2 shows a wavelet which is sourced in the same location in Grid A and B with the same spatial step
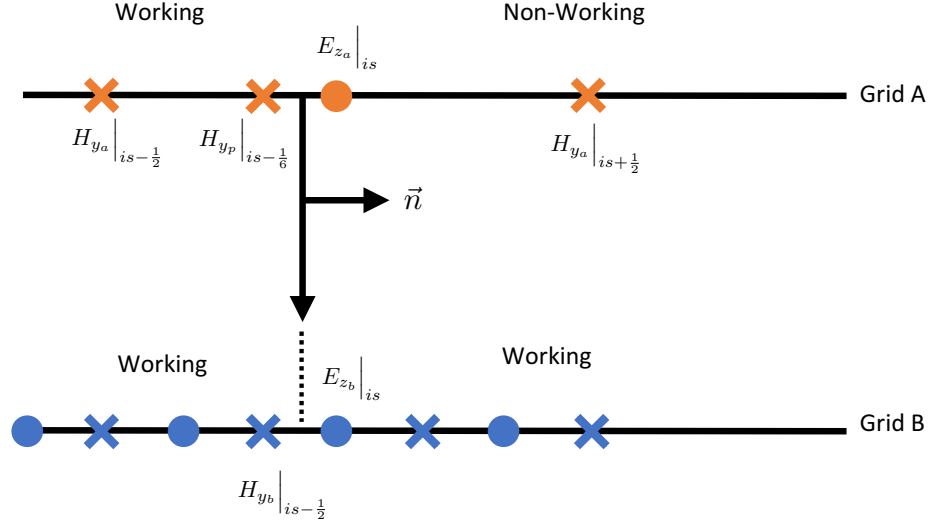
Figure 9.1: Incident field at the inner in the HSG for a 1:3 subgridding.
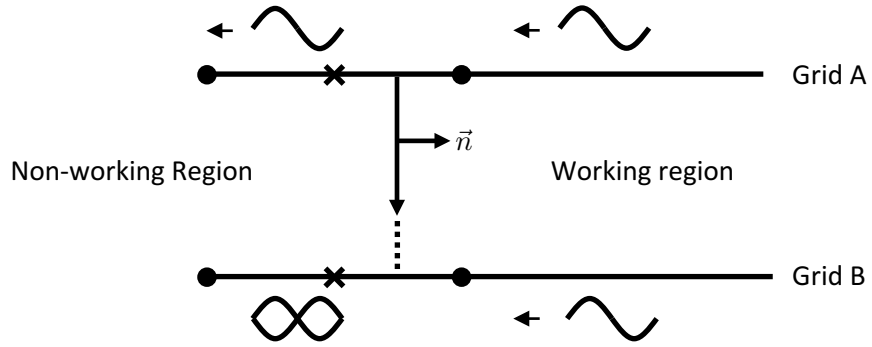
Figure 9.2: SHSG arrangement showing two identical wavelets propagating in each grid from the working region toward an anti-Huygen's surface. Subsequently, in the non-working region, the field in the grid B is annihilated with the flipped from from grid A.

and Courant number. The wavelet in each grid propagates toward an anti-Huygen's surface which radiates energy into the lower grid. The fields to the right of the surface are equal because they share the same update equations. This equality means that the incident electric field at the surface and the field at the same position in the sub-grid are equal. This is given by

$$
E_{z_a}\Big|_{i+1}^{ns} = E_{z_b}\Big|_{i+1}^{ns} \tag{9.1}
$$

Now, consider the 1d update equation for the magnetic field in the lower grid at the anti-Huygen's surface.

$$H_{y_b}\Big|_{i+\frac{1}{2}}^{ns+\frac{1}{2}} = H_{y_b}\Big|_{i+\frac{1}{2}}^{ns-\frac{1}{2}} + \frac{\Delta t}{\mu_0 \Delta x}\left(E_{z_b}\Big|_{i+1}^{ns} - E_{z_b}\Big|_{i-1}^{ns}\right) - \frac{\Delta t}{\mu_0 \Delta x}E_{z_a}\Big|_{i+1}^{ns} \qquad (9.2)$$

Substituting Equation 9.1 into Equation 9.2 gives

$$H_{y_b}\Big|_{i+\frac{1}{2}}^{ns+\frac{1}{2}} = H_{y_b}\Big|_{i+\frac{1}{2}}^{ns-\frac{1}{2}} - \frac{\Delta t}{\mu_0 \Delta x}E_{z_b}\Big|_{i-1}^{ns} \qquad (9.3)$$

The RHS terms are initially equal to zero when there are no sources in the lower grid to the left of the surface. Additionally, they are not dependent on any additional incident fields. Therefore the magnetic field on the LHS is always equal to zero.

$$H_{y_b}\Big|_{i+\frac{1}{2}}^{ns+\frac{1}{2}} = 0 \qquad (9.4)$$

The same argument can be made if electric and magnetic field nodes are switched and the magnetic field is the incident field. In both cases, the interior nodes have zero magnitudes. Notice also that the anti-Huygen's surface acts as a Huygen's surface when wavelet approached from the other side in Grid A and that sets up the initial correct sourcing criteria.

The field cancellation requires that the incoming fields are equal in both grids. This condition is satisfied by placing a Huygen's surface before the anti-Huygens surface as shown in Figure 9.3. These two surfaces are the basis of the SHSG. They form the new surfaces at the Outer Surface and the Inner Surfaces.

The new arrangement of Huygen's surfaces invokes a set of propositions which differ from HSG. These are as follows:

Proposition 9.1.1. *Fields which are radiated from non-working regions of each grid are viewed from the working regions of the opposing grid.*

Proposition 9.1.2. *Fields radiated between the working regions and the IS-OS gap are equal to the fields that would have propagated through a single space to those locations given the third proposition.*

Proposition 9.1.3. *Fields radiated from working regions are not viewed from the non-working regions of either grid.*
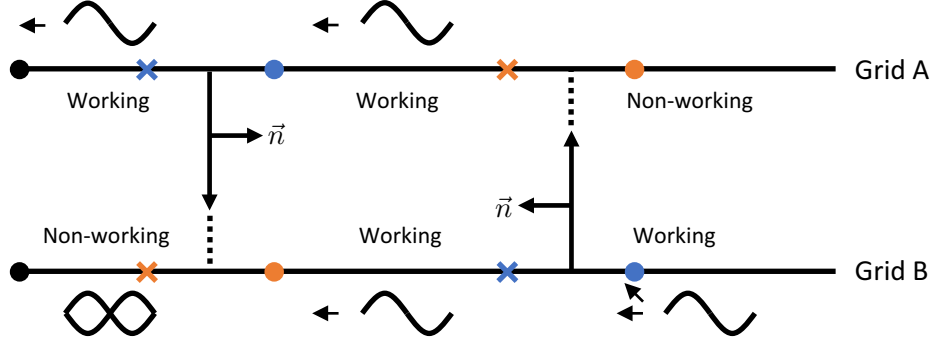
Figure 9.3: SHSG arrangement showing the action of a Huygens surface and an anti-Huygens surface on a wavelet sourced in the working region of grid B. The crosses indicate the positions of the magnetic fields and the circles indicate the positions of the electric fields. Orange is used to depict the fields which are updated by the SHSG algorithm, and blue is used to indicate the fields which are used by the SHSG algorithm.

The propositions are proven by considering the propagation of a wavelet sourced in the working region of Grid A and the non-working region of Grid B. The arrangement of the SHSG Huygen's surfaces for both of these problems are shown in Figure 9.4 and Figure 9.5 respectively.

In Figure 9.4 a wavelet is sourced in the working region of grid A. The OS radiates it into the working region of Grid B. The wavelets in the IS-OS gap are now equal. This is the first proof of the second proposition. Next at the IS, the wavelet in the IS-OS gap in Grid A propagates into the non-working region of Grid A. Simultaneously, the wavelet at the same location in Grid B passes into the working region of Grid B. Also, The IS radiates and flips the field into grid A. The resulting wavelets in grid A cancel out. This is the first proof of the third proposition. The wavelet in the working region of Grid B is now effectively a new source. The wavelet is radiated into the IS-OS gap of Grid A by the IS. The fields in both IS-OS gaps are now equal. This is the second proof of proposition two. The wavelet is then radiated and flipped from Grid A to Grid B via the anti-Huygen's surface. The fields in the non-working region of Grid B are equal and opposite and therefore cancel each other out. This is the second proof of proposition three.

The first proposition is proven by considering the propagation of a wavelet from the non-working region of grid B. The process is illustrated in Figure 9.5. First, the wavelet propagates into the IS-OS gap in Grid B. This is a working region. Therefore this is the first proof of the first proposition. Additionally, the second proposition is broken. The wavelet is then radiated and flipped into the non-working region of Grid A. The wavelet in Grid B is then radiated into Grid A where it cancels with the existing
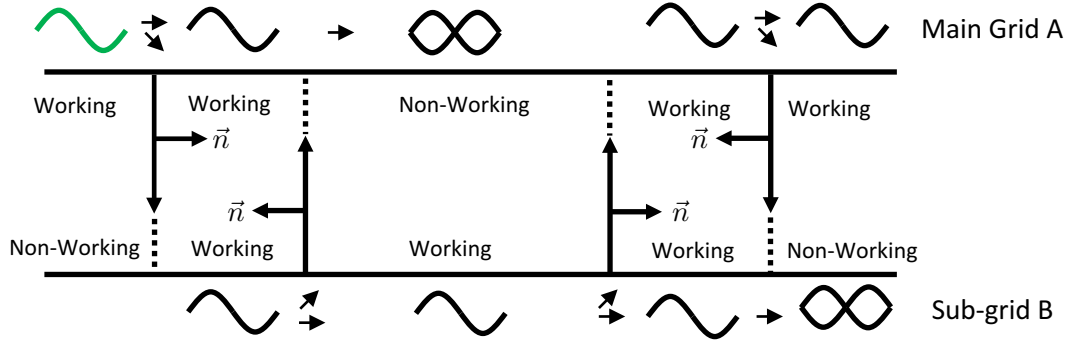
Figure 9.4: The arrangement of the Huygen's surfaces in the SHSG sub-gridding. The action of the SHSG on wavelets sourced in the working region of grid A is shown. It illustrates that the fields in working regions are always correct and the fields in non-working regions are zero provided there is no sourcing in those regions.
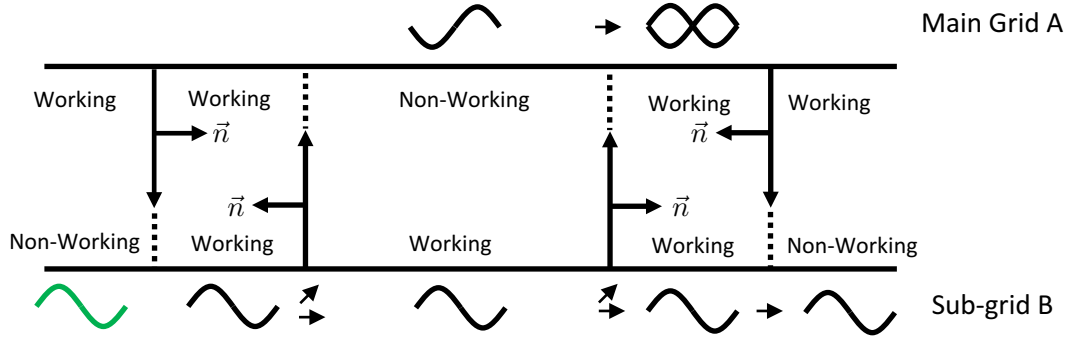
Figure 9.5: The arrangement of the Huygen's surfaces in the SHSG sub-gridding. The action of the SHSG on wavelets sourced in the non-working region of grid B is shown. It illustrates that the fields in working regions are incorrect when a wavelet is sourced in the working regions.

wavelet. The wavelet in grid B propagates into the IS-OS region. Again the second proposition is broken and the third proposition is proven.

The first proposition appears problematic as non-physical fields are radiated into the working region. However, there is **no requirement** to place sources within the non-working region and there should never be one. As all field values are zero at the start of the process, in theory, they should remain so. Furthermore, any scatterers which are placed in the non-working region do not give rise to reflections. This is because the total field in these regions is zero due to proposition three.

Another benefit of the SHSG is that the fields in the IS-OS gap **in either grid** are the physical fields. In the HSG the sum of these fields is the physical field. Subsequently,

to obtain the correct field in the IS-OS gap in the sub-grid the main grid fields must be interpolated in space and time. However, in the SHSG the fields are simply sampled as needed and the correct field is obtained directly.

9.1.2 Numerical Proof of Propositions

Bérenger (2006) proved numerically the HSG propositions in 1d. In these experiments, the working region of the main grid was sourced at Point 1 in Figure 9.6. The resulting field is monitored at the numerical locations also shown in Figure 9.6. Additionally, PEC plates are placed in the locations of Object A and Object B. The propositions were proved by observing the resulting fields at points 1-6 with and without the PEC sheets.

The experiments are repeated to prove the propositions of the SHSG. In the first experiment, the field is sourced at location 1a in Figure 9.6 using the pulse given by Bérenger (2006). The sub-gridding ratio is equal to 99. Note that a PML has not been used to truncate the sub-grid. The resulting fields are shown in Figure 9.7. From proposition two, the fields at 2a and 2b should be identical. This is clearly shown from the agreement of the solutions. At 3a proposition three states the field is zero. The solution at 3a is in very good agreement. The fields at 3b and 6a show that the wavelet propagates through the SHSG as expected.
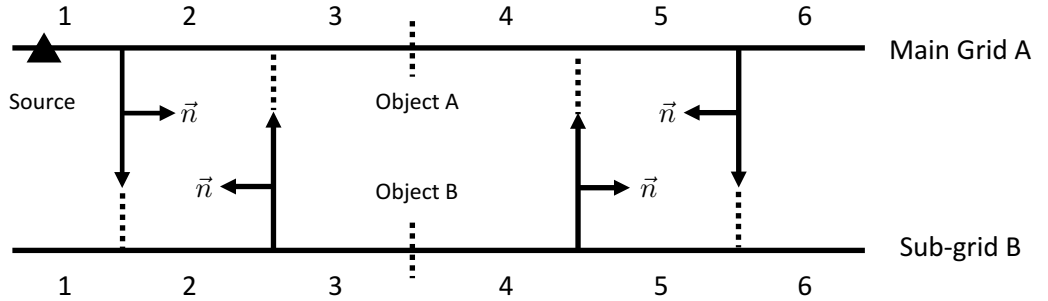
Figure 9.6: The arrangement of the Huygen's surface in the SHSG and the positions of the receivers for the proof of propositions and thin lossy layer experiments.

In the next experiment, a PEC material is placed at the location of Object A. The purpose of which is to reflect any incoming field into the working region of the main grid. As in the first experiment the field is sourced at 1a. The E_z field at the locations 1a, 2a, 2b, 3a, 6a are shown in Figure 9.8.

Solutions 1a, 2a, 2b, 3a, 6a are in excellent agreement with those in the first experiment. This shows that the PEC placed in the non-working region does not affect the solution in the working regions. The reason for this is that the field in this region is zero. This is proved by the zero magnitudes of the solution at 3a.

In the next experiment the PEC material is placed in the working region of the sub-grid at location object B. The E_z field at the locations 1a, 3a, 5a, 5b, 6a is shown in Figure 9.9.

The solution at 1a shows the initial pulse propagation followed by the inverted pulse reflected from the PEC in the sub-grid. The E_z field at the other locations is zero. At 6a the field should be zero as there is no transmission through the PEC. Additionally, the E_z at locations 5a and 5b is zero. This is in agreement with proposition two. In the HSG these fields are non-zero and equal and opposite and magnitude.
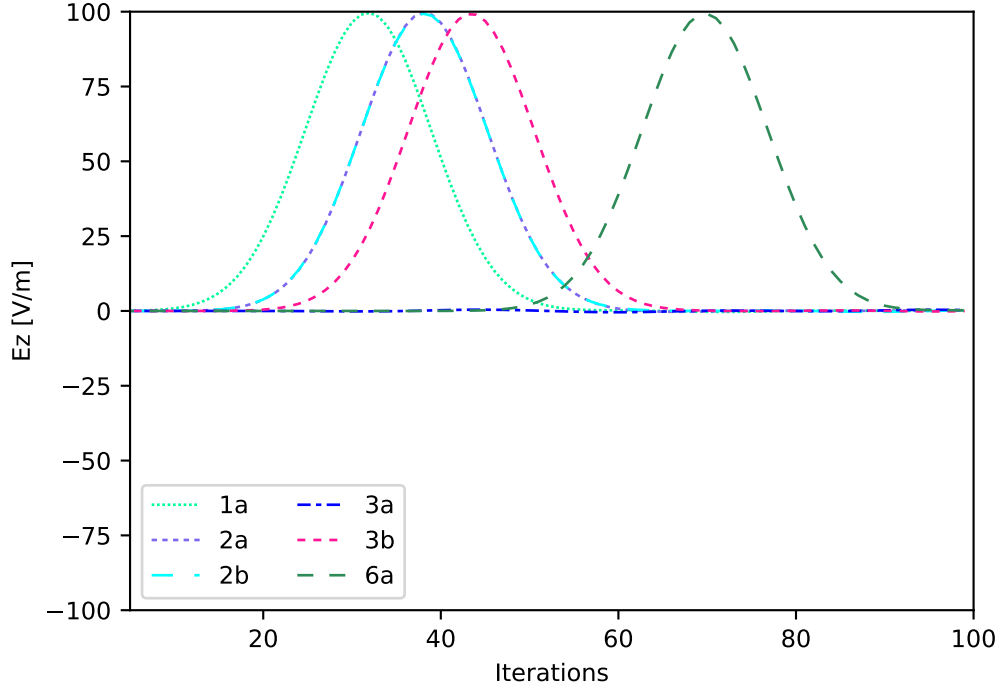
Figure 9.7: Electric fields measured at the receivers indicated in figure 9.6
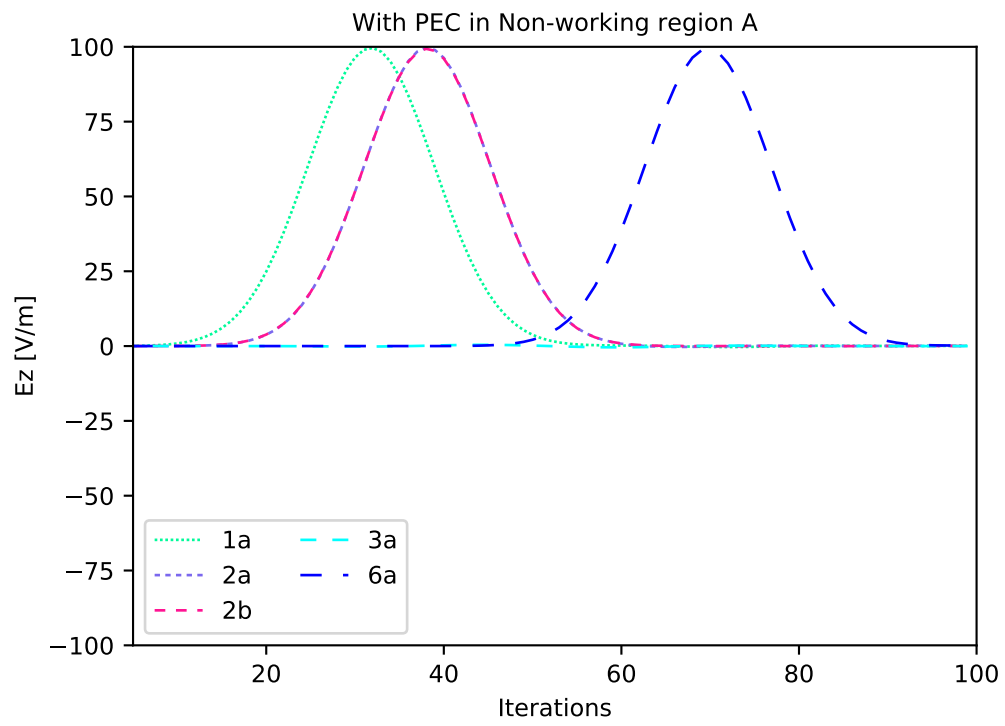
Figure 9.8: Electric fields measured at the receivers indicated in figure 9.6 with PEC at the location of Object A
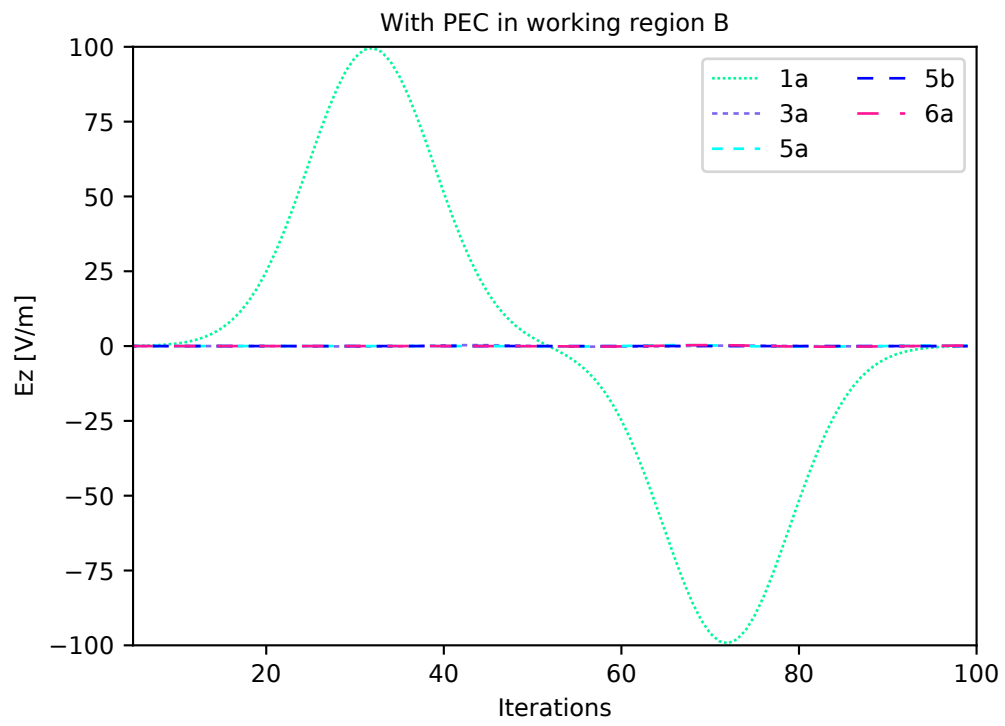
Figure 9.9: Electric fields measured at the receivers indicated in figure 9.6 with PEC at the location of Object B

9.1.3 Loss factors

The propositions state that the field in the non-working region is zero. Consequently, the fields in the regions can be attenuated using electric and magnetic loss terms, σ_e, σ_m without affecting the physical solution.

In lossy, isotropic, linear medium the update equations in these regions are given by

$$H_y\Big|_{i+\frac{1}{2}}^{ns+\frac{1}{2}} = \frac{1-l_m}{1+l_m}H_y\Big|_{i+\frac{1}{2}}^{ns-\frac{1}{2}} + \frac{\frac{\Delta t}{\mu\Delta x}}{1+l_m}\left(E_z\Big|_{i+1}^{ns} - E_z\Big|_{i-1}^{ns}\right) \tag{9.5}$$

and

$$E_z\Big|_{i}^{ns} = \frac{1-l_e}{1+l_e}E_z\Big|_{i}^{ns-1} + \frac{\frac{\Delta t}{\mu\Delta x}}{1+l_e}\left(H_y\Big|_{i+\frac{1}{2}}^{ns-\frac{1}{2}} - H_y\Big|_{i-\frac{1}{2}}^{ns-\frac{1}{2}}\right) \tag{9.6}$$

where the loss factors l_m and l_e are given by

$$l_m = \frac{\sigma_m \Delta t}{2\mu} \tag{9.7}$$

and

$$l_e = \frac{\sigma_e \Delta t}{2\epsilon} \tag{9.8}$$

At the left OS, the update equation for H_y is given by

$$H_{y_b}\Big|_{i+\frac{1}{2}}^{ns+\frac{1}{2}} = \frac{1-l_m}{1+l_m}H_{y_b}\Big|_{i+\frac{1}{2}}^{ns-\frac{1}{2}} + \frac{\frac{\Delta t}{\mu\Delta x}}{1+l_m}\left(E_{z_b}\Big|_{i+1}^{ns} - E_{z_b}\Big|_{i-1}^{ns}\right) -$$
$$\frac{\frac{\Delta t}{\mu\Delta x}}{1+l_m}E_{z_{inc}}\Big|_{i+1}^{ns} \tag{9.9}$$

At the right OS, the update equation for H_y is given by

$$H_{y_b}\Big|_{i+\frac{1}{2}}^{ns+\frac{1}{2}} = \frac{1-l_m}{1+l_m}H_{y_b}\Big|_{i+\frac{1}{2}}^{ns-\frac{1}{2}} + \frac{\frac{\Delta t}{\mu\Delta x}}{1+l_m}\left(E_{z_b}\Big|_{i+1}^{ns} - E_{z_b}\Big|_{i-1}^{ns}\right)+$$

$$\frac{\frac{\Delta t}{\mu\Delta x}}{1+l_m}E_{z_{inc}}\Big|_{i-1}^{ns} \qquad (9.10)$$

The update for the E_z at the OS is unaltered. This field cannot be attenuated as it is a physical non-zero field. However, the E_z update equation at the IS is modified as they are within the non-working region.

At the left IS the update equation E_z is given by

$$E_{z_a}\Big|_i^{ns} = \frac{1-l_e}{1+l_e}E_{z_a}\Big|_i^{ns-1} + \frac{\frac{\Delta t}{\mu\Delta x}}{1+l_e}\left(H_{z_a}\Big|_{i+\frac{1}{2}}^{ns-\frac{1}{2}} - H_{z_a}\Big|_{i-\frac{1}{2}}^{ns-\frac{1}{2}}\right)+$$

$$\frac{\frac{\Delta t}{\mu\Delta x}}{1+l_e}H_{y_{inc}}\Big|_{i-\frac{1}{2}}^{ns-\frac{1}{2}} \qquad (9.11)$$

At right IS the update equation E_z is given by

$$E_{z_a}\Big|_i^{ns} = \frac{1-l_e}{1+l_e}E_{z_a}\Big|_i^{ns-1} + \frac{\frac{\Delta t}{\mu\Delta x}}{1+l_e}\left(H_{z_a}\Big|_{i+\frac{1}{2}}^{ns-\frac{1}{2}} - H_{z_a}\Big|_{i-\frac{1}{2}}^{ns-\frac{1}{2}}\right)-$$

$$\frac{\frac{\Delta t}{\mu\Delta x}}{1+l_e}H_{y_{inc}}\Big|_{i+\frac{1}{2}}^{ns-\frac{1}{2}} \qquad (9.12)$$
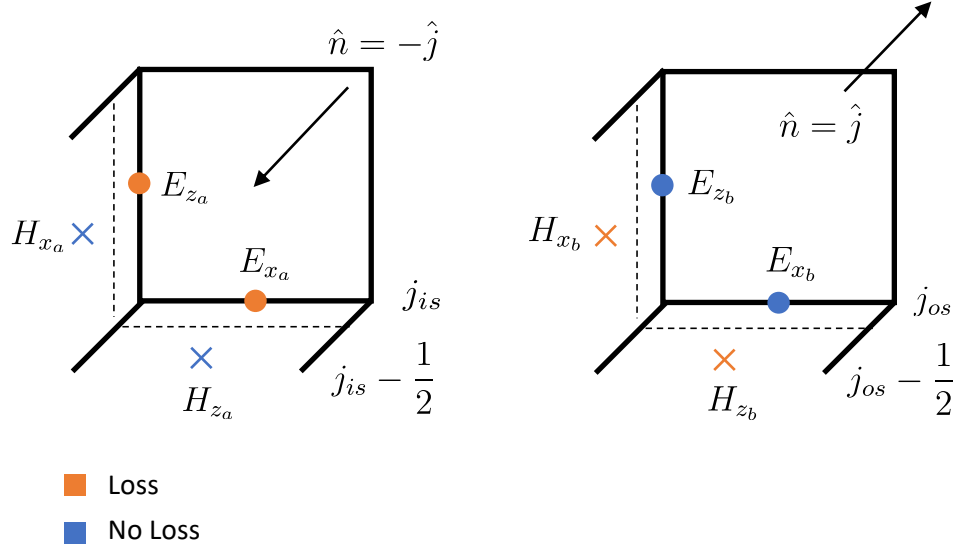
Figure 9.10: Positions of the lossy nodes in the front face in the front faces of the Inner and Outer Surfaces in the SHSG.

9.1.4 Thin Conductive Sheet Experiments

This experiment measures the transmission co-efficient from a thin conductive sheet embedded within the sub-grid. The experiment was first introduced by Bérenger (2006) as a test of HSG's accuracy. For comparison, the equivalent experiment for the SHSG is repeated here.

A region in the main grid is sub-gridded using a ratio of 99. A 10 cell thick conductive layer is positioned at Object B in Figure 9.6. The conductivity of the layer is varied between 100, 1000, 3000, 10000 $\mathrm{S\,m^{-1}}$. The transmission coefficient is calculated as the ratio of the Fourier transformed transmitted field to the incident field. The incident field is obtained numerically from an initial trial run where the conductive layer is removed.

The experiment was run using the SHSG and the HSG. In the HSG case, both the PML and the 3 node filter were required to stabilise the solution for the required number of iterations to obtain a well-resolved solution in the frequency domain. In the SHSG case, the filter was not applied. Additionally, no PML was placed in the non-working region. Instead the loss factors $l_m = 1$ and $l_e = 1$ were used in the main grid and the sub-grid at the points described by Equations 9.9 9.10, 9.11 and 9.12. The simulation is stable for at least the same duration as the HSG.

The transmission coefficients for the SHSG are shown in Figure 9.11. The agreement

is very good over the range of frequencies studied in the literature. Figure 9.12 shows the transmission coefficients obtained for the HSG. The results show a far poorer agreement. The literature shows the results for the HSG where a PEC layer is placed at the location of object A in Figure 9.6. These results are shown in Figure 9.13 and show a similar agreement to the SHSG results. The explanation given for the improvement in the agreement is that the cancellation of the fields at the Huygen's surfaces is not perfect at high frequencies and subsequently these frequencies penetrate the non-working region and corrupt the response. The PEC layer reflects the spurious field and therefore the cancellation at the right-hand IS is improved. This indicates a similar process occurs with the loss factor. The loss factor attenuates the spurious field and a better agreement is observed.
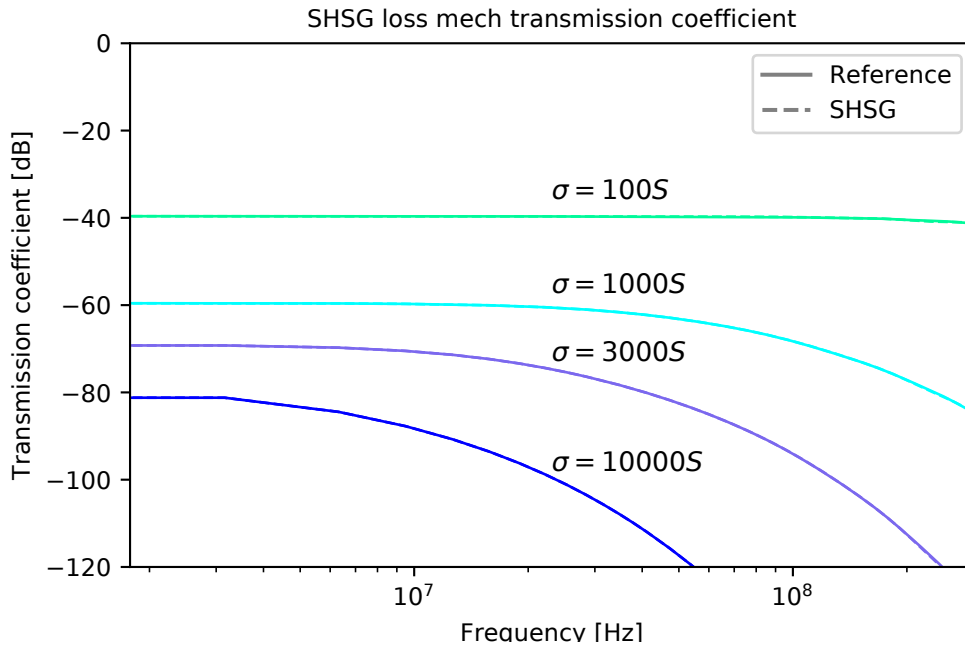
Figure 9.11: Transmission coefficient measured for a thin loss layer with different conductivities in the SHSG.

Bérenger (2006) does not analyse the effects of the HSG on the reflection coefficient. This is presumably because the PEC layer reflects the spurious field toward the source and corrupts the solution.

In this experiment, the reflection coefficient from the thin conductive layer is measured for the HSG and the SHSG. In the HSG case, the PEC is placed at location object A. In the SHSG the loss factor is used at the IS and OS as demonstrated previously. The reflection coefficients for the HSG and SHSG are shown in Figure 9.14 and Figure 9.15 respectively.
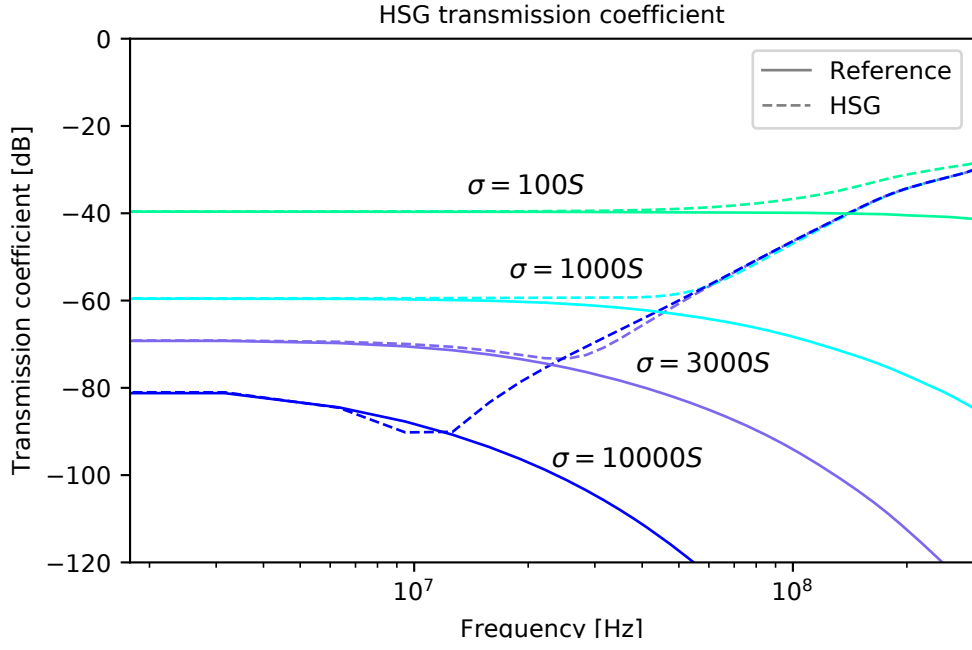
Figure 9.12: Transmission coefficient measured for a thin loss layer with different conductivities in the HSG.
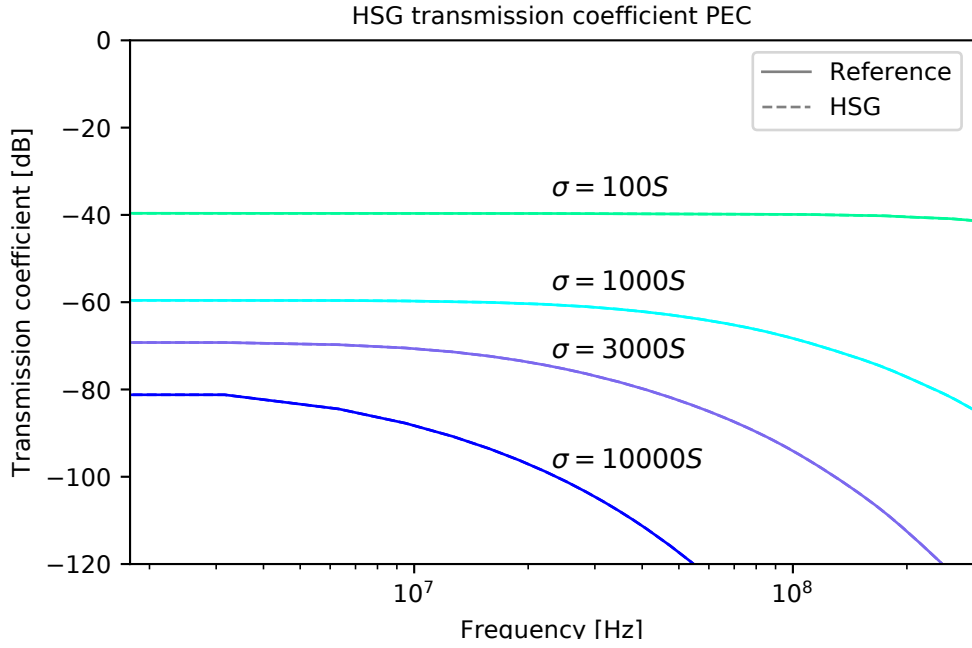
Figure 9.13: Transmission coefficient measured for a thin loss layer with different conductivities in the HSG and PEC at Object A location.

The agreement between the reflection coefficients and the reference solution are poorer than the transmission coefficients for both sub-griddings. The agreement be-

tween the SHSG and the reference solution is better than the HSG. This result demonstrates that the attenuation of the spurious field by the loss factor yields a more accurate result than the PEC method. The reason for this is the loss factor method does not reflect the spurious field toward the source.
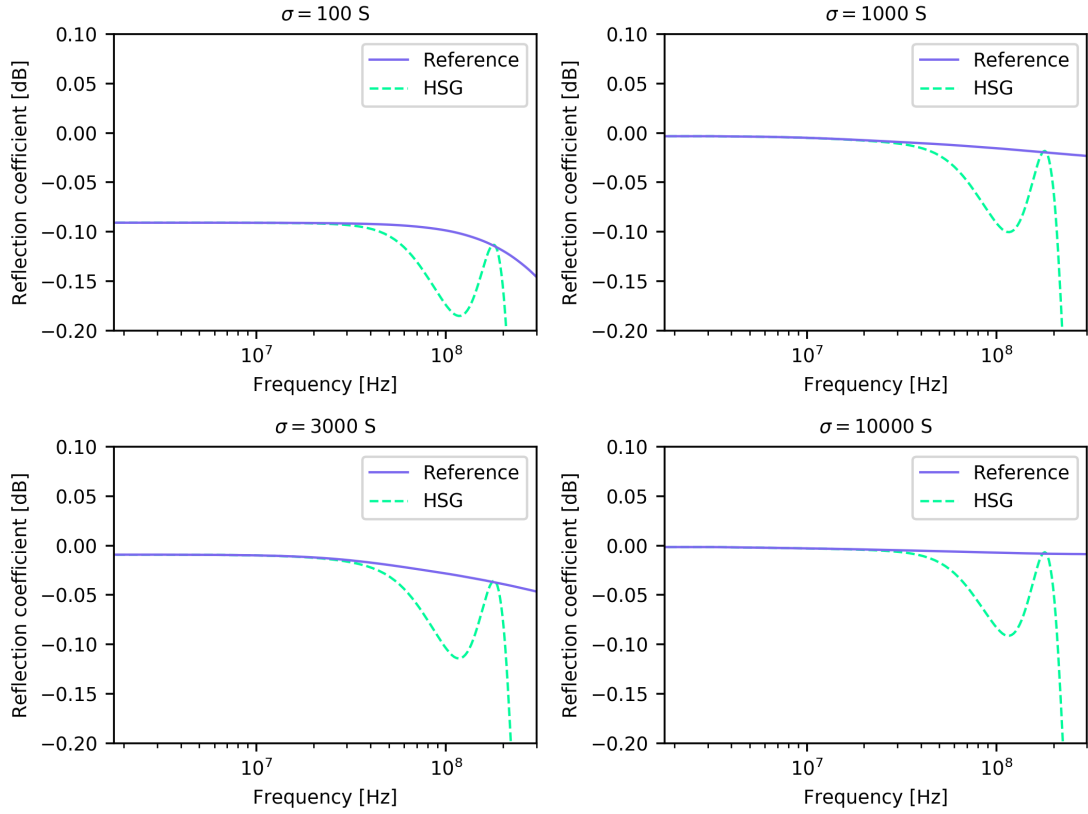
Figure 9.14: Reflection coefficient for a thin lossy layer embedded in a 1d HSG sub-grid. The conductivity of the layer is varied from 100-1000 S.
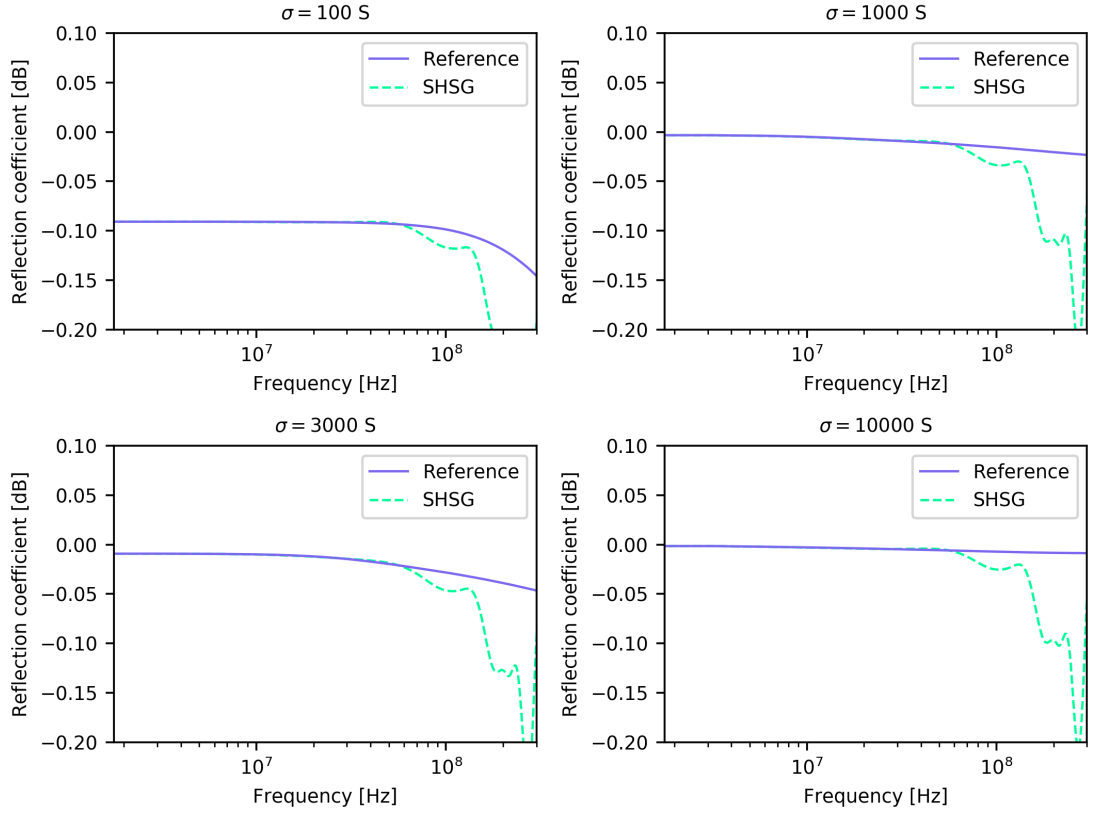
Figure 9.15: Reflection coefficient for a thin lossy layer embedded in a 1d SHSG sub-grid. The conductivity of the layer is varied from 100-1000 S.

9.2 3D Switched Huygen's Sub-Gridding

The SHSG is extended from 1d to 3d by considering the 3d Huygen's surfaces and their surface normals. Figure 9.10 shows the front faces of Inner Surface and the Outer surface. In the SHSG the Inner Surface surface normal points out of the sub-grid and the Outer Surface surface normal points into the sub-grid. Additionally, the loss factor is applied to the fields in the opposite direction from the surface normal. From these observations, the 3d updates equations at the front IS are given below. The equations are expressed in terms of the incident field which is obtained using the precursor formulation described in chapter 6. Additionally, the update equations for the back, left, right, bottom and top surface are simply permutations of these equations.

Update equations for the fields at the front Inner Surface.

$$
\begin{aligned}
E_{x_a}\Big|_{i+\frac{1}{2},j,k}^{ns+1} = {}& \frac{1-l_e}{1+l_e} E_{x_a}\Big|_{i+\frac{1}{2},j,k}^{ns} \\
& + \frac{\frac{\Delta t}{\epsilon \Delta l}}{1+l_e}\left(\left\{ H_{z_a}\Big|_{i+\frac{1}{2},j+\frac{1}{2},k}^{ns+\frac{1}{2}} - H_{z_a}\Big|_{i+\frac{1}{2},j-\frac{1}{2},k}^{ns+\frac{1}{2}} \right\} - \left\{ H_{y_a}\Big|_{i+\frac{1}{2},j,k+\frac{1}{2}}^{ns+\frac{1}{2}} - H_{y_a}\Big|_{i+\frac{1}{2},j,k}^{ns+\frac{1}{2}} \right\}\right) \\
& + \frac{\frac{\Delta t}{\epsilon \Delta l}}{1+l_e} H_{z_{inc}}\Big|_{i+\frac{1}{2},j_{is}-\frac{1}{2},k}^{ns+\frac{1}{2}} \quad (9.13)
\end{aligned}
$$

$$
\begin{aligned}
E_{z_a}\Big|_{i,j,k+\frac{1}{2}}^{ns+1} = {}& \frac{1-l_e}{1+l_e} E_{z_a}\Big|_{i,j,k+\frac{1}{2}}^{ns} \\
& + \frac{\frac{\Delta t}{\epsilon \Delta l}}{1+l_e}\left(\left\{ H_{y_a}\Big|_{i+\frac{1}{2},j,k+\frac{1}{2}}^{ns+\frac{1}{2}} - H_{y_a}\Big|_{i-\frac{1}{2},j,k+\frac{1}{2}}^{ns+\frac{1}{2}} \right\} - \left\{ H_{x_a}\Big|_{i,j+\frac{1}{2},k+\frac{1}{2}}^{ns+\frac{1}{2}} - H_{x_a}\Big|_{i,j-\frac{1}{2},k}^{ns+\frac{1}{2}} \right\}\right) \\
& - \frac{\frac{\Delta t}{\epsilon \Delta l}}{1+l_e} H_{x_{inc}}\Big|_{i,j-\frac{1}{2},k+\frac{1}{2}}^{ns+\frac{1}{2}} \quad (9.14)
\end{aligned}
$$

$$
\begin{aligned}
H_{z_a}\Big|_{i,j+\frac{1}{2},k+\frac{1}{2}}^{ns+\frac{1}{2}} = {}& H_{z_a}\Big|_{i,j+\frac{1}{2},k+\frac{1}{2}}^{ns-\frac{1}{2}} \\
& + \frac{\Delta t}{\mu \Delta l}\left(\left\{ E_{x_a}\Big|_{i+\frac{1}{2},j+1,k}^{ns} - E_{x_a}\Big|_{i+\frac{1}{2},j,k}^{ns} \right\} - \left\{ E_{y_a}\Big|_{i+1,j,k+\frac{1}{2}}^{ns} - E_{y_a}\Big|_{i,j,k+\frac{1}{2}}^{ns} \right\}\right) \\
& + \frac{\Delta t}{\mu \Delta l} E_{x_{inc}}\Big|_{i+\frac{1}{2},j+1,k}^{ns} \quad (9.15)
\end{aligned}
$$

$$
\begin{aligned}
H_{x_a}\Big|_{i,j+\frac{1}{2},k+\frac{1}{2}}^{ns+\frac{1}{2}} = {}& H_{x_a}\Big|_{i,j+\frac{1}{2},k+\frac{1}{2}}^{ns-\frac{1}{2}} \\
& + \frac{\Delta t}{\mu \Delta l}\left(\left\{ E_{y_a}\Big|_{i,j+\frac{1}{2},k+1}^{ns} - E_{y_a}\Big|_{i,j+\frac{1}{2},k}^{ns} \right\} - \left\{ E_{z_a}\Big|_{i,j+1,k+\frac{1}{2}}^{ns} - E_{z_a}\Big|_{i,j,k+\frac{1}{2}}^{ns} \right\}\right) \\
& - \frac{\Delta t}{\mu \Delta l} E_{z_{inc}}\Big|_{i,j+1,k+\frac{1}{2}}^{ns} \quad (9.16)
\end{aligned}
$$

Update equations for the fields at the front Outer Surface.

$$
E_{x_b}\Big|_{i+\frac{1}{2},j,k}^{ns+1} = E_{x_b}\Big|_{i+\frac{1}{2},j,k}^{ns}
$$

$$
+ \frac{\Delta t}{\epsilon \Delta l}\left(\left\{H_{z_b}\Big|_{i+\frac{1}{2},j+\frac{1}{2},k}^{ns+\frac{1}{2}} - H_{z_b}\Big|_{i+\frac{1}{2},j-\frac{1}{2},k}^{ns+\frac{1}{2}}\right\} - \left\{H_{y_b}\Big|_{i+\frac{1}{2},j,k+\frac{1}{2}}^{ns+\frac{1}{2}} - H_{y_b}\Big|_{i+\frac{1}{2},j,k}^{ns+\frac{1}{2}}\right\}\right)
$$

$$
- \frac{\Delta t}{\epsilon \Delta l}H_{z_{inc}}\Big|_{i+\frac{1}{2},j_{is}-\frac{1}{2},k}^{ns+\frac{1}{2}} \qquad (9.17)
$$

$$
E_{z_b}\Big|_{i,j,k+\frac{1}{2}}^{ns+1} = E_{z_b}\Big|_{i,j,k+\frac{1}{2}}^{ns}
$$

$$
+ \frac{\Delta t}{\epsilon \Delta l}\left(\left\{H_{y_b}\Big|_{i+\frac{1}{2},j,k+\frac{1}{2}}^{ns+\frac{1}{2}} - H_{y_b}\Big|_{i-\frac{1}{2},j,k+\frac{1}{2}}^{ns+\frac{1}{2}}\right\} - \left\{H_{x_b}\Big|_{i,j+\frac{1}{2},k+\frac{1}{2}}^{ns+\frac{1}{2}} - H_{x_b}\Big|_{i,j-\frac{1}{2},k}^{ns+\frac{1}{2}}\right\}\right)
$$

$$
+ \frac{\Delta t}{\epsilon \Delta l}H_{x_{inc}}\Big|_{i,j-\frac{1}{2},k+\frac{1}{2}}^{ns+\frac{1}{2}} \qquad (9.18)
$$

$$
H_{z_b}\Big|_{i,j+\frac{1}{2},k+\frac{1}{2}}^{ns+\frac{1}{2}} = \frac{1-l_m}{1+l_m}H_{z_a}\Big|_{i,j+\frac{1}{2},k+\frac{1}{2}}^{ns-\frac{1}{2}}
$$

$$
+ \frac{\frac{\Delta t}{\mu \Delta l}}{1+l_m}\left(\left\{E_{x_b}\Big|_{i+\frac{1}{2},j+1,k}^{ns} - E_{x_b}\Big|_{i+\frac{1}{2},j,k}^{ns}\right\} - \left\{E_{y_b}\Big|_{i+1,j,k+\frac{1}{2}}^{ns} - E_{y_b}\Big|_{i,j,k+\frac{1}{2}}^{ns}\right\}\right)
$$

$$
- \frac{\frac{\Delta t}{\mu \Delta l}}{1+l_m}E_{x_{inc}}\Big|_{i+\frac{1}{2},j+1,k}^{ns} \qquad (9.19)
$$

$$
H_{x_b}\Big|_{i,j+\frac{1}{2},k+\frac{1}{2}}^{ns+\frac{1}{2}} = \frac{1-l_m}{1+l_m}H_{x_b}\Big|_{i,j+\frac{1}{2},k+\frac{1}{2}}^{ns-\frac{1}{2}}
$$

$$
+ \frac{\frac{\Delta t}{\mu \Delta l}}{1+l_m}\left(\left\{E_{y_b}\Big|_{i,j+\frac{1}{2},k+1}^{ns} - E_{y_b}\Big|_{i,j+\frac{1}{2},k}^{ns}\right\} - \left\{E_{z_b}\Big|_{i,j+1,k+\frac{1}{2}}^{ns} - E_{z_b}\Big|_{i,j,k+\frac{1}{2}}^{ns}\right\}\right)
$$

$$
+ \frac{\frac{\Delta t}{\mu \Delta l}}{1+l_m}E_{z_{inc}}\Big|_{i,j+1,k+\frac{1}{2}}^{ns} \qquad (9.20)
$$

9.2.1 SHSG Accuracy

The accuracy of the 3d SHSG is measured by considering the total reflected energy of a plane wave incident on an empty sub-grid. This is computed by placing an empty sub-grid within the total field region of the total-field scattered-field formulation and

illuminating it with a Gaussian pulse. In the ideal case, there is no reflection. However, any reflected field is an indication of the error generated by the Huygen's surfaces.

Figure 9.16 shows the cumulative reflected squared electric field from a $14\Delta l \times l14\Delta l \times 14\Delta l$ sub-grid. The results show the SHSG can also be used with a range of sub-gridding ratios without any coherent effect on the accuracy.
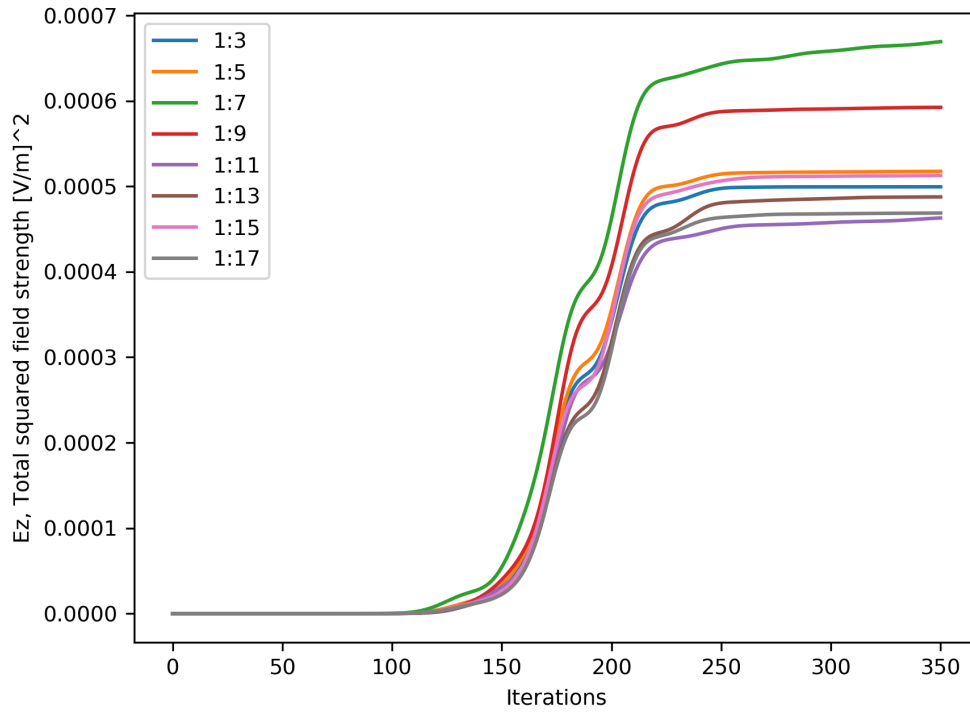
Figure 9.16: Comparison of the reflection from the SHSG sub-grid when illuminated by a Gaussian plane wave

9.2.2 Stability of the Huygen's Sub-gridding Schemes

A comparison of the stability in the HSG and SHSG is made in the following numerical experiments. A stringent test of the stability of the sub-gridding is to perform the sub-gridding within a resonant cavity. The cavity ensures that no energy leaves the system and thus the only way for unstable energy to leave the system is by the additional stability methods. Also, a small sub-grid is to encourage instability. This is because corner and edge nodes introduce greater errors since they require 2 updates. When the sub-grid is small the error is larger as the contribution to the total field from the edges and corners is greater.

In each of the following experiments the resonant cavity consists of a square computation domain with dimensions $36\Delta l \times 36\Delta l \times 36\Delta l$ where $\Delta l = 5 \times 10^{-2}$ m. The sub-grid is bounded by a PEC wall which ensures total reflection of the fields. The sub-grid is positioned at the centre of the domain and has dimensions $12\Delta l \times 12\Delta l \times 12\Delta l$. The sub-gridding ratio is set to 3. The sub-grid is excited at its centre by a y polarised Hertzian dipole source. The dipole is fed with a normalised first derivative Gaussian pulse with centre frequency 100 MHz. The highest significant frequency of interest is 350 MHz and is resolved in space by $N_\lambda = 17$. The resulting E_y field is measured in the main grid throughout the simulation.

The sub-gridding is advanced for three cases. In the first case there is no PML present in the non-working region of the sub-grid and the 3-node filter is switched off. This scenario corresponds to the HSG with no additional stability methods and thus most unstable case. In the second case, a six-cell PML is positioned three cells from the OS within the non-working region of the sub-grid. In the third case, the 3-node filter is switched on in addition to the PML. This case has the maximum possible stability.

The E_y field for each case is shown in Figure 9.17. The results show that the introduction of each method increases the stability of the HSG. In the first case where there are no stability methods, the instability emerges at ≈ 1000 iterations. The application of the PML increases the number of stable iterations to ≈ 3000. The combination of the 3-node filter and the PML increase the stable period to ≈ 9000 iterations.
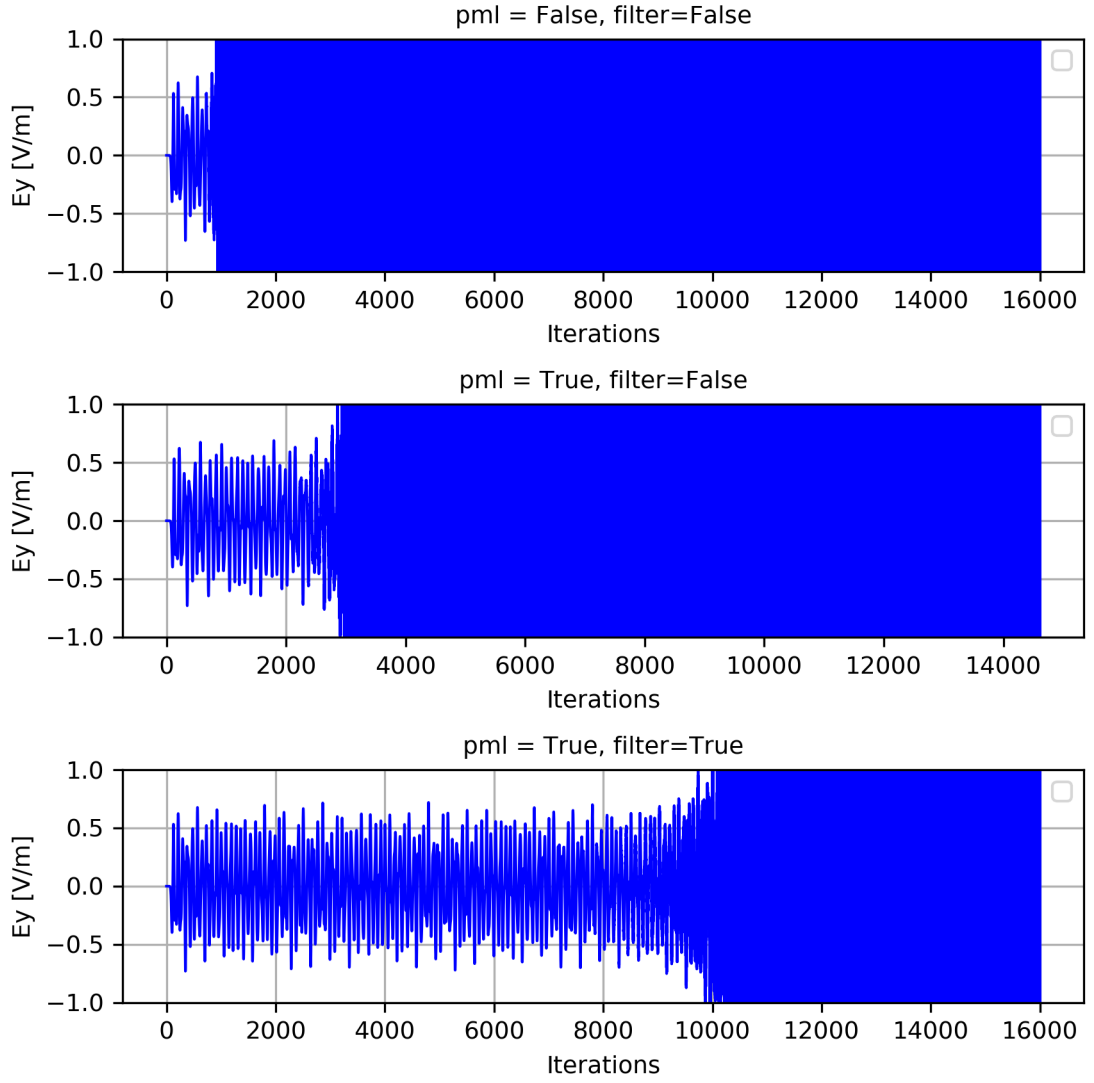
Figure 9.17: Ey field demonstrating the the stability of the HSG under a resonant test for each stability method.

9.2.3 HSG Artificial Loss

Artificial losses have previously been introduced to the HSG to reduce the instability. Zhou (2012) found that the smallest loss factors which maintained the stability for 40000 iterations were $l_e = 0.0375$ and $l_m = 0.0375$. However, the loss factors were found to attenuate the field within the non-dispersed region of the spectrum.

In this experiment the loss factors $l_e, l_m = 0.0375$ and $l_e, l_m = 1$ are applied to the fields in HSG and the SHSG at the locations shown in Figure 9.10. In addition the PML is removed from both experiments. The E_y responses are shown in comparison with a fine grid reference solution in Figure 9.18.

The HSG results show that when the loss factors are equal to 1 the solution is stable for at least 4000 iterations. However, the signal is rapidly attenuated. This is due to the presence of electric and magnetic conductivity in the physical problem. Also, the phase and magnitudes of the sub-grid signal rapidly diverge from the reference solution. One reason for this is the field is partially reflected from the conductive layer. Consequently, this field interferes with the physical field and results in a non-physical field. An important implication of this is the physical signal can not be recovered by applying a time-varying gain. A similar result is shown when the loss factors are equal to 0.0375 although the rate of attenuation is lower. Also, the onset of instability is quicker. Clearly, in both cases, the loss factor causes an unacceptable error in the response.

The result of the SHSG with $l_e, l_m = 1$ experiment show a good agreement with the reference solution. This finding is contrary to the HSG experiments where the loss factor resulted in immediate attenuation of the signal. Also, the experiment was stable for approximately 8000 iterations. This corresponds to $\times 8$ increase in stability over the HSG. And $\times 2.7$ times increase over the HSG with the PML. These findings suggest that the application of loss factors to the SHSG extends its stability beyond the stability of the HSG. And also, the accuracy of the SHSG with loss factors is significantly increased than the HSG with loss factors.
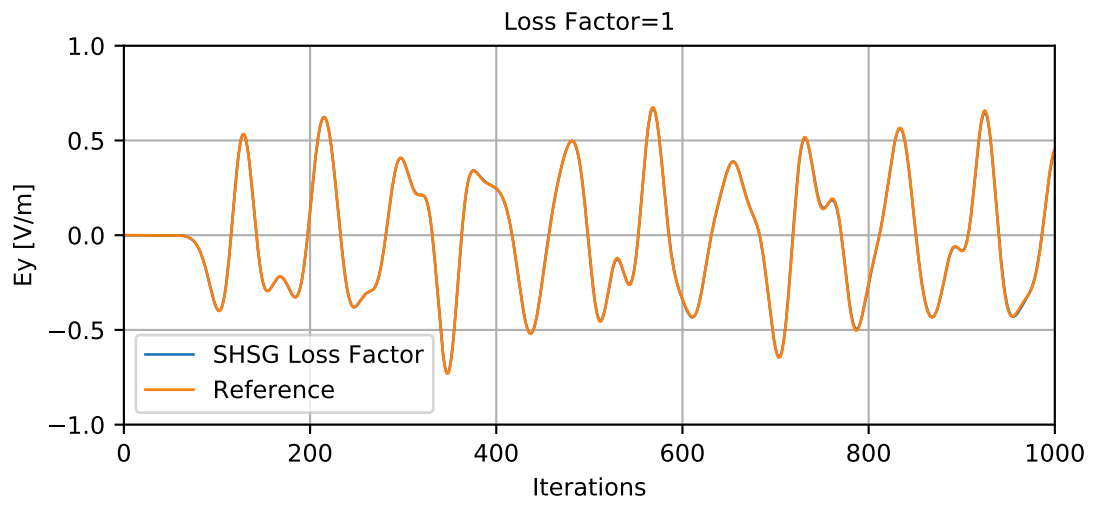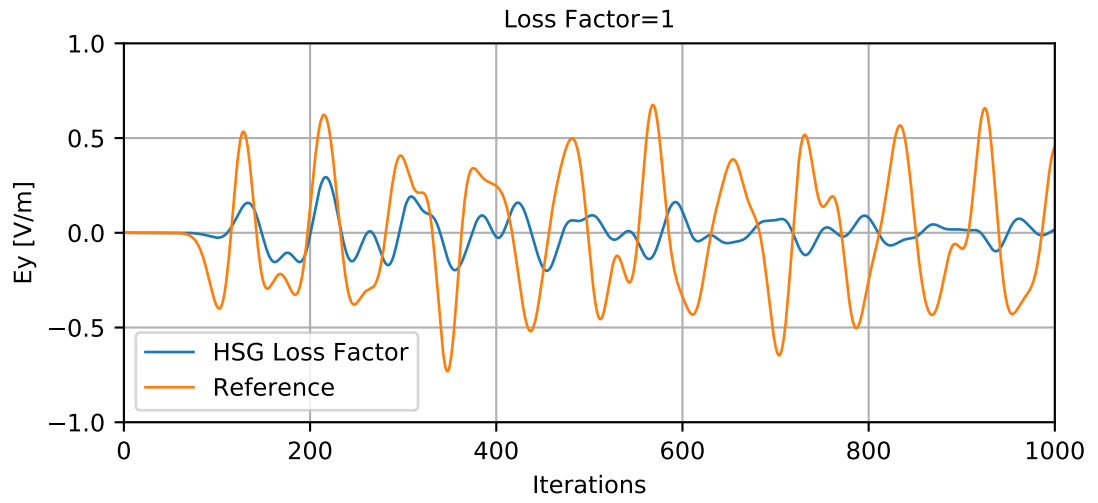
Figure 9.18: Ey field demonstrating the the stability of the HSG under the application of loss factor.

9.2.4 Parametric Loss Factor Studies

Zhou (2012) showed that the application of the loss factor at the IS or the OS or at both surfaces resulted in differing levels of attenuation and stability. In these experiments, the stability of the SHSG is explored for all possible combinations of the loss factor at the IS and OS.

9.2.5 Loss Factor = 1

The loss factor is applied at the locations show in Figure 9.10. Also, loss factors are applied to the electric and magnetic fields in the non-working regions. This is permitted as these fields are also predicted to be zero since they are decoupled from the fields in the working region. The locations of the loss factors are referred to as follows: l_{m_s} is used to refer to the magnetic loss factor in the sub-grid, l_{e_s} is used to refer to the electric loss in the sub-grid, l_m is used to refer to the magnetic loss factor in the main grid and l_e is used to refer to the electric loss in the main grid.

Figure 9.24 shows the E_y solution for every simulation which has greater stability than the HSG with a PML. The most stable solution is obtained when the loss factors are applied at l_{m_s}, and l_e. This result shows that the loss factors are most effective when they are applied to the fields which are directly involved in the SHSG update, at the locations shown in Figure 9.10.

The relative error of the solution $l_{m_s}, l_e = 1$ is shown in Figure 9.24. This error is compared to the equivalent error when those loss factors are applied to the HSG and for the HSG case with a PML. The results show that the rate of increase in relative error for the HSG experiment is greater than the SHSG with PML.
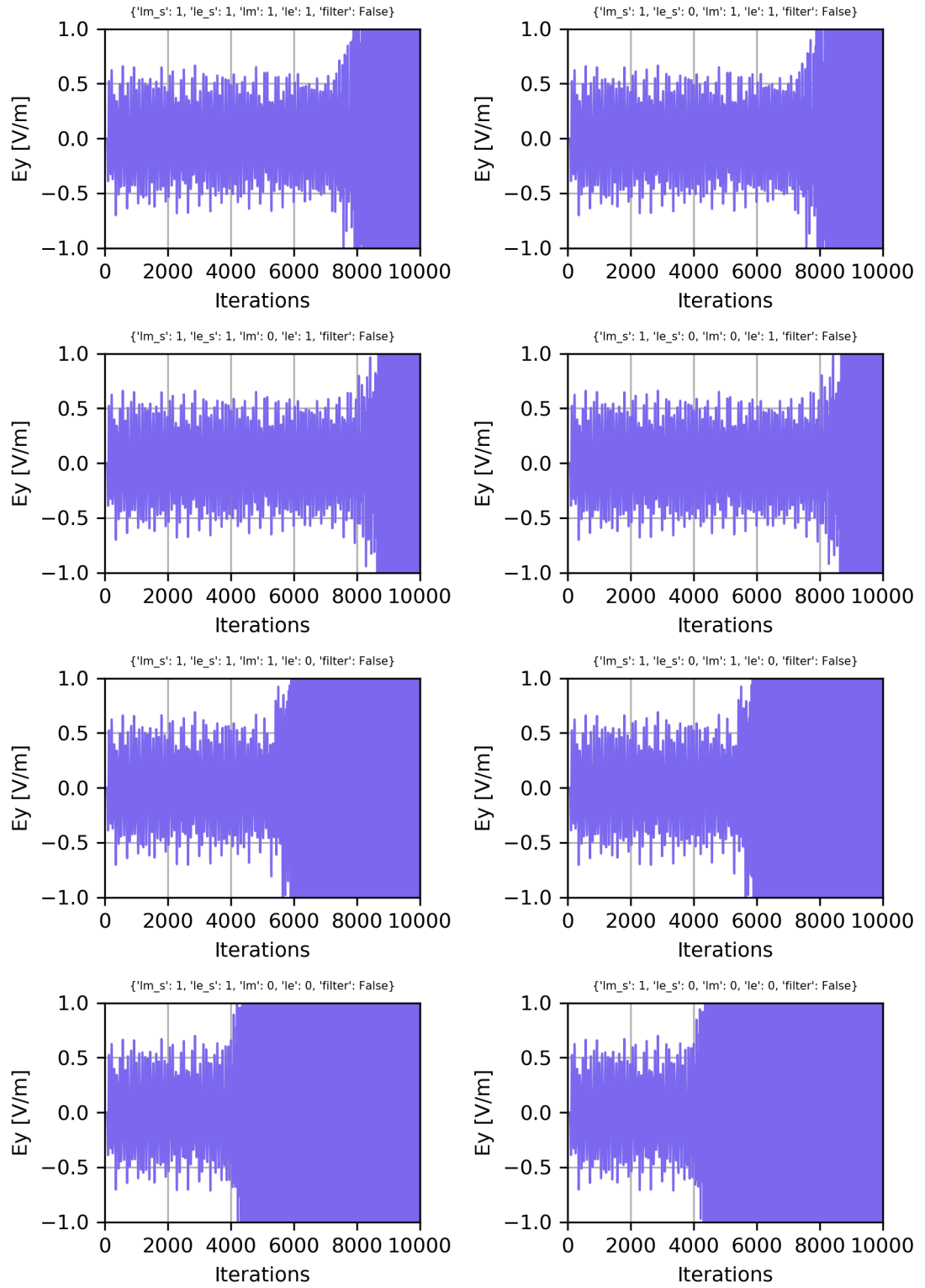
Figure 9.19: Varying the location of the loss factor 1 without filter
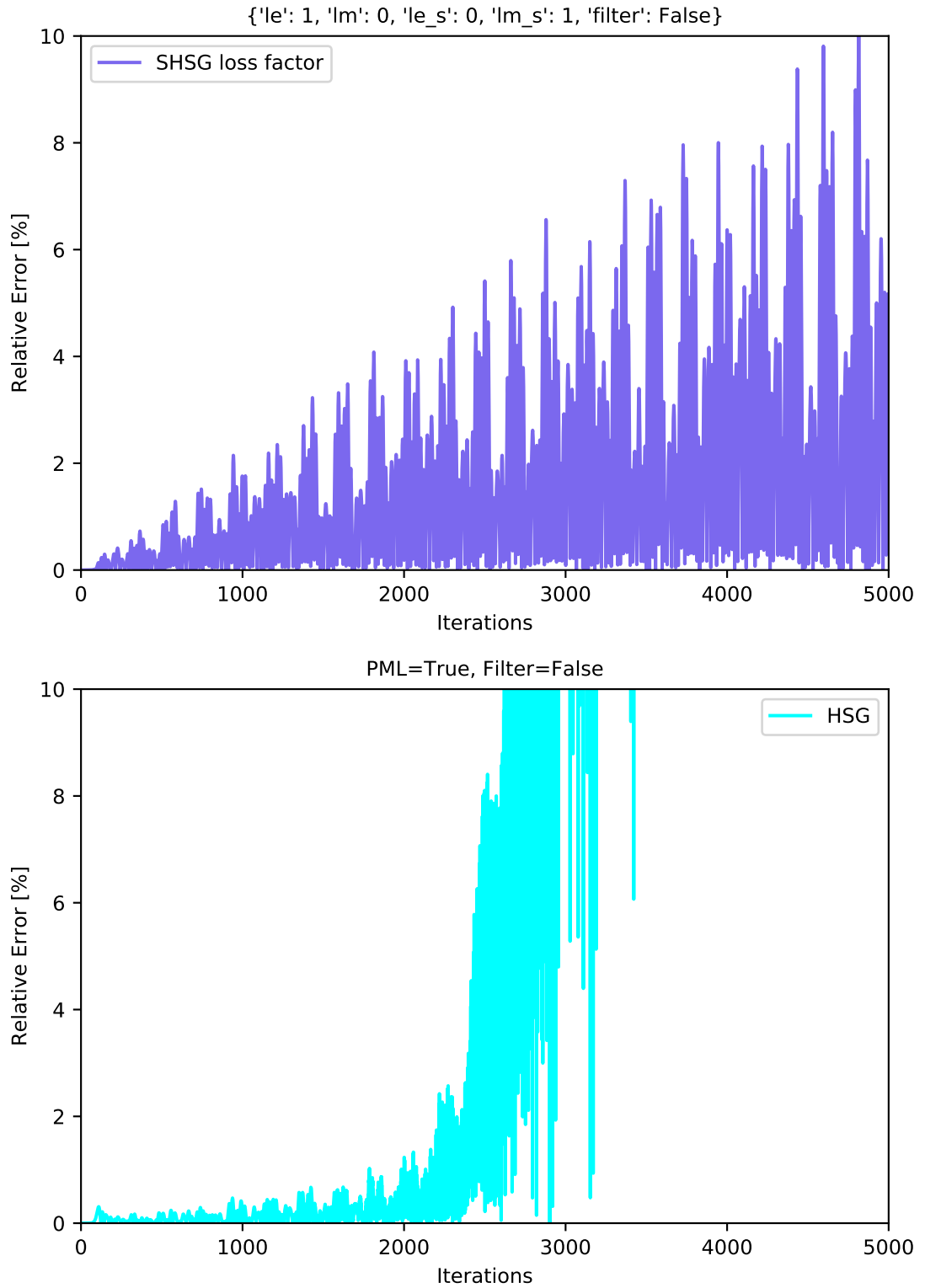
Figure 9.20: Comparison of most stable loss factor combination applied to the SHSG, HSG and the HSG without filter and PML applied.

9.2.6   Loss Factor = 0.0375

The previous results showed that the SHSG under-performs the HSG in terms of accuracy when $l_e, l_m = 1$. In this numerical experiment, the parametric study is repeated and the loss factor is reduced to $l_e, l_m = 0.0375$. The solutions for the experiments which are more stable than the HSG with PML are shown in Figure 9.21.

The results show that as the loss factor is decreased the number of stable iterations decreases. The most stable configuration of the loss factors is $l_e, l_m, l_{e_s}, l_{m_s} = 0.0375$. This corresponds to placing the loss factor at all the available locations. In this case, the simulation is stable for ≈ 6000 iterations. This corresponds to $\times 2$ increase in the number of stable iterations in comparison to the HSG with a PML. Interestingly the lower loss factor is more effective in the non-working regions l_{e_s}, l_m. This is presumably because the lower conductivity increases the skin depth of the conductive medium and thus allow more attenuation of the unstable field within the non-working region.

Figure 9.22 shows a comparison of the relative errors for the SHSG with $l_e, l_m, l_{e_s}, l_{m_s} = 0.0375$ and HSG with PML. The relative error in the HSG increases more rapidly than in the SHSG. For example, after 2000 iterations the SHSG error is $\approx 1.25\%$ whereas the error in the HSG is $\approx 2.5\%$. This result indicates than the loss-factor SHSG attenuates the sub-gridding error more efficiently than the PML in the HSG.

Interestingly, the relative error function grows linearly. This suggests that the error increases by a fixed amount each time the wavelet traverses the sub-grid. This is useful to know as it suggests a prediction of the relative error can be made for a certain number of grid traversals. For example, even after 1000 iterations, many grid traversals have been made and the error remains around 0.5%. The suggests that the SHSG application to the GPR problem will be successful because fewer grid traversals will occur during transient behaviour.

Figure 9.21: Varying the location of the loss factor $l = 0.0375$ without the 3-node filter.

Figure 9.22: Comparison of the relative error with respect to a fine grid reference solution. Loss factors l_e, l_m, l_{e_s}, $l_{m_s} = 0.0375$ applied in the SHSG. A PML is applied to in the HSG. No filter is used in either sub-gridding.

9.2.7 Parametric Loss Factor Studies with the 3-node Filter

To recap, when the 3-node filter is introduced to the HSG the stable period increases to around 9000 iterations. Without the filter, the SHSG was stable up to around 6000 iterations. Therefore the HSG with filter is more stable than the SHSG with loss factors.

In these experiments, the accuracy and stability of the SHSG with the introduction of a 3-node filter is compared to the HSG with a PML and the filter.

In the SHSG the filter is positioned at the OS. This is because the OS radiates the field from the main grid into the sub-grid as opposed to HSG which radiates into the sub-grid at the IS. Consequently, an interesting property of the SHSG is that the filter can be used when the outer nodes at the IS and OS of the SHSG are set to PEC and PMC. This is not the case in the HSG as the filter requires fields which are within the non-working region, in essence, fields located within the PEC.

9.2.8 Loss Factor = 1

In this experiment the resonance test is repeated with the addition of the loss factors and the 3-node filter. The loss factors are $l_e, l_m, l_{e_s}, l_{m_s} = 1$. Each simulation which has a stable period greater than 9000 iterations is shown in Figure 9.23.

Similarly to the results without the filter the greatest stability is obtained with the combinations $l_{m_s}, l_e = 1$ and $l_m, l_{e_s} = 0$. Adding loss to the non-working nodes in the non-working region of the sub-grid does not increase the stability. And adding loss to the non-working magnetic field in the main-grid reduces the stability.

The relative error for the most stable case $l_{m_s}, l_e = 1$ and $l_m, l_{e_s} = 0$ and relative error in the HSG with PML and 3-node filter are compared in Figure 9.24. The result show that the rate of increase of the relative error in the SHSG is significantly larger than in the HSG.
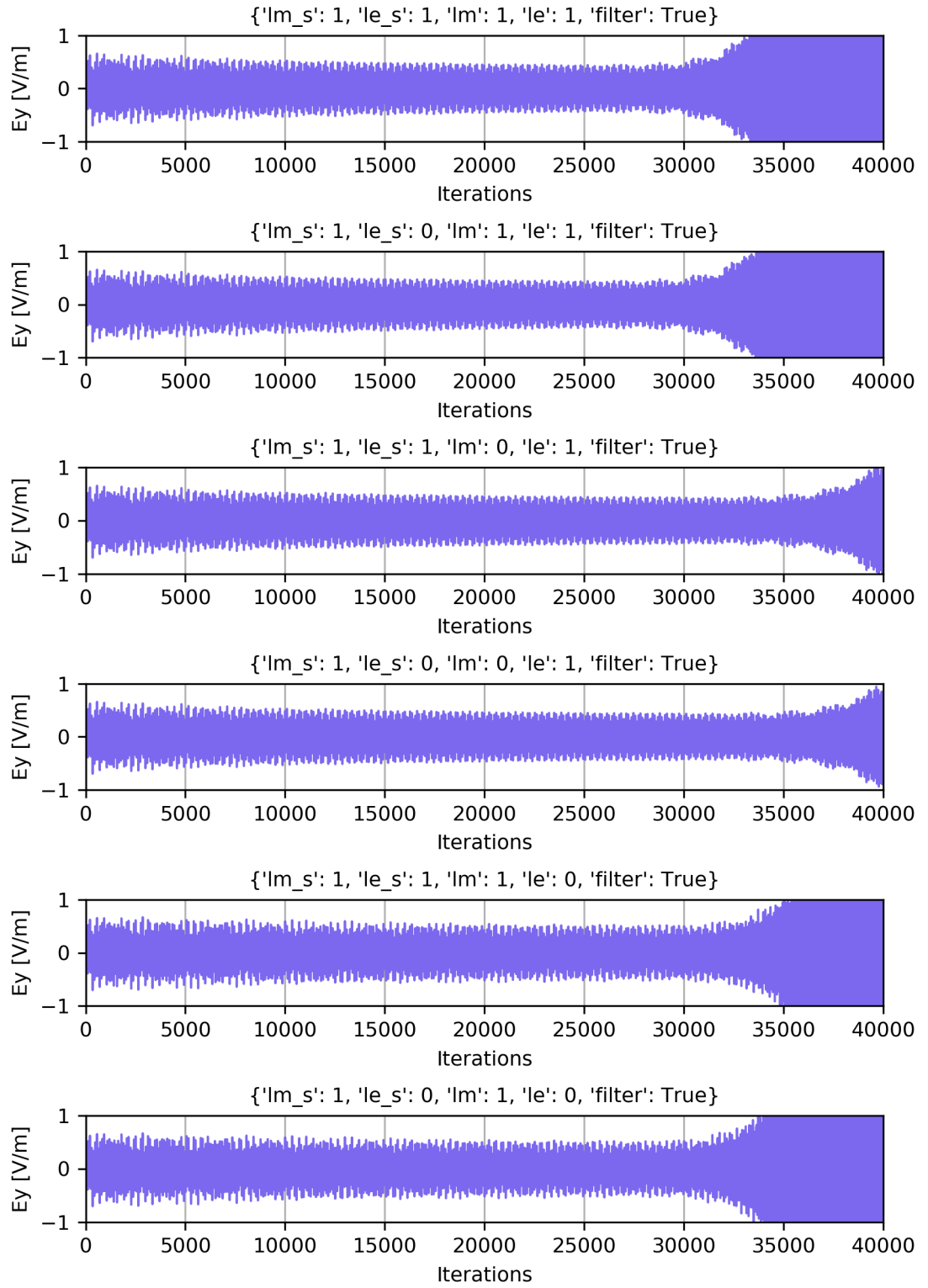
Figure 9.23: Varying the location of the loss factor 1 with filter
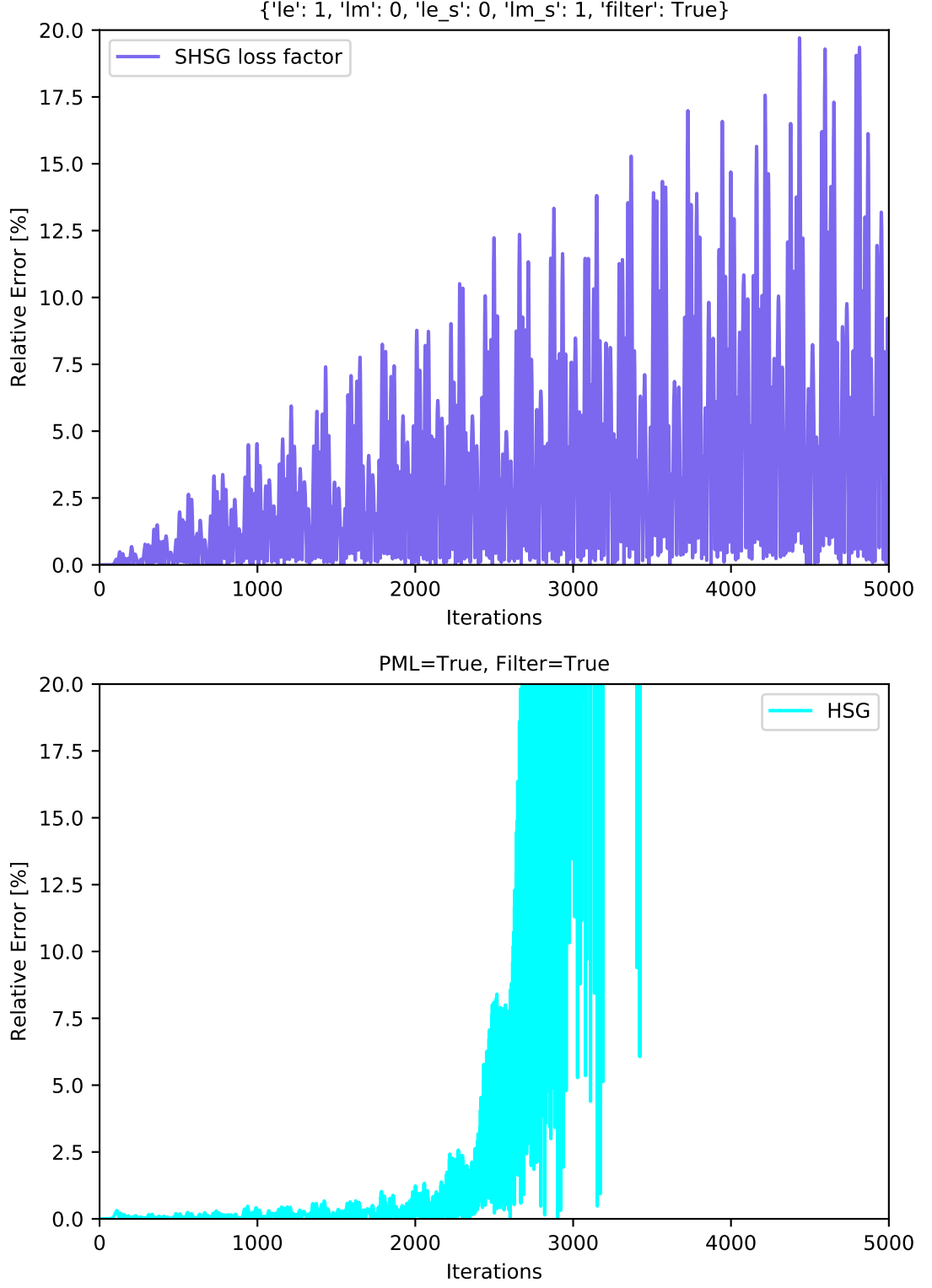
Figure 9.24: Comparison of the relative error with respect to a fine grid reference solution. Loss factors $l_e = 1$, $l_m = 0$, $l_{e_s} = 0$, $l_{m_s} = 1$ applied in the SHSG. A PML is applied to in the HSG. A filter is used in both sub-griddings.

9.2.9   Loss Factor = 0.0375

The previous experiment showed that the loss factors $l_{m_s}, l_e = 1$ and $l_m, l_{e_s} = 0$ is combination with the filter resulted in a relative error which greatly exceeded the HSG with PML and the filter. In this experiment, the parametric study is repeated with the reduced loss factor, $l = 0.0375$. The results for each simulation which has a stable period above 9000 iterations are shown in Figure 9.25.

Similarly to the results without the 3-node filter, the greatest stability is obtained for the combination $l_e, l_m, l_{e_s}, l_{m_s} = 0.0375$. The period of stability has been extended from 9000 iterations to at least 50000 iterations. This represents a $5.5\times$ increase in stability.

The relative errors of the most stable case and the HSG with PML and a 3-node filter are compared in Figure 9.26.

The data shows that the relative error approximately doubles with the addition of the filter in comparison to Figure 9.22 where the loss factor is the same but the filter is switched off. This is the case for the SHSG and HSG. The results show that the relative error is greatly reduced from the $l = 1$ with filter case shown in Figure 9.24. Figure 9.26 shows that the error in the SHSG is slightly greater than the HSG. For instance, the error for the SHSG at 2000 iterations is $\approx 3\%$ whereas it is $\approx 2.5\%$ in the HSG. Nevertheless, given the improvement in stability, this is a positive result.
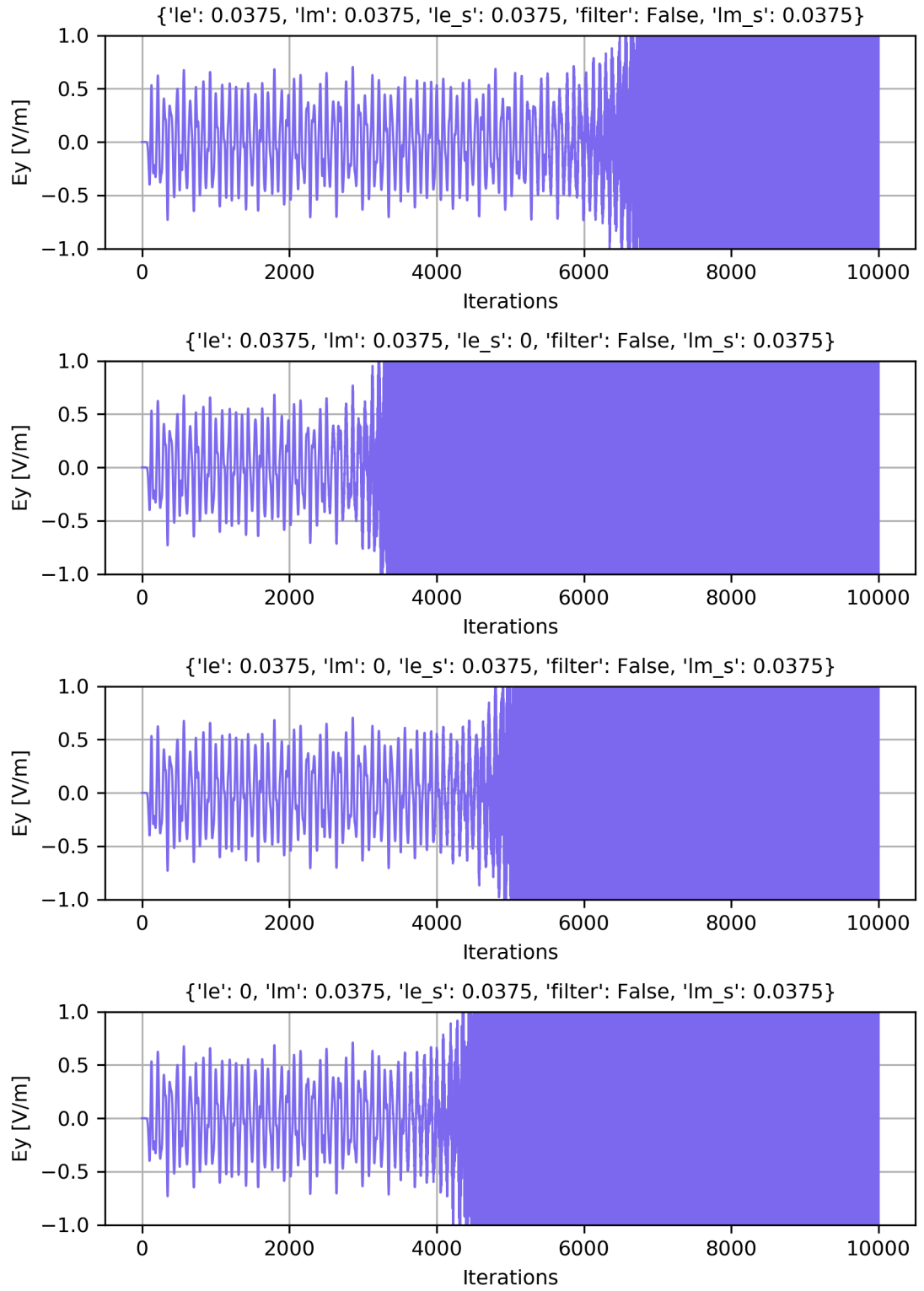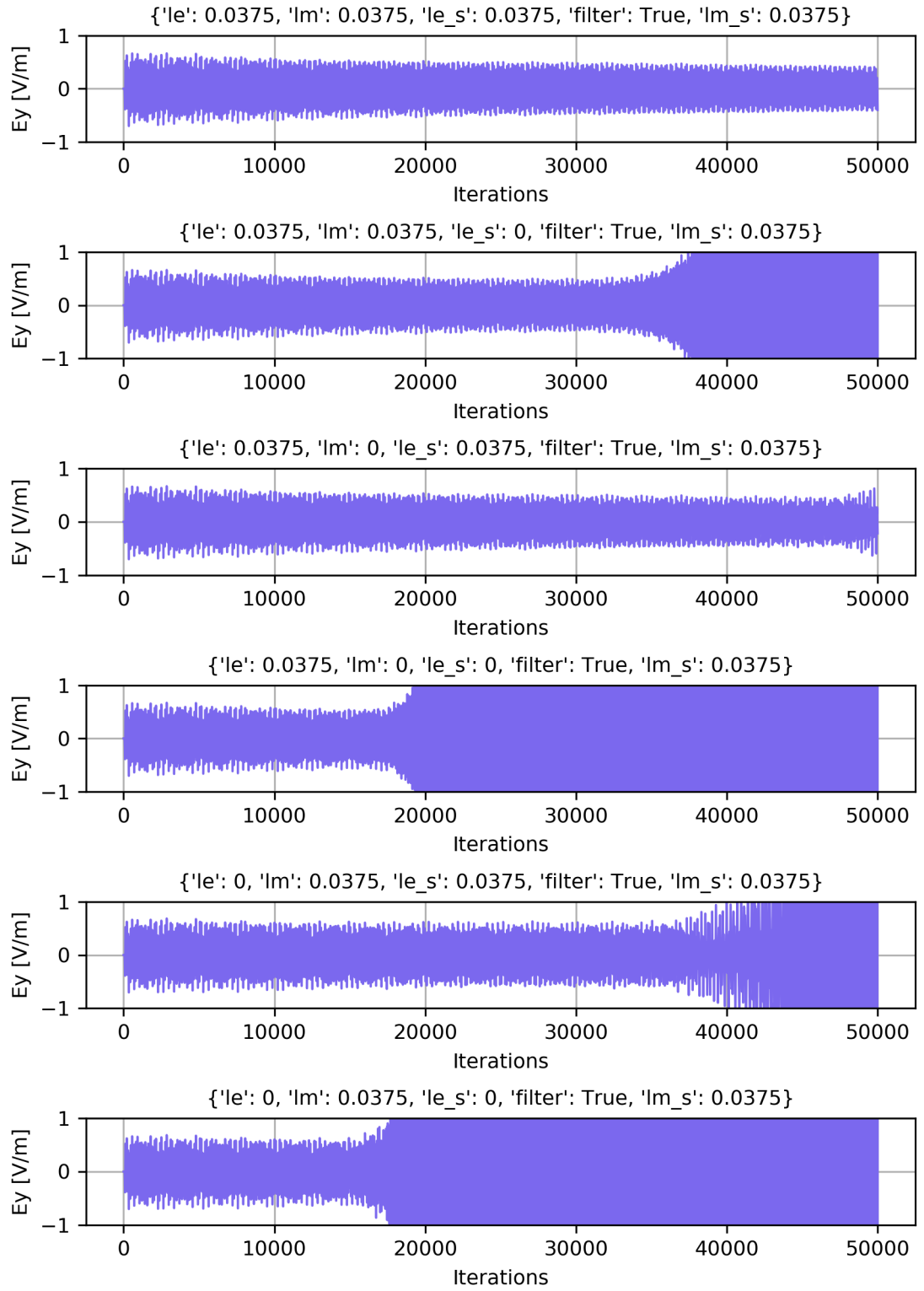
Figure 9.25: Varying the location of the loss factor 0.0375 with filter
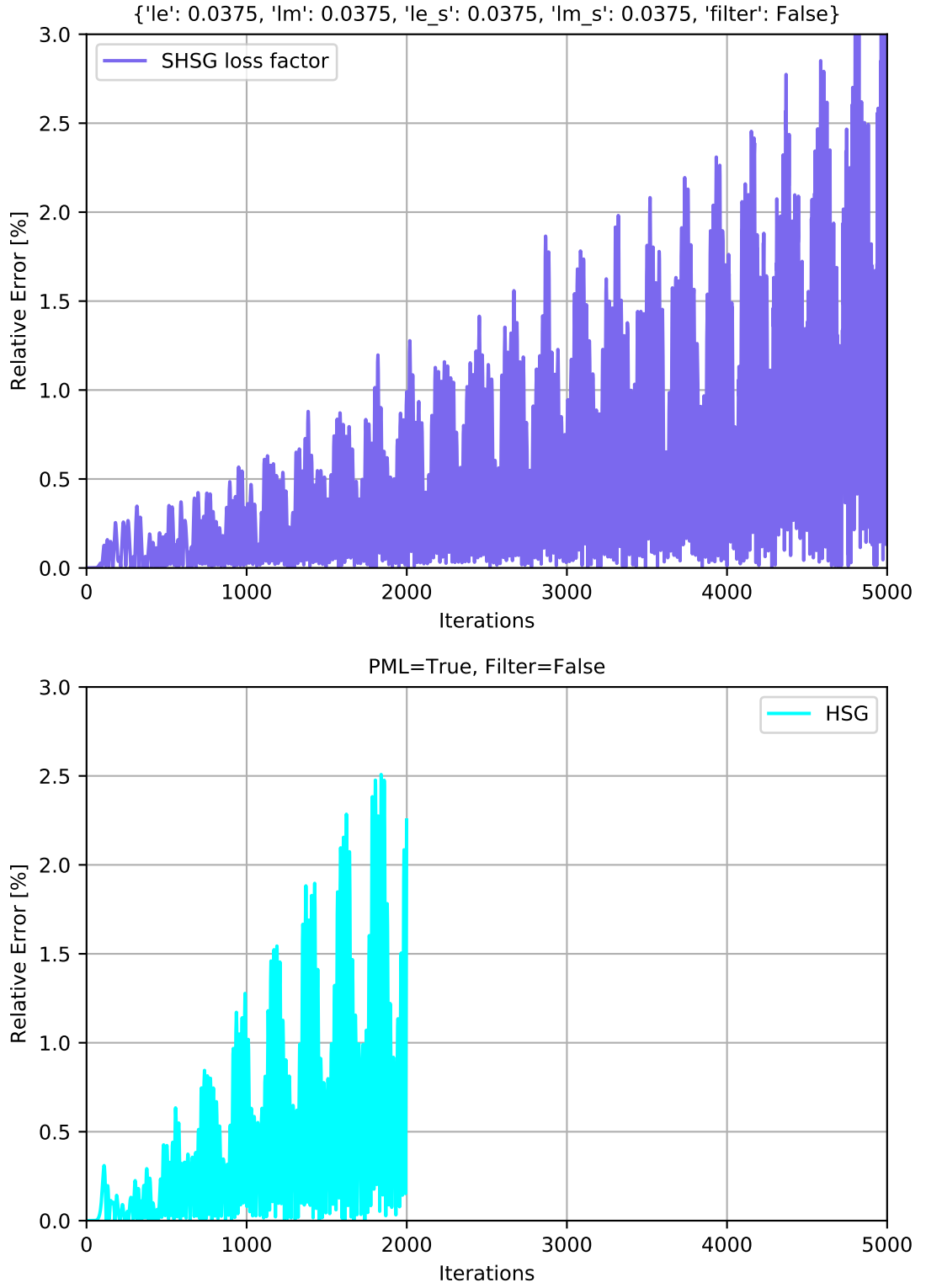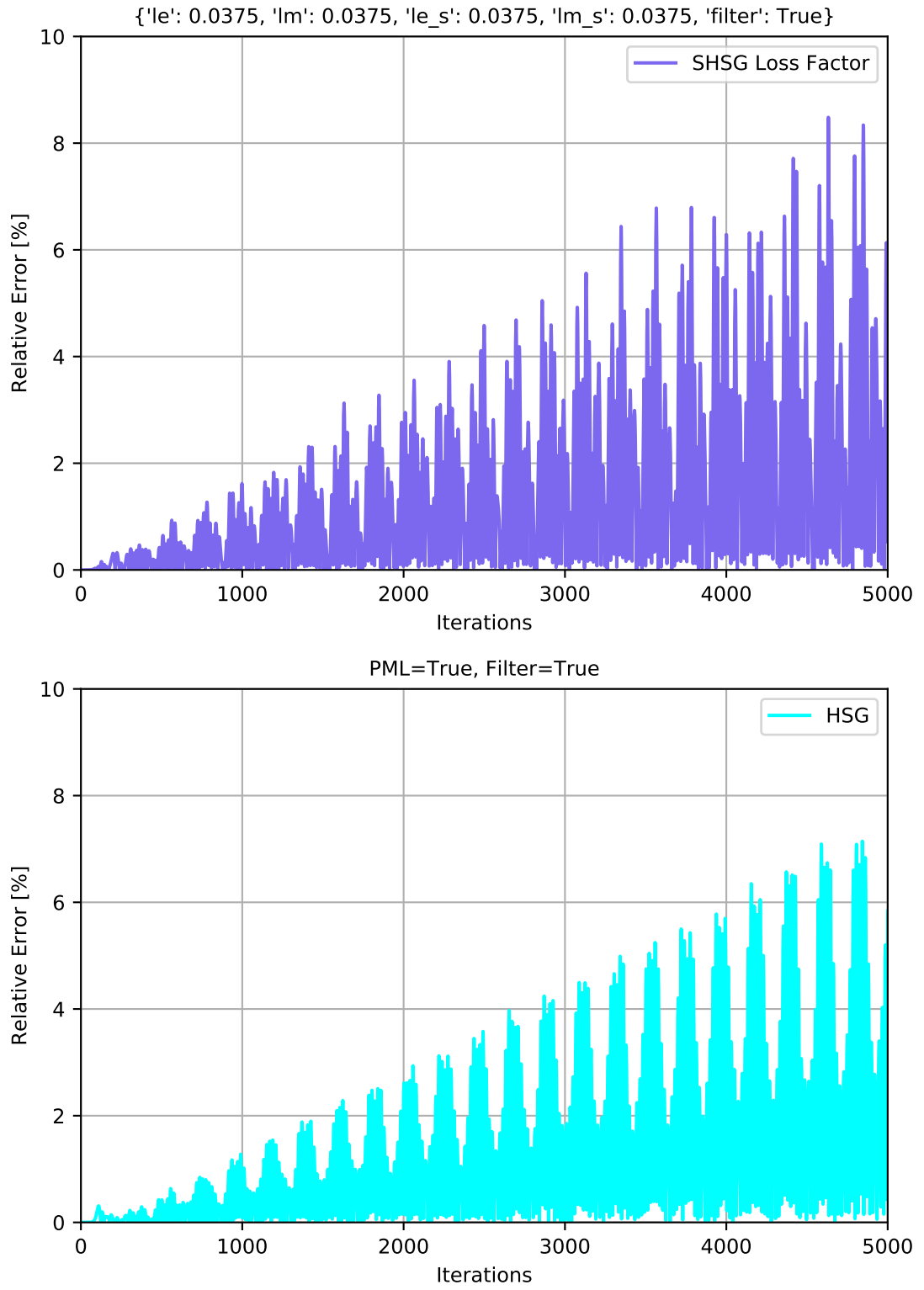
Figure 9.26: Comparison of the relative error with respect to a fine grid reference solution. Loss factors l_e, l_m, l_{e_s}, $l_{e_s} = 0.0375$ applied in the SHSG. A PML is applied to in the HSG. A filter is used in both sub-griddings.

9.2.10 Parametric Study Different Loss Factor

The previous loss factor studies showed that the accuracy and stability of the SHSG depend on the magnitude and location of the loss factor. Also, it was shown that lower loss factors are more effective when they are used in combination across the non-working regions of the sub-grids and that decreasing the loss factors increased the accuracy of the SHSG.

Following on from these observations a parametric study is conducted to find a set of loss factors which maximise the accuracy and stability of the SHSG. The study differs in that a range of loss factors are considered and applied separately to the sub-grid and main grid. This is done under the assumption that the loss factor acts independently in similarity to the Huygen's surfaces. The loss factors tested are 1, 0.5, 0.25, 0.1, 0.0375. The factors are designed to span the feature space exponentially so that only a small number of experiments are needed. Although an optimisation approach could be used to find the most stable/accurate loss factors, this method gives an insight into the physical characteristic of the field over the whole feature space and thus gives an idea of the behaviour of the loss factors. As opposed to an optimisation where only a limited sample of the feature space is explored.

In the first experiment, the loss factors are applied to the Outer Surface only for the filtered and non-filtered cases. The resulting solutions are shown in Figure 9.27.

Turning first to the experiments which are performed without a filter, the results show that the relationship between the stability and the magnitude of the loss factor is not linear. Although the stability between the highest and lowest loss factors is increased, the stable periods are similar given the lower loss factors $l = 1, 0.25, 0.1$. This is surprising because there is an order of magnitude difference between the loss factors. The results in which the filter is applied also show that the relationship between the loss factor and period of stability is complex. For example, the $l = 0.1$ case is more stable than $1 = 1$ case.

Nevertheless, previous experiments have shown the accuracy is improved at lower loss factors. Therefore $l = 0.25$, $l = 0.1$ are good compromises stability in favour of accuracy for the filtered and non-filtered cases respectively.

Moving now to the IS, it has been shown in previous experiments that lower loss factors in the non-working regions result in greater stability, see Figure 9.25. However, not shown is that $l_e = 0$ increases accuracy with only a small reduction in stability. For example, the relative error after 5000 iterations is 3% in the SHSG and 7% for the

HSG. Therefore, in the second experiment $l_e = 0$ and $l_m = 0.0375, 0.1, 0.25, 0.5, 1$ are applied to Inner Surface. This has the effect of increasing the accuracy at the cost of reduced stability. The results are shown in Figure 9.28.

The results show that the loss factors are less effective in the main grid. For example, consider the $l_{e_s}, l_{m_s} = 1$ case where the filter is on. The simulation is stable for more than 10000 iterations. However, for $l_m = 1$ the simulation is stable for around 3000 iterations only. These findings are similar to those of Bérenger (2011) in which the PML in the main grid was found to have less impact on the stability in comparison to the sub-grid PML.

In summary, when the simulation is not filtered the best stability is obtained for $l = 0.5$. When the filter is switched on the best stability is obtained for 0.0375. Counter-intuitively the filtered results show that a lower loss factor gives greater stability. Interestingly, the results also indicate that the lower loss factors give good stability when they are used in conjunction with the filter. This is beneficial because lower factors improve accuracy.
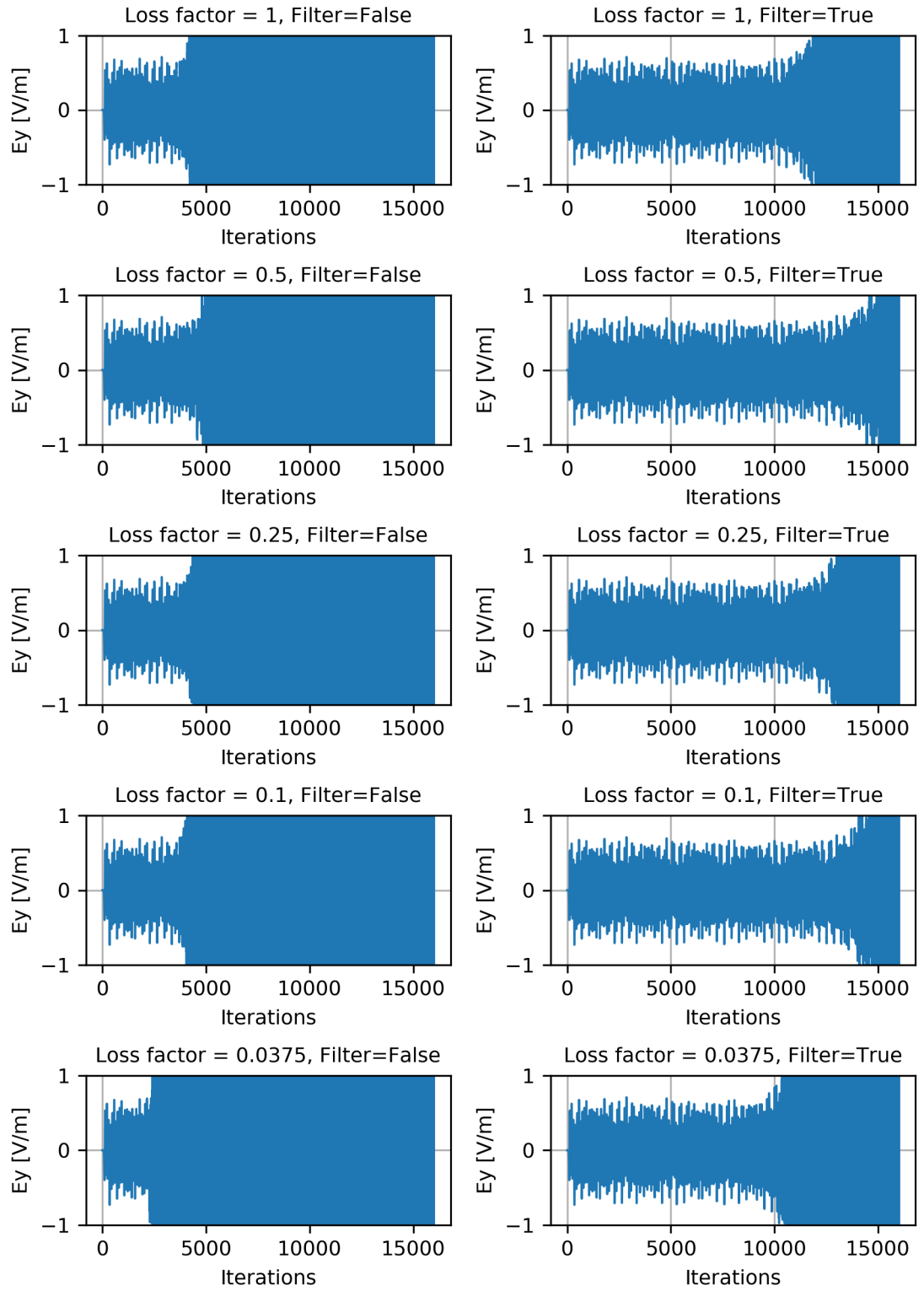
Figure 9.27: Loss factors applied only to the subgrid
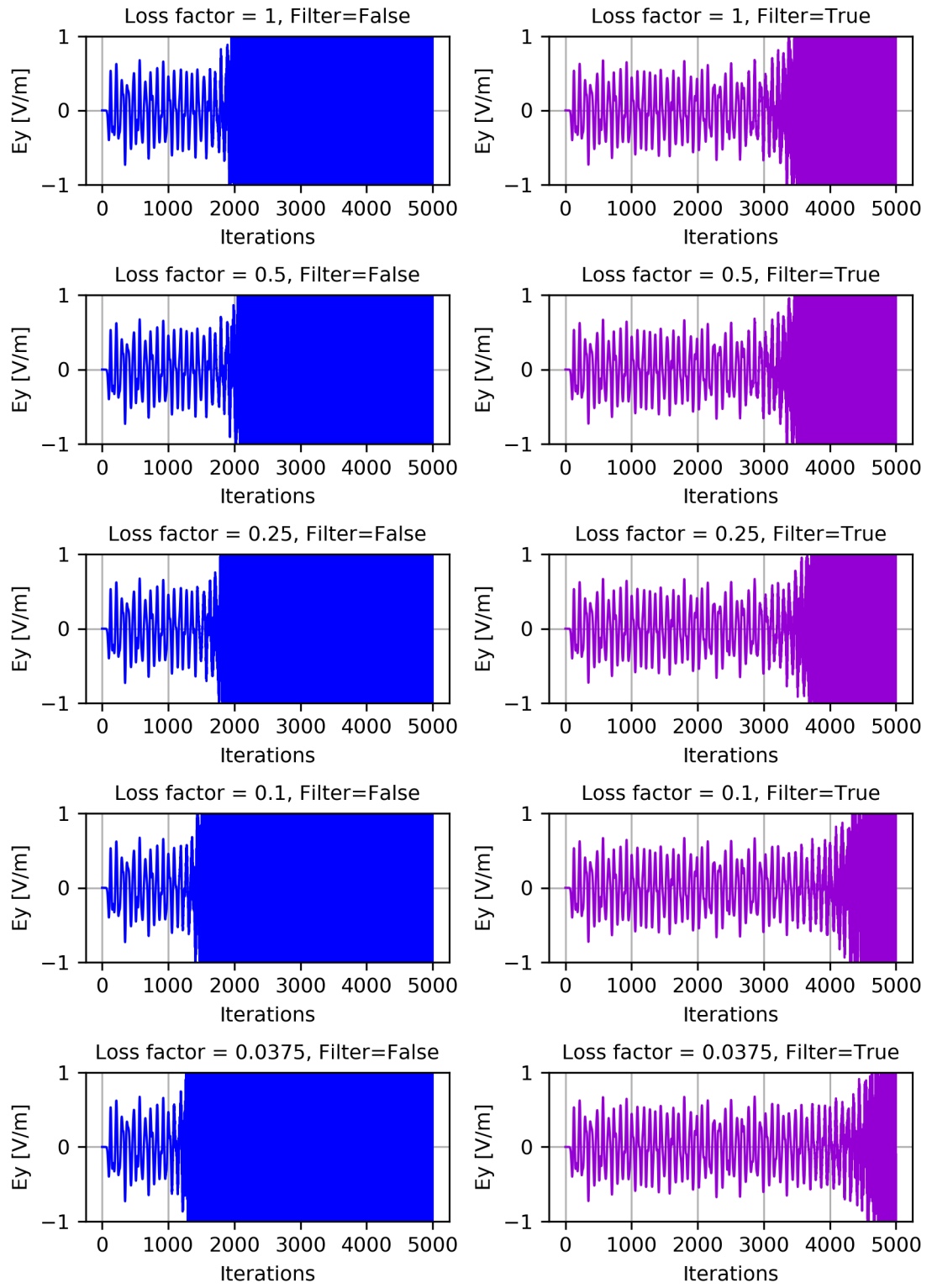
Figure 9.28: Loss factors in the main grid

216

9.2.11 Recommended Loss Factors

The previous three studies have the stability and accuracy of the SHSG with loss factors in comparison to the HSG. In the first study the loss factors 1, 0.0375 were used. And the parameter space of the possible locations for the loss factors was explored. In the second study, the magnitude of the loss factors applied at fixed IS and OS locations were explored.

In this section, the recommended parameters for the loss factors are given for the filtered and non-filtered cases.

In the non-filtered case, it was shown that the combination of loss factors $l = 0.0375$ at the IS and OS offered the best accuracy and stability and surpassed the HSG against both measures. However, the second study indicated that the $l = 0.25$ case offered increased stability. An experiment is run with loss factor $l = 0.25$ at the IS and the OS. The results are shown in Figure 9.30.

The results show that the SHSG is stable for around 25000 iterations. In comparison, the HSG with PML is stable for around 3000 iterations and the HSG with the PML and filter is stable for around 9000 iterations. This corresponds to an increase in the number of stable iterations by 8.3× and 2.7× respectively. Also, the relative error after 2000 iterations in HSG with PML was 2.5% and in the SHSG was 2.5%. This result shows that the accuracy of the two schemes is similar.

In the filtered case it was found in the previous section that $l_{s_e}, l_{s_e} = 0.1$ and $l_m = 0.0375$ offered a good compromise between stability and accuracy. In this experiment, the losses at each surface are combined in a single simulation run. The results and the relative error are shown in Figure 9.30.

The results show the simulation is stable for around 50000 iterations. Also, the relative error at 5000 iterations is 3.5%. In comparison, the HSG with the application of the PML and filter is stable for around 9000 iterations. Also, a relative error of 7% is present at 5000 iterations. These results show that the SHSG can improve upon the HSG when optimised factors are used. In summary, the stability is increased by 5.6× and the accuracy is increased by 2×.
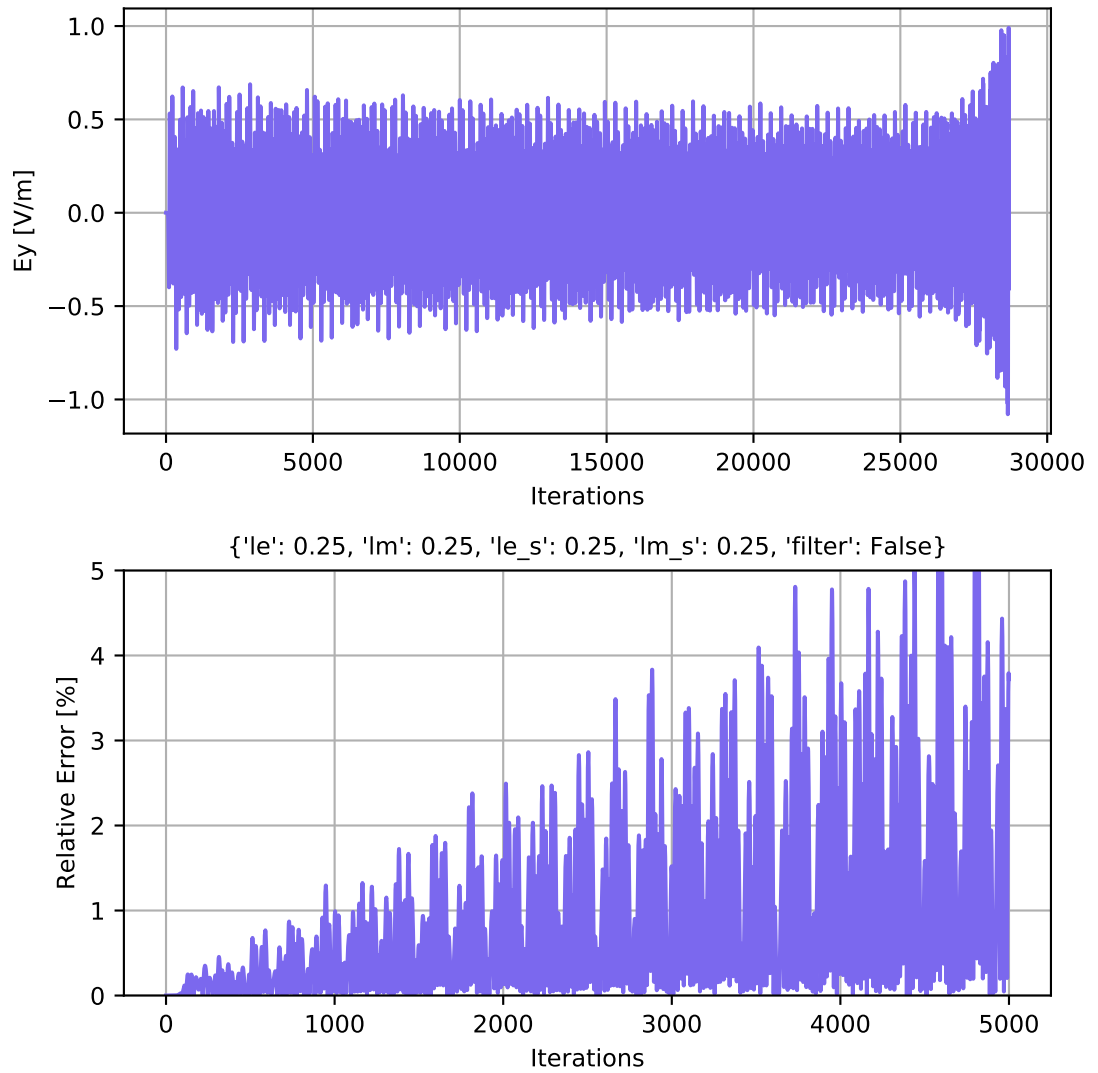
Figure 9.29: Loss factors 0.25 in sub-grid and 0.25 in the main grid
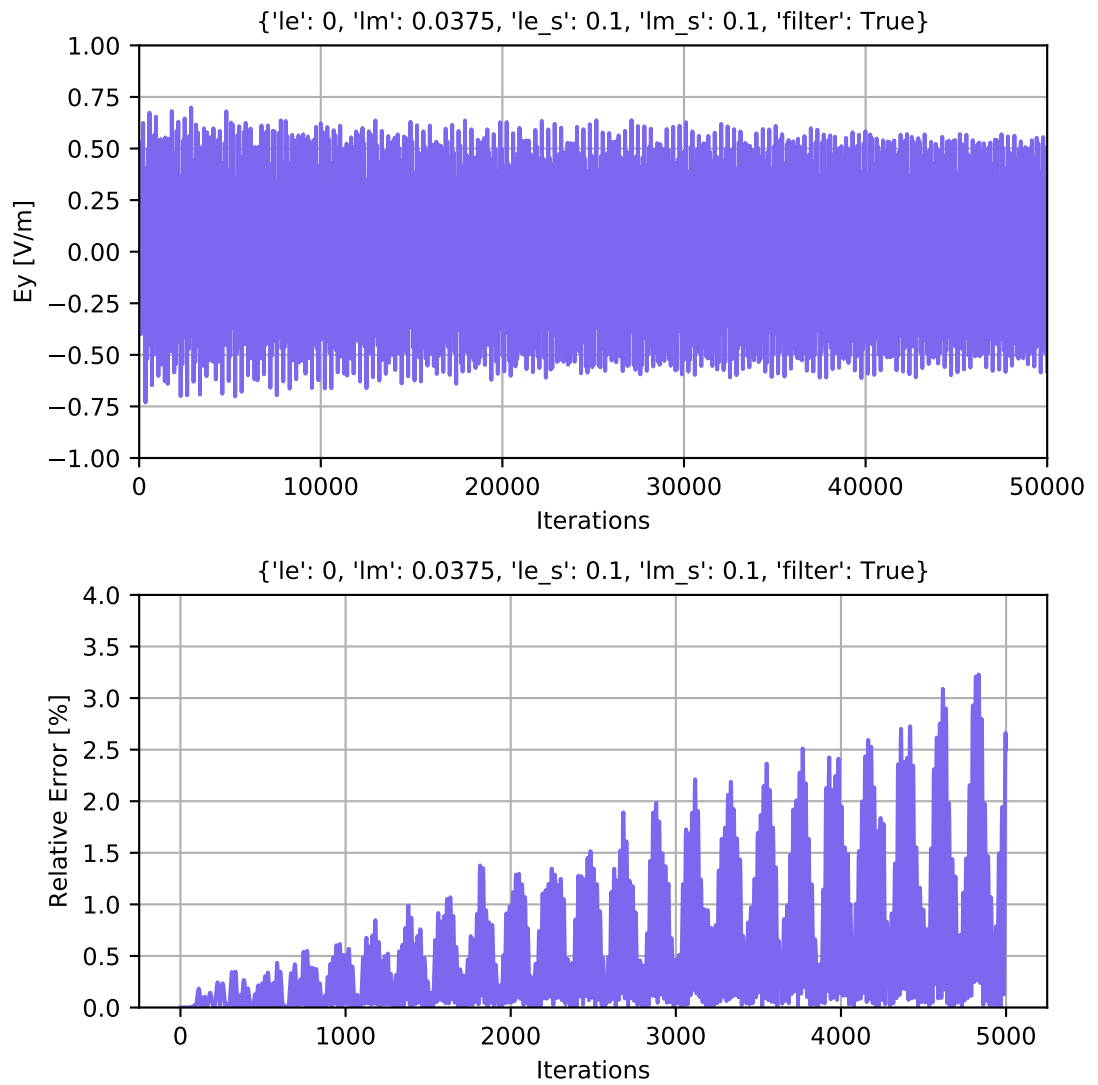
Figure 9.30: Loss factors 0.1 in subgrid and 0.0375 in the main grid

9.3 Summary

This chapter introduced a novel sub-gridding scheme. The SHSG scheme is similar to HSG because it also uses Huygens's surfaces to radiate fields between the grids. However, the different arrangement of the IS and OS results in several interesting properties which offer improvements over the original HSG scheme. For example, the field in the SHSG can be sampled correctly at any position within the working regions of the grids. And, there are stability and performance benefits.

Previous researchers have used loss factors to reduce the instabilities in the HSG. However, these attempts resulted in a significant attenuation of the solution. The novel arrangement of the SHSG permits attenuation of the instability without excessive attenuation of the solution. In fact, it was shown that the accuracy is similar to the HSG when appropriate loss factors are chosen. Furthermore, it was shown that in stringent resonant cases the loss factors increase the stability of the solution up to $5.6\times$ both with the 3-node filter. Also, loss factors benefit from their high computation performance. This is because they can be easily implemented using the standard update equations. This is opposed to the PML regions in the HSG which require additional computation.

Chapter 10

Application of the SHSG to the GPR Half-Space Problem

Chapter 9 introduced the Switched Huygens Sub-Gridding. One dimensional analysis showed the SHSG was able to model the transmission coefficient of a thin lossy sheet more accurately than the HSG. The method was then extended to the general 3d case and a microwave cavity problem was investigated. It was shown that the stability of the SHSG was significantly greater than the HSG when an artificial loss was applied at the OS and IS and non-working regions of the main grid and sub-grid. Whilst previous attempts to introduce loss factors to the HSG were successful in attenuating the instability, the accuracy of the solution was significantly deteriorated. In contrast, the SHSG attenuates the instability whilst preserving the accuracy of the solution at a similar rate to the HSG.

The performance of the SHSG varies with the magnitude of the loss factors and their position in the main grid and sub-grid. Furthermore larger loss factors reduce the accuracy of the solution. Therefore loss factors were recommended which maximise accuracy and stability. In this chapter the SHSG with the recommended loss factors are applied to the GSSI 1.5 GHz half-space problem in Chapter 8. The results are then compared with the findings of the HSG experiments.

10.1 Sub-gridded GSSI $1.5\,\mathrm{GHz}$ Over Buried Plastic Water Pipe in Dispersive Soil

In this experiment the SHSG is used to sub-grid the GSSI $1.5\,\mathrm{GHz}$ above a half-space of type-A soil containing a buried plastic water pipe. As in the previous experiment both the antenna and the water pipe are sub-gridded.

The implementation of the SHSG differs slightly from the microwave cavity resonator due to the background material in the sub-grid. The sub-gridded water pipe's background material is soil which has an intrinsic conductivity. Therefore the question arises of whether to use the intrinsic or loss factor conductivity at the IS, OS and non-working regions.

Costen and Bérenger (2010a) suggested that there is no instability when the sub-grid is embedded within a dispersive material. This is because the effective conductivity attenuates the solution at a rate faster than the growth of the instability. This was demonstrated by Abalenkovs et al. (2012) where numerical experiments conducted with the sub-grid embedded in human tissue showed no instability. Contrary to these findings, the parametric studies of loss factors showed that this is not always the case as the growth of the instability depends on the magnitude of the intrinsic effective conductivity. Indeed, Abalenkovs et al. (2012) likely found no instability because human tissue is highly dispersive and has a large intrinsic conductivity $\approx 1\,\mathrm{S\,m^{-1}}$.

The decision of which conductivity to use for update equations within the non-working regions is made based upon comparing the conductivity of the medium to be modelled and the equivalent loss factor conductivity for the recommended loss factors defined at the time-step in question. The equivalent electric and magnetic conductivities are given by

$$\sigma_e = \frac{2\sqrt{3}c_0 l_e \epsilon}{\Delta l} \tag{10.1}$$

$$\sigma_m = \frac{2\sqrt{3}c_0 l_m \mu}{\Delta l} \tag{10.2}$$

Evaluating the conductivities for the recommended loss factors in the main grid, $\Delta l = 3\,\mathrm{mm}$, and the sub-grid, $\Delta l = 1\,\mathrm{mm}$, gives in $\sigma_{e_s} = 0.9\,\mathrm{S\,m^{-1}}$, $\sigma_{m_s} = 130503$ and $\sigma_m = 16313$.

The magnetic loss factor can be used in the main grid and the sub-grid as the soil material has no magnetic loss. Type-A soil has an electrical conductivity $\sigma_e = 0.4\,\text{mS}\,\text{m}^{-1}$. The loss factor loss is far greater than the intrinsic conductivity. This suggests that the intrinsic conductivity will attenuate the instability less than the loss factor. Therefore, to maximise the stability, in the following experiments the intrinsic conductivities are replaced with the equivalent conductivities from the two sets of recommended loss factors.

The loss factor $l_e = 0$ could be replaced by the equivalent loss factor of the intrinsic conductivity of the soil. However, the intrinsic conductivity is so small in comparison to the loss factors tested in the previous chapter suggests that the effect on the instability would be small.

In addition to the recommended loss factors, the numerical experiment was conducted using a higher loss factor $l = 0.25$ from the parametric testing in Chapter 9. The reason for this is to determine whether these loss factors reduce the accuracy significantly as was the case in the resonance test. The argument could be made that as the sub-grid is traversed fewer times the impact of the loss factors is lessened and therefore lower loss factors could be used.

The experiment is run with the same simulation parameters as the HSG numerical simulation. The only difference in the dimensions is the sub-grid occupies a single cell beyond the OS. Whereas in the HSG there are 8 cells which are occupied by 6 PML cells and 2 gap cells. It was found the increasing the number of cells between the OS and the PEC boundary of the sub-grid did not improve the stability of the SHSG simulation. Therefore the size of sub-grid can be reduced.

10.1.1   Accuracy

Figure 10.1 shows a comparison of the fields received by the antenna for the two sets loss factors, the filtered and unfiltered HSG with PML and a fine grid reference solution. The results show that the solutions for each of the simulations are in good agreement with the reference solution. The SHSG solutions do not show any artefacts of attenuation. This finding supports the statement that the SHSG can be used to sub-grid finely detailed models of GPR antennas with a similar degree of accuracy to the HSG.

To assess this statement quantitatively, the relative errors for the unfiltered SHSG and HSG with PML are determined and shown in Figure 10.2. The results show relative

errors of the SHSG and HSG are similar. However, the relative error for the HSG is slightly lower than the SHSG. The max peak difference in relative error is $\approx 0.1\%$ and the peak error is $\approx 1.2\%$. This is not greatly significant given the FDTD method has an error $\approx 1\%$ in comparison with the analytic solution of the Hertzian dipole. Furthermore, this result is in line with the result of the previous sub-gridding of buried objects. For example, Wei et al. (2017) find a peak relative error of 5% and Xiao et al. (2007) find a peak relative of 1.5% for the case of a simple buried pipe and a Hertzian dipole source.

This finding shows that the SHSG can be used with loss factors to sub-grid GPR antennas with a high level of accuracy in comparison with sub-griddings reported in the literature.

A comparison of the relative errors for the filtered SHSG and HSG with PML are shown in Figure 10.3. The results show that there is a larger variation in the relative error between the HSG and SHSG. The worst of these is $\approx 0.4\%$. Nevertheless, the peak relative error is below 1% which indicates that the filtered SHSG is also sufficiently accurate to model GPR antennas in the half-space problem.
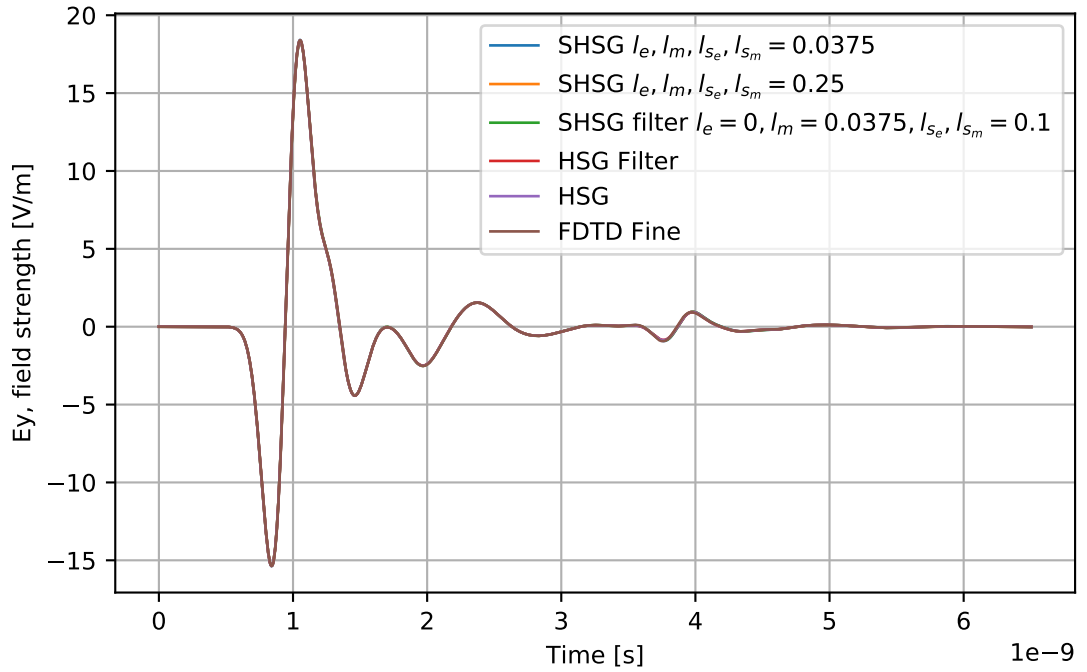
Figure 10.1: E_y received by GSSI 1.5 GHz. Comparison of the SHSG and HSG with stability parameters and a fine grid reference solution.
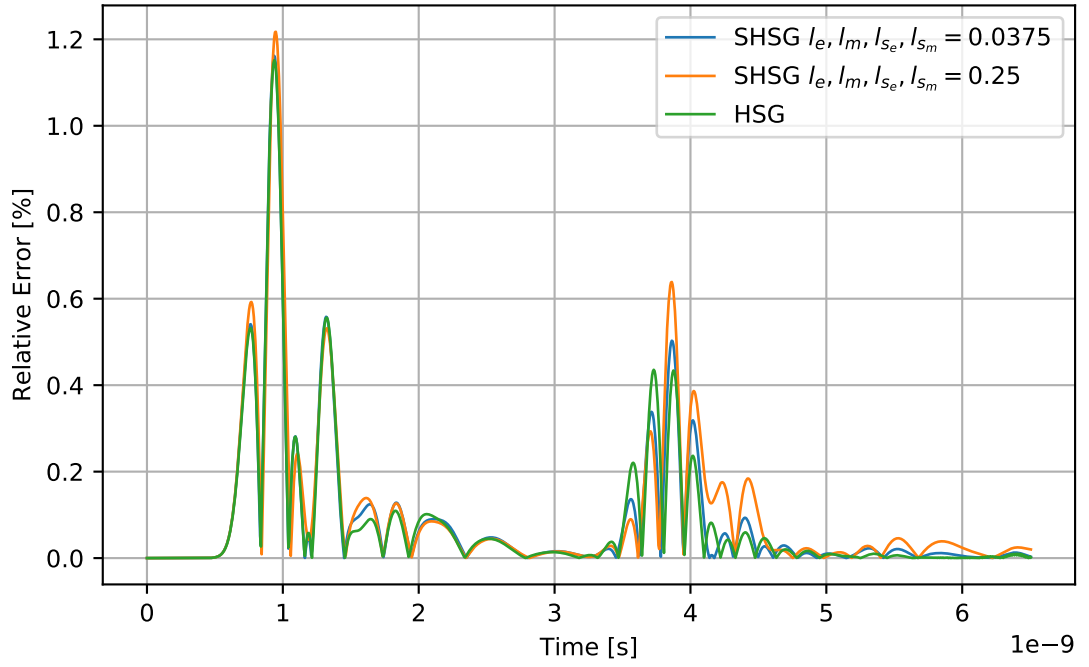
Figure 10.2: Relative error in E_y measurement at the GSSI 1.5 GHz. Comparison for the SHSG with two different loss factors and the HSG with PML.
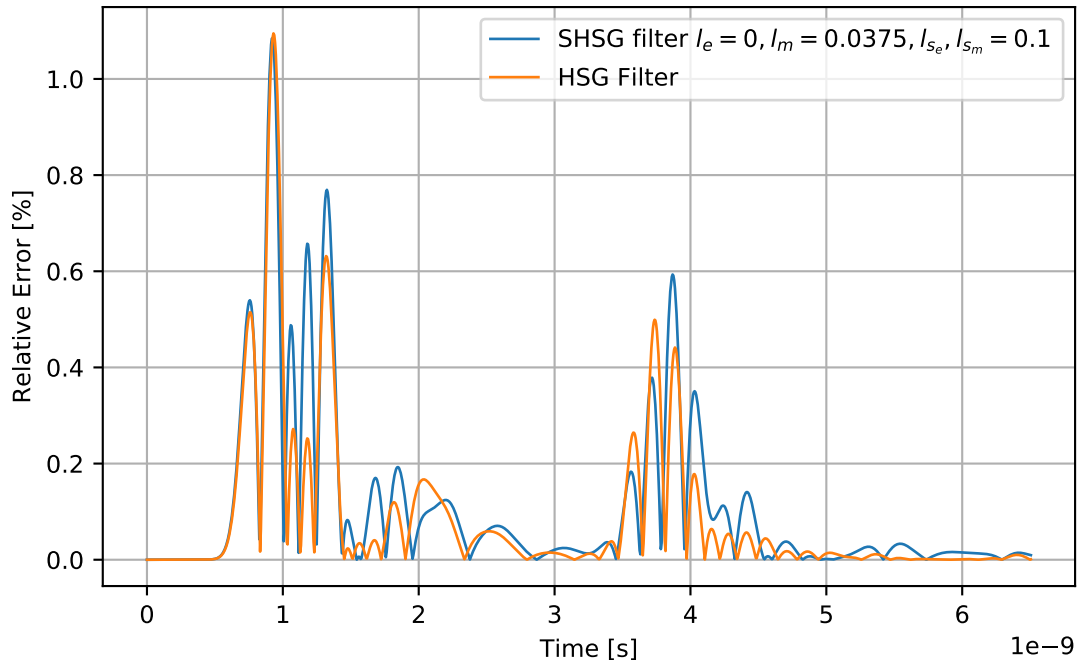
Figure 10.3: Relative error in E_y measurement at the GSSI 1.5 GHz. Comparison for the filtered SHSG with two different loss factors and the filtered HSG with PML.

10.1.2 Stability

In this experiment, each sub-gridding is repeated and terminated at the point at which the amplitude of the solution is equal to the peak amplitude in the direct wave. The results of the stability test are shown in Figure 10.4.

The results show that the sub-griddings are stable for the following number of iterations. The HSG with PML is stable for 1400 iterations. The filtered HSG with PML is stable for 2500 iterations. The SHSG is stable for 3400 iterations. Filtered SHSG is stable for 7000 iterations. These results show periods of stability are significantly shorter than in the resonance test for the HSG and the SHSG. For example, in the cavity resonator, the SHSG was stable for 50000 iterations and the HSG was stable for 9000 iterations.

The SHSG and the filtered SHSG are both more stable than the HSG with PML and the filtered HSG with PML. For instance, the filtered SHSG is $2.8\times$ more stable than the filtered HSG with PML. And the SHSG is $1.36\times$ is more stable than the filtered HSG with PML. The results also show that the resonance in the signal caused by resonance in the water pipe overlaps the instability. This is shown in more detail in Figure 10.5.

This Figure shows that the HSG with PML is not able to model the entire waveform within its stable period. To a lesser degree, this is also true of the filtered HSG and the SHSG. However, the filtered SHSG can model the waveform after it has decayed significantly from the peak amplitude of the direct wave.

The findings show that the SHSG is more stable than the HSG for the sub-gridding of a GPR antenna over a dispersive soil containing a water-filled plastic pipe. Given that this scenario is particularly common in GPR modelling it is not unreasonable to suggest the SHSG is better suited to GPR modelling than the HSG. Furthermore, the SHSG was able to model the resonant effects in the late time response whereas the HSG was not.

10.1.3 Performance

The main aim of the sub-gridding is to improve the computational performance of GPR modelling using FDTD. Therefore the performance of the SHSG and the HSG algorithms is important.

An indication of the performance of the SHSG was not given in the previous chapter.
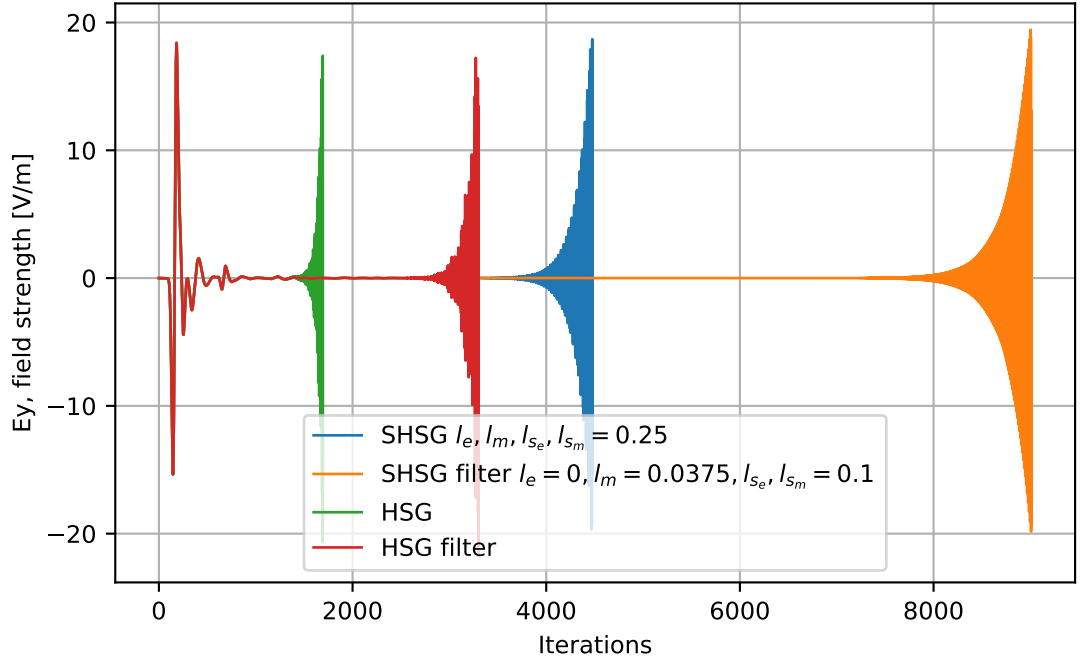
Figure 10.4: E_y received by the GSSI 1500 MHz over 9000 iterations. Comparison of the stability of each sub-gridding method.
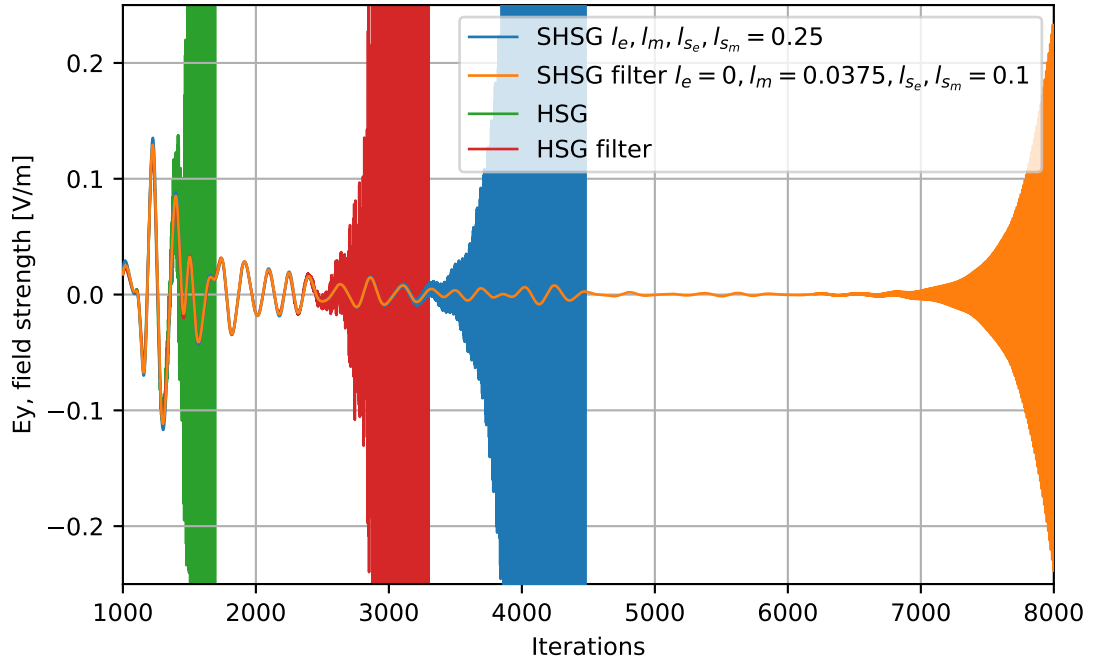
Figure 10.5: E_y received by the GSSI 1.5 GHz. Zoomed in view of the later time signals for each sub-gridding method.

This is because the performance of the algorithm is dependent on its application. For instance, the ratio of volumes of the sub-grids and main grids are highly dependent

on the particular problem. When the ratio is low a good performance relative to the fine grid solution is obtained. Therefore if a pipe is buried particularly shallowly the performance of the sub-gridding is reduced. However, the performance is improved if the pipe is buried deeply.

Also, whilst a relative measure of performance can always be made between the HSG and SHSG, it is not particularly useful as it does not give an insight into the absolute performance for a particular GPR modelling scenario.

The absolute performance of each algorithm is given here for the particular problem of the sub-gridded antenna above a dispersive half-space with a buried plastic water pipe. The intention is to give an impression of the performance that could be expected for a range of similar problems. And act as a guide to the improvements that would be available to optimisation problems where several iterations are required.

The performance metrics are the total time for the execution of gprMax process and the RAM which is allocated. Also, the real-time is computed. This is the process time in minutes divided by the total number of cores in the CPU. This gives a measure of the run time that could be expected if the system were dedicated only to the simulation.

More sophisticated metrics such as throughput have been used in the literature to measure the performance of FDTD implementations Warren (2009). These measures give a good comparison of like-for-like models with different implementations. However, they are not suitable in this case as the number of cells is necessarily lower in the sub-gridding. Consequently, the number of cells per second calculated would be reduced.

The results for the fine grid solution, HSG with PML and the SHSG only are calculated. This is because the computational cost of the filter is insignificant in terms of the solve time for the fields. And because the magnitude of the loss factor does not result in greater computation.

The simulations were run on a Supermicro Workstation 7048GR-TR system with 2 x Xeon E5-2640 v4 (2.4 GHz, 20 cores) CPU. Only one of the CPUs is utilised as there is no domain decomposition. The system also features four GPUs. However, no comparison is made to the GPU performance. This is because the HSG and SHSG are architecture-independent. Subsequent implementation of the sub-gridding algorithm for GPGPU would improve performance even more than the CPU implementation.

The results for the fine grid solution, HSG with PML and the SHSG experiments are shown in Table 10.1.

The results show that sub-gridding the antenna and pipe significantly improve the computational performance of the solver. For example, the HSG and SHSG are 17× and 28× faster than the FDTD solution respectively. Also, there is a reduction in memory allocation of 16× and 17× respectively.

What stands out in the table is the difference of 11 in the speed-up factors for the SHSG and HSG. The reason for this is the SHSG does not require any PML cells within the non-working region of the sub-grid. This reduces the overhead because PML cells are computationally more expensive than the basic FDTD update. This is less important when the sub-grid is small such as the tests in Bérenger (2011). However, the number of PML cells scales quadratically with the sub-grid length (the PML depth is fixed at 6 cells). Therefore for larger sub-grid sizes such as the sub-gridded antenna, the performance is worse. In contrast, the SHSG scales better as it does not require PML. Only a single Yee cell is required beyond the Outer Surface.

Model	Process time [s]	Real Time [min]	Speed up factor	Memory [GB]	Memory factor
FDTD Ref.	59806	49.8	1	33.7	1
HSG with PML	3570	2.98	17	2.2	16
SHSG	2163	1.80	28	2.0	17

Table 10.1: Simulation statistics. Process time and RAM allocated in the GSSI 1.5 MHz over a buried water filled pipe experiment. Results computed on a on a Supermicro SYS-7048GR-TR system with 2 x Xeon E5-2640 v4 (2.4 GHz, 20 cores) CPU.

An interesting finding of the results is that the memory requirement for the sub-gridding is very low. The simulations shown here could easily be performed on a PC. Another interesting implication of the low memory footprint is that in a GPU implementation multiple simulations could be run on a single GPU simultaneously. For instance, 12 simulations could be included on an NVIDIA TITAN RTX 24 GB GPU.

10.2   Summary

In this chapter, the SHSG algorithm has been applied to the GPR problem of a finely detailed antenna model over a dispersive half-space containing a water-filled plastic pipe. The computational cost in computing the fine grid solution has been reduced by sub-gridding the antenna and the pipe.

To stabilise the SHSG the recommended loss factors were applied to each sub-grid. It was also recommended that the loss factors be used in place of any conductivity intrinsic to the background material in the sub-grid provided that they are smaller than the equivalent conductivity resulting from the loss factor.

It was shown the accuracy of the SHSG was comparable to the HSG. Also, it was shown the SHSG is up to $2.8\times$ more stable than the filtered HSG. And that the computation of the SHSG solution was $28\times$ faster than the reference solution. Whereas the HSG computation was only $17\times$ faster. The increase in speed was attributed to the elimination of the sub-grid PML. This is also advantageous as the implementation is simplified.

Chapter 11

Conclusions

The main aim of this work was to develop an FDTD sub-gridding method and apply it to the problem of modelling finely detailed GPR antennas located in realistic environments. The reason for doing this was to reduce significantly the computation time and memory requirements required to simulate realistic antennas in large domains. This is particularly important in GPR research because optimising antenna designs and solving inverse problems usually require antennas modelled in situ and hence model sizes can be very large and computationally expensive to solve. It is also necessary to reduce the overall computation time for predictive methods in GPR. This is because these types of analysis rely on optimisation algorithms. These algorithms solve for model parameters using iterative methods which in turn required many simulation runs.

Previous work in this area has focused on sub-gridding targets. This has enabled researchers to reduce the computation overhead for modelling containing localised region of high dielectric strength or complex geometries. Typically, plastic pipes and water-filled pipes have been sub-gridded. But, realistic antennas have not. Another limitation of this research is that the underlying sub-gridding methodologies did not support high sub-gridding ratios. In the context of sub-gridding antennas, this is problematic as the advantage sub-gridding low-frequency antennas cannot be leveraged.

This research extends these works by embedded GPR antennas in sub-grids and using techniques which permit larger sub-gridding ratios. Firstly, this approach is more difficult as the field distribution around antennas are more complex and therefore a greater emphasis is placed on the accuracy of the sub-gridding technique. Secondly, employing large sub-gridding ratios allows for greater speed ups and opens more modelling opportunities for modelling low-frequency antennas.

Another approach to reducing computation time would have been to use existing computational techniques. For instance, GPUs could have been used to improve simulation times. For example, GPUs can compute FDTD solutions very quickly using massively parallel processing architectures. Equally, a domain decomposition approach would have yielded fast results. However, this work provides a more fundamental response to the problem.

The reason for this is that the sub-gridding approach can also be implemented on parallel architecture since the algorithms are general. Also, these approaches do not reduce the total memory requirements of large GPR models. For example, a cross-hole GPR model could encompass $4 \times 6 \times 1\,\mathrm{m}$ discretised at $\Delta l = 1\,\mathrm{mm}$ which would require $\approx 8\,\mathrm{TB}$ of RAM (Klotzsche et al., 2010). Sub-gridding can massively alleviate these memory requirements as it only needs about $12\,\mathrm{GB}$. Many sub-gridded GPR models can be run on a single node / GPU.

A secondary aim of this work was to improve the state of modelling of the interfaces between dispersive media and dielectrics. In particular those which are common in GPR modelling and for the range of frequencies typically found in GPR models. There are two reasons for this.

This is a novel concept which has not been examined in GPR modelling. Firstly, improvements in this area indirectly but significantly increase the performance of sub-gridding algorithms used in half-space problems. This effect can be explained by examining what happens to the accuracy of the FDTD method at material interfaces. In general material interfaces in FDTD are only accurate to first-order. Therefore the error decreases linearly when the discretisation is reduced. By restoring close to second-order accuracy at material interfaces the accuracy in the main grid is maintained to a greater degree. Achieving this level of accuracy is particularly important in sub-gridding algorithms because the discretisation in the main grid is artificially reduced.

Secondly, modelling dielectric/dispersive interfaces in GPR problems is a novel treatment. Previous work has only examined the techniques within the optical range and results in GPR simulations have only been obtained for frequency-independent materials. Also, the results for GPR materials have been taken largely at face value without analytical comparison.

11.1 Outcomes and Significance

11.1.1 Effective Permittivities of dispersive materials

Commonly, the accuracy of effective permittivity techniques assessed by comparing the analytical and simulated Mie scattering of a sphere of a given material. Typically in FDTD, this Mie scattering is evaluated by a near to far-field transformation for a range of frequency discrete frequency components. Since there is no existing Mie scattering implementation in gprMax, a set of tools were developed.

- Implementation of a total-field scattered-field formulation for illuminating targets with plane waves. This enables the calculation of the scattered field from any target for a broadband pulse. This result is very general and as such can be used to compute the scattering from any object such as a drone, or an aeroplane.

- Implementation of a near-field to far-field transformation. Scattered fields are transformed into the far-field. This feature alleviates the need to model the intermediate space in the Mie scattering.

An effective permittivity technique was developed for grid aligned surfaces. The technique showed that the arithmetic and harmonic averaged of the permittivities at the surface for Debye materials can be found and used directly with the PLRC technique for dispersive materials. This is a novel approach as it does not require any field splitting.

The performance of the arithmetic average was evaluated for GPR type behaviour. The Mie scattering of a series of spheres whose material properties were those of simple soil models with varying water content for broadband pulse used in GPR. The results showed that the smoothing kept the relative error below 20% whereas the non-smoothed produced errors of 80% within the range of acceptable dispersion. Although the relative errors are very high, it is important to note that only the reduction in error is important since the total-field scattered-field and near-field to far-field formulations introduce errors which are not present in the GPR simulation.

Also, numerical examples of dipoles over arithmetically averaged half-spaces were performed for the soil models and compared with non-averaged half-spaces. The results showed significant variation in comparison with a fine grid solution. For soils with 10% moisture content, the error was 15% greater. This result implies that soils modelled without effective permittivities are likely not representative of the real problem unless very fine spatial steps are used.

Furthermore, layered half-space tests confirmed that in dispersive/dispersive averaging the 4-pole Debye average can be reduced by fitting a 2 pole function to the data for similar soils with varying water content. This is important because decreasing the dimensionality of the soil model reduces the computation time significantly

11.1.2   HSG

The Huygen's sub-gridding algorithm was implemented in gprMax. This was not a trivial implementation in the context of FDTD programming. In comparison to many formulations in FDTD, sub-gridding algorithms are very complex to implement, and particularly so in 3d. Also, the algorithm had to be written as an extension module to gprMax. Although this implementation was considerably more difficult than a standalone code, there were large benefits.

Firstly, gprMax contains several advanced modelling features which can increase the range of applications for sub-gridded models. For instance, the state of the art formulations of PML and dispersive materials can be used to truncate the main grid, sub-grid and model more accurately dispersive materials. Secondly, sub-gridded models can include realistically modelled antennas from gprMax's antenna library. Consequently, this work has been able to simulate realistic antennas embedded in sub-grids in complex environments. In contrast, other GPR sub-gridding works have examined less complex models. This is most likely because they have had to implement and test every additional feature directly.

Furthermore, one of the main successes of the gprMax implementation is it can be used by a broad audience. Researchers will hopefully be able to produce sub-gridded models without needing a fundamental understanding of the underlying HSG algorithm. This is particularly important for many researchers who are not directly concerned with FDTD forward modelling. For instance, researchers studying in inverse modelling or antennas design.

Also, researchers interested in FDTD will be able to verify and extend the results presented here and develop the algorithms more easily.

An overview of the findings relating to the HSG aims is given below

- This work demonstrates that there is a need to model GPR problems with sub-gridding ratios up to at least 13.

- Demonstrated the HSG can sub-grid Hertzian dipoles with ratios up to 17 with

excellent results. The results show that as the results converge to the coarse solution as the ratio increases. This is evidence that the HSG can be used for a broad range of applications in GPR modelling that are not possible with other sub-gridding techniques.

- It was assumed that the PML did not contribute to the accuracy of the solution. However, it was shown that the leakage at the Huygen's surfaces can be reduced by including the PML. It was also shown that there is some dependence on the sub-gridding ratio.

- Demonstrated that a two-cell IS-OS gap could be used for very transient problems. This could be important for large sub-gridding ratios where the total number of cells should be minimised.

- A range of numerical experiments showed that the HSG can be used to sub-grid sub-surface targets, metal pipes, plastic water-filled pipes over dispersive soils. The results showed consistently that relative errors of less than 1% can be achieved in comparison with a fine grid solution. This result could be said to precise since it is of the order of the numerical dispersion error.

- It was shown that a novel effective permittivity model for dispersive soils indirectly reduces the relative error present in a buried water-pipe half-space problem from 5% to 0.6%. This result recovers the accuracy observed in the non-dispersive half-space tests. It is suggested that the reason Abalenkovs et al. (2012) observed propagation errors is that the dispersive interfaces have not been properly treated.

- A GSSI 1.5 GHz like antennas was embedded within a sub-grid with a ratio of 1:3 over a sub-gridded water-filled plastic pipe. The results show a peak error of $\approx$ 1.2%. A reduction of 17$\times$ and 16$\times$ was observed in computation time and memory usage. These results show a large increase in performance and an accuracy very comparable to the target sub-gridding. Clearly, the HSG can be used to model realistic antennas with only a small reduction in accuracy.

- The GSSI 1.5 MHz experiment was repeated with the antenna in contact with the ground. In the material traversal case, the HSG performs equally well to the non-material traverse. This result opens up the range of GPR modelling possibilities. For instance, separate components of the antenna such as the antenna structure could be sub-gridded for gain even greater performance.

- A GSSI 400 MHz like antenna was embedded in within a sub-grid with a ratio of 9 over a dispersive soil containing a buried metal plate. The results showed a peak error of 1.4%. This is the first time a sub-gridding ratio of 9 has been used to

sub-grid objects in GPR modelling. The results compare very well with spatially-filtered sub-gridding. The solution was computed $20\times$ more quickly than the fine grid solution and required $19\times$ less memory. The speed improvement is similar to the 1:3 case even though the sub-gridding ratio is greater. This is because the antenna occupies a large proportion of the domain. Since the metal plate is only $\approx 0.5\,\mathrm{m}$ below the surface much larger models are indeed possible. However, these models have not been evaluated as the solution to the reference problem quickly becomes intractable at larger sizes.

11.1.3 SHSG

A novel sub-gridding technique called the switched Huygen's sub-gridding was developed. The sub-gridding scheme has the properties of an extensible sub-gridding ratio and is also suitable for modelling GPR problems. However, it is more stable and only requires a conductive loss term rather than a PML to attenuate the stability.

Although previous attempts have been made to adopt artificial loss terms in the HSG, their inclusion has always resulted in an unacceptable attenuation of the physical solution. In the SHSG the Huygen's surfaces are arranged in a novel way as to permit the inclusion of artificial loss without significant direct attenuation of the solution. The following developments have been made.

- 1d derivation of a Huygen's surfaces arrangement and FDTD update equations which result in a zero field in the non-working regions.

- 1d numerical experiments of the reflection and transmission coefficient of a thin lossy layer with the SHSG and HSG. SHSG is more accurate for transmission and reflection coefficients.

- 3d derivation of a Huygen's surfaces arrangement and update equations which result in zero fields in non-working regions.

- Showed that the HSG suffers from rapid attenuation in the presence of loss factors and the SHSG does not.

- Parametric study to find loss factors which result in greatest stability whilst maintaining comparable accuracy to the HSG for late time resonant cases.

- Using recommended loss factor and 3 node filter, the SHSG is $5.6\times$ more stable than the HSG for the given resonance study.

- The GSSI 1.5 MHz antenna over a buried water-filled pipe experiment is replicated using the SHSG. The SHSG computes the solution $28\times$ faster than the reference solution. This surpasses the increase in the speed of the HSG ($17\times$) although the memory performance is slightly worse at $17\times$. The reason for the increase in speed is due to the elimination of the PML. In addition, the SHSG with the 3 node filter is $2.8\times$ more stable than the HSG with the filter.

Overall the aims of the research have been achieved. A sub-gridding algorithm has been successfully implemented and has been used to increase the computational performance of realistic antenna modelling in half space type problems. Furthermore, a novel sub-gridding scheme has been developed which offers better computational performance in terms of stability and compute time than the HSG whilst maintaining its key characteristics. Also, it has been demonstrated that smoothing the dispersive properties of materials in the coarse grid markedly improves the sub-gridding results in half-space problems. This is also true in general for any dispersive material in the main grid.

11.2 Future Work

Although the aims of the research have been largely met several interesting questions still remain. It is hoped that some of the following ideas could form the basis of future research.

11.2.1 Effective Permittivities of dispersive materials

In this work only grid aligned interfaces were explored. However, for large sub-gridding ratios, there may be features, such as the surface of the ground, which do not align with the coarse grid. For a non-grid aligned surface harmonic averages could be investigated. Also, some ground surfaces are geometrically complex, such as those resulting from fractal distributions. The CR method with the arithmetic, harmonic averages developed here could be explored.

11.2.2 SHSG

The parametric studies which investigated the stability for different loss factors demonstrated that there was no straightforward pattern to which loss factors were successful.

This was even more so, particularly in the filtered case. In particular, it was seen that using the loss factor at the IS electric field resulted in reflections whereas it did not in the 1d tests. Further investigation is required to understand why this is the case.

Also, some authors have demonstrated that stability in sub-gridding algorithms can be obtained when each field that is updated is also used to update the field that updated it. Since the Huygen's sub-gridding occurs over two surfaces this is not possible. Research on the possibility a single surface could lead a new algorithm which satisfies these requirements.

The results showed that materials can traverse the sub-gridding boundary. However, the material traversal implementation possible is not straight forward. This is because the material at each side of the Huygen's surface should be matched. The is particularly difficult where fractal surfaces or soil distributions cross the surfaces. A code which can automatically generate the correct materials at the interface would allow the sub-gridding algorithms to be applied in more realistic scenarios.

It has been shown that the HSG can be combined with implicit FDTD approaches. However, The HSG can actually be extended to couple any two schemes. This is because the method is based on the physical principle of equivalent currents. Extending this work by coupling it to another numerical scheme could be beneficial. For example, the responses of geometrically complex antennas simulated in free-space are modelled more accurately and efficiently using time-domain integral equations. However, soils are described as more accurately by FDTD methods. Antenna optimisation for antennas in realistic environments could be improved by hybridising the two techniques using a Huygen's surfaces approach.

Bibliography

M. Abalenkovs, F. Costen, J. P. Bérenger, R. Himeno, H. Yokota, and M. Fujii. Huygens subgridding for 3-D frequency-dependent finite-difference time-domain method. *IEEE Transactions on Antennas and Propagation*, 60(9):4336–4344, 2012.

I. Ahmed and Z. Chen. A hybrid ADI-FDTD subgridding scheme for efficient electromagnetic computation. *International Journal of Numerical Modelling: Electronic Networks, Devices and Fields*, 17(3):237–249, 2004.

A. P. Annan. Radio Interferometry Depth Sounding: Part i - Theoretical Discussion. *GEOPHYSICS*, 38(3):557–580, 1973.

A. P. Annan. GPR-History, Trends and Future Developments. *Subsurface Sensing Technologies and Applications*, 3(4):253–270, 2002.

A. P. Annan. 11. Ground-Penetrating Radar. In *Near-Surface Geophysics*, chapter 11, pages 357–438. Society of Exploration Geophysicists, 2005.

A. P. Annan, W. M. Waller, D. W. Strangway, J. R. Rossiter, J. D. Redman, and R. D. Watts. Electromagnetic response of a low-loss, 2-layer, dielectric earth for horizontal electric dipole excitation. *Geophysics*, 40(2):285–298, 1975.

J. T. Bailey, S. Evans, and G. D. Q. Robin. Radio echo sounding of polar ice sheets. *Nature*, 204(4957):420–421, 1964.

C. A. Balanis. *Antenna Theory: Analysis and Design*. Wiley-Blackwell, 3rd revise edition, 2005.

C. A. Balanis. *Advanced engineering electromagnetics*. John Wiley & Sons, Hoboken, 2nd ed. edition, 2012.

C. A. Balanis. *Antenna theory : analysis and design*. Hoboken, fourth edi edition, 2016.

S. Behnel, R. Bradshaw, C. Citro, L. Dalcin, D. S. Seljebotn, and K. Smith. Cython: The Best of Both Worlds. *Computing in Science Engineering*, 13(2):31–39, 2011a.

S. Behnel, R. Bradshaw, C. Citro, L. Dalcin, D. S. Seljebotn, and K. Smith. Cython: The Best of Both Worlds. *Computing in Science & Engineering*, 13(2):31–39, 2011b.

A. Benson. Application of ground penetrating radar in assesing some geological hazards: examples of ground water contamination, faults, and cavities. *Applied geophysics*, 33:177–193, 1995.

J.-P. Bérenger. A perfectly matched layer for the absorption of electromagnetic waves. *Journal of Computational Physics*, 114(2):185–200, 1994.

J.-P. Bérenger. A FDTD subgriding based on Huygens surfaces. In *2005 IEEE Antennas and Propagation Society International Symposium*, volume 2A, pages 98–101. IEEE, 2005.

J.-P. Bérenger. A Huygens Subgridding for the FDTD Method. *IEEE Transactions on Antennas and Propagation*, 54(12):3797–3804, 2006.

J. P. Bérenger. Perfectly Matched Layer (PML) for computational electromagnetics. *Synthesis Lectures on Computational Electromagnetics*, 8:1–120, 2007a.

J.-P. Bérenger. On the Huygens absorbing boundary conditions for electromagnetics. *Journal of Computational Physics*, 226(1):354–378, 2007b.

J.-P. Berenger. Three dimensional huygens subgridding for FDTD. In *2009 IEEE Antennas and Propagation Society International Symposium*, pages 1–4. IEEE, 2009a.

J.-P. Berenger. Extension of the FDTD Huygens Subgridding Algorithm to Two Dimensions. *IEEE Transactions on Antennas and Propagation*, 57(12):3860–3867, 2009b.

J.-P. Bérenger. Extension of the FDTD Huygens Subgridding Algorithm to Two Dimensions. *IEEE Transactions on Antennas and Propagation*, 57(12):3860–3867, 2009.

J.-P. Bérenger. The Huygens subgridding for the numerical solution of the Maxwell equations. *Journal of Computational Physics*, 230(14):5635–5659, 2011.

J.-P. Bérenger. A historical review of the absorbing boundary conditions for electromagnetics. *Forum for Electromagnetic Research Methods and Application Technologies*, 9, 2015.

T. Bergmann, J. O. A. Robertsson, and K. Holliger. Finitedifference modeling of electromagnetic wave propagation in dispersive and attenuating media. *GEOPHYSICS*, 63(3):856–867, 1998.

Bing-Zhong Wang, Yingjun Wang, Wenhua Yu, and R. Mittra. A hybrid 2-D ADI-FDTD subgridding scheme for modeling on-chip interconnects. *IEEE Transactions on Advanced Packaging*, 24(2):528–533, 2001.

J. Bourgeois and G. Smith. A fully three-dimensional simulation of a ground-penetrating radar: FDTD theory compared with experiment. *IEEE Transactions on Geoscience and Remote Sensing*, 34(1):36–44, 1996.

A. C. Cangellaris and D. B. Wright. Analysis of the Numerical Error Caused by the Stair-Stepped Approximation of a Conducting Boundary in FDTD Simulations of Electromagnetic Phenomena. *IEEE Transactions on Antennas and Propagation*, 39 (10):1518–1525, 1991.

S. P. Chaudhuri, A. L. Crandall, and D. M. Reidy. Multisensor data fusion for mine detection. In *Sensor Fusion III*, volume 1306, pages 187–204. SPIE, 1990.

M. W. Chevalier, R. J. Luebbers, and V. P. Cable. FDTD local grid with material traverse. *IEEE Transactions on Antennas and Propagation*, 45(3):411–421, 1997.

W. C. Chew and W. H. Weedon. A 3D perfectly matched medium from modified maxwell's equations with stretched coordinates. *Microwave and Optical Technology Letters*, 7(13):599–604, 1994.

R. A. Chilton and R. Lee. Conservative and Provably Stable FDTD Subgridding. *IEEE Transactions on Antennas and Propagation*, 55(9):2537–2549, 2007.

F. Collino, T. Fouquet, and P. Joly. Conservative space-time mesh refinement methods for the FDTD solution of Maxwell's equations. *Journal of Computational Physics*, 211(1):9–35, 2006.

J. C. Cook. Radar transparencies of mine and tunnel rocks. *Geophysics*, 40(5):865–885, 1975a.

J. C. Cook. RADAR TRANSPARENCIES OF MINE AND TUNNEL ROCKS. *Geophysics*, 40(5):865–885, 1975b.

F. Costen and J. P. Bérenger. Extension of the FDTD huygens subgridding to frequency dependent media. *Annales des Telecommunications/Annals of Telecommunications*, 65(3-4):211–217, 2010a.

F. Costen and J. P. Bérenger. Extension of the FDTD huygens subgridding to frequency dependent media. *Annales des Telecommunications/Annals of Telecommunications*, 65(3-4):211–217, 2010b.

F. Costen, J.-P. Bérenger, and A. Brown. Comparison of FDTD Hard Source With FDTD Soft Source and Accuracy Assessment in Debye Media. *IEEE Transactions on Antennas and Propagation*, 57(7):2014–2022, 2009.

D. J. Daniels. *Ground Penetrating Radar*. Institution of Engineering and Technology, 2nd edition, 2007a.

D. J. Daniels. An assessment of the fundamental performance of GPR against buried landmines. In *Detection and Remediation Technologies for Mines and Minelike Targets XII*, volume 6553, pages 103–117. International Society for Optics and Photonics, SPIE, 2007b.

D. J. Daniels. Ground penetrating radar for buried landmine and IED detection. *NATO Science for Peace and Security Series B: Physics and Biophysics*, pages 89–111, 2009.

J. L. Davis and A. P. Annan. Ground-Penetrating Radar for High-Resolution Mapping O F Soil and Rock Stratigraphy. *Geophysical Prospecting*, 37(1989):531–551, 1989.

A. Deinega and I. Valuev. Subpixel smoothing for conductive and dispersive media in the finite-difference time-domain method. *Optics Letters*, 32(23):3429, 2007.

S. Dey and R. Mittra. A locally conformal finite-difference time-domain (FDTD) algorithm for modeling three-dimensional perfectly conducting objects. *IEEE Microwave and Guided Wave Letters*, 7(9):273–275, 1997.

N. Diamanti. *An Efficient Ground Penetrating Radar Finite-Difference Time-Domain Subgridding Scheme and its Application to the Non-Destructive Testing of Masonry Arch Bridges*. PhD thesis, The University of Edinburgh, 2008.

N. Diamanti and A. P. Annan. Characterizing the energy distribution around GPR antennas. *Journal of Applied Geophysics*, 99:83–90, 2013.

N. Diamanti and A. Giannopoulos. Implementation of ADI-FDTD subgrids in ground penetrating radar FDTD models. *Journal of Applied Geophysics*, 67(4):309–317, 2009.

N. Diamanti, A. Giannopoulos, and M. C. Forde. Numerical modelling and experimental verification of GPR to investigate ring separation in brick masonry arch bridges. *NDT and E International*, 41(5):354–363, 2008.

M. Dobson, F. Ulaby, M. Hallikainen, and M. El-rayes. Microwave Dielectric Behavior of Wet Soil-Part II: Dielectric Mixing Models. *IEEE Transactions on Geoscience and Remote Sensing*, GE-23(1):35–46, 1985.

B. Donderici and F. L. Teixeira. Improved FDTD subgridding algorithms via digital filtering and domain overriding. *IEEE Transactions on Antennas and Propagation*, 53(9):2938–2951, 2005.

F. H. Drossaert and A. Giannopoulos. A nonsplit complex frequency-shifted PML based on recursive integration for FDTD modeling of elastic waves. *Geophysics*, 72 (2):T9–T17, 2007.

N. Engheta, C. H. Papas, and C. Elachi. Radiation patterns of interfacial dipole antennas. *Radio Science*, 17(6):1557–1566, 1982.

B. Engquist and A. Majda. Absorbing Boundary Conditions for the Numerical Simulation of Waves. *Mathematics of Computation*, 31(139):629, 1977.

A. Farjadpour, D. Roundy, A. Rodriguez, M. Ibanescu, P. Bermel, J. D. Joannopoulos, S. G. Johnson, and G. W. Burr. Improving accuracy by subpixel smoothing in the finite-difference time domain. *Optics Letters*, 31(20):2972, 2006.

M. Gaffar and D. Jiao. An Explicit and Unconditionally Stable FDTD Method for Electromagnetic Analysis. *IEEE Transactions on Microwave Theory and Techniques*, 62(11):2538–2550, 2014.

M. Gaffar and D. Jiao. An alternative method for making an explicit FDTD unconditionally stable. In *2015 IEEE MTT-S International Microwave Symposium*, pages 1–4. IEEE, 2015.

S. Garcia, Tae-Woo Lee, and S. Hagness. On the accuracy of the ADI-FDTD method. *IEEE Antennas and Wireless Propagation Letters*, 1(1):31–34, 2002.

S. Gedney. An anisotropic perfectly matched layer-absorbing medium for the truncation of FDTD lattices. *IEEE Transactions on Antennas and Propagation*, 44(12):1630–1639, 1996.

I. Giannakis and A. Giannopoulos. A novel piecewise linear recursive convolution approach for dispersive media using the finite-difference time-domain method. *IEEE Transactions on Antennas and Propagation*, 62(5):2669–2678, 2014.

I. Giannakis, A. Giannopoulos, and C. Warren. A Realistic FDTD Numerical Modeling Framework of Ground Penetrating Radar for Landmine Detection. *IEEE Journal of Selected Topics in Applied Earth Observations and Remote Sensing*, 9(1):1–15, 2015.

I. Giannakis, A. Giannopoulos, and C. Warren. A Realistic FDTD Numerical Modeling Framework of Ground Penetrating Radar for Landmine Detection. *IEEE Journal of Selected Topics in Applied Earth Observations and Remote Sensing*, 9(1):37–51, 2016a.

I. Giannakis, A. Giannopoulos, and A. Yarovoy. Model-Based Evaluation of Signal-to-Clutter Ratio for Landmine Detection Using Ground-Penetrating Radar. *IEEE Transactions on Geoscience and Remote Sensing*, 54(6):3564–3573, 2016b.

I. Giannakis, A. Giannopoulos, and C. Warren. Realistic FDTD GPR Antenna Models Optimized Using a Novel Linear/Nonlinear Full-Waveform Inversion. *IEEE Transactions on Geoscience and Remote Sensing*, pages 1–11, 2018.

I. Giannakis, A. Giannopoulos, and C. Warren. A Machine Learning-Based Fast-Forward Solver for Ground Penetrating Radar With Application to Full-Waveform Inversion. *IEEE Transactions on Geoscience and Remote Sensing*, 57(7):4417–4426, 2019a.

I. Giannakis, A. Giannopoulos, and C. Warren. Realistic FDTD GPR Antenna Models Optimized Using a Novel Linear/Nonlinear Full-Waveform Inversion. *IEEE Transactions on Geoscience and Remote Sensing*, 57(3):1768–1778, 2019b.

I. Giannakis, F. Tosti, L. Lantini, and A. M. Alani. Health Monitoring of Tree Trunks Using Ground Penetrating Radar. *IEEE Transactions on Geoscience and Remote Sensing*, 57(10):8317–8326, 2019c.

A. Giannopoulos. Modelling ground penetrating radar by GprMax. *Construction and Building Materials*, 19(10):755–762, 2005.

A. Giannopoulos. An improved new implementation of complex frequency shifted PML for the FDTD method. *IEEE Transactions on Antennas and Propagation*, 56(9): 2995–3000, 2008.

A. Giannopoulos. Unsplit implementation of higher order PMLs. *IEEE Transactions on Antennas and Propagation*, 60(3):1479–1485, 2012.

A. Giannopoulos. Multipole Perfectly Matched Layer for Finite-Difference Time-Domain Electromagnetic Modeling. *IEEE Transactions on Antennas and Propagation*, 66(6):2987–2995, 2018a.

A. Giannopoulos. Multipole Perfectly Matched Layer for Finite-Difference Time-Domain Electromagnetic Modeling. *IEEE Transactions on Antennas and Propagation*, 66(6):2987–2995, 2018b.

A. Giannopoulos and N. Diamanti. Numerical modelling of ground-penetrating radar response from rough subsurface interfaces. *Near Surface Geophysics*, 6(6):357–369, 2008.

D. J. Griffiths. *Introduction to electrodynamics*. Cambridge University Press, 4th edition, 2019.

M. H. El-said. Geophysical Prospection of Underground Water in the Desert by Means of Electromagnetic Interference Fringes. *Proceedings of the IRE*, 44(1):24–30, 1956.

M. T. Hallikainen, F. T. Ulabz, M. C. Dobson, M. A. El-Rayes, and L. K. Wu. Microwave Dielectric Behavior of Wet Soil-Part I: Empirical Models and Experimental Observations. *IEEE Transactions on Geoscience and Remote Sensing*, GE-23(1): 25–34, 1985.

R. F. Harrington. *Field Computation by Moment Methods.* Wiley-IEEE Press, 1993.

T. W. Hertel and G. S. Smith. On the convergence of common FDTD feed models for antennas. *IEEE Transactions on Antennas and Propagation*, 51(8):1771–1779, 2003.

R. L. Higdon. Absorbing boundary conditions for difference approximations to the multidimensional wave equation. *Mathematics of Computation*, 47(176):437–437, 1986.

R. L. Higdon. Numerical Absorbing Boundary Conditions for the Wave Equation. *Mathematics of Computation*, 49(179):65, 1987.

J. Hipp. Soil electromagnetic parameters as functions of frequency, soil density, and soil moisture. *Proceedings of the IEEE*, 62(1):98–103, 1974.

Z. Huang, G. G. Pan, and K. S. Chen. A synchronized multigrid time domain method via huygens subgridding and implicit algorithms. *IEEE Transactions on Antennas and Propagation*, 61(5):2605–2614, 2013.

C. Hüelsmeyer. Wireless Transmitting and Receiving Mechanism for Electric Waves, 1904.

A. Ishimaru. *Electromagnetic Wave Propagation, Radiation, and Scattering.* John Wiley & Sons, Inc., Hoboken, NJ, USA, second edi edition, 2017.

G. Junkin and A. P. Anderson. Limitations in microwave holographic synthetic aperture imaging over a lossy half-space. *IEE Proceedings F: Communications Radar and Signal Processing*, 135(4):321–329, 1988.

T. Jurgens, A. Taflove, K. Umashankar, and T. Moore. Finite-difference time-domain modeling of curved surfaces (EM scattering). *IEEE Transactions on Antennas and Propagation*, 40(4):357–366, 1992.

Kane Yee. Numerical solution of initial boundary value problems involving maxwell's equations in isotropic media. *IEEE Transactions on Antennas and Propagation*, 14 (3):302–307, 1966.

N. Kaneda, B. Houshmand, and T. Itoh. FDTD analysis of dielectric resonators with curved surfaces. *IEEE Transactions on Microwave Theory and Techniques*, 45(9): 1645–1649, 1997.

D. Kelley and R. Luebbers. Piecewise linear recursive convolution for dispersive media using FDTD. *IEEE Transactions on Antennas and Propagation*, 44(6):792–797, 1996.

T. W. B. Kibble and F. H. Berkshire. *Classical mechanics*. Imperial College Press, 2004.

I. S. Kim and W. J. R. Hoefer. A local mesh refinement for the time domain finite diference method using Maxwells Curl Equations. *IEEE Transactions on Microwave Theory and Techniques*, 38(6):812–815, 1990.

R. W. P. King and G. S. Smith. *Antennas in Matter: Fundamentals, Theory, and Applications*. MIT Press, 1981.

A. Klotzsche, J. Van Der Kruk, G. A. Meles, J. Doetsch, H. Maurer, and N. Linde. Full-waveform inversion of cross-hole ground-penetrating radar data to characterize a gravel aquifer close to the Thur River, Switzerland. *Near Surface Geophysics*, 8(6): 635–649, 2010.

A. Klotzsche, H. Vereecken, and J. van der Kruk. GPR full-waveform inversion of a variably saturated soil-aquifer system. *Journal of Applied Geophysics*, 170:103823, 2019.

K. Kunz and L. Simpson. A Technique for Increasing the Resolution of Finite-Difference Solutions of the Maxwell Equation. *IEEE Transactions on Electromagnetic Compatibility*, EMC-23(4):419–422, 1981.

M. Kuzuoglu and R. Mittra. Frequency dependence of the constitutive parameters of causal perfectly matched anisotropic absorbers. *IEEE Microwave and Guided Wave Letters*, 6(12):447–449, 1996.

Kyu-Pyung Hwang and A. Cangellaris. Effective permittivities for second-order accurate FDTD equations at dielectric interfaces. *IEEE Microwave and Wireless Components Letters*, 11(4):158–160, 2001.

K. H. Lee, C. C. Chen, F. L. Teixeira, and R. Lee. Modeling and investigation of a geometrically complex UWB GPR antenna using FDTD. *IEEE Transactions on Antennas and Propagation*, 52(8):1983–1991, 2004.

A. Lestari. Capacitively tapered bowtie antenna. Technical report, Delft University of Technology, 2007.

A. Lestari, A. Yarovoy, and L. Ligthart. RC-Loaded Bow-Tie Antenna for Improved Pulse Radiation. *IEEE Transactions on Antennas and Propagation*, 52(10):2555–2563, 2004.

Z. Liao, K. Huang, and B. Yang. A transmitting boundary for transient wave analysis. *Science Sinica, Ser A-27-10*, pages 1063–1076, 1984.

J. Liu, M. Brio, and J. V. Moloney. Subpixel smoothing finite-difference time-domain method for material interface between dielectric and dispersive media. *Optics Letters*, 37(22):4802, 2012.

R. Luebbers, K. Kunz, M. Schneider, and F. Hunsberger. A finite-difference time-domain near zone to far zone transformation (electromagnetic scattering). *IEEE Transactions on Antennas and Propagation*, 39(4):429–433, 1991.

R. Luebbers, D. Steich, and K. Kunz. FDTD calculation of scattering from frequency-dependent materials. *IEEE Transactions on Antennas and Propagation*, 41(9):1249–1257, 1993.

J. G. Maloney and G. S. Smith. Accurate Modeling of Antennas for Radiating Short Pulses, FDTD Analysis and Experimental Measurements. In *Ultra-Wideband, Short-Pulse Electromagnetics*, pages 149–156. Springer US, Boston, MA, 1993.

J. G. Maloney, G. S. Smith, and W. R. Scott. Accurate Computation of the Radiation from Simple Antennas Using the Finite-Difference Time-Domain Method. *IEEE Transactions on Antennas and Propagation*, 38(7):1059–1068, 1990.

J. G. Maloney, K. L. Shlager, and G. S. Smith. c. *IEEE Transactions on Antennas and Propagation*, 42(2):289–292, 1994.

D. E. Merewether, R. Fisher, and F. W. Smith. On Implementing a Numeric Huygen's Source Scheme in a Finite Difference Program to Illuminate Scattering Bodies. *IEEE Transactions on Nuclear Science*, 27(6):1829–1833, 1980.

A. Mohammadi, H. Nadgaran, and M. Agio. Contour-path effective permittivities for the two-dimensional finite-difference time-domain method. *Optics Express*, 13(25):10367, 2005.

R. M. Morey. Continuous Subsurface Profiling by Impulse Radar. *Proceedings of Engineering Foundations Conference on Subsurface Exploration for Underground Excavations and Heavy Construction*, pages 213–232, 1974.

G. Mur. Absorbing Boundary Conditions for the Finite-Difference Approximation of the Time-Domain Electromagnetic-Field Equations. *IEEE Transactions on Electromagnetic Compatibility*, EMC-23(4):377–382, 1981.

T. Namiki. 3-D ADI-FDTD method-unconditionally stable time-domain algorithm for solving full vector maxwell's equations. *IEEE Transactions on Microwave Theory and Techniques*, 48(10):1743–1748, 2000.

247

Y. Nishioka. FDTD analysis of resistor-loaded bow-tie antennas covered with ferrite-coated conducting cavity for subsurface radar. *IEEE Transactions on Antennas and Propagation*, 47(6):970–977, 1999.

M. Okoniewaki, M. Mrozowski, and M. Stuchly. Simple treatment of multi-term dispersion in FDTD. *IEEE Microwave and Guided Wave Letters*, 7(5):121–123, 1997.

M. Okoniewski, E. Okoniewska, and M. A. Stuchly. Three-dimensional subgridding algorithm for FDTD. *IEEE Transactions on Antennas and Propagation*, 45(3):422–429, 1997.

A. F. Oskooi, D. Roundy, M. Ibanescu, P. Bermel, J. D. Joannopoulos, and S. G. Johnson. Meep: A flexible free-software package for electromagnetic simulations by the FDTD method. *Computer Physics Communications*, 181(3):687–702, 2010.

N. Peplinski, F. Ulaby, and M. Dobson. Dielectric properties of soils in the 0.3-1.3-GHz range. *IEEE Transactions on Geoscience and Remote Sensing*, 33(3):803–807, 1995.

D. Popovic and M. Okoniewski. Effective permittivity at the interface of dispersive dielectrics in FDTD. *IEEE Microwave and Wireless Components Letters*, 13(7): 265–267, 2003.

L. J. Porcello, R. L. Jordan, J. S. Zelenka, G. F. Adams, R. J. Phillips, W. E. Brown, S. H. Ward, and P. L. Jackson. The Apollo lunar sounder radar system. *Proceedings of the IEEE*, 62(6):769–783, 1974.

M. Potter and J.-P. Bérenger. A Review of the Total Field/Scattered Field Technique for the FDTD Method. *Forum for Electromagnetic Research Methods and Applications Technologies*, 19, 2017.

D. Prescott and N. Shuley. A method for incorporating different sized cells into the finite-difference time-domain analysis technique. *IEEE Microwave and Guided Wave Letters*, 2(11):434–436, 1992.

J. Randa, M. Kanda, and R. Orr. Resistively-tapered-dipole electric-field probes up to 40 GHz. In *IEEE 1991 International Symposium on Electromagnetic Compatibility*, pages 265–266. IEEE, 1991.

D. J. Robinson and J. B. Schneider. On the Use of the Geometric Mean in FDTD Near-to-Far-Field Transformations. *IEEE Transactions on Antennas and Propagation*, 55 (11):3204–3211, 2007.

J. A. Roden and S. D. Gedney. Convolution PML (CPML): An efficient FDTD implementation of the CFS-PML for arbitrary media. *Microwave and Optical Technology Letters*, 27(5):334–339, 2000.

C. D. Sarris. Extending the stability limit of the FDTD method with spatial filtering. *IEEE Microwave and Wireless Components Letters*, 21(4):176–178, 2011.

M. Sato, Y. Hamada, X. Feng, F.-N. Kong, Z. Zeng, and G. Fang. GPR using an array antenna for landmine detection. *Near Surface Geophysics*, 2(1):7–13, 2004.

J. Schneider. Plane Waves in FDTD Simulations and a Nearly Perfect Total-Field/Scattered-Field Boundary. *IEEE Transactions on Antennas and Propagation*, 52(12):3280–3287, 2004.

J. B. Schneider. Understanding the Finite-Difference Time-Domain Method, 2010.

J. B. Schneider and C. L. Wagner. FDTD Dispersion Revisited: Faster-Than-Light Propagation. *IEEE Microwave and Guided Wave Letters*, 9(2):54–56, 1999.

Scottprahl. miepython, 2019.

Sensors and Software. PulseEKKO For The GPR Professional, 2016.

K. L. Shlager, G. S. Smith, and J. G. Maloney. Optimization of Bow-Tie Antennas for Pulse Radiation. *IEEE Transactions on Antennas and Propagation*, 42(7):975–982, 1994.

G. Smith. Directive properties of antennas for transmission into a material half-space. *IEEE Transactions on Antennas and Propagation*, 32(3):232–246, 1984a.

G. Smith. Directive properties of antennas for transmission into a material half-space. *IEEE Transactions on Antennas and Propagation*, 32(3):232–246, 1984b.

S. Stadler. *A Forward Modeling Study for the Investigation of the Vertical Water-Content Distribution of Using Guided GPR Waves.* Master's thesis, Freiberg University of Mining and Technology, 2017.

S. Stadler and J. Igel. A numerical study on using guided GPR waves along metallic cylinders in boreholes for permittivity sounding. *2018 17th International Conference on Ground Penetrating Radar, GPR 2018*, pages 1–4, 2018a.

S. Stadler and J. Igel. A numerical study on using guided GPR waves along metallic cylinders in boreholes for permittivity sounding. In *2018 17th International Conference on Ground Penetrating Radar (GPR)*, pages 1–4. IEEE, 2018b.

S. W. Staker, C. L. Holloway, A. U. Bhobe, and M. Piket-May. Alternating-direction implicit (ADI) formulation of the finite-difference time-domain (FDTD) method: Algorithm and material dispersion implementation. *IEEE Transactions on Electromagnetic Compatibility*, 45(2):156–166, 2003.

B. O. Steenson. *Radar Methods for the Exploration of Glaciers*. PhD thesis, California Institute of Technology, 1951.

Supriyo Dey and R. Mittra. A conformal finite-difference time-domain technique for modeling cylindrical dielectric resonators. *IEEE Transactions on Microwave Theory and Techniques*, 47(9):1737–1739, 1999.

A. Taflove and M. E. Brodwin. Numerical Solution of Steady-State Electromagnetic Scattering Problems Using the Time-Dependent Maxwell's Equations. *IEEE Transactions on Microwave Theory and Techniques*, 23(8):623–630, 1975.

A. Taflove and S. Hagness. *Computational Electrodynamics. The finite difference time-domain method.* Artech House, Boston, Mass, 3rd edition, 2005.

A. Taflove, K. Umashankar, and T. Jurgens. Validation of FD-TD modeling of the radar cross section of three-dimensional structures spanning up to nine wavelengths. *IEEE Transactions on Antennas and Propagation*, 33(6):662–666, 1985.

T. Tan and M. Potter. 1-D Multipoint Auxiliary Source Propagator for the Total-Field/Scattered-Field FDTD Formulation. *IEEE Antennas and Wireless Propagation Letters*, 6:144–148, 2007.

F. Teixeira, Weng Cho Chew, M. Straka, M. Oristaglio, and T. Wang. Finite-difference time-domain simulation of ground penetrating radar on dispersive, inhomogeneous, and conductive soils. *IEEE Transactions on Geoscience and Remote Sensing*, 36(6): 1928–1937, 1998.

The SciPy community. What is NumPy?, 2019.

P. Thoma and T. Weiland. A Consistent Subgridding Scheme for the Finite Difference Time Domain Method. *International Journal of Numerical Modelling: Electronic Networks, Devices and Fields*, 9(5):359–374, 1996.

G. C. Topp, J. L. Davis, and A. P. Annan. Electromagnetic determination of soil water content: Measurements in coaxial transmission lines. *Water Resources Research*, 16 (3):574–582, 1980.

D. Uduwawala and M. Norgren. An Investigation of Some Geometrical Shapes and Selection of Shielding and Lumped Resistors of Planar Dipole Antennas for GPR Applications Using FDTD. *IEEE Transactions on Geoscience and Remote Sensing*, 44(12):3555–3562, 2006.

D. Uduwawala, M. Norgren, P. Fuks, and A. Gunawardena. A complete fdtd simulation of a real GPR antenna system operating above lossy and dispersive grounds. *Progress In Electromagnetics Research*, 50:209–229, 2005.

K. Umashankar and A. Taflove. A novel method to analyze electromagnetic scattering of complex objects. *IEEE Transactions on Electromagnetic Compatibility*, EMC-24 (4):397–405, 1982.

K. R. Umashankar. Numerical analysis of electromagnetic wave scattering and interaction based on frequency-domain integral equation and method of moments techniques. *Wave Motion*, 10(6):493–525, 1988.

University of Edinburgh. Archer Hardware, 2019.

R. R. Unterberger. Radar Propagation in Rock Salt. *Geophysical Prospecting*, 26(2): 312–328, 1978.

A. Vaccari, R. Pontalti, C. Malacarne, and L. Cristoforetti. A robust and efficient subgridding algorithm for finite-difference time-domain simulations of Maxwell's equations. *Journal of Computational Physics*, 194(1):117–139, 2004.

J. van der Kruk, N. Gueting, A. Klotzsche, G. He, S. Rudolph, C. von Hebel, X. Yang, L. Weihermüller, A. Mester, and H. Vereecken. Quantitative multi-layer electromagnetic induction inversion and full-waveform inversion of crosshole ground penetrating radar data. *Journal of Earth Science*, 26(6):844–850, 2015.

S. van der Walt, S. C. Colbert, and G. Varoquaux. The NumPy Array: A Structure for Efficient Numerical Computation. *Computing in Science & Engineering*, 13(2): 22–30, 2011.

R. Vickers. Ultra-wideband radar-potential and limitations. In *1991 IEEE MTT-S International Microwave Symposium Digest*, pages 371–374. IEEE, 1991.

C. L. Wagner and J. B. Schneider. Divergent fields, charge, and capacitance in FDTD simulations. *IEEE Transactions on Microwave Theory and Techniques*, 46(12 PART 1):2131–2136, 1998.

A. H. Waite and S. J. Schmidt. Gross Errors in Height Indication from Pulsed Radar Altimeters Operating over Thick Ice or Snow. *Proceedings of the IRE*, 50(6):1515–1520, 1962.

S. Wang and F. Teixeira. Some Remarks on the Stability of Time-Domain Electromagnetic Simulations. *IEEE Transactions on Antennas and Propagation*, 52(3):895–898, 2004.

C. Warren. *Numerical Modelling of High Frequency Ground Penetrating Radar Antennas*. PhD thesis, University of Edinburgh, 2009.

C. Warren and A. Giannopoulos. Creating finite-difference time-domain models of commercial ground-penetrating radar antennas using Taguchi's optimization method. *Geophysics*, 76(2):G37–G47, 2011.

C. Warren and A. Giannopoulos. Characterisation of a ground penetrating radar antenna in lossless homogeneous and lossy heterogeneous environments. *Signal Processing*, 132:221–226, 2017.

C. Warren, A. Giannopoulos, and I. Giannakis. gprMax: Open source software to simulate electromagnetic wave propagation for Ground Penetrating Radar. *Computer Physics Communications*, 209:163–170, 2016a.

C. Warren, A. Giannopoulos, and I. Giannakis. gprMax: Open source software to simulate electromagnetic wave propagation for Ground Penetrating Radar. *Computer Physics Communications*, 209:163–170, 2016b.

C. Warren, A. Giannopoulos, A. Gray, I. Giannakis, A. Patterson, L. Wetter, and A. Hamrah. A CUDA-based GPU engine for gprMax: Open source FDTD electromagnetic simulation software. *Computer Physics Communications*, 237:208–218, 2019.

M. E. Watts and R. E. Diaz. Perfect plane-wave injection into a finite FDTD domain through teleportation of fields. *Electromagnetics*, 23(2):187–201, 2003.

X.-K. Wei, X. Zhang, N. Diamanti, W. Shao, and C. D. Sarris. Subgridded FDTD Modeling of Ground Penetrating Radar Scenarios Beyond the Courant Stability Limit. *IEEE Transactions on Geoscience and Remote Sensing*, 55(12):7189–7198, 2017.

X.-K. Wei, W. Shao, S. Ding, and B.-Z. Wang. Hybrid sub-gridded ADE-FDTD method for modeling ground-penetrating radar on dispersive soils. *Journal of Electromagnetic Waves and Applications*, 32(11):1416–1426, 2018.

T. Weiland. On the unique numerical solution of Maxwellian eigenvalue problems in three dimensions. *Particle Accelerators*, 17:227–242, 1985.

Wenhua Yu and R. Mittra. A conformal finite difference time domain technique for modeling curved dielectric surfaces. *IEEE Microwave and Wireless Components Letters*, 11(1):25–27, 2001.

W. Wiscombe. Mie scattering calculations: advances in techniques and fast, vector-speed computer codes. Technical Report June, University Corporation for Atmospheric Research, 1979.

K. Xiao, D. J. Pommerenke, and J. L. Drewniak. A three-dimensional FDTD subgridding algorithm with separated temporal and spatial interfaces and related stability analysis. *IEEE Transactions on Antennas and Propagation*, 55(7):1981–1990, 2007.

Xu Li, A. Taflove, and V. Backman. Modified FDTD near-to-far-field transformation for improved backscattering calculation of strongly forward-scattering objects. *IEEE Antennas and Wireless Propagation Letters*, 4:35–38, 2005.

A. Yarovoy, A. Schukin, I. Kaploun, and L. Ligthart. The dielectric wedge antenna. *IEEE Transactions on Antennas and Propagation*, 50(10):1460–1472, 2002.

Z. Ye, C. Liao, X. Xiong, and M. Zhang. A Novel FDTD Subgridding Method with Improved Separated Temporal and Spatial Subgridding Interfaces. *IEEE Antennas and Wireless Propagation Letters*, 16:1011–1015, 2016.

W. Yu and R. Mittra. New subgridding method for the finite-difference time-domain (FDTD) algorithm. *Microwave and Optical Technology Letters*, 21(5):330–333, 1999.

L. Zhou. *The Study of RF Burns and AMI Exposure*. PhD thesis, WASHINGTON STATE UNIVERSITY, 2012.

L. Zhou, J. B. Schneider, and R. G. Olsen. Using Artificial Loss to Control the Instability in the Huygens Subgridding Method. Technical report, School of Electrical Engineering & Computer Science Washington State University, 2010.

M. Zhou, Z. David Chen, W. Fan, X. Bo, and W. Wei. A subgridding scheme with the unconditionally stable explicit FDTD method. In *2016 IEEE MTT-S International Conference on Numerical Electromagnetic and Multiphysics Modeling and Optimization (NEMO)*, pages 1–3. IEEE, 2016.

S. Zivanovic, K. Yee, and K. Mei. A subgridding method for the time-domain finite-difference method to solve Maxwell's equations. *IEEE Transactions on Microwave Theory and Techniques*, 39(3):471–479, 1991.

Appendices

Appendix A

FDTD Update Equations

$$
\begin{aligned}
\left.E_x\right|_{i+1/2,j,k}^{q+1/2} &= \frac{1-\frac{\sigma\Delta t}{2\epsilon}}{1+\frac{\sigma\Delta t}{2\epsilon}}\left.E_x\right|_{i+1/2,j,k}^{q-1/2} + \frac{\frac{\Delta t}{\epsilon}}{1+\frac{\sigma\Delta t}{2\epsilon}}\left(\frac{\left.H_z\right|_{i+1/2,j+1/2,k}^{q} - \left.H_z\right|_{i+1/2,j-1/2,k}^{q}}{\Delta y}\right. \\
&\qquad\qquad - \frac{\left.H_y\right|_{i+1/2,j,k+1/2}^{q} - \left.H_y\right|_{i+1/2,j,k-1/2}^{q}}{\Delta z} \\
&\qquad\qquad \left. - \left.J_{ix}\right|_{i+1/2,j,k}^{q}\right) \qquad\qquad\qquad\text{(A.1)}
\end{aligned}
$$

$$
\begin{aligned}
\left.E_y\right|_{i,j+1/2,k}^{q+1/2} &= \frac{1-\frac{\sigma\Delta t}{2\epsilon}}{1+\frac{\sigma\Delta t}{2\epsilon}}\left.E_y\right|_{i,j+1/2,k}^{q-1/2} + \frac{\frac{\Delta t}{\epsilon}}{1+\frac{\sigma\Delta t}{2\epsilon}}\left(\frac{\left.H_x\right|_{i,j+1/2,k+1/2}^{q} - \left.H_x\right|_{i,j+1/2,k-1/2}^{q}}{\Delta y}\right. \\
&\qquad\qquad - \frac{\left.H_z\right|_{i+1/2,j+1/2,k}^{q} - \left.H_z\right|_{i-1/2,j+1/2,k}^{q}}{\Delta z} \\
&\qquad\qquad \left. - \left.J_{iy}\right|_{i,j+1/2,k}^{q}\right) \qquad\qquad\qquad\text{(A.2)}
\end{aligned}
$$

$$
E_z\Big|_{i,j,k+1/2}^{q+1/2} = \frac{1 - \frac{\sigma\Delta t}{2\epsilon}}{1 + \frac{\sigma\Delta t}{2\epsilon}} E_z\Big|_{i,j,k+1/2}^{q-1/2} + \frac{\frac{\Delta t}{\epsilon}}{1 + \frac{\sigma\Delta t}{2\epsilon}} \left(\frac{H_y\Big|_{i+1/2,j,k+1/2}^{q} - H_y\Big|_{i-1/2,j-1/2,k}^{q}}{\Delta y} \right.
$$

$$
- \frac{H_x\Big|_{i,j+1/2,k+1/2}^{q} - H_x\Big|_{i,j-1/2,k+1/2}^{q}}{\Delta z}
$$

$$
\left. - J_{iz}\Big|_{i,j,k+1/2}^{q} \right) \tag{A.3}
$$

$$
H_x\Big|_{i,j+1/2,k+1/2}^{q} = \frac{1 - \frac{\sigma_m\Delta t}{2\mu}}{1 + \frac{\sigma_m\Delta t}{2\mu}} H_x\Big|_{i,j+1/2,k+1/2}^{q-1} + \frac{\frac{\Delta t}{\mu}}{1 + \frac{\sigma_m\Delta t}{2\mu}} \left(\frac{E_y\Big|_{i,j+1/2,k+1}^{q+1/2} - E_y\Big|_{i,j+1/2,k}^{q+1/2}}{\Delta z} \right.
$$

$$
- \frac{E_z\Big|_{i,j,k+1/2}^{q+1/2} - E_z\Big|_{i,j+1,k+1/2}^{q+1/2}}{\Delta y}
$$

$$
\left. - K_{ix}\Big|_{i,j+1/2,k+1/2}^{q+1/2} \right) \tag{A.4}
$$